The self-associative properties and therapeutic applications of chiral Supramolecular Self-Associating Amphiphiles

By Precious I. A. Popoola

A thesis submitted to the University of Kent for the degree of

Master of Science by Research in Chemistry

September 2022

Number of pages: 187

University of Kent

Division of Natural Sciences

School of Physical Sciences

Abstract

Reports estimate that globally, antimicrobial resistance directly caused 1.27 million deaths and indirectly caused 4.95 million deaths in 2019, while cancer directly caused 9.9 million deaths in 2020. With a growing resistance to current antibiotics and cancer treatments, there is an imperative need for new antimicrobial and anticancer agents to tackle this crisis. Supramolecular Self-associating Amphiphiles (SSAs) are a class of amphiphilic salts with the ability to undergo hydrogen bonded self-association and have been previously reported to act as both antimicrobial and anticancer agents. The SSA observed to have the greatest antimicrobial and anticancer activity was subsequently modified to create eight novel SSA compounds. Investigations into the physicochemical and self-associative properties of these novel compounds were conducted in the solid phase, gaseous phase and in solution using various techniques including quantitative ^{1}H NMR, mass spectrometry, tensiometry, dynamic light scattering, zeta potential and circular dichroism. Initial results showed that the novel compounds showed better antimicrobial and anticancer activity than the SSA they were derived from.

Contents

Abstract i

Contents ii

Acknowledgements vi

Abbreviations viii

1. Introduction 1

1.1. Supramolecular Chemistry 1

1.1.1. Definition 1

1.1.2. History 2

1.2. Noncovalent Interactions 4

1.3. Amphiphiles and Supra-amphiphiles 11

1.3.1. Amphiphiles 11

1.3.2. Supra-amphiphiles 14

1.4. Project Background, Aim and Objectives 17

1.4.1. Project Background 17

1.4.2. Project Aim 20

1.4.3. Project Objectives 21

2. Results and Discussion 22

2.1. Introduction 22

2.2. Self-association in the Solid Phase 24

2.3. Self-association in the Gaseous Phase 26

2.4. Self-association in Solution 29

2.4.1. Quantitative ^{1}H NMR Studies 29

2.4.2. ^{1}H NMR Self-association Studies 34

2.4.3. ^{1}H NMR DOSY Studies 37

2.4.4. Tensiometry Studies and CAC Determination 40

2.4.5. Dynamic Light Scattering Studies 43

2.4.6. Zeta Potential Studies 46

2.4.7. Circular Dichroism Studies 47

2.4.8. Membrane Fluidity 49

*2.4.9. Further Discussion - Compounds **17** and **19** 51*

2.5. Antimicrobial, Anticancer and Toxicity Assays 57

2.5.1. Introduction 57

2.5.2. Antimicrobial Assays 59

2.5.3. Anticancer Assays 61

2.5.4. Toxicity and Haemolysis Assays 63

2.5.5. DLS and ZP Studies in Biological Media 65

3. Conclusions 68

4. Future Work 69

5. Experimental Techniques and Synthesis 70

5.1. Chemical Experimental Techniques 70

5.2. Biological Experimental Techniques 74

5.3. Synthesis 77

6. References 83

7. Appendix 97

7.1. Characterisation NMR 97

7.2. Quantitative ^{1}H NMR Studies 101

7.2.1. DMSO-d_6/ 1.0 % DCM 101

7.2.2. D_2O/ 5.0 % EtOH 104

7.3. ^{1}H DOSY NMR Studies 106

7.4. ^{1}H NMR Self-association Studies 110

7.5. DLS Studies 118

7.5.1. Size Distribution Data in EtOH:H_2O (1:19) 118

7.5.2. Summary 124

7.5.3. Size Distribution Data in TSB 124

7.5.4. Summary 131

7.5.5. Size Distribution Data in IMDM with 10 % FBS 132

7.5.6. Summary 139

7.5.7. Size Distribution Data in PBS 139

7.5.8. Summary 146

7.6. Zeta Potential Studies 147

7.6.1. Zeta Potential in EtOH:H_2O (1:19) 147

7.6.2. Summary 150

7.6.3. Zeta Potential in TSB 151

7.6.4. Summary 154

7.6.5. Zeta Potential in IMDM with 10 % FBS 155

7.6.6. Summary 158

7.6.7. Zeta Potential in PBS 159

7.6.8. Summary 162

7.7. Single Crystal X-ray Structures 163

7.7.1. Hydrogen Bonding Tables 167

7.8. Mass Spectroscopy..... 167

7.8.1. Summary 171

7.9. Circular Dichroism Studies 172

7.10. Biological Assays..... 173

7.10.1. Antimicrobial (MIC) Data 173

7.10.2. Anticancer (GI_{50}) Data 173

7.10.3. Toxicity and Haemolysis Data 174

Acknowledgements

First, I want to give thanks to my Almighty Abba and Rock, the one and only true God – I couldn't have made it this far without You ordering my steps. Help me to keep going for my good and Your glory!

I'd like to extend my deepest gratitude to the Hiscock group: thank you for believing in me and pushing me to be a better chemist.

Next, I'd like to thank my amazing family for encouraging me throughout this whole year and being there for me.

To my 4lifers a.k.a. the Exodus crew: thanks for keeping me sane throughout this year. Love you guys!

From me to me: well done for enduring and making it to the end. It was far from easy, but you worked hard and tried your best, and that's all you can do. Now buckle up – we've got another 4 years to go! #noragrets (iykyk)

I dedicate this thesis to my loving grandmother Princess Esther Olaseni Adeosun (25/03/1907 – 15/03/2021), my beautiful sister and friend Jennifer ‘JP’ Phillips (21/12/1995 – 15/09/2021), and my big brother Ashley ‘Biggz’ Williams (24/02/1992 – 11/09/2022) – it hurts that you guys aren’t here anymore, and I still can’t comprehend it but now you can rest peacefully in the glorious arms of the Father.

Abbreviations

^{13}C NMR – carbon-13 nuclear magnetic resonance

1D - one-dimensional

^{1}H NMR – hydrogen-1 or proton nuclear magnetic resonance

2D - two-dimensional

3D - three-dimensional

Å - Ångstrom

AMR – antimicrobial resistance

br – broad (NMR)

CAC – critical aggregate concentration

CD - circular dichroism

CMC – critical micelle concentration

CoEK – co-operative equal K

cpw - cells per well

CTAB – cetyltrimethylammonium bromide

D – dextrorotatory (enantiomer configuration)

d – doublet (NMR)

DCM - dichloromethane

DEPT - Distortionless Enhancement by Polarization Transfer

d_H – hydrodynamic diameter

dH_2O – distilled water

DLS - dynamic light scattering

DMSO – dimethyl sulfoxide

DMSO-d_6 - deuterated dimethyl sulfoxide

DOSY - diffusion ordered NMR spectroscopy

DPH - 1,6-Diphenyl-1,3,5-hexatriene

E. Coli - *Escherichia coli*

EDG(s) – electron donating group(s)

EK – equal K

ESI - electrospray ionisation

ESI-MS - electrospray ionisation mass spectrometry

EtOH – ethanol

EtOAc – ethyl acetate

EWG(s) – electron withdrawing group(s)

FBS - foetal bovine serum

FP – fluorescence polarisation

FTIR - Fourier-transform infrared spectroscopy

g - grams

GI_{50} - concentration required to reduce cell growth by 50% versus untreated cells

HBA(s) – hydrogen bond acceptor(s)

HBD(s) – hydrogen bond donor(s)

H_2O - water

IMDM - Iscove's modified Dulbecco's medium

J - Coupling constant (NMR)

K – Kelvin

K_{dim} – dimerization constant

K_e – equal constant

L – laevorotatory (enantiomer configuration)

LCP – left circularly polarised

LDF(s) – London dispersion force(s)

m – multiplet (NMR)

m/z - mass-to-charge ratio

MIC - minimum inhibitory concentration required to decrease microbial growth

MIC_{50} –minimum inhibitory concentration required to decrease microbial growth by 50%

MIMA - mechanically interlocked molecular architecture

mol – mole(s)

MRSA – methicillin-resistant *Staphylococcus aureus*

MS – mass spectrometry

NMR - Nuclear magnetic resonance spectroscopy

°C – degrees Celsius

OD_{600} – optical density measured at a wavelength of 600 nm

PBS – phosphate-buffered saline

PDI – polydispersity index

q -quartet (NMR)

qNMR – quantitative nuclear magnetic resonance

RCP – right circularly polarised

RT – room temperature

s – singlet (NMR)

S. aureus - *Staphylococcus aureus*

SB-8 – sulfobetaine 8

SDS – sodium dodecyl sulphate

SRB - sulforhodamine B

SSA(s) – supramolecular self-associating amphiphile(s)

t – triplet (NMR)

TCA - trichloroacetic acid

TBA – tetrabutylammonium

TSB - tryptic soy broth

vdW – van der Waals

VT – variable temperature

XRD – x-ray diffraction

ZP – zeta potential

1. Introduction

1.1. Supramolecular Chemistry

1.1.1. Definition

First named by Jean-Marie Lehn in 1969, supramolecular chemistry is widely defined as 'chemistry beyond the molecule' [1] - an interdisciplinary field that studies the highly complex and organised molecular systems that result from the interaction of two or more chemical species held together by noncovalent interactions. [2–5] A pioneer in the field of supramolecular chemistry, Lehn later elaborated further, stating, '*Beyond molecular chemistry based on the covalent bond, there lies the field of supramolecular chemistry whose goal is to gain control over the intermolecular bond. It is concerned with the next step in increasing complexity beyond the molecule towards the supermolecule and organised molecular systems […]*'.[1,6] Supramolecular chemistry can be divided into two categories: host-guest chemistry and self-assembly. Coined by Donald James Cram, host-guest chemistry studies the complexes formed between large 'host molecules and smaller 'guest' molecules.[7] On the other hand, self-assembly concerns the spontaneous formation of a large aggregate from the components of one system.[8] In both cases, the weak and reversible noncovalent interactions serve as a form of molecular recognition between the host and guest components, and between the components in the self-assembled aggregate respectively, controlled by thermodynamics.[5,8]

1.1.2. History

Preceding the establishment of supramolecular chemistry as a recognised field were the principles and theories of many scientists, beginning with Johannes Diderik van der Waals who hypothesised the existence of intermolecular forces in his 1873 doctoral thesis.[9–11] Shortly after, in 1894, Hermann Emil Fischer proposed the lock-and-key concept to explain the substrate selectivity of enzymes, which would later serve as the basis for host-guest chemistry. Fischer hypothesised that an enzyme's active site (i.e., the lock/host) could only be occupied by a substrate with a specific complementary shape (i.e., the key/guest) and that this subsequent complex was held together by intermolecular forces.[12] By 1920, intermolecular forces, particularly the hydrogen bond, were understood in more depth due to the work of Wendell Mitchell Latimer and Worth Huff Rodebush,[13] which was developed from the work of Tom Sidney Moore and Thomas Field Winmill.[14] These fundamental concepts were then taken and applied, providing the breakthroughs that birthed supramolecular chemistry and cemented by the 1987 Nobel Prize in Chemistry which was awarded to Lehn, Charles John Pedersen and Cram for their work that formed the basis of host-guest chemistry (Figure 1).[4,15–17]

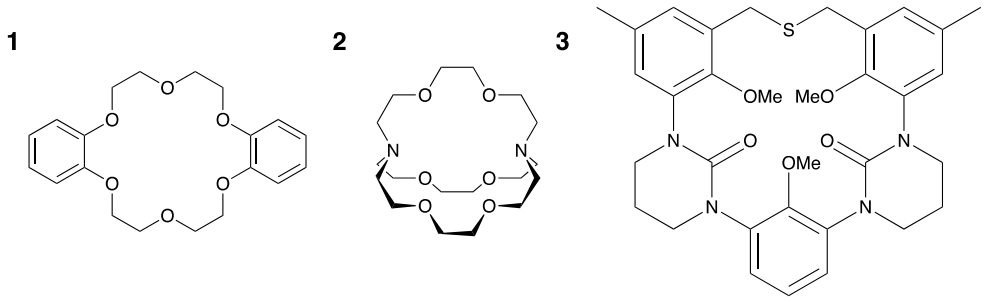

Figure 1 - Examples of host-guest complexes developed by **1**) Pedersen (dibenzo-18-crown-6); **2**) Lehn ([2.2.2]cryptand); and **3**) Cram (spherand).

Supramolecular chemistry evolved further Jean-Pierre Sauvage, Sir James Fraser Stoddart and Bernard Lucas Feringa were awarded the 2016 Nobel Prize in Chemistry for their work in the synthesis and development of molecular machines.[18] Sauvage took the first step in 1983 when he synthesised a catenane (Figure 2a), an assembly consisting of two interlocked molecular rings held by mechanical bonds and an example of a mechanically interlocked molecular architecture (MIMA) - the two rings can move freely with respect to each other but cannot be separated unless the bond interlocking them is broken.[19] Afterwards, in 1991, Fraser Stoddart developed rotaxanes: MIMAs consisting of macrocyclic rings able to move on the molecular axles formed between two bulky molecular 'stoppers' when introduced to external stimuli (Figure 2b).[20] This was particularly important as it showed that supramolecular complexes could act as motors and consequently gave way to Feringa's work, which saw the development of molecular motors and the construction of the nanocar in 1999.[21]

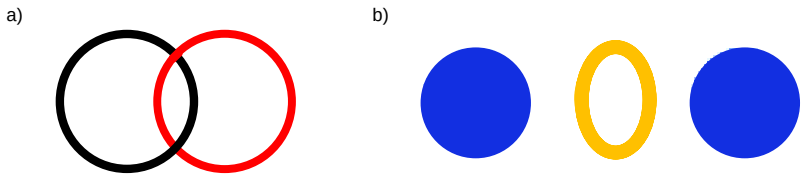

Figure 2 - General graphic representations of a) a catenane and b) a rotaxane.

1.2. Noncovalent Interactions

As previously mentioned in Section 1.1.1., supramolecular chemistry is dependent on noncovalent interactions because they serve as a form of molecular recognition and are weak and reversible, allowing the formation of complex supramolecular aggregates (see Section 1.3). Although they are weak, an increased number of noncovalent interactions in a system result in increased stability.[7,8] Noncovalent interactions are mainly intermolecular (i.e., they involve the distribution of electrons between two or more molecules) and Coulombic (i.e., based on the attraction between two opposing charges) in nature, although some exhibit covalent characteristics.[22] The types of noncovalent interactions include van der Waals (vdW) forces, pi–pi (π– π) interactions, hydrogen bonding, ion-dipole interactions, and ion-ion interactions.[23]

The weakest form of noncovalent interactions, vdW forces are comprised of three interactions that contribute to the overall attraction between the molecules in a system:[24,25]

a. Permanent dipole-permanent dipole interactions (also referred to as Keesom interactions) occur when two molecules with permanent dipoles (or polar molecules) close to each other interact, with a relative binding strength of ≤ 25 kJ mol^{-1}.[24,26]
b. Permanent dipole-induced dipole interactions (also referred to as Debye interactions) occur when a polar molecule repels the electrons of (and thereby induces a dipole in) a nearby non-polar molecule and have a relative binding strength of ≤ 3 kJ mol^{-1}.[24,26]
c. Instantaneous dipole-induced dipole interactions (also referred to as London dispersion forces or LDFs) occur when the electron distribution of a non-polar molecule randomly fluctuates and is unsymmetrical. This produces an instantaneous temporary dipole that subsequently induces a dipole on another non-polar molecule nearby, causing them to attract each other. LDFs can also occur between atoms and do not require permanent dipoles. The relative binding strength of LDFs is ≤ 45 kJ mol^{-1} [24] however, this depends on the size and polarizability of the molecules involved.[8,23,26] Compared to Keesom and Debye interactions, LDFs tend to make up the majority of vdW attraction forces in a system.[24,25]

π–π interactions are interactions that occur between conjugated π-systems, predominantly aromatic rings. There are different types but, regarding supramolecular chemistry, only two are of main importance:[8]

a. π–π interactions are interactions between two conjugated π-systems with binding strengths ranging between 0 – 50 kJ mol^{-1},[8] and can arise when the π-systems are in one of three conformations (Figure 3a):
    i. Edge-to-face or CH–π interactions arise when a hydrogen atom interacts with the centre of a π-system, resulting in a charge transfer between the C–H orbital and the delocalised π-system.[7,27,28]
    ii. Offset stacked interactions arise between the centre of one π-system and the edge of another. [7,27,28]
    iii. Face-to-face stacked interactions arise between the centres of two π-systems.[7,27,28] Unlike edge-to-face interactions or offset stacked interactions, face-to-face interactions tend to be electrostatically unfavourable and repulsive, for example between two benzene rings. However, the interaction between the faces of the electron-rich benzene and the electron-poor hexafluorobenzene is attractive.[29,30]
b. Cation–π interactions are interactions between a cation and the face of a π-system, with binding strengths ranging between 5 – 80 kJ mol^{-1} (Figure 3b). [7,8,31]

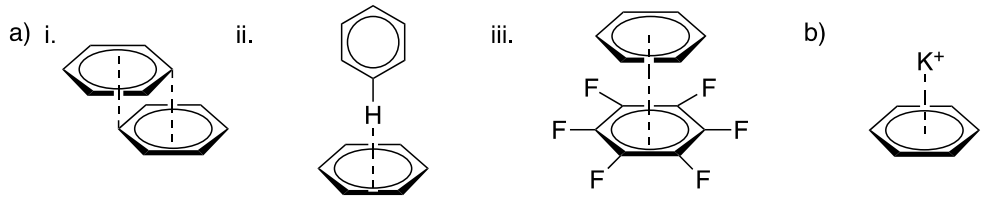

Figure 3 - Illustrations showing a) the three different types of π-π interactions: i. edge-to-face; ii. offset stacked; iii. face-to-face stacked, and b) an example of cation-π interactions between benzene and a potassium ion.

Hydrogen bonding is a specific type of permanent dipole-permanent dipole interaction (which also has covalent characteristics) and results from the interaction between a proton donor group and a proton acceptor group, also known as the hydrogen bond donor (HBD) and the hydrogen bond acceptor (HBA) respectively (Figure 4).[7,8,24,32,33]

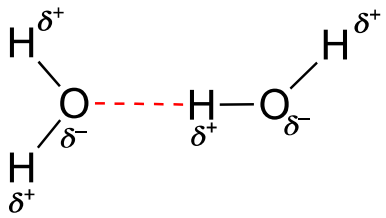

Figure 4 - An example of hydrogen bonding in water. Here, one of the partially positive hydrogen atoms in one water molecule is the HBD, while the partially negative oxygen atom in the other water molecule is the HBA, with the hydrogen bond represented with a red dashed line.

HBD groups consist of a hydrogen atom covalently bonded to a more electronegative heteroatom (e.g., fluorine, oxygen, nitrogen, chlorine etc.) – this difference in electronegativity creates a permanent dipole and positively polarises the hydrogen atom slightly, resulting in a partial charge (denoted by the ∂^+ symbol). HBA groups consist of either electronegative atoms that have a lone pair or the delocalised electron cloud in aromatic systems.[7,8,23] Additionally, functional groups can form hydrogen bonds, either as an HBD, HBA, or both. For example, ketone and nitrile groups can be HBAs, while hydroxyl and imine groups can be both HBDs and HBAs. [34] The strength of hydrogen bonds varies from 4 – 120 kJ mol^{-1} [8] and is influenced by the nature of the electronegative atom in the HBA group and/or the HBD group, and whether the HBD and HBA groups are already participants in other hydrogen bonds. Another influence on the strength of hydrogen bonds is the geometry the hydrogen-bonded system adopts as a result of the direct interactions between the HBD group and HBA group (otherwise known as primary hydrogen bond interactions). Hydrogen bonds are typically short, highly directional, and optimise at 180 ° to give a linear geometry. However, the longer the distance between the HBD group and the HBA group, the less directional the bond and the less linear the geometry - the different geometries that can be formed are shown in Figure 5.[7,8,35,36]

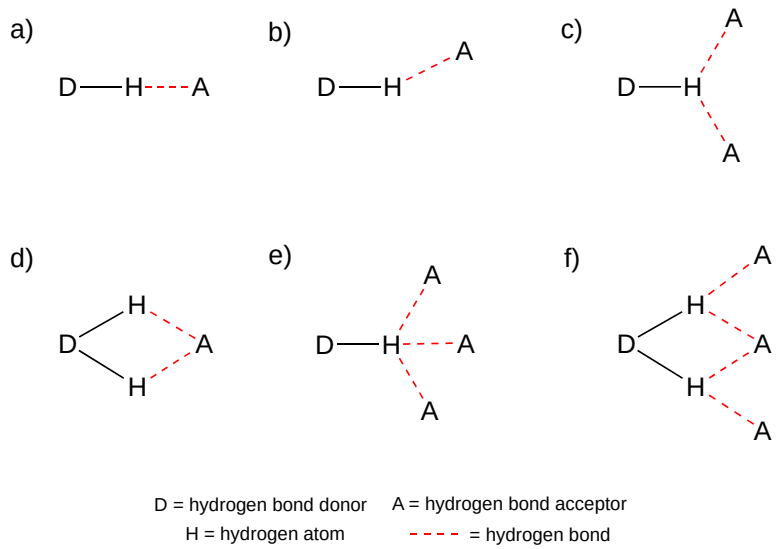

Figure 5 - The six different hydrogen bonding geometries that can potentially form as a result of primary hydrogen bond interactions: a. linear; b. bent; c. donating bifurcated; d. accepting bifurcated; e. trifurcated; f. three-centre bifurcated.

In addition to primary bond interactions, there are secondary hydrogen bond interactions that occur between neighbouring groups that can also affect the strength of the hydrogen bond, either by increasing attraction and strengthening the hydrogen bond, or increasing repulsion and weakening the hydrogen bond.[8] Furthermore, other factors that affect the ability of the HBD group to donate a proton and/ or the HBA group to accept a proton (such as substituents in an aromatic system, or conjugation) or factors that affect the entire system (including temperature, pressure, and bond angles) can also affect the strength of the hydrogen bond.[7,8,35,37,38]

The last two noncovalent interactions include the presence of ions: ion-dipole interactions and ion-ion interactions. Ion-dipole interactions occur between ions and polar molecules and have strengths ranging between 50 – 200 kJ mol^{-1}.[7,8] Examples include the interactions in the 15-crown-5 potassium complex and the interactions between sodium ions and water molecules (Figures 6a and 6b). Ion-ion interactions are the strongest form of noncovalent interactions, occurring between ions of opposite charge with strengths ranging from 100 – 350 kJ mol^{-1}, similar to the strength of a covalent bond.[7,8,23] Examples include tetrabutylammonium chloride (TBA Cl) and sodium chloride (Figures 6c and 6d).

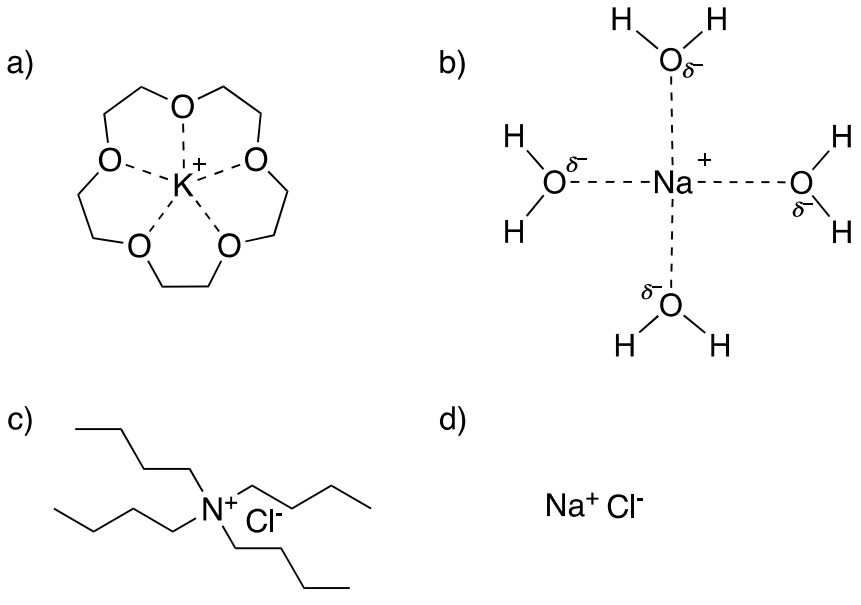

Figure 6 - Examples of ion-dipole interactions in a) the potassium complex of 15-crown-5 and b) sodium ions in water, and of ion-ion interactions in c) tetrabutylammonium chloride (TBA Cl), and d) sodium chloride.

1.3. Amphiphiles and Supra-amphiphiles

1.3.1. Amphiphiles

Amphiphiles are molecules that possess both hydrophilic (water-loving or polar) and hydrophobic (fat-loving or non-polar) components covalently bound to one another and can self-assemble into a vast range of structures when in solution or at an interface. Traditional examples of amphiphiles include a hydrophilic head connected to a long hydrophobic hydrocarbon chain. However, there are different classes of amphiphiles depending on the nature of the hydrophilic head:[39]

a. Anionic amphiphiles contain a negatively charged head group with a positive counterion (Figure 7, **4**, SDS) and are mainly used in cleaning products such as washing up liquid and shampoos.[40]
b. Cationic amphiphiles contain a positively charged head group, typically a quaternary ammonium salt, with a negative counterion (Figure 7, **5**, CTAB). The presence of the quaternary ammonium salt produces properties that are desirable for a variety of applications e.g., some possess the ability to reduce surface tension so are used as wetting agents, while others possess antimicrobial properties and are used in pharmaceuticals.[40,41]
c. Nonionic amphiphiles (Figure 7, **6**, sorbitan laurate) have a head group that possesses no charge (e.g., alcohols, esters, polyethers etc.), with vast applications when alone (e.g., as emulsifiers, defoaming agents or in pharmaceuticals etc.) or when paired with

anionic amphiphiles (typically in household cleaning agents such as laundry and dishwasher detergents).[39,42]

d. Amphoteric or zwitterionic amphiphiles have both positive and negative charges in the head group (Figure 7, **7**, SB-8) and possess non-toxic and biodegradable properties, allowing use in cosmetic and personal care products.[43]

4

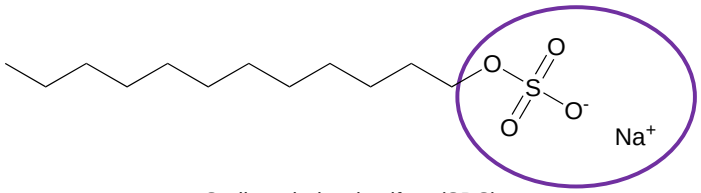

Sodium dodecyl sulfate (SDS)

5

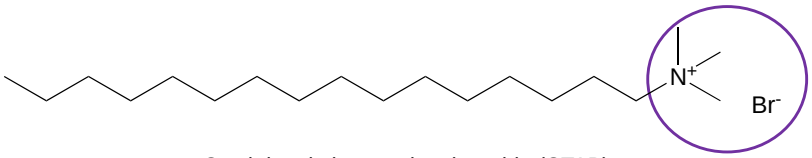

Cetyltrimethylammonium bromide (CTAB)

6

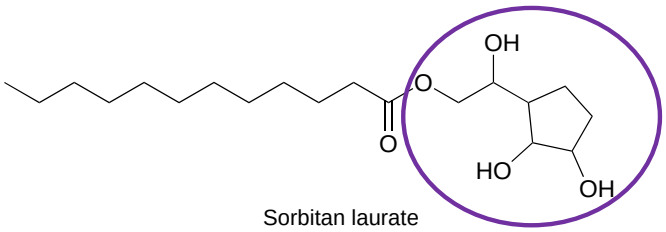

Sorbitan laurate

7

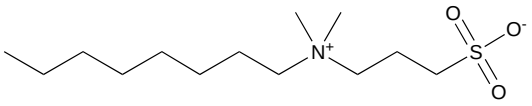

Sulfobetaine 8 (SB-8)

Figure 7 - Examples of the different types of amphiphiles: **4**) anionic, **5**) cationic, **6**) nonionic, and **7**) zwitterionic. The hydrophilic head is highlighted by a purple circle, the anionic area is highlighted in red, and the cationic area is highlighted in green.

A main characteristic of amphiphiles is their ability to self-assemble and form aggregates upon reaching a certain concentration known as either the critical micelle concentration (CMC) or, more accurately, the critical aggregate concentration (CAC). However, depending on factors such as the pressure, pH, polarity, or temperature of the solvent environment the amphiphile is in, the type of aggregate or morphology formed may differ (Figure 8).[8,39,44,45] For example, with regard to the polarity of the solvent environment, micelles and bilayers are formed in aqueous solutions as the hydrophilic head favours the polar environment, whereas reverse micelles are formed in nonpolar solutions. The structure of the amphiphile can also influence the morphology – amphiphiles with a single hydrophobic tail commonly form either micelles or reverse micelles but amphiphiles with multiple hydrophobic tails commonly form bilayers.[39,46]

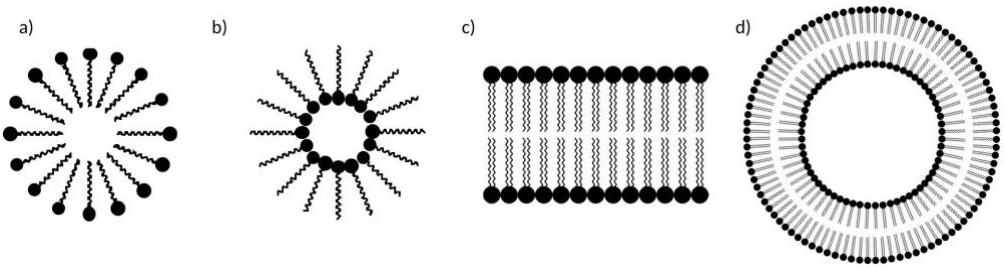

Figure 8 - Graphic representations showing four of the possible morphologies amphiphiles can form in solution: a) micelle, b) reverse micelle, c) bilayer and d) vesicle.

1.3.2. Supra-amphiphiles

Supra-amphiphiles are amphiphiles that form supramolecular complexes using noncovalent interactions and host-guest molecular recognition.[47–49] For instance, supra-amphiphiles have been formed using charge-transfer interactions,[50] electrostatic interactions,[51,52] hydrogen bonds,[53] metal-ligand interactions,[54] and π-π interactions.[55] Supra-amphiphiles have also been formed using covalent bonds,[56] including imine bonds as reported by Minkenberg *et. al*.[57]

The formation of supra-amphiphiles using host-guest molecular recognition can be done through the use of hydrogen bonding, using the urea functional group in particular (Figure 9).

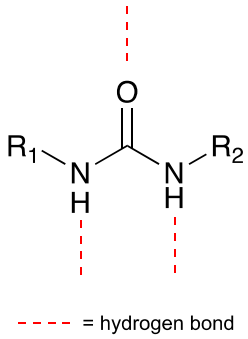

Figure 9 - The general structure of the urea functional group, with red dashed lines indicating where hydrogen bonds can form.

The urea group is desirable as it is a strong HBD group due to the two NHs and, by incorporating electron-withdrawing groups (EWGs) such as aromatic rings, the acidity of the protons increases, thereby increasing its strength as an HBD group and its affinity to the guest molecule. [58–60]

Hiscock *et al.* used the urea functionality in their design of **S**upramolecular **S**elf-associating **A**mphiphiles (**SSA**s) – Figure 10 shows the general structure of the SSA consisting of a urea group containing both HBD (the two NHs) and HBA (the X group) groups, a hydrophobic region, an anionic hydrophilic region with an HBA group (the Y^- anion), and a counter cation.[61]

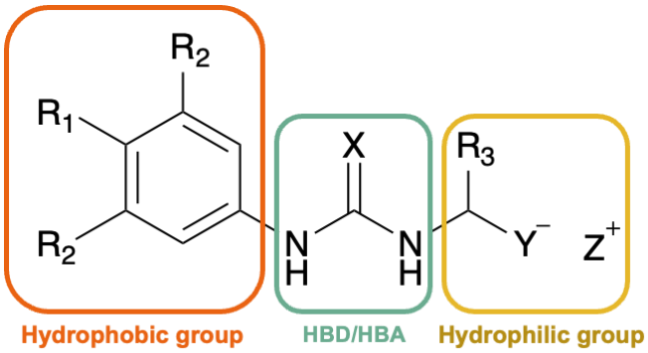

Figure 10 - The general structure of a supramolecular self-associating amphiphile (SSA).

Due to the HBD group and the two HBA groups, SSAs can self-associate via hydrogen bonding and adopt four binding modes but not at the same time, resulting in a 'frustrated system' (Figure 11).[61,62] The binding mode adopted depends on the structure of the SSA, the solvent system, and the counter cation.

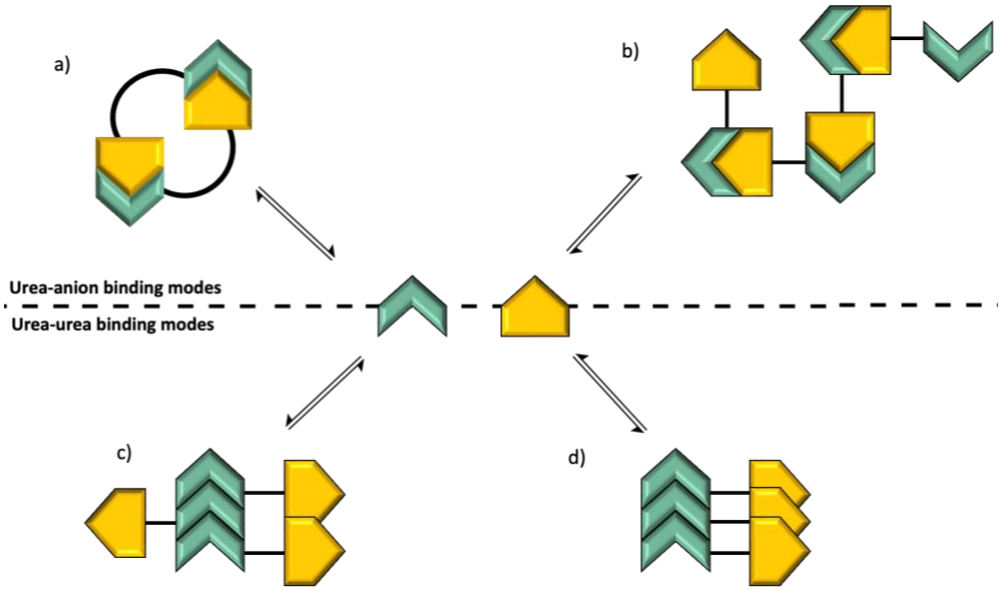

Figure 11 - The four possible modes of hydrogen-bonded self-association of SSAs: a) urea-anion dimer formation, b) urea-anion stacking, c) anti-urea-urea stacking or d) syn-urea-urea stacking.

Using the first SSA as a template, modifications were made to inform the design of the next generation of SSAs synthesised, and to establish the structure-activity relationship. This was done in a variety of ways:

- By increasing or decreasing the number of the R groups on the aromatic ring and modifying the R groups to include either EWGs or electron-donating groups (EDGs).[62–66]
- By creating analogues in two ways: using either a urea group or a thiourea group in the urea region or using either a carboxylate group or sulphonate group as the anion.[62,64–67]
- By changing the counter cation used.[62,64,66]

1.4. Project Background, Aim and Objectives

1.4.1. Project Background

With the extensive library of SSAs created through these modifications, Hiscock *et al.* conducted antimicrobial and anticancer assays to determine whether the SSAs had antimicrobial and/or anticancer properties and, if so, which SSA showed the best activity. Subsequently, some SSAs have been reported to act as antimicrobial agents against clinically relevant bacteria,[66] antibiotic delivery agents,[63,66] antimicrobial efficacy enhancers,[68] and anticancer agents by enhancing the efficacy of cytotoxic chemotherapies such as cisplatin.[69] With reports estimating that antimicrobial resistance (AMR) caused 4.95 million deaths in 2019,[70] and cancer caused 9.9 million deaths in 2020,[71] the need for new antimicrobial and anticancer agents is vital and the continuous development and production of next-generation SSAs is proving to be valuable towards this need.

SSAs **8**, **9**, **10** and **11** (Figure 12) are carboxylate salts that are analogues of each other:

- **8** and **9** possess a urea group, while **10** and **11** possess a thiourea group.
- **8** and **10** possess hydrogen as the counter cation (i.e., have a carboxylic acid group), whereas **9** and **11** possess tetrabutylammonium (TBA) as the counter cation.

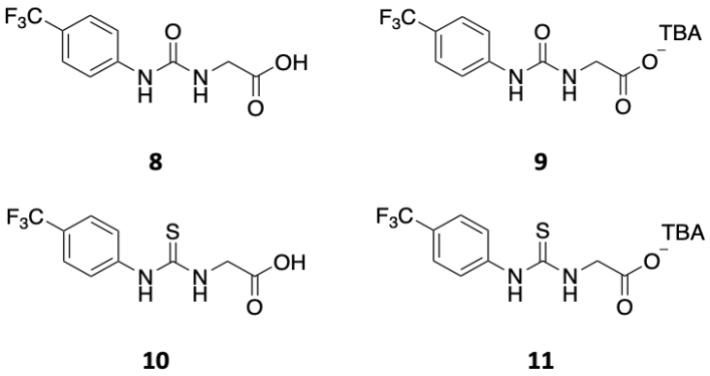

Figure 12 - The structures of SSAs **8**, **9**, **10** and **11**.[64,66]

In 2020, Hiscock *et al.* reported that **9** was the most effective against both the Gram-positive methicillin-resistant *Staphylococcus aureus* (MRSA) USA 300 strain and the Gram-negative *Escherichia coli* (*E*. coli) DH10B strain compared to 46 varying SSAs (including its analogues **8**, **10** and **11**) and 4 quaternary ammonium chloride salts (Table 1).[66] Therefore, it was established that the presence of both the urea group and TBA cation increased antimicrobial activity.

Table 1 - The minimum inhibitory concentration required to decrease microbial growth by 50% (MIC_{50}, mM) values determined for **8**, **9**, **10** and **11** against Gram-positive MRSA USA 300 and Gram-negative E. coli DH10B strains, with Ampicillin used as a control to test the validity of the antimicrobial MIC_{50} determination methods. Fail = compound failed initial antimicrobial screening. [a] = endpoint of experiment predicted due to compound solubility.[66]

MIC_{50} (mM)		
SSA	**MRSA USA 300**	**E. coli DH10B**
8	Fail	Fail
9	1.14	1.25
10	0.83	Fail
11	0.77	Fail
TBA Cl	3.18	6.36[a]
Ampicillin	0.0003	0.003

Consequently, this project aims to use **9** as a backbone for the design of the next generation of SSAs to investigate structure-activity relationships and determine if the modifications made improve the antimicrobial and anticancer activity. Herein, eight novel SSA compounds are characterised and studied to assess their self-associative, antimicrobial, and anticancer activities. Modifications made included replacing one of the prochiral hydrogen atoms in **9** to introduce chirality, then subsequently creating analogues of these chiral molecules to introduce a change in functionality (Figure 13):

- Compounds **12** – **15** are derived from the amino acid phenylalanine, with the carboxylate group in **12** and **14** being tert-butyl protected and **13** and **15** having TBA as a counter cation.
- Compounds **16** – **19** are derived from the amino acid leucine, with the carboxylate group in **16** and **18** being tert-butyl protected and **17** and **19** having TBA as a counter cation.

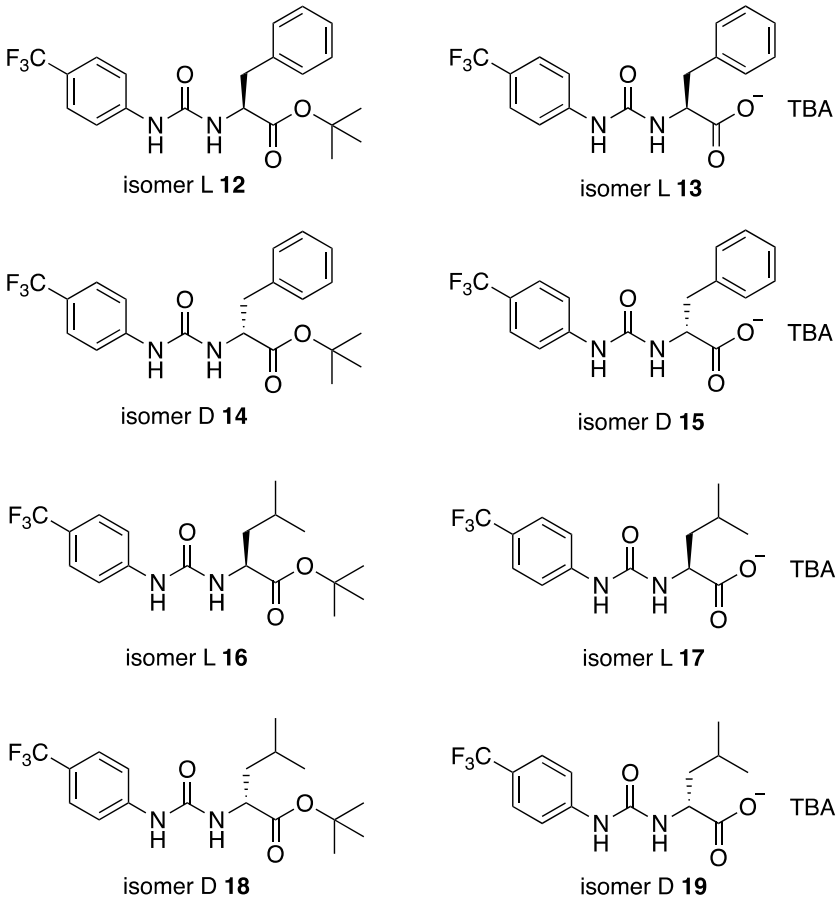

Figure 13 - The structures of the novel SSA compounds **12** – **19** synthesised for this project.

1.4.2. Project Aim

To synthesise and characterise a novel class of supramolecular self-associating amphiphiles (SSAs) and assess their self-associative, antimicrobial, and anticancer activities.

1.4.3. Project Objectives

- To synthesise and characterise the physicochemical properties of novel compounds **12** – **19**.
- To assess the self-associative properties of **12** – **19**.
- To investigate the effect the modifications made to **9** to design **12** – **19** have on antimicrobial and anticancer efficacy.

2. Results and Discussion

2.1. Introduction

The self-association of SSAs can be studied in the solid phase, gas phase and solution. But, as the assemblies that form are complex, a range of techniques are used to complete the physicochemical characterisation and observe the self-association of these SSA compounds. This process is outlined as a flow chart as shown in Figure 14. The techniques that are used for physicochemical characterisation include electrospray ionisation mass spectrometry (ESI-MS), Fourier-transform infrared spectroscopy (FTIR), melting point and NMR (^{1}H, ^{13}C and DEPT). To observe self-association, multiple techniques can be used in the solid, gaseous, and liquid phases. In the solid phase, single-crystal X-ray diffraction (XRD) is used to detect self-association (Section 2.1), while ESI-MS is used to additionally observe self-association in the gaseous phase (Section 2.2).[61] In solution (Section 2.3), multiple techniques are used to detect self-association in either organic solvents, aqueous solvents, or both – these techniques include quantitative ^{1}H NMR (qNMR), tensiometry (to obtain the CAC), dynamic light scattering (DLS), zeta potential (ZP), self-association studies and diffusion ordered NMR spectroscopy (DOSY). Other techniques are also used, such as circular dichroism (CD) and membrane fluidity.

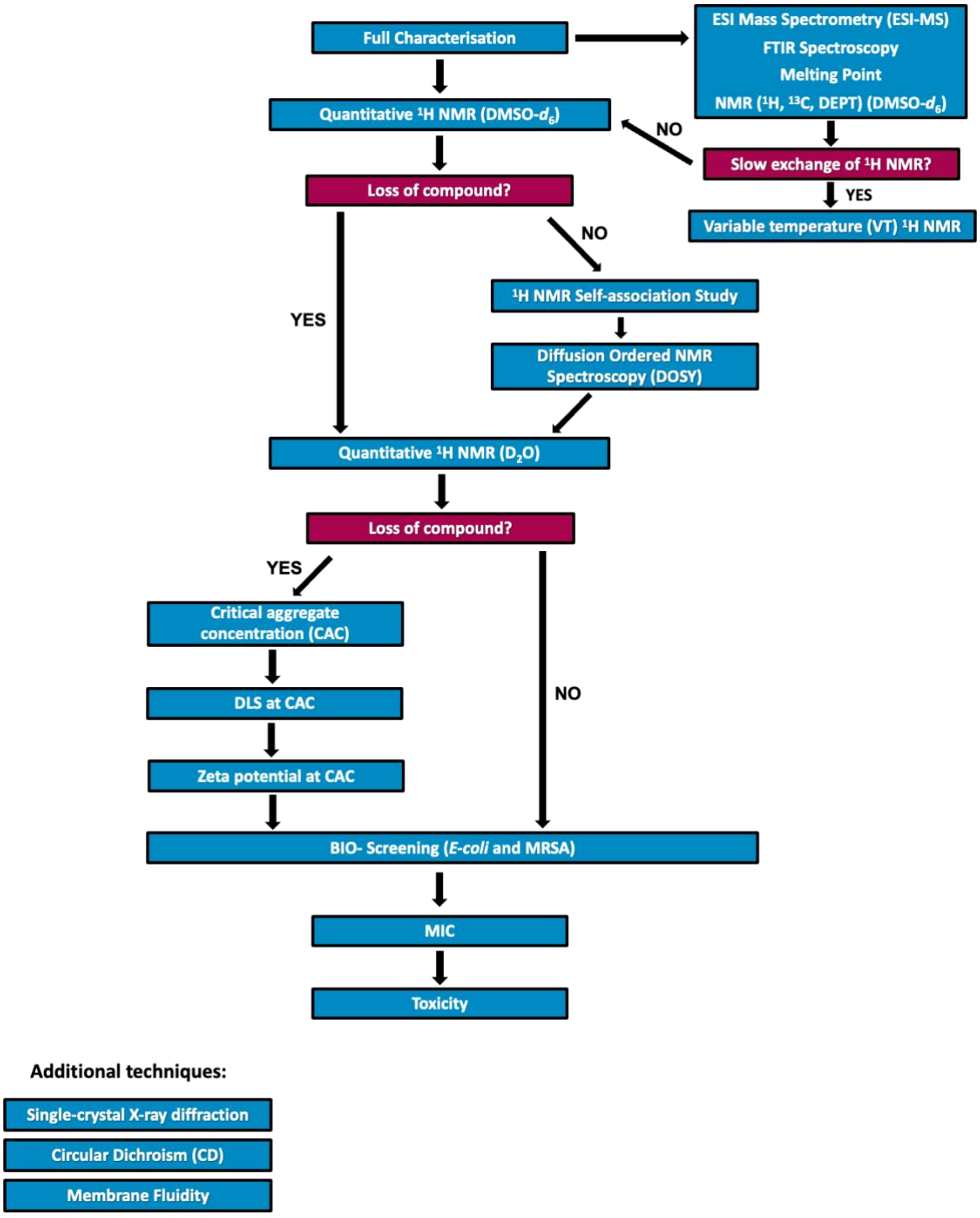

Figure 14 - A flow chart showing all the techniques used to characterise novel SSA compounds. A blue box represents an action and a red box represents a decision to make if an issue arises.

2.2. Self-association in the Solid Phase

Single-crystal XRD is a non-destructive analytical technique, first developed by Max von Laue.[72] The technique was further developed by Walter Friedrich and Paul Knipping who were consequently awarded the 1914 Nobel Prize in Physics.[73] Single-crystal XRD is commonly used in supramolecular chemistry to obtain and identify three-dimensional (3D) structures of repeating units within a single crystal.[74] The novel single crystal x-ray structures obtained and discussed in this section were obtained by Dr Jennifer R. Hiscock.

Single crystals of **12**, **14**, **16** and **18** were obtained through selective precipitation using chloroform and hexane - they do not contain an anionic functionality, as the anionic group is protected by a tert-butyl ester, however they still exhibit hydrogen bonded self-association. For isomers **12** and **14**, three bonds were formed between the urea N-H, the urea oxygen, and the oxygen of the protected carboxylic acid, with one urea N-H forming two bonds with the urea oxygen and the oxygen of the protected carboxylic acid (see Figure 15). However, while **16** and **18** also showed self-association through hydrogen bonds between the urea N-H and the oxygen of the protected carboxylic acid, only two bonds are formed (see Figure 16).

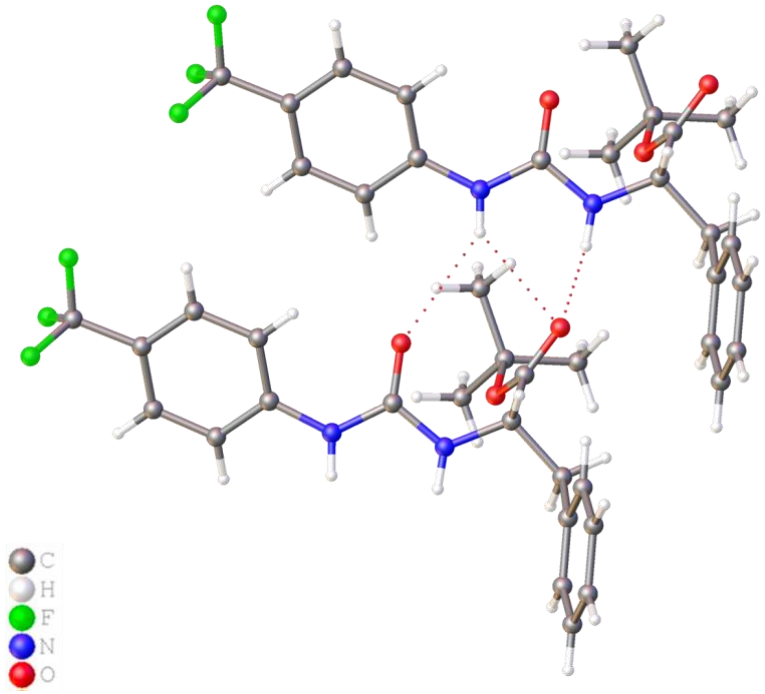

Figure 15 - Single crystal X-ray structure of **12**, where red = oxygen, green = fluorine, blue = nitrogen, white = hydrogen, and grey = carbon. TBA cation omitted for clarity.

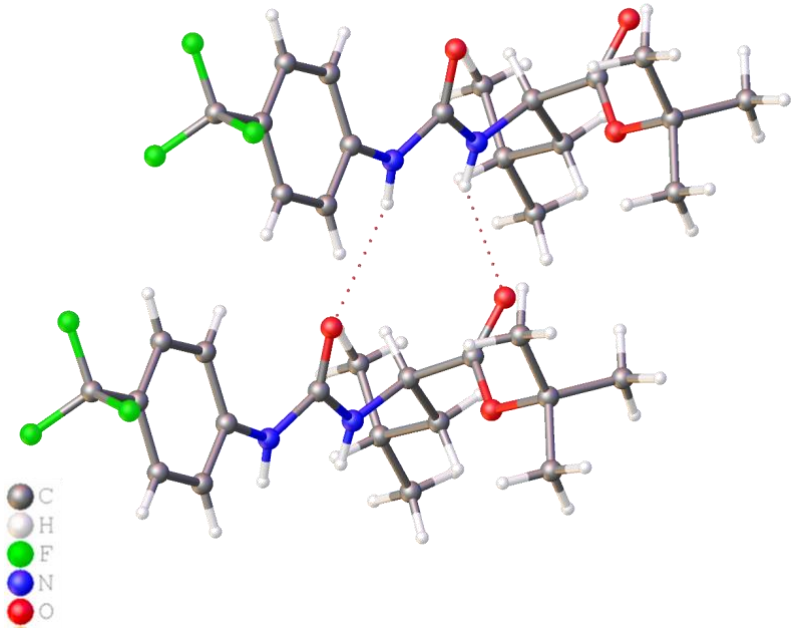

Figure 16 - Single crystal X-ray structure of **16**, where red = oxygen, green = fluorine, blue = nitrogen, white = hydrogen, and grey = carbon. TBA cation omitted for clarity.

All single crystal X-ray structures for **12**, **14**, **16** and **18** are presented in the appendix (see Section 7.7.). Single crystals could not be obtained for SSAs **13**, **15**, **17** and **19** upon completion of this project, but efforts are ongoing to obtain these.

2.3. Self-association in the Gaseous Phase

ESI-MS is comprised of two techniques: electrospray ionisation (ESI) and mass spectrometry (MS). MS is an analytical technique used to measure the mass-to-charge ratio (m/z) of ions but can also be used to calculate molecular weight to identify unknown samples or to identify the structural and chemical properties of molecules.[75] This technique requires the components in the sample to have an electrical charge and this is done through ionisation of the sample. There are two types of ionisation – hard ionisation uses greater amounts of energy to ionise the sample which causes more of the bonds in the molecules to break and creates fragments, while soft ionisation uses lesser amounts of energy to ionise the sample, creating little to no fragments (or none at all) compared to hard ionisation.[76,77] ESI is a soft ionisation that uses an electrospray to apply a high voltage to a liquid sample to create an aerosol. As a soft ionisation technique, ESI is often used to analyse fragile macromolecules and supramolecular complexes due to the lack of fragmentation and the preservation of noncovalent interactions in the gaseous phase.[75,78,79]

In this project, ESI-MS was used to both characterise and determine whether self-association is present in the anionic component of the novel compounds. Each compound was run at a concentration of ~ 1 x 10^{-6} mol in methanol (MeOH). The data obtained showed that **12** – **19** exist as anionic monomeric $[M]^-$ species and **13**, **15**, **17** and **19** also exist as protonated self-associated dimeric $[M + M + H]^-$ species (Table 2). As **12**, **14**, **16** and **18** are tert-butyl protected, there are no anionic or ionisable components which explains why protonated dimeric species were not observed for these compounds.

Table 2 - High-resolution electrospray ionisation mass spectrometry (ESI-MS) theoretical and experimentally derived values.

	m/z $[M]^-$		m/z $[M + M + H]^-$	
SSA	**Theoretical**	**Actual**	**Theoretical**	**Actual**
12	408.1661	408.1227	N/A	N/A
13	351.0962	351.0952	703.1996	703.1970
14	408.1661	408.1502	Not observed	
15	351.0962	351.0937	703.1996	703.1859
16	374.1817	374.1739	N/A	N/A
17	317.1118	317.1110	635.2308	635.2271
18	374.1817	374.1763	Not observed	
19	317.1118	317.1160	635.2308	635.2408

Using **13** as an example, the theoretical $[M]^-$ m/z value was calculated to be 351.0962 while the theoretical $[M + M + H]^-$ m/z value was calculated to be 703.1996 (351.0962 + 351.0962 + 1.0072). The ESI-

spectrum in Figure 17 shows the presence of the $[M]^-$ species with an actual m/z of 351.0952, and the presence of the $[M + M + H]^-$ species with an actual m/z of 703.1859.

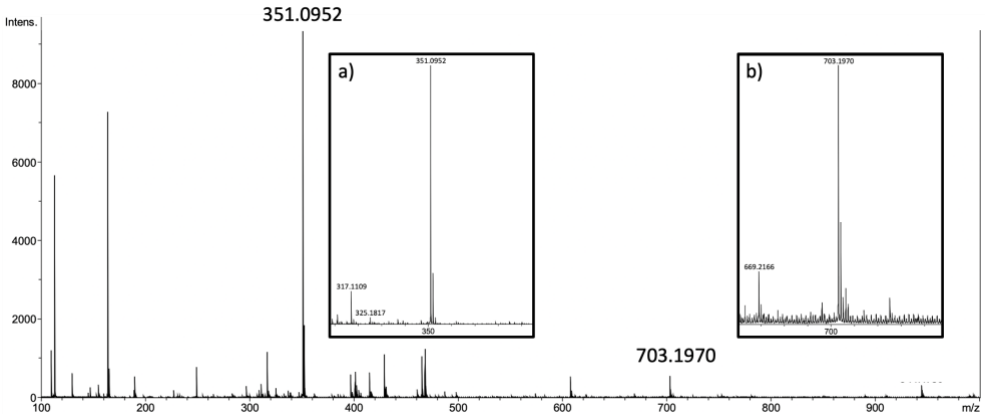

Figure 17 - The ESI-MS spectrum of **13**, showing both a) the anionic monomeric species $[M]^-$ with an m/z of 351.0952 and b) the protonated dimeric species $[M + M + H]^-$ with an m/z of 703.1859.

To summarise, it was observed that self-association occurs in the gas phase providing there is an anionic or ionisable component, indicating that the noncovalent interactions that form in the dimers are strong enough to withstand ionisation. The exact strength of these interactions cannot be determined in the gaseous phase therefore these compounds were further explored in the solution state using different techniques. All ESI-MS spectra for **12** – **19** are presented in the appendix (see Section 7.8.).

2.4. Self-association in Solution

The study of self-association in the solid and gaseous phases allows observation without the need for a solvent. Nevertheless, solvent interactions must be considered when studying self-association as the binding modes of SSAs depend on the solvent environment. For example, it has been shown previously that SSAs tend to form dimers in dimethyl sulfoxide (DMSO) but form spherical aggregates in water with 5 % ethanol (EtOH).[61–65,67,80,81] This is because of the influence the hydrophobicity, hydrophilicity and hydrogen bonding nature of the solvent has on the formation of self-associated complexes e.g., both water and DMSO interact with SSAs due to their HBD and HBA groups but because they have a different number of HBDs/HBAs, their interactions with SSAs differ.[82,83] As a result, a range of techniques were used to observe the self-association of the novel SSAs in solution.

2.4.1. Quantitative ^{1}H NMR Studies

Quantitative ^{1}H NMR (qNMR) is a technique used to quantify the concentration of molecules with low molecular weight (LMW) and produces initial evidence of species such as dimers and larger aggregates.[84] Based on this, the Hiscock group have applied qNMR to quantify the concentration of various molecular components visible to solution-state NMR against an internal standard to determine if SSAs form aggregates that adopt solid-like properties, which leave them unobservable using

solution-state NMR.[65] In this project, qNMR was used to quantify the concentration of **13**, **15**, **17** and **19** using an organic solvent system and an aqueous solvent system: deuterated DMSO (DMSO-d_6) doped with 1.0 % dichloromethane (DCM) at 112 mM, and deuterated water (D_2O) doped with 5 % EtOH at 5.56 mM respectively. DCM and EtOH are the internal standards used as both solvents are miscible in their respective main solvents and their NMR signals do not overlap or appear near any signals attributed to the compounds being studied. The doped solvent signal is comparatively integrated against the anionic component and, if present, the cationic component of the SSA to calculate the apparent percentage '*loss*' of the compound. Using **13** as an example (Equation 1), the ratio of **13** to DCM is first calculated, before the actual value of the signal is taken away from the expected value based on the characteristic ^1H spectrum and this resultant value is divided by the expected value and multiplied by 100 to give a percentage '*loss*' of 6 % of the anionic component and 4 % of the cationic component (Figure 18). This calculation process is then repeated for in EtOH, the dopant used in D_2O (Figure 19).

Equation 1 – The process for calculating percentage '*loss*' for the qNMR conducted in DMSO-d_6/ 1.0 % DCM: the ratio of DCM (0.08 mM) to **13** (0.0556 mM in 0.50 mL) is found to be 1.43 per proton but, as DCM has two protons, the peak at 5.75 ppm integrates for 2.86. With this integration, the percentage '*loss*' of the anionic and cationic components is calculated.

$$\frac{33.25\ mg}{593.81\ g/mol} = 0.0556\ mol \qquad \frac{0.08\ mmol}{0.0556\ mmol} = 1.43 \times 2 = 2.86$$

For the anionic component: no '*loss*' shown

For the cationic component:

$$8 - 7.9580 = 0.0420 \qquad \frac{0.0420}{8} \times 100 = 0.53\ \%$$

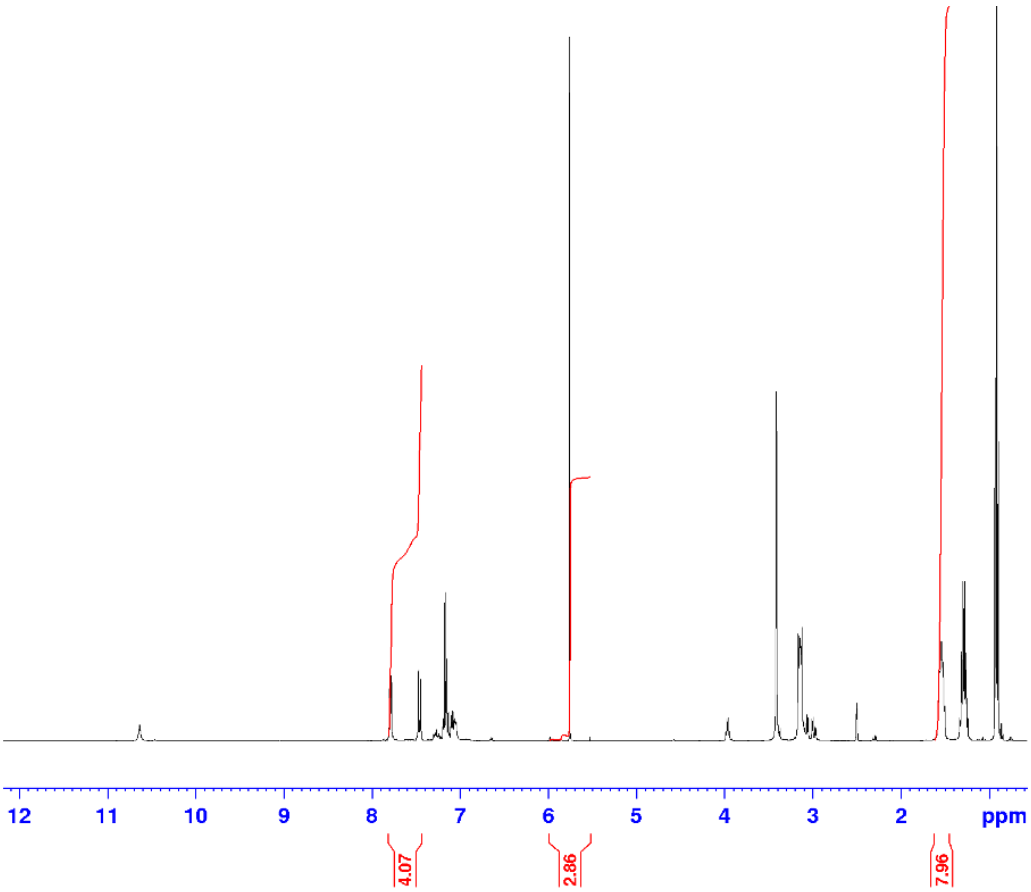

Figure 18 - ^{1}H NMR spectrum (d_1 = 60 s) of compound **13** (112 mM) in DMSO-d_6/1.0 % DCM. Comparative integration indicates no loss of the anionic component and 0.53 % of the cationic component of **13** has become NMR silent.

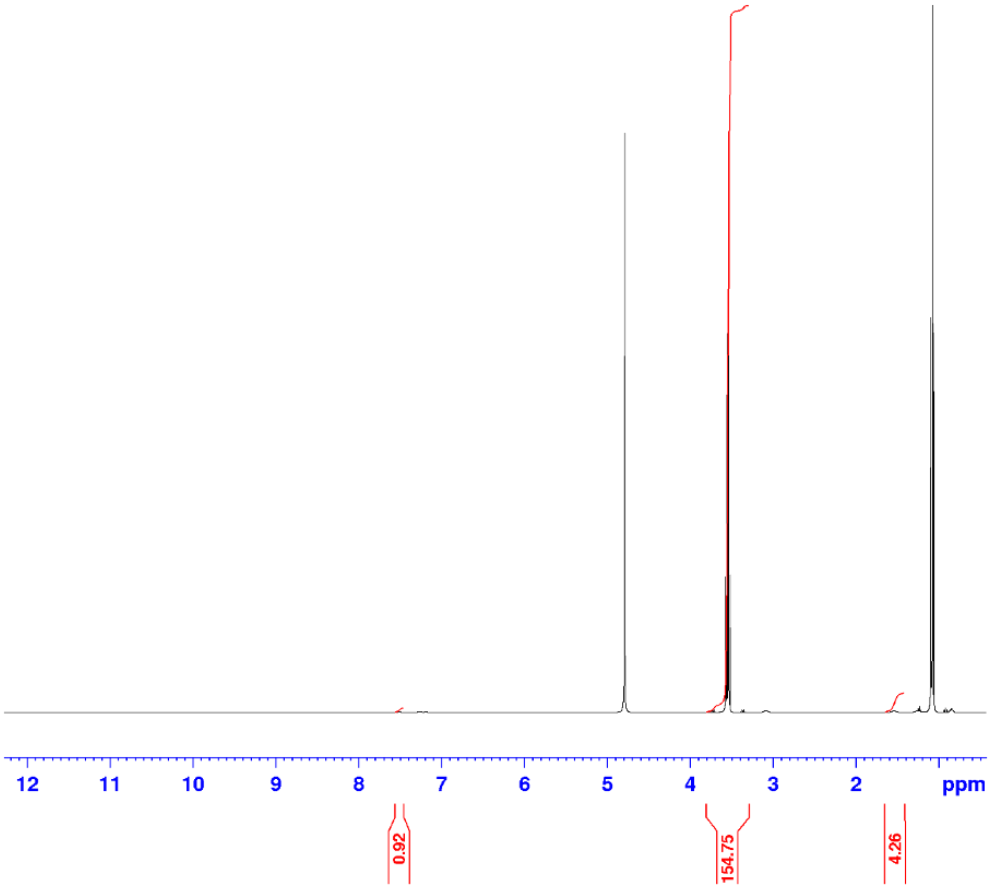

Figure 19 - ^{1}H NMR spectrum (d_1 = 60 s) of compound **13** (5.56 mM) in D_2O/5.0 % EtOH. Comparative integration indicates 77 % of the anionic component and 47 % of the cationic component of **13** has become NMR silent.

In DMSO-d_6, there is no apparent percentage '*loss*' of signal for the anionic component of **13**, but little apparent percentage '*loss*' of signal for the anionic and cationic components of compounds **15**, **17** and **19**, as shown in Table 3. However, the '*loss*' seen in **15**, **17** and **19** may be due to the temperature the experiments were conducted in. Given the volatile nature of DCM, the '*loss*' may have occurred due to the evaporation of the dopant at temperatures even slightly higher than room temperature (RT) before the study was carried out. This is further corroborated by the results

obtained from the ^{1}H NMR DOSY studies (see Section 2.4.3.), which show no indication of the formation of large self-associated aggregates. To investigate this, the qNMR studies for **15**, **17** and **19** in DMSO-d_6 must be repeated however, this could not be completed within the time allocated for this project.

In D_2O, **13**, **15**, **17** and **19** all show percentage '*loss*' for both the anionic and cationic components - because of this '*loss*' of signal of the compound, the self-association of the SSAs cannot be observed or studied further using this solvent system with solution-state NMR. The '*loss*' of signal is due to the formation of larger higher-order self-associated aggregates that have solid-like characteristics in a predominantly aqueous solution that are '*invisible*' to the NMR i.e., they are NMR silent. As **13**, **15**, **17** and **19** showed little '*loss*' of signal in DMSO-d_6, all of the compounds can continue to be observed using solution state NMR in this solvent, allowing determination of self-association constants (^{1}H self-association studies, see Section 2.4.2.) and the sizes of the aggregates found (^{1}H NMR DOSY, see Section 2.4.3.). On the other hand, as all the compounds showed a '*loss*' of signal in D_2O, different studies must be carried out to determine the size (DLS, see section 2.4.5.) and stability (ZP, see Section 2.4.6.) of these aggregates in this solvent.

Table 3 - Overview of results of qNMR studies. Values given in % represent the observed proportion of the anionic component of the compound that has become NMR silent. SSAs were at concentrations of 111.12 mM in DMSO-d_6, and 5.56 mM in D_2O for **13**, **15**, **17** and **19**.

Compound	DMSO-d_6/1.0 % DCM (%)		D_2O/5.0 % EtOH (%)	
	Anionic component	Cationic component	Anionic component	Cationic component
13	0	0.53	77	47
15	6	4	81	56
17	2	4	48	47
19	15	18	51	49

All qNMR spectra for **13**, **15**, **17** and **19** are presented in the appendix (see Section 7.2.).

2.4.2. ^{1}H NMR Self-association Studies

If there is no observable "*loss*" of signal in qNMR, the next step is to conduct ^{1}H self-association studies (as shown in Figure 14). NMR can observe weak and non-covalent interactions,[85] such as halogen bonding,[86] hydrogen bonding,[65,87–89] and π-π interactions.[90,91] To directly monitor the hydrogen bonds that form between the HBD urea N-Hs and the HBAs in the SSAs, a series of ^{1}H NMR dilution studies were conducted in a DMSO-d_6/ 0.5 % H_2O solution - this allows for the direct observation of the HBD urea N-H resonances in a competitive solvent system. Binding constants were also calculated by fitting data to two binding models using Bindfit.[92,93] The equal K (EK) model presumes all association events are equal, while the co-operative equal K (CoEK) model presumes the first association event differs from that of any subsequent events that are identical.[94,95] However, both models assume that only one component, one dimensional (1D) homogenous aggregates are formed, meaning that data showing evidence

of more than one species/ type of association event cannot be fitted to these models.[96]

The results from these self-association studies show that as the concentration of SSA decreases, the signals for the N-H protons shift upfield (Figures 20 and 21, using **13** as an example) - this change in chemical shift is due to the formation of the hydrogen bond. Kumar *et al*. suggested that the greater the chemical shift, the greater the strength of the hydrogen bond formed.[88]

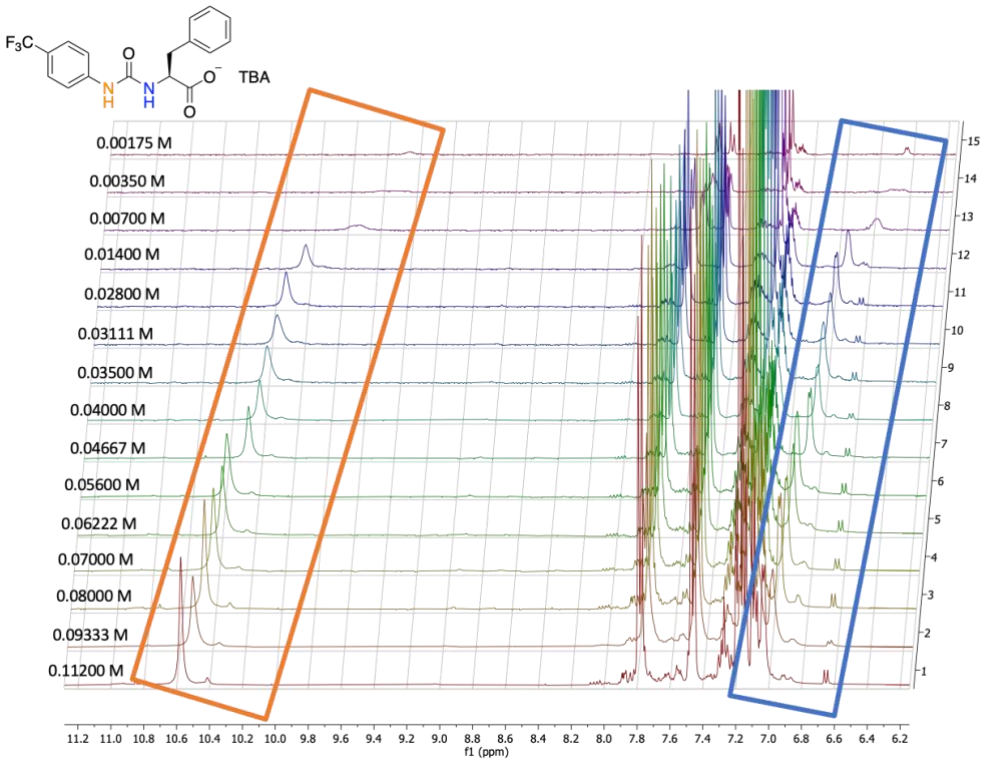

Figure 20 - Enlarged ^{1}H NMR stack plot of compound **13** in a DMSO-d_6 / 0.5 % H_2O solution. Samples were prepared in series with an aliquot of the most concentrated solution undergoing serial dilution.

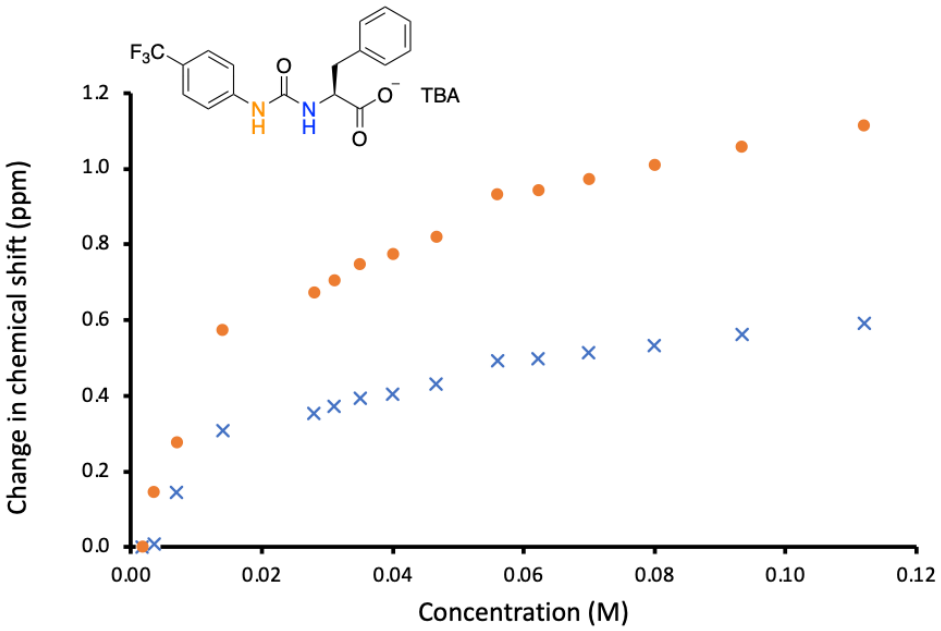

Figure 21 - Graph illustrating the ^{1}H NMR down-field change in chemical shift of urea N-H resonances with increasing concentration of compound **13** in DMSO-d_6 0.5% H_2O (298 K).

The changes in chemical shift from these studies were then fitted to the EK and CoEK models on Bindfit to quantify the strength of the hydrogen bonds formed during self-association events (Table 4). While the constants K_e and K_{dim} are similar for isomers **13** and **15** in both models (2 % difference), this is not the case for isomers **17** and **19** (29 % difference). This is unusual as the physical properties of enantiomers (excluding optical rotation) should be identical, unless interactions with another enantiomer are involved. This discrepancy is also seen for **17** and **19** in the DLS and ZP studies and is further discussed in depth in Section 2.4.9.

Table 4 - The self-association constants (M^{-1}) calculated for **13**, **15**, **17** and **19** in DMSO-d_6/ 0.5% H_2O solution at 298 K. Constants were obtained for the EK and CoEK models by fitting ^1H NMR self-association data to Bindfit v0.5.

Compound	EK model (M^{-1})		CoEK model (M^{-1})		
	K_e	K_{dim}	K_e	K_{dim}	ρ
13	55.52 (± 4 %)	27.76 (± 2 %)	21.17 (± 6%)	10.58 (± 3 %)	2.86 (± 15 %)
15	45.90 (± 5 %)	22.95 (± 3 %)	17.84 (± 9 %)	8.92 (± 4 %)	2.62 (± 20 %)
17	242.72 (± 4 %)	121.36 (± 2 %)	560.90 (± 5 %)	280.45 (± 3 %)	2.29 (± 9 %)
19	180.55 (± 6 %)	90.27 (± 3 %)	351.80 (± 7 %)	175.90 (± 4 %)	3.41 (± 13 %)

All ^1H NMR self-association spectra and Bindfit links for **13**, **15**, **17** and **19** are presented in the appendix (see Section 7.4.).

2.4.3. ^1H NMR DOSY Studies

After the ^1H NMR self-association studies, NMR diffusion ordered NMR spectroscopy (DOSY) is conducted. NMR DOSY is a technique that separates the NMR signals of a sample depending on the diffusion coefficient (*D*) of each molecule present in it, allowing mixtures of compounds to be analysed.[97] The diffusion coefficient is then converted into the hydrodynamic diameter (d_H) via the Stokes-Einstein equation (Equation 2).[98]

Equation 2 – The Stokes-Einstein equation, which enables the calculation of the hydrodynamic diameter (d_H) using the diffusion coefficient.

$$d_H = \frac{k_B \times T}{3\pi\eta D}$$

d_H = hydrodynamic diameter (m)
k_B = Boltzmann constant
T = temperature (K)
η = solvent viscosity (kg m^{-1} s^{-1})
D = diffusion coefficient (m^2 s^{-1})

However, the use of the Stokes-Einstein equation to calculate d_H is a limitation of the NMR DOSY technique, as the equation assumes the molecules are spherical. Therefore, the calculated d_H of molecules using this technique and equation must be considered estimations.

To obtain d_H for **13**, **15**, **17** and **19**, ^{1}H NMR DOSY studies were carried out at 55.56 mM in a DMSO-d_6/ 0.5 % H_2O solution, and the obtained *D* was applied to the Stokes-Einstein equation. Using **13** as an example (Figure 22), it was observed that the anionic component diffused at different rates compared to the cationic component, meaning that d_H is different for each component. As the anionic components and cationic components differ in diffusion rate, this shows that the cationic component (TBA) does not co-ordinate strongly with the anionic SSA component when in solution.

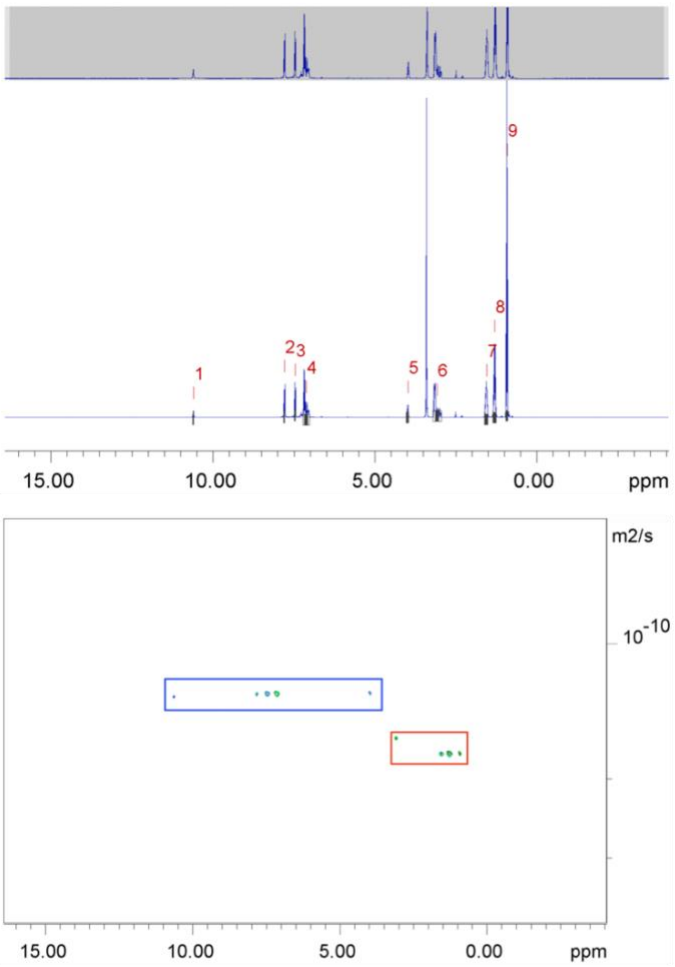

Peak name	F2 [ppm]	Io	error	D [m2/s]	error
1	10.610	7.03e+08	5.841e+04	1.30e-10	2.408e-14
2	7.797	2.75e+09	5.991e+04	1.30e-10	6.279e-15
3	7.468	2.79e+09	5.845e+04	1.29e-10	6.016e-15
4	7.124	8.56e+09	1.197e+05	1.29e-10	4.018e-15
5	3.988	1.34e+09	7.616e+04	1.29e-10	1.627e-14
6	3.078	9.81e+09	1.471e+05	1.62e-10	5.304e-15
7	1.553	8.47e+09	9.874e+04	1.75e-10	4.419e-15
8	1.301	1.14e+10	9.922e+04	1.77e-10	3.329e-15
9	0.923	1.84e+10	8.030e+04	1.75e-10	1.654e-15

Figure 22 - ^{1}H DOSY NMR of compound **13** (55.56 mM) in a DMSO-d_6/ 0.5 % H_2O solution conducted at 298 K and a table reporting the diffusion constants calculated for each peak used to determine the hydrodynamic diameter (d_H) of the anionic component. The anionic component is highlighted in blue and corresponds to peaks 1-5, while the cationic component is highlighted in red and corresponds to peaks 6-9. d_H = 1.70 nm.

Table 5 – The calculated d_H for **13**, **15**, **17** and **19** using the Stokes-Einstein equation.

Compound	d_H (nm) (DOSY)
13	1.70
15	1.67
17	1.66
19	1.70

Overall, the results obtained from the DOSY studies show no indication that large self-associated aggregates form in a DMSO-d_6/ 0.5% H_2O solution as the d_H of the anionic components are less than or equal to 1.70 nm (Table 5) – this diameter is hypothesised to be indicative of lower-order complex aggregates such as monomers, dimers, and trimers.

All ^{1}H NMR DOSY spectra for **13**, **15**, **17** and **19** are presented in the appendix (see Section 7.3.).

2.4.4. Tensiometry Studies and CAC Determination

Because there was a '*loss*' of compound in the qNMR studies conducted in the D_2O/ 5.0 % EtOH solvent system, the larger aggregates can no longer be observed using NMR, as they are beyond the scope of the NMR instrument. Consequently, different techniques must be employed in order to observe the larger aggregates in solution, including techniques to

determine CAC, dynamic light scattering (DLS) and zeta potential (ZP), as shown in Figure 14.

The main characteristic of amphiphiles is the ability to self-assemble and form aggregates upon reaching a certain concentration (see Section 1.3.1.). The morphology of the aggregate formed depends on various factors, but the most common morphology seen is the micelle, where the hydrophilic head favours and seeks to interact with an aqueous environment while the hydrophobic tail is packed internally to the structure, isolated from the aqueous environment.[8,99] A surface-active agent, or surfactant, is a specific type of amphiphile that lowers the surface tension of the environment it is present in.[8] At low concentrations, a dynamic equilibrium occurs where the surfactants either aggregate or gather and adsorb at the surface, disrupting the cohesive energy and lowering the surface tension. Increasing amphiphile concentration increases adsorption until the surface is fully saturated and there is no longer an effect on surface tension (Figure 23)[100–103] – this point is defined as the CAC. Once the CAC is reached, any further increase in concentration results in continuous formation of the self-assembled morphologies in the bulk of the solution. This concentration is more commonly referred to as the CMC however, this limits the aggregate morphology formed to micelles or spherical aggregates only when other morphologies can be formed, therefore the term CAC is preferred.

In this project, compounds **13**, **15**, **17**, **19** and the racemic mixtures of isomers **13**+**15** and isomers **17**+**19** were studied using pendant drop tensiometry measurements to determine the CAC and surface tension of serially diluted solutions of each compound, with a top concentration of 5.56 mM in EtOH:H_2O (1:19) solution. Unfortunately, the CAC and surface tension could not be obtained due to solubility issues – the surface tension continued to decrease at 5.56 mM and no further measurements could be obtained due to the solubility limit (5.56 mM in 1 mL of EtOH:H_2O (1:19)). As a result, dynamic light scattering (DLS) and zeta potential (ZP) studies were conducted at 5.56 mM.

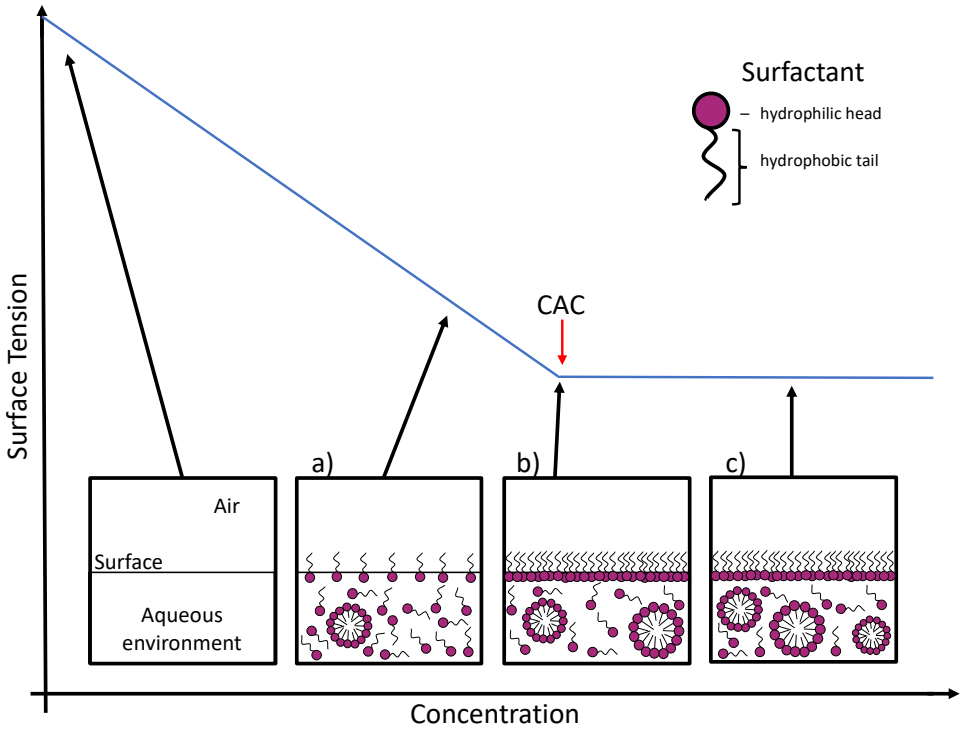

Figure 23 – Graphical representation of CAC determination by Williams *et al.*[102]: a) surfactants adsorb at the surface in equilibrium with aggregate formation, b) surface

is fully saturated and CAC is reached, and c) continued aggregate formation as concentration increases after CAC.

2.4.5. Dynamic Light Scattering Studies

Once the CAC for each compound and the racemic mixtures, the next technique to use is dynamic light scattering (DLS). DLS is a non-invasive technique normally used to characterise nanoparticles, determine the size of macromolecules, or detect aggregates in macromolecular solutions.[104–106] This technique uses the Brownian motion of particles (i.e., particles are continuously colliding with solvent molecules) and light scattering to calculate the size of the particles in solution - the size of the particles affects the intensity of scattered light.[106] The Stokes-Einstein equation (Equation 2) can be used to calculate d_H,[107] but this calculation is limited to a range of 1 – 1000 nm,[105] meaning that while low-order aggregates will be visible, their sizes cannot be calculated. Additionally, with the use of the Stokes-Einstein equation, there is an assumption that all aggregates formed are spherical (as previously mentioned in Section 2.4.3.). The results from these DLS studies are intensity distribution graphs weighted by size, so therefore cannot be treated as comparative numbers. Because the compounds observed within this project are novel, the refractive indices are unknown, thus number or volume distribution of the compounds cannot be obtained however, the polydispersity index (PDI)

can be considered instead - the higher the PDI, the larger the size of the aggregate.

To obtain d_H, samples of **13**, **15**, **17**, **19**, and racemic mixtures of isomers **13**+**15** and isomers **17**+**19** at 5.56 mM in EtOH:H_2O (1:19) solution were first annealed (heated to 313 K and cooled down to 298 K) to guarantee any self-associated aggregates present had achieved a thermodynamic minimum. Then, the average intensity particle size distribution was obtained from 10 DLS measurements. Evidence of large aggregates was first obtained through the qNMR studies conducted in 1 EtOH:H_2O (1:19) solution for compounds **13**, **15**, **17** and **19** in Section 2.4.1. The data from the DLS studies in EtOH:H_2O (1:19) solution corroborate this evidence, with d_H (equal to the peak maxima) ranging between 100 – 300 nm (Table 6). Additionally, with PDI ranging between 13 – 23 %, the lower PDI indicates that the aggregates formed are similar in size, thus have increased homogeneity.

Table 6 - The peak maxima obtained from the average intensity particle size distribution (calculated from 10 DLS runs) for compounds **13**, **15**, **17** and **19**, and racemic mixtures of isomers **13**+**15** and isomers **17**+**19** obtained at 5.56 mM in EtOH:H_2O (1:19). An annealing process was applied in which the samples were heated to approximately 313 K before being cooled down to a measurement temperature of

at 298 K. [a] 1:1 mixture. Error = standard error of the mean and given to 1 decimal place.

Compound	Peak maxima (nm)	PDI (%)
13	118.54 (± 1.0)	13.09 (± 0.9)
15	132.50 (± 1.2)	14.15 (± 0.7)
13 + **15**[a]	208.71 (± 3.4)	19.08 (± 0.8)
17	296.71 (± 4.4)	18.51 (± 1.6)
19	221.30 (± 3.3)	22.76 (± 0.3)
17 + **19** [a]	172.99 (± 1.8)	18.31 (± 0.7)

As mentioned previously in Section 2.4.2., discrepancies were observed between the K_e and K_{dim} values for isomers **17** and **19**. The differences between the d_H values obtained by DLS were also observed – there's a difference of 11 % between isomers **13** and **15**, and a difference of 29 % between isomers **17** and **19**. As there are also discrepancies in the ZP studies between isomers **17** and **19** (see Section 2.4.6.), investigations into the significance of this difference in d_H are being conducted but could not be completed within the time allocated for this project. This is discussed further in Section 2.4.9.

All DLS data for **13**, **15**, **17** and **19**, and racemic mixtures of isomers **13**+**15** and isomers **17**+**19** are presented in the appendix (see Section 7.5.).

2.4.6. Zeta Potential Studies

Zeta potential (ZP) is a technique that defines the electrical potential of a colloid particle and is frequently used to define the stability of colloidal particles or aggregates in solution.[107,108] ZP is a good indication of colloidal stability: measurements between ± 0 – 10 mV are considered unstable, while measurements between ± 10 – 20 mV are considered moderately stable, and measurements greater than ± 30 mV are considered stable.[109,110] However, this is simply a general indication as factors such as environmental conditions are not taken into consideration e.g., liposomes in the cell have a ZP of – 10 to – 40 mV and are considered to be stable.[111]

ZP was measured for **13**, **15**, **17** and **19**, and racemic mixtures of isomers **13**+**15** and isomers **17**+**19** at 5.56 mM in EtOH:H_2O (1:19) solution (Table 7). All have a ZP greater than ± 30 mV, meaning they can be considered '*stable*' aggregates.

Table 7 - Summary of the zeta potential (mV) for compounds **13**, **15**, **17** and **19**, and the racemic mixtures of isomers **13**+**15** and isomers **17**+**19** at 5.56 mM in EtOH:H_2O (1:19). [a] 1:1 mixture.

SSA	Zeta Potential (mV)
56	- 63.95
57	- 62.55
56 + **57**[a]	- 65.75
72	- 68.81
73	- 56.64
72 + **73**[a]	- 60.29

As mentioned previously in Sections 2.4.2. and 2.4.5, differences were observed between the K_e, K_{dim} and d_H values for isomers **17** and **19**. There are also discrepancies in the ZP measurements, with a 19 % difference in ZP between **17** and **19**. An investigation into the significance of these reoccurring differences is ongoing but could not be completed within the allocated project time. This is discussed further in Section 2.4.9.

All ZP data for **13**, **15**, **17** and **19**, and racemic mixtures of isomers **13**+**15** and isomers **17**+**19** are presented in the appendix (see Section 7.6.).

2.4.7. Circular Dichroism Studies

Circular dichroism (CD) spectroscopy is a technique that measures the difference in absorbance of right and left circularly polarised (RCP and LCP respectively) light.[112–114] When in solution, chiral molecules present CD signals at wavelengths where light is absorbed, and this difference in absorbance can be measured as optically active molecules absorb RCP and LCP light differently – if the molecule is achiral, no CD signals will be observed.[112] CD spectroscopy is a desirable technique for several different reasons including its sensitivity to asymmetry, the use of low sample concentrations (thereby circumventing any issues with solubility) and the ability to test molecules of any size with either flexible or rigid systems to name a few.[112] For these reasons, CD spectroscopy is widely used to study the structures of biological molecules, predominantly macromolecules such

as proteins, nucleotides and peptides etc.[112,114] However, in this project, CD was used to confirm that the novel compounds **13**, **15**, **17** and **19** are chiral, and the isomeric pairs (**13** and **15**, and **17** and **19**) are enantiomers. The CD studies were run with the appropriate SSA in EtOH:H_2O (1:19) solution at a concentration of 1 mM. Enantiomers will absorb circularly polarised light the same way (i.e., the CD signals for both isomers should have identical traces) but show opposite absorbances, appearing as mirror images. Using **13** and **15** as examples (Figure 24), the CD signals for each isomer were plotted on the same graph. This data shows that the CD signal traces are identical with opposite absorbances, thus confirming they are enantiomers of each other.

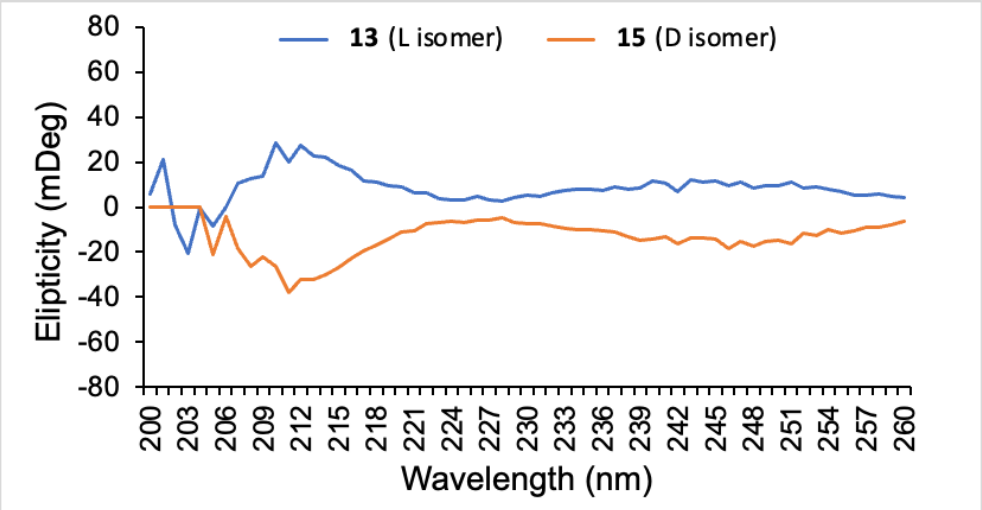

Figure 24 - The graph comparing the circular dichroism (CD) signal traces of isomers **13** (blue) and **15** (orange) at 1 mM in EtOH:H_2O (1:19) solution.

All CD graphs for **13**, **15**, **17** and **19** are presented in the appendix (see Section 7.9.).

2.4.8. Membrane Fluidity

Though it lacks an exact definition, membrane fluidity generally refers to the mobility of the cell membrane, specifically the semi-permeable phospholipid bilayer.[115–117] The phospholipid bilayer (Figure 8c) is the result of lipid molecules self-assembling and forming a semi-permeable bilayer that sees the hydrophilic lipid head interacting with the aqueous environment surrounding the cell, while the hydrophobic fatty acid tails are held in the interior of the bilayer. This bilayer structure acts as a barrier to regulate the transport and passive diffusion of small neutral molecules (e.g., CO_2, O_2 or H_2O) across the cell membrane while preventing the transport of larger polar molecules (e.g., glucose) and ions (e.g., Na^+, K^+ or Cl^-).[118,119] The phospholipid bilayer has various components interposed within it that aid regulation through different molecular transport events (e.g., transport protein pumps, carbohydrates, peripheral proteins, other lipids such as cholesterol etc.),[118–120] however the properties that membrane fluidity is concerned with are mainly due to the structure of the lipid, particularly the fatty acid tails.[116,121,122] Any structural modifications made to the fatty acid tail (i.e., length of and/or saturation in the tail)[121] or the R group in the phospholipid head group,[123] in addition to environmental factors (e.g., temperature or osmotic stress)[116,121] affect the membrane fluidity, which can consequently affect membrane permeability and certain functions such as enzyme activity.[117] This must be taken into account when designing novel antimicrobial and anticancer therapeutic agents, as the phospholipid bilayer could either aid in drug delivery,[124–126]

or produce cellular resistance.[127,128] Thus, novel technologies that aim to target and alter membrane fluidity have been developed accordingly.[115,129] Examples include the design of a class of novel compounds called cyclotides by Craik *et al.* which have been identified as anticancer agents,[130] or the class of SSAs developed by the Hiscock group which have previously been reported to permeate bacterial and cancer cell membranes.[63,67–69,131]

One method used to measure membrane fluidity is fluorescence polarisation (FP). In this technique, the lipid bilayer is first intercalated or '*labelled*' with a hydrophobic fluorescent dye, commonly 1,6-diphenyl-1,3,5-hexatriene (DPH).[122] Next, the '*labelled*' sample is excited with polarised UV light and emits polarised light/ fluorescence that is then measured by separating the emitted fluorescence into either perpendicular or parallel waves according to the polarisation of excited light.[132,133] If there is a decrease in FP values, there is an increase in membrane fluidity and vice versa. This technique was previously used by the Hiscock group, who observed a decrease in FP for **9** when used with synthesised polar phospholipid membranes and concluded that '*the presence of a carboxylate ion results in selective increases in membrane fluidity for model bacterial cell membranes*.'[134]

For this project, fluorescence polarisation measurements were to be obtained, however due to time restraints, these could not be completed

within the time allocated for this project. Further work would include the investigation into whether the novel SSA compounds (**13**, **15**, **17** and **19**) and their isomeric pairs (**13**+**15** and **17**+**19**) have an effect on membrane fluidity via this technique (see Section 4).

2.4.9. Further Discussion - Compounds **17** and **19**

Enantiomers have identical physical properties and form the same products when reacting with optically inactive reagents -any difference between enantiomers only arises either when interacting with other chiral molecules or plane-polarised light, with optical rotation being the only physical property that is not identical for enantiomers.[135–137] Therefore, it is expected that data from the physicochemical characterisation and self-association studies are the same for the isomeric pairs, or at least similar considering any errors that may have been made during the process – the only exception is any study completed using racemic mixtures, as the sample is no longer 100 % enantiomerically pure but a 1:1 mixture of both isomers. However, notable differences were observed between the data obtained for isomers **17** and **19** in three studies: ^{1}H NMR self-association (Section 2.4.2), DLS (Section 2.4.5) and ZP (Section 2.4.6). Under the same conditions, the data for isomers **13** and **15** from these studies do not show such major discrepancies, with the biggest difference being 11 % between their d_H values compared to the 29 % difference for both the K_{dim} and d_H values of **17** and **19** (Table 8).

Table 8 - An overview of the self-association constant (M^{-1}, fit to the EK model), the hydrodynamic diameter (d_H, nm) and the zeta potential (mV) for compounds **13**, **15**, **17** and **19**, and the percentage differences between the relevant values between the respective isomers.

Compound	**K_{dim} (M^{-1})**	**d_H (nm)**	**Zeta Potential (mV)**
13	27.76	118.54	- 63.95
15	22.95	132.50	- 62.55
Percentage difference	2 %	11 %	2 %
17	121.36	296.71	- 68.81
19	90.27	221.30	- 56.64
Percentage difference	29 %	29%	19 %

There are two hypotheses as to why these discrepancies are seen, one being the presence of a contaminant that was not properly removed during the synthesis of **17** and/ or **19**. If true, it is thought to be an inorganic contaminant that could not be detected via ^{1}H or ^{13}C characterisation NMR, as there was no indication of contamination throughout the physicochemical characterisation process. A potential contaminant is zinc bromide, which was used in the synthetic method to remove the tert-butyl protecting group from **12**, **14**, **16** and **18** to form the corresponding carboxylic acidsand synthesise **13**, **15**, **17** and **19** respectively by then adding TBA hydroxide (Scheme 1; see Section 5.3 for the full synthetic method used).

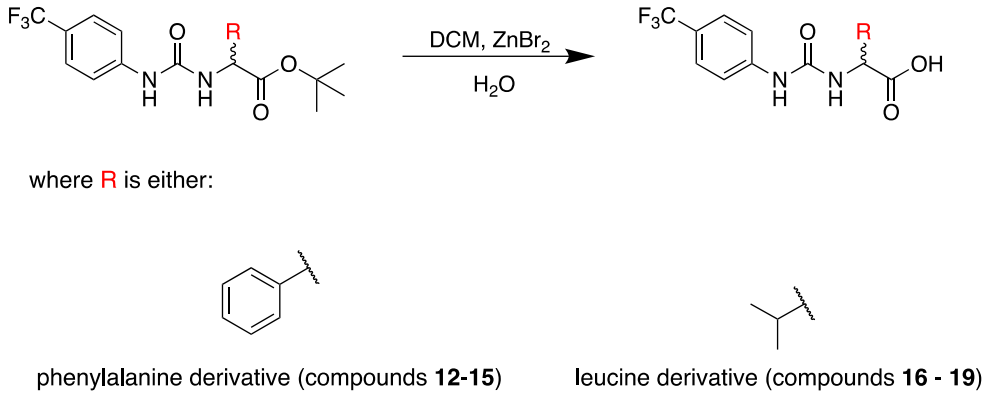

Scheme 1 – The deprotection of the tert-butyl protected compounds **12**, **14**, **16** and **18** to then synthesise **13**, **15**, **17** and **19** upon addition of TBA hydroxide.

Another hypothesis is that, during the physicochemical characterisation studies (involving ^{1}H, ^{13}C and DEPT NMR, FTIR, ESI-MS and melting point; see Section 2.1, Figure 14), **17** and/ or **19** underwent a phenomenon in which the trifluoromethyl group (-CF_3) on the aromatic ring is converted to a carboxylic acid (-COOH) functionality. Hiscock *et al*. previously reported this unusual phenomenon with **9**, as it had occurred during crystallisation of **9** over many weeks to produce crystals for single crystal XRD studies. However, instead of obtaining single crystal X-ray structures of **9**, the structure of **9a**/**9b** (Figures 25 and 26) was observed .[64] High resolution mass spectrometry studies were subsequently carried out using the remaining crystallised sample, which confirmed the presence of **9a** but not the presence of **9**. This occurrence was unusual and, while investigations into what influences this conversion are still ongoing, it was found that storing **9** at -18 °C prevents this process from occurring, suggesting that temperature may potentially drive the conversion. During

the physicochemical characterisation processes, **17** and **19** were stored at room temperature so it is possible that the same phenomenon occurred for one of or both of the isomers. However, it is important to note that this is only a hypothesis and there is no evidence to support or refute this, especially considering single crystal X-ray structures could not be obtained for **13**, **15**, **17** and **19** within the allocated project time.

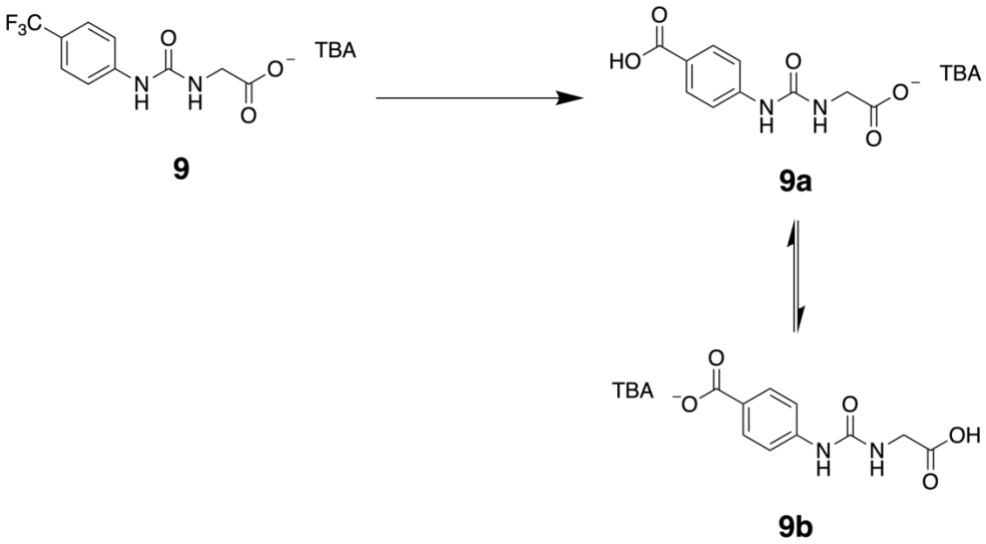

Figure 25 – The irreversible conversion of the -CF_3 group in **9** to the -COOH group, forming compound **9a** as reported by Hiscock *et al*. Note that **9a** may be in an equilibrium in which the counter cation for the two carboxylate groups changes between a proton and TBA, forming **9b** .[64]

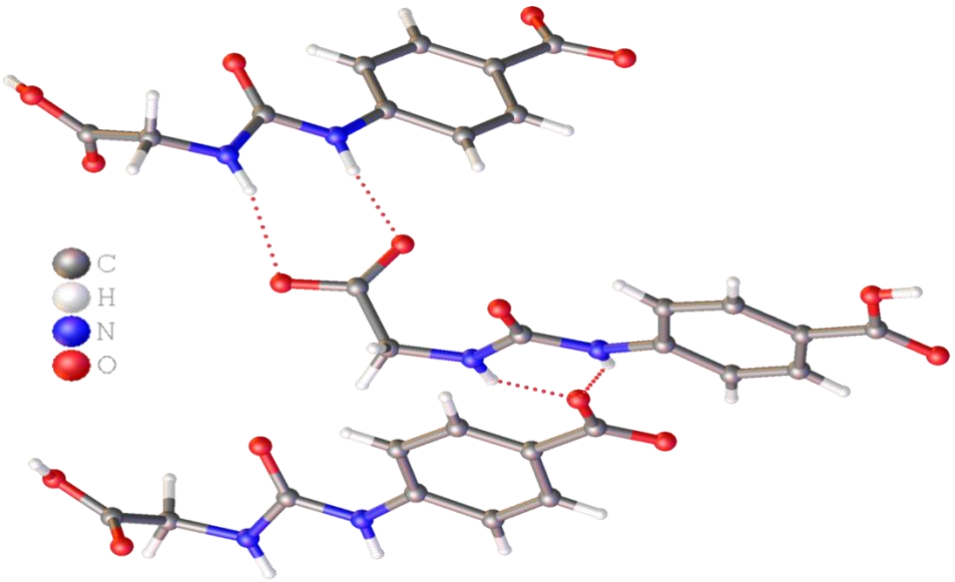

Figure 26 – The single crystal X-ray structure of **9a/b** crystallised from a solution of **9** as reported by Hiscock *et al*.[64] TBA cation omitted for clarity.

To investigate this, **17** and **19** were to be resynthesised using a new method and new ZP measurements would be obtained to compare to the initial data acquired, while storing the compounds at -18 °C . First, a new deprotection method using trifluoroacetic acid (TFA) was used during the synthesis of **19** (Scheme 2). The ^{1}H characterisation NMR was repeated to confirm the absence of any organic contaminants (Figure 27), before repeating the ZP measurement to compare to the initial ZP measurement (Table 9; Section 7.6.1. Figure S93) and determine whether the issue was with the initial batch of **19** and, if so, whether **19** was contaminated or had been '*breaking down*'. The new ^{1}H characterisation NMR showed no evidence of contamination, and the new ZP measurement obtained for **19** (- 58.09 mV) was similar to the initial ZP measurement (- 56.64 mV).

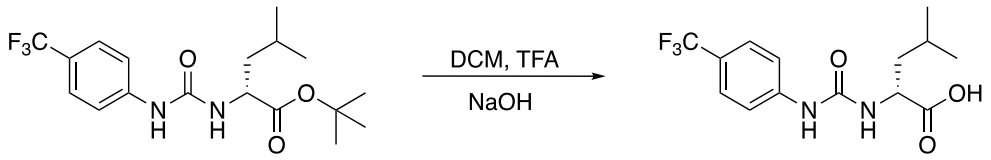

Scheme 2 – The new method for deprotection of compound **19**.

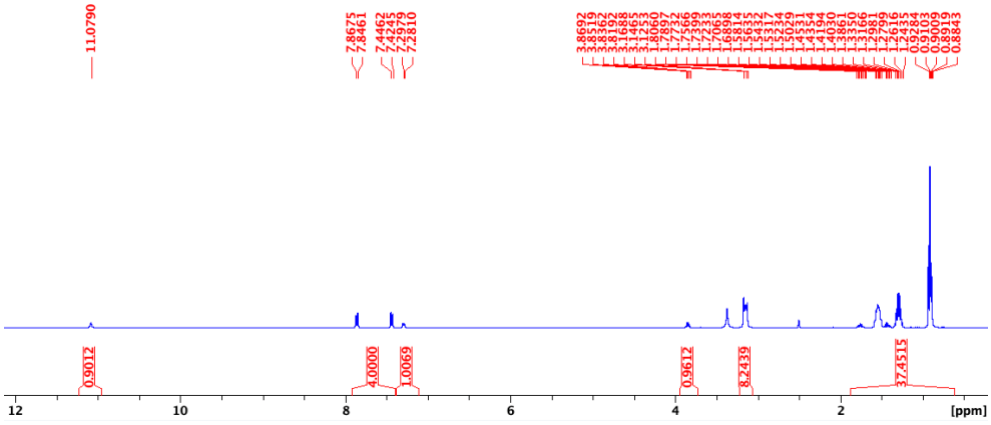

Figure 27 – ^{1}H NMR of compound **19** in DMSO-d_6 conducted at 298 K.

Table 9 – The zeta potential (ZP) for the initial and newly synthesised batches of compound **19** at 5.56 mM in EtOH:H_2O (1:19) solution.

	Zeta Potential (mV)	
Compound	**Initial**	**New**
19	- 56.64	- 58.09

Unfortunately, this process could not be completed for **17** within the allocated time, however the ^{1}H characterisation NMR was repeated on the initial batch of **17** to observe whether anything had changed since its

synthesis. Although small, new signals in the aromatics region of the spectrum were found (Figure 28), which may be an indication that **17** had been undergoing this phenomenon during the physicochemical characterisation and the self-association studies. However, this remains a hypothesis and cannot be considered true until thorough investigation provides more evidence and the cause for these discrepancies is identified.

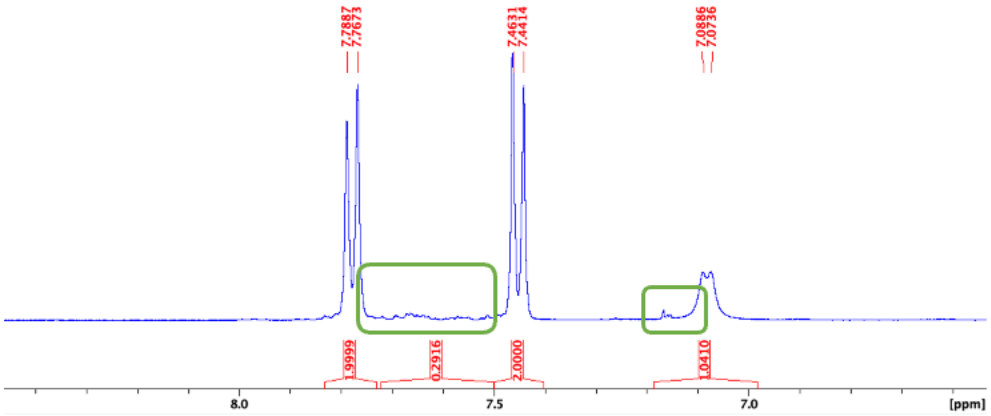

Figure 28 – Enlarged ^{1}H NMR of compound **17** in DMSO-d_6 conducted at 298 K. New signals not seen in previous ^{1}H spectra are encircled in green.

2.5. Antimicrobial, Anticancer and Toxicity Assays

2.5.1. Introduction

In 2019, it was estimated that antimicrobial resistance directly caused 1.27 million deaths and indirectly caused 4.95 million deaths,[70] with cancer estimated to have directly caused 9.9 million deaths in 2020.[71] Resistance to current antibiotics and cancer treatments is rapidly increasing,

highlighting the urgent need for new and more efficient antimicrobial and anticancer agents to tackle this crisis.

As mentioned previously in Section 1.4.1., Hiscock *et al.* made various modifications to the anionic component and/or the counter cation to build a comprehensive library of SSAs. Tests were then carried out to ascertain whether the SSAs had antimicrobial and/or anticancer properties and, if so, which SSA showed the best activity. Some were found to act as antimicrobial agents against clinically relevant bacteria,[66] antibiotic delivery agents,[63,66] antimicrobial efficacy enhancers,[68] and anticancer agents by enhancing the efficacy of current cytotoxic chemotherapies (e.g. cisplatin).[69] Consequently, Hiscock et al. proposed the following as the mode of action for both antimicrobial and anticancer activity: in its self-associated form, the SSA travels to the cell surface and, upon arrival, the monomeric components selectively interact with polar phospholipids like phosphatidylethanolamine (PE) that are present in higher proportions in bacterial and cancer cell membranes than eukaryotic cell membranes. This then disrupts the membrane, allowing internalisation of the SSA (and, when used, the antimicrobial or anticancer drug) and consequently inhibiting growth.[66,69,134]

To test the therapeutic activity of **13**, **15**, **17**, **19**, and the racemic mixtures of the isomers (**13**+**15** and **17**+**19**), antimicrobial and anticancer assays were conducted (Sections 2.5.2 and 2.5.3.), with investigations into toxicity

and haemolysis also being conducted (Section 2.5.4.). Despite the discrepancies observed for some of their physical properties, isomers **17** and **19** were still tested for their therapeutic, toxic, and haemolytic properties as differences in results are to be expected once they are introduced to the chiral environment in cells.[138,139] As explained in Section 2.4.9., more investigation is needed in order to determine the exact cause of the discrepancies observed however, the physicochemical characterisation studies provided no initial evidence to suggest presence of any impurities, so it was deemed fit to continue with the following assays for **17** and **19** due to the allocated time given for this project.

2.5.2. Antimicrobial Assays

To test the antimicrobial activity of the novel compounds, the lowest concentration required to inhibit the growth of bacteria, or the minimum inhibitory concentration (MIC), was calculated for **9**, **13**, **15**, **17**, **19** and racemic mixtures of the isomers (**13**+**15** and **17**+**19**) against seven different Gram-positive bacteria strains (Table 10). Each sample tested was either the appropriate SSA, cisplatin or TBA chloride (5.56 mM) in a 1:3 mixture of EtOH:H_2O (1:19) solution to TSB respectively, with a final top concentration of 1.39 mM for each compound. These assays were conducted by Kira Hilton, Dr Jennifer R. Hiscock, and Dr Charlotte Hind.

Table 10 – The minimum inhibitory concentration (MIC) values determined for **9**, **13**, **15**, **17**, **19** and racemic mixtures of the isomers (**13**+**15** and **17**+**19**) against 7 different Gram-positive *Staphylococcus aureus* (*S. aureus*), *Enterococcus faecalis* (*E. faecalis*) and *Enterococcus faecium* (*E. faecium*) bacteria strains. [a] racemic (1:1) mixture.

MIC (mM)							
Compound	***S. aureus* 9144**	***S. aureus* 13616**	***S. aureus* USA 300**	***S. aureus* 1199B**	***E. Faecalis* NCTC 775**	***E. Faecalis* NCTC 12201**	***E. Faecium* NCTC 12204**
9	1.390	> 2.780	> 2.780	> 2.780	> 2.780	> 2.780	> 2.780
13	0.087	0.087	0.087	0.174	> 2.780	> 2.780	> 2.780
15	0.174	0.087	0.087	0.174	2.780	> 2.780	> 2.780
13 + 15 [a]	0.087	0.087	0.087	0.087 – 0.349	> 2.780	> 2.780	> 2.780
17	0.087	0.087	> 2.780	0.087	> 2.780	> 2.780	> 2.780
19	0.174	0.087	> 2.780	2.780	2.780	> 2.780	> 2.780
17 + 19 [a]	0.174	0.087	0.174	0.174	> 2.780	> 2.780	> 2.780

The results show that the racemic mixture of **13** and **15** is the most effective against all seven bacteria strains, while **9** was the least effective. Interestingly, **13**, **15**, **17**, **19** and their respective racemic mixtures show the same effect for the *S. aureus* 13616 strain but for the *S. aureus* 9144 strain, there are noticeable trends in the data i.e., the L isomers (**13** and **17**) have lower MIC values compared to the D isomers (**15** and **19**), however the racemic mixture of **13** and **15** had the same MIC as **13** while the racemic mixture of **17** and **19** have the same MIC as **19**. This suggests the mode of action includes chiral selectivity - in this case, the preference of the L configuration over the D configuration for the *S. aureus* 9144 strain. Overall, the chiral compounds and their racemic mixtures were either more

or just as effective as **9** for the seven bacteria strains, showing that the addition of a chiral centre improves antimicrobial efficacy.

2.5.3. Anticancer Assays

To test the anticancer activity of the novel SSA compounds, the concentration required to inhibit cellular growth by 50 % (GI_{50}) is being determined for **9**, **13**, **15**, **17**, **19**, racemic mixtures of the isomers (**13**+**15** and **17**+**19**), cisplatin and TBA chloride against non-cancerous RPE-1 cells, ovarian cancer cells (A780) and cisplatin-resistant ovarian cancer cells (A2780 CisR). Each sample tested is either the appropriate SSA, cisplatin or TBA chloride (10 mM) in a 1:5 mixture of EtOH:H_2O (1:19) solution to Iscove's modified Dulbecco's medium (IMDM) with 10 % fetal bovine serum (FBS) respectively, with a final top concentration of 1.67 mM for each compound. These assays are ongoing and are being conducted by Chandni Manwani and Dr Michelle Garrett, however any data obtained so far is presented in Table 11.

Table 11 – The concentration of compound required to reduce/ inhibit cellular growth by 50% (GI_{50}) determined for **9**, **13**, **15**, **17**, **19** , racemic mixtures of the isomers (**13**+**15** and **17**+**19**), cisplatin and TBA chloride against non-cancerous RPE-1 cells, ovarian cancer cells (A2780) and cisplatin resistant ovarian cancer cells (A2780 CisR). [a] racemic (1:1) mixture. – not yet determined.

	RPE-1 SRB Assays			A2780 SRB Assays			A2780 CisR SRB Assays		
Compound	**Mean GI_{50} (μM)**	**SD +/-**	**$R^2 > 0.9$ n=**	**Mean GI_{50} (μM)**	**SD +/-**	**$R^2 > 0.9$ n=**	**Mean GI_{50} (μM)**	**SD +/-**	**$R^2 > 0.9$ n=**
Cisplatin	3.593	1.01	2	0.532	0.3	4	12.7175	6	4
TBA Cl	162.65	30.61	2	113.78	3.36	4	222.46	5.64	3
9	194	96.87	2	120.75	9.9	4	325.06	35.3	3
13	-	-	-	176.08	13.86	4	390.28	23.06	3
15	-	-	-	99.97	10.10	5	196.9	9.04	4
13 + 15 [a]	-	-	-	86.81	1	3	160.35	5.37	3
17	-	-	-	-	-	-	-	-	-
19	-	-	-	-	-	-	-	-	-
17 + 19 [a]	-	-	-	-	-	-	-	-	-

From the available data, it shows that the racemic mixture of **13** and **15** is the most effective against the ovarian cancer cells and cisplatin-resistant ovarian cancer cells. There is also evidence of chiral selectivity – **15** is more effective as an anticancer agent than an antimicrobial agent, while **13** is more effective as an antimicrobial agent than an anticancer agent. This suggests that there's a difference in protein selectivity when the SSAs approach and interact with a cancer cell membrane compared to a bacterial cell membrane. Overall, **15** and the racemic mixture of **13** and **15** were more effective as **9** against the ovarian and cisplatin-resistant ovarian cancer cell lines, however **13** was less effective, showing that while the addition of a chiral centre improves anticancer efficacy, the D configuration or the racemic combination of both the L and D configurations are preferred by the cancer cell membrane in some way.

2.5.4. Toxicity and Haemolysis Assays

Toxicity assays were conducted on **9**, **13**, **15**, **17**, **19** and racemic mixtures of the isomers (**13**+**15** and **17**+**19**) by injecting galleria moth caterpillars with 10 µL of the appropriate compound and incubating them for five days at 310 K (Table 12). Each sample tested was a the appropriate SSA, cisplatin or TBA chloride (5.56 mM) in a 1:3 mixture of EtOH:H_2O (1:19) solution to phosphate buffered saline (PBS) solution respectively, giving a final top concentration of 1.39 mM for each compound. Based on the number of deaths after five days, compound **19** was found to be the least toxic while the racemic mixture of isomers **17** and **19** was the most toxic. Additionally, a pattern can be observed, where the compounds with the D configuration (**15** and **19**) are less toxic compared to their enantiomers with the L configuration (**13** and **17**), similar to what was observed in the anticancer assays conducted.

Table 12 – The toxicity of **9**, **13**, **15**, **17**, **19** and racemic mixtures of the isomers (**13**+**15** and **17**+**19**) determined by observing the number of Galleria moth larvae that survived out of 10 after injection of compound. PBS and EtOH:H_2O (1:19) solution were used as controls. [a] racemic (1:1) mixture.

	Galleria moth larvae survived				
Compound	**Day 1**	**Day 2**	**Day 3**	**Day 4**	**Day 5**
9	10	9	8	6	6
13	10	4	4	4	4
15	9	9	9	7	5
13 + 15 [a]	9	8	4	4	4
17	9	9	9	6	5
19	10	9	8	8	8
17 + 19 [a]	7	7	7	4	3
PBS	10	10	10	10	10
EtOH:H_2O (1:19)	10	10	10	10	10

Haemolysis assays were conducted to determine whether red blood cells would lyse after contact with the compounds at a top concentration of 1.39 mM in EtOH:H_2O (1:19) solution (Table 13) – it was observed that none of the compounds caused lysis of red blood cells.

Table 13 - The haemolysis of red blood cells determined for **9**, **13**, **15**, **17**, **19** and racemic mixtures of the isomers (**13**+**15** and **17**+**19**) obtained at 1.39 mM. EtOH:H_2O (1:19) solution was used as a control. [a] racemic (1:1) mixture.

Compound	**Haemolysis at 1.39 mM (%)**	**Standard deviation**
9	0.30	0.56
13	0.50	0.48
15	- 0.34	0.54
13 + 15 [a]	0.30	0.52
17	- 0.44	1.78
19	- 0.23	1.22
17 + 19 [a]	0.80	0.54
1:19 EtOH/H_2O	0.50	0.05

Both the toxicity and haemolysis assays were conducted by Kira Hilton, Dr Jennifer R. Hiscock, and Dr Charlotte Hind.

2.5.5. DLS and ZP Studies in Biological Media

DLS and ZP measurements were conducted to estimate the size and stability of the SSA compounds and the racemic mixtures in the three different media used for the antimicrobial, anticancer and toxicity assays. The three media used were TSB (Table 14) for the antimicrobial assays, IMDM with 10 % FBS (Table 15) for the anticancer assays, and PBS (Table 16) for the toxicity assays.

Table 14 - A summary of the average intensity particle size distribution calculated from 10 DLS runs and ZP for **9**, **13**, **15**, **17**, **19** and racemic mixtures of the isomers (**13**+**15** and **17**+**19**) obtained at 1.39 mM in a 1:3 SSA (5.56 mM in 1:19 EtOH/H_2O):TSB. An annealing process was applied in which the samples were heated to approximately 313 K before being cooled down to a measurement temperature of 298 K. [a] 1:1 mixture. Error = standard error of the mean and given to 1 decimal place.

Compound	Peak maxima (nm)	PDI (%)	Zeta potential (mV)
9	285.38 (± 11.3)	27.89 (± 0.8)	- 6.76
13	227.49 (± 3.7)	17.25 (± 0.4)	- 23.11
15	215.37 (± 3.0)	14.21 (± 0.9)	- 24.00
13 + 15 [a]	226.14 (± 2.2)	18.34 (± 0.6)	- 22.72
17	276.19 (± 4.1)	14.28 (± 1.3)	- 21.71
19	213.25 (± 2.1)	17.16 (± 0.7)	- 21.13
17 + 19 [a]	255.38 (± 2.7)	14.94 (± 1.0)	- 20.15

Table 15 – A summary of the average intensity particle size distribution calculated from 10 DLS runs for **13**, **15**, **17** and **19**, and racemic mixtures of isomers **13**+**15** and isomers **17**+**19** obtained at 1.67 mM in a 1:5 solution of 5 % EtOH in H_2O: IMDM with 10 % FBS. An annealing process was applied in which the samples were heated to approximately 313 K before being cooled down to a measurement temperature of 298 K. [a] 1:1 mixture. Error = standard error of the mean and given to 1 decimal place.

Compound	Peak maxima (nm)	PDI (%)	Zeta potential (mV)
9	16.98 (± 2.3)	24.44 (± 0.6)	- 6.20
13	181.42 (± 6.4)	28.11 (± 0.6)	- 14.13
15	194.28 (± 3.1)	19.51 (± 0.6)	- 14.70
13 + 15 [a]	208.27 (± 3.1)	17.52 (± 0.7)	- 15.80
17	159.59 (± 6.1)	30.57 (± 0.4)	- 12.91
19	175.01 (± 3.3)	24.40 (± 0.4)	- 12.38
17 + 19 [a]	172.44 (± 2.5)	28.61 (± 0.6)	- 13.91

Table 16 - A summary of the average intensity particle size distribution calculated from 10 DLS runs and ZP for **9**, **13**, **15**, **17**, **19** and racemic mixtures of the isomers (**13**+**15** and **17**+**19**) obtained at 1.39 mM in a 1:3 SSA (5.56 mM in 1:19 EtOH/H_2O):PBS. An annealing process was applied in which the samples were heated to approximately 313 K before being cooled down to a measurement temperature of 298 K. [a] 1:1 mixture. Error = standard error of the mean and given to 1 decimal place.

Compound	Peak maxima (nm)	PDI (%)	Zeta potential (mV)
9	439.80 (± 18.1)	27.62 (± 0.9)	- 9.05
13	191.38 (± 1.7)	15.50 (± 1.2)	- 31.47
15	355.86 (± 3.9)	23.48 (± 0.3)	- 41.64
13 + 15 [a]	355.32 (± 4.9)	23.34 (± 0.2)	- 28.34
17	319.84 (± 2.4)	15.29 (± 1.2)	- 27.11
19	359.73 (± 7.1)	21.75 (± 1.0)	- 20.90
17 + 19 [a]	275.00 (± 3.0)	19.06 (± 1.0)	- 23.16

The results show that larger aggregates were formed in the PBS solution for all compounds compared to the aggregates formed in the TSB, IMDM with 10 % FBS media, and EtOH:H_2O (1:19) solution (see Section 2.4.5.). However, the aggregates formed in the different media are not as stable as those formed in EtOH:H_2O (1:19) solution (see Section 2.4.6.). However, this data should be treated with caution as not only are there limitations to these techniques in general (see Sections 2.4.5. and 2.4.6.), but different concentrations of compound and different ratios of compound to medium were used depending on the medium used. This data was obtained to give an indication on the size and stability of any

aggregates formed by the compounds in the different media using the same techniques used for the solution-state self-association studies of the novel SSAs.

All DLS and ZP data for **13**, **15**, **17** and **19**, and racemic mixtures of isomers **13**+**15** and isomers **17**+**19** in TSB, IMDM with 10 % FBS and PBS are presented in the appendix (Sections 7.5.3. to 7.5.8. and 7.6.3. to 7.6.8. respectively).

3. Conclusions

In conclusion, eight novel compounds were designed and synthesised based on the structure of compound **9**. These novel compounds were characterised, and self-association was studied in the solid phase, gaseous phase and in solution using a wide range of methods. As enantiomers, the isomeric pairs should show no difference in physical properties, however discrepancies in the data for isomers **17** and **19** were observed, suggesting either the presence of an inorganic contaminant or that the -CF_3 group is being converted into a -COOH group, a phenomenon previously reported by the Hiscock group that occurred to compound **9**.[64] Further investigation into these hypotheses and repeats of physicochemical characterisation and self-association studies are required to identify the cause of the discrepancies found in the data for the isomers **17** and **19**.

The antimicrobial and anticancer assays conducted showed that the four novel compounds of interest (**13**, **15**, **17** and **19**) and racemic mixtures of the isomers (**13**+**15** and **17**+**19**) had greater antimicrobial and anticancer activity than **9**, with the racemic mixture of isomers **13** and **15** showing the best activity in both assays so far. Chiral selectivity was also observed as the L isomers (**13** and **17**) were more effective antimicrobial agents than the D isomers (**15** and **19**). The opposite of this was then seen when observing the available data for the anticancer assays, which showed that **15** was more effective as an anticancer agent than **13**. This suggests the mode of action of the chiral SSAs when interacting with bacterial cells compared to cancer cells depend on the configuration of the isomer for greater efficacy, however, the anticancer assays need to be completed before a final conclusion is drawn from these findings.

4. Future Work

1. The continued investigation into the inconsistencies in data for compounds **17** and **19** and how significant they are (as discussed in Section 2.4.9), including obtaining single crystal X-ray structures of compounds **13**, **15**, **17** and **19** to observe how they self-associate and whether the ‘ same phenomenon previously seen in compound **9** also occurs.
2. The completion of the anticancer assays and determination of the structure-activity relationships seen.

3. Fluorescence polarisation measurements for compounds **13**, **15**, **17** and **19**, and their respective racemic mixtures to determine whether they have an effect on the membrane fluidity of cell membranes.
4. An investigation into the mode of action of the compounds when interacting with bacterial and cancer cells and whether there's a protein the compounds target that inhibits cell growth.

5. Experimental Techniques and Synthesis

5.1. Chemical Experimental Techniques

General Remarks: A positive pressure of nitrogen and oven dried glassware were used for all reactions. All solvents and starting materials were purchased from known chemical suppliers or available stores and used without any further purification unless specifically stipulated. The NMR spectra were obtained using a Bruker AV2 400 MHz or AVNEO 400 MHz spectrometer. The data was processed using TopSpin 4.1.4. software. NMR chemical shift values are reported in parts per million (ppm) and calibrated to the centre of the residual solvent peak set (s = singlet, br = broad, d = doublet, t = triplet, q = quartet, m = multiplet). Tensiometry measurements were undertaken using the Biolin Scientific Theta Attension optical tensiometer. The data was processed using Biolin OneAttension software. A Hamilton (309) syringe was used for these measurements. The melting point for each compound was measured using Stuart SMP10 melting point

apparatus. High resolution mass spectrometry was performed using a Bruker microTOF-Q mass spectrometer and spectra recorded and processed using Bruker's Compass Data Analysis software. Infrared spectra were obtained using Shimadzu IR-Affinity-1 model Infrared spectrometer. The data was analysed in wavenumbers (cm^{-1}) using IRsolution software. DLS and Zeta Potential studies were carried out using an Anton Paar Litesizer™ 500 and processed using Kalliope™ professional.

^{1}H NMR Diffusion Ordered Spectroscopy (DOSY): The hydrodynamic diameter was derived from diffusion rates obtained from ^{1}H NMR DOSY measurements using the Stokes-Einstein equation. The viscosity value used for the calculation was 0.00199 mPa (DMSO).

Quantitative ^{1}H NMR (qNMR): A ^{1}H NMR spectrum was obtained with a delay (d_1 = 60 s) for an SSA (112 mM) in DMSO-d_6/ 1.0 % DCM and/or an SSA (5.56 mM) in D_2O/ 5.0 % EtOH. Through comparative integration of the SSA anionic and cationic component signals with the ethanol signal, the proportion of these SSA components to become 'lost' from solution, through the adoption of solid-like characteristics can be calculated.

Self-association Constant Calculation: Self-association constants were determined using Bindfit v0.5 (http://app.supramolecular.org/bindfit/). All the data can be accessed online using the hyperlinks provided.

Tensiometry Studies: All the samples were prepared in an EtOH:H_2O (1:19) solution. All samples underwent an annealing process in which the various solutions were heated to approximately 313 K before being allowed to cool to RT, allowing each sample to reach a thermodynamic minimum. All samples were prepared through serial dilution of the most concentrated sample. Three surface tension measurements were obtained for each sample at a given concentration using the pendant drop method. The average values were then used to calculate the CAC.

Mass Spectrometry: Approximately 1 mg of each compound was dissolved in 1 mL of methanol. This solution was further diluted 100-fold before undergoing analysis where 10 µL of each sample was injected directly into a flow of 10 mM ammonium acetate in 95 % water (flow rate = 0.02 mL/min).

Dynamic Light Scattering (DLS) Studies: All solvents used were filtered to remove any particulates that may interfere with the results obtained. All samples underwent an annealing process, in which they were heated to

313 K before being allowed to cool to 298 K to allow each sample to reach a thermodynamic minimum. A series of 10 runs were recorded at 298 K.

Zeta Potential (ZP) Studies: All solvents used were filtered to remove any particulates that may interfere with the results obtained. All samples underwent an annealing process in which they were heated to 313 K before being allowed to cool to 298 K to allow each sample to reach a thermodynamic minimum. The final ZP value given is an average of the number of experiments conducted at 298 K.

Crystal X-ray Studies: Single crystals were produced through selective precipitation using chloroform and hexane. A suitable crystal was selected and mounted on a Rigaku Oxford Diffraction Supernova diffractometer. Data were collected using Cu Kα radiation at 100 K. Structures were solved with the ShelXT[1] or ShelXS structure solution programs via Direct Methods and refined with $ShelXL_1$ by least Squares minimisation. Olex2 was used as an interface to all ShelX programs (CCDC 2122929).

Circular Dichroism (CD) Studies: All circular dichroism experiments were performed on the JASCO J-175 spectropolarimeter using a 1 mm pathlength quartz cuvette. Far UV-spectra were obtained between 200-260 nm with an average of 4 scans at 100 nm/min, 0.5 nm step resolution, 1.0

second response and 0.5 nm bandwidth. Samples were prepared between 1 mM in 400 µL of EtOH:H_2O (1:19).

5.2. Biological Experimental Techniques

Preparation of bacterial plates: Sterile TSB agar plates were streaked using the desired bacteria [*Staphylococcus aureus* (9144, 13616, USA 300 and 1199B), *Enterococcus faecalis* (NCTC 775 and 12201) and *Enterococcus faecium* (NCTC 12204)] and incubated at 37 °C overnight.

Preparation of Inoculum: An initial culture was made up by inoculating TSB (5 mL) with 3 single colonies of the desired bacteria under sterile conditions and incubated at 37 °C overnight. The optical density at 600 nm (OD_{600}) was adjusted using sterile distilled H_2O (dH_2O) to equal ~1 x 10^6 bacteria/mL.

Preparation of 96 well microplate for MIC: A solution of each compound in EtOH:H_2O (1:19) was made at a top concentration of 5.56 mM on the day of experiment. The compound solution (200 µL) was added to and diluted 50:50 down the plate. The bacterial suspension (100 µL) was dispensed into each well under sterile conditions. The plates were sealed using parafilm and incubated at 37 °C for 20 hours, after which the OD_{600} was measured.

Haemolysis assay: Protocol modified from Travis et al.[140] Heparinised human red blood cells collected from a volunteer and washed three times in PBS (pH 7.4). SSAs were serial diluted using PBS buffer across a 96-well V bottom Greiner plate. Negative control (100 µL PBS), and positive control (100 µL 0.1% (v/v) Triton-X-100) were added to the plate. 100 µL of 10% (v/v) of blood suspension added to all wells. Plates were incubated for 60 minutes at 37 ^{o}C. After incubation, plates were centrifuged for 15 mins at 4680 rpm. The resultant supernatant was then transferred to a 96-well flat bottom plate and absorbance read at 540 nm (Fluostar Omega). Percent haemolysis was calculated using the formula as shown in Equation S1.

Equation S1 - Percentage haemolysis calculation.

$$\text{Haemolysis } (\%) = \frac{A_{sample} - A_{negative}}{A_{Triton} - A_{negative}} \; X \; 100$$

***G. mellonella* treatment assay**: *G. mellonella* larvae were purchased from Livefood UK Ltd. (Rooks Bridge, UK) and maintained on wood chips in the dark at 15 ^{o}C until use. *Galleria* larvae were injected with 10 µL of SSA in EtOH:H_2O (1:19), incubated at 37 ^{o}C for 5 days and the deaths counted. Groups of 10 *Galleria* were injected per compound.

Cell culture: The RPE-1 retinal pigment epithelial, A2780 human ovarian carcinoma, and A2780 CisR cisplatin resistant human ovarian carcinoma cell lines were purchased from the Health Protection Agency (Salisbury,

UK) and American Type Culture Collection (ATCC, USA) respectively. The A2780 and A2780 CisR cell lines were cultured in IMDM supplemented with 10% FBS at 37 °C and 5% CO_2, while the RPE-1 cell line was cultured in a 1:1 mixture of Dulbecco's Modified Eagle Medium and Ham's F-12 Nutrient Mixture (DMEM/F-12) at 37 °C and 5% CO_2.

SRB Assay: Cells were seeded into 96-well plates at 800 cells per well [(cpw), A2780], 1600 cpw (A2780 CisR) or 400 cpw (RPE-1) in cell culture medium and cultured for 48 hours followed by addition of each compound over an eight-point concentration range (each concentration in triplicate). Plates were then cultured for a further 96 hours, after which the cell culture medium was removed from each well and the cells fixed with addition of 70 μL/well of 10% (w/v) trichloroacetic acid (TCA) in distilled water followed by incubation for 30 minutes at RT. Each plate was then washed with distilled water five times before addition of 70 μL SRB dye (0.4% (w/v) SRB dye (ThermoFisher Scientific, USA) solubilised in 1% (v/v) acetic acid/distilled water) and incubation for 30 minutes at RT, followed by washing three times with 1% (v/v) acetic acid and drying in a 37 °C oven overnight. Once dry, 100 μl of 10 mM Tris-base (ThermoFisher Scientific, USA) was added to each well and plates put on a microplate shaker for 10 minutes at 200 rpm to solubilize the dye. Absorbance values were then read at wavelength 490 nm on a Victor X4 multi-label plate reader

(PerkinElmer Life Sciences, USA), data analysed using Microsoft Excel and graphs produced using GraphPad Prism 6.0 and the GI_{50} value calculated.

5.3. Synthesis

Compound 9: This compound was synthesised in line with previously published methods.[64] ^{1}H NMR (400 MHz, 298 K, DMSO-d_6): δ: 9.86 (s, 1H), 7.63 (d, *J* = 8.60 Hz, 2H), 7.50 (d, *J* = 8.72 Hz, 2H), 6.56 (s, 1H), 3.17 - 3.13 (m, 8H), 1.60 - 1.52 (m, 8H), 1.35 - 1.26 (m, 8H), 0.93 (t, *J* = 14.68 Hz, 12H).

Compound 12: 1-Isocyanato-4-(trifluoromethyl) benzene (0.29 mL, 2.00 mM) was added to a stirring solution of L-Phenylalanine tert-butyl ester hydrochloride (0.52 g, 2 mM) in pyridine (10 mL) and left at RT overnight. The mixture was the placed on the rotary-evaporator, dried and dissolved in chloroform (5 mL). Hexane was added dropwise, and the precipitate removed by filtration. The pure product was collected via flash column chromatography as a white solid with a yield of 61 % (0.50 g, 1.22 mM); melting point: > 200 °C; ^{1}H NMR (400 MHz, 298 K, DMSO-d_6): δ: 9.12 (s, 1H), 7.56 (s, 4H), 7.32 - 7.21 (m, 5H), 6.54 (d, *J* = 7.88 HZ, 1H), 4.42 (q, *J* = 21.16 Hz, 1H), 3.00 (d, *J* = 6.84 Hz, 2H), 1.35 (s, 9H); ^{13} C{^{1}H} NMR (100 MHz, 298 K, DMSO-d_6): δ: 171.5 (CO), 154.7 (CO), 144.2 (d, *J* = 1.17 Hz, ArC), 137.2 (C), 129.8 (ArCH), 128.7 (ArCH), 127.0 (ArCH), 126.5 – 126.3 (m, ArCH) 121.7 (q, *J* = 95.4 Hz, CF_3), 123.7 (ArC), 117.7 (ArCH), 81.4 (C), 54.6

(CH), 37.9 (CH_2), 27.9 (CH_3); HRMS for the carboxylate urea ($C_{21}H_{23}F_3N_2O_3$) (ESI^-): m/z: act: 408.1227 $[M]^-$ cal: 408.1661 $[M]^-$.

Compound 13: Zinc bromide (2.25 g, 10 mM) was added to a stirring solution of compound **12** (0.50 g, 1.22 mM) in dichloromethane (5 mL) and stirred at RT for 24 hours. Water (20 mL) was added, and the mixture was stirred at RT for 4 hours, before removal of the precipitate via filtration. TBA hydroxide (1 M) in methanol (0.41 mL) was added to the precipitate and taken to dryness. The pure product was collected via flash column chromatography as a brown solid with a yield of 54 % (0.27 g, 0.45 mM); melting point: 160 °C; ^{1}H NMR (400 MHz, 298 K, DMSO-d_6): δ: 9.81 (s, 1H), 7.64 (d, *J* = 8.60 Hz, 2H), 7.49 (d, *J* = 8.72 Hz, 2H), 7.14 - 7.04 (m, 5H), 6.60 (d, *J* = 5.00 Hz, 1H), 3.96 (q, *J* = 15.60 Hz, 1H), 3.17 - 2.97 (m, 10 H), 1.59 – 1.51 (m, 8H), 1.34 – 1.25 (m, 8H), 0.92 (t, *J* = 14.64 Hz, 12H); ^{13} C{^{1}H} NMR (100 MHz, 298 K, DMSO-d_6): δ: 173.2 (CO), 155.2 (CO), 146.0 (d, *J* = 1.1 Hz, ArC), 140.3 (C), 130.1 (ArCH), 127.9 (ArCH), 126.1 – 125.7 (m, CF_3), 124.0 (ArC), 120.3 (ArCH), 119.9 (ArCH), 117.3 (ArCH), 57.9 (t, *J* = 5 Hz, CH_2); 56.7 (CH_2), 39.1 (CH_2), 23.5 (CH_2), 19.7 (CH_2), 13.9 (CH_3); IR (film): ν = 2962 (NH stretch), 1693, 1487, 1319, 881; HRMS for the carboxylate urea ($C_{17}H_{14}F_3N_2O_3^-$) (ESI^-): m/z: act: 351.0952 $[M]^-$ cal: 351.0962 $[M]^-$.

Compound 14: 1-Isocyanato-4-(trifluoromethyl) benzene (0.29 mL, 2.00 mM) was added to a stirring solution of D-phenylalanine tert-butyl ester

hydrochloride (0.52 g, 2 mM) in pyridine (10 mL) and left at RT overnight. The mixture was then taken to dryness and dissolved in chloroform (5 mL), followed by dropwise additions of hexane, resulting in precipitation. The precipitate removed by filtration and the pure product was collected via flash column chromatography with a 3:2 mixture of hexane: ethyl acetate as a white solid with a yield of 62 % (0.51 g, 1.25 mM) melting point: 166 °C; ^{1}H NMR (400 MHz, 298 K, DMSO-d_6): δ: 9.12 (s, 1H), 7.56 (s, 4H), 7.32 – 7.21 (m, 5H), 6.54 (d, *J* = 7.84, 1H), 4.42, (q, *J* =21.12, 1H), 3.00 (d, *J* = 6.84, 2 H), 1.35 (s, 9H); ^{13} C{^{1}H} NMR (100 MHz, 298 K, DMSO-d_6): δ: 171.5 (CO), 154.7 (CO), 144.3 (d, *J* = 10 Hz, ArC), 137.3 (C), 129.8 (ArCH), 128.7 (ArCH), 127.1 (ArCH), 126.5 – 126.4 (m, ArCH), 123.7 (ArC), 121.8 (q, *J* = 95.3 Hz, CF_3), 117.1 (ArCH), 81.5 (C), 54.6 (CH), 37.9 (CH_2), 28.0 (CH_3); HRMS for the carboxylate urea ($C_{21}H_{23}F_3N_2O_3$) (ESI^-): m/z: act: 408.1502 $[M]^-$ cal: 408.1661 $[M]^-$.

Compound 15: Zinc bromide (2.25 g, 10 mM) was added to a stirring solution of compound **14** (0.51 g, 1.25 mM) in dichloromethane (5 mL) and stirred at RT for 24 hours. Water (20 mL) was added, and the mixture was stirred at RT for 4 hours, before removal of the precipitate via filtration. TBA hydroxide (1 M) in methanol (0.51 mL) was added to the precipitate and taken to dryness. The pure product was collected via flash column chromatography with 100 % ethyl acetate followed by 100 % methanol as a brown solid with a yield of 54 % (0.28 g, 0.47 mM); melting point: > 200 °C;

^{1}H NMR (400 MHz, 298 K, DMSO-d_6): δ: 9.39 (s, 1H), 7.57 (d, *J* = 8.84 Hz, 2H), 7.50 (d, *J* = 9.00 Hz, 2H), 7.17 - 7.06 (m, 5H), 6.40 (d, *J* = 6.4 Hz, 1H), 3.86 (q, *J* = 15.12 Hz, 1H), 3.18 - 3.02 (m, 10 H), 1.60 – 1.51 (m, 8H), 1.35 – 1.25 (m, 8H), 0.92 (t, *J* = 14.68 Hz, 12H); ^{13} C{^{1}H} NMR (100 MHz, 298 K, DMSO-d_6): δ: 173.2 (CO), 155.2 (CO), 145.9 (ArC), 140.2 (C), 130.1 (ArCH), 127.9 (ArCH), 126.1 – 125.7 (m, CF_3), 123.9 (ArC), 120.3 (ArCH), 120.0 (ArCH), 117.3 (ArCH), 57.9 (t, *J* = 4.99 Hz, CH_2); 56.7 (CH_2), 39.1 (CH_2), 23.5 (CH_2), 19.7 (CH_2), 13.9 (CH_3); IR (film): ν = 2962 (NH stretch), 1695, 1487, 1319, 881; HRMS for the carboxylate urea ($C_{17}H_{14}F_3N_2O_3^-$) (ESI^-): m/z: act: 351.0937 $[M]^-$ cal: 351.0962 $[M]^-$.

Compound 16: 1-Isocyanato-4-(trifluoromethyl) benzene (0.29 mL, 2.00 mM) was added to a stirring solution of L-Leucine tert-butyl ester hydrochloride (0.45 g, 2 mM) in pyridine (10 mL) and left at RT overnight. The mixture was the placed on the rotary-evaporator, dried and dissolved in chloroform (5 mL). Hexane was added dropwise, and the precipitate removed by filtration. The pure product was collected via flash column chromatography as a white solid with a yield of 53 % (0.40 g, 1.07 mM); melting point: > 200 °C; ^{1}H NMR (400 MHz, 298 K, DMSO-d_6): δ: 8.98 (s, 1H), 7.58 (s, 4H), 6.57 (d, *J* = 8.16 Hz, 1H), 4.14 (q, *J* = 22.76 Hz, 1H), 1.71 – 1.64 (m, 1 H), 1.50 (m, 2H), 1.41 (s, 9H); ^{13} C{^{1}H} NMR (100 MHz, 298 K, DMSO-d_6): δ: 172.8 (CO), 154.9 (CO), 144.3 (d, *J* = 1.13 Hz, ArC), 129.8 (ArCH), 129.1 (ArCH), 126.5 (q, *J* = 11.5 Hz, ArCH), 123.7 (ArC), 121.7 (q, *J* =

95.3 Hz, CF_3), 117.7 (ArCH), 81.1 (C), 51.8 (CH), 41.2 (CH_2), 28.1 (CH_3), 24.8 (CH_3), 23.1 (CH_3), 22.1 (CH_3); HRMS for the carboxylate urea ($C_{18}H_{25}F_3N_2O_3$) (ESI^-): m/z: act: 374.1739 $[M]^-$ cal: 374.1817 $[M]^-$.

Compound 17: Zinc bromide (2.25 g, 10 mM) was added to a stirring solution of compound **16** (0.40 g, 1.07 mM) in dichloromethane (5 mL) and stirred at RT for 24 hours. Water (20 mL) was added, and the mixture was stirred at RT for 4 hours, before removal of the precipitate via filtration. TBA hydroxide (1 M) in methanol (0.40 mL) was added to the precipitate and taken to dryness. The pure product was collected via flash column chromatography as a brown solid with a yield of 62 % (0.25 g, 0.45 mM); melting point: 131 °C; ^{1}H NMR (400 MHz, 298 K, DMSO-d_6): δ: 10.89 (s, 1H), 7.82 (d, *J* = 8.60 Hz, 2H), 7.44 (d, *J* = 8.72 Hz, 2H), 7.21 (d, *J* = 6.84, 1H), 3.84 (q, *J* = 20.04 Hz, 1H), 3.17 – 3.12 (m, 8H), 1.80 – 1.67 (m, 1H), 1.59 – 1.49 (m, 9H), 1.46 – 1.37 (m, 1H), 1.35 – 1.22 (m, 8H), 0.93 – 0.87 (m, 18H); $^{13}C\{^1H\}$ NMR (100 MHz, 298 K, DMSO-d_6): δ: 174.9 (CO), 155.4 (CO), 146.3 (ArC), 126.7 (C), 125.9 (d, *J* = 3.7 Hz, ArCH), 124.0 (ArC), 120.1 (CF_3), 119.8 (CF_3), 117.2 (ArCH), 57.9 (CH_2), 54.2 (CH), 44.5 (CH_2), 25.0 (CH_3), 23.7 (CH_3), 23.5 (CH_2), 23.4 (CH_3), 19.6 (CH_2), 13.9 (CH_3); IR (film): v = 2960 (NH stretch), 1697, 1458, 1319, 877; HRMS for the carboxylate urea ($C_{14}H_{16}F_3N_2O_3^-$) (ESI^-): m/z: act: 317.1110 $[M]^-$ cal: 317.1118 $[M]^-$.

Compound 18: 1-Isocyanato-4-(trifluoromethyl) benzene (0.29 mL, 2.00 mM) was added to a stirring solution of D-Leucine tert-butyl ester hydrochloride (0.45 g, 2 mM) in pyridine (10 mL) and left at RT overnight. The mixture was the placed on the rotary-evaporator, dried and dissolved in chloroform (5 mL). Hexane was added dropwise, and the precipitate removed by filtration. The pure product was collected via flash column chromatography as a white solid with a yield of 75 % (0.56 g, 1.50 mM); melting point: > 200 °C; ^{1}H NMR (400 MHz, 298 K, DMSO-d_6): δ: 8.96 (s, 1H), 7.57 (s, 4H), 6.55 (d, *J* = 8.12 Hz, 1H), 4.13 (q, *J* = 22.80 Hz, 1H), 1.70 – 1.62 (m, 1 H), 1.52 – 1.48 (m, 2H), 1.41 (s, 9H); ^{13} C{^{1}H} NMR (100 MHz, 298 K, DMSO-d_6): δ: 172.8 (CO), 154.9 (CO), 144.3 (d, *J* = 1.19 Hz, ArC), 129.1 (ArCH), 126.5 (q, *J* = 11.2 Hz, ArCH), 123.7 (ArC), 121.7 (q, *J* = 94.9Hz, CF_3), 117.7 (ArCH), 81.1 (C), 51.8 (CH), 41.2 (CH_2), 28.1 (CH_3), 24.8 (CH_3), 23.1 (CH_3), 22.1 (CH_3); HRMS for the carboxylate urea ($C_{18}H_{25}F_3N_2O_3$) (ESI^-): m/z: act: 374.1763 $[M]^-$ cal: 374.1817 $[M]^-$.

Compound 19: Zinc bromide (2.25 g, 10 mM) was added to a stirring solution of compound **18** (0.56 g, 1.50 mM) in dichloromethane (5 mL) and stirred at RT for 24 hours. Water (20 mL) was added, and the mixture was stirred at RT for 4 hours, before removal of the precipitate via filtration. TBA hydroxide (1 M) in methanol (0.56 mL) was added to the precipitate and taken to dryness. The pure product was collected via flash column chromatography as a brown solid with a yield of 68 % (0.38 g, 0.68 mM);

melting point: 120 °C; ^{1}H NMR (400 MHz, 298 K, DMSO-d_6): δ: 11.07 (s, 1H), 7.85 (d, *J* = 8.56 Hz, 2H), 7.43 (d, *J* = 8.68 Hz, 2H), 7.29 (d, *J* = 6.76, 1H), 3.84 (q, *J* = 20.00 Hz, 1H), 3.17 – 3.12 (m, 8H), 1.80 – 1.70 (m, 1H), 1.58 – 1.50 (m, 9H), 1.45 – 1.38 (m, 1H), 1.34 – 1.24 (m, 8H); 0.93 – 0.88 (m, 18H); ^{13}C{^{1}H} NMR (100 MHz, 298 K, DMSO-d_6): δ: 174.9 (CO), 155.4 (CO), 146.3 (ArC), 126.7 (C), 125.9 (d, *J* = 3.7 Hz, ArCH), 124.0 (ArC), 120.1 (CF_3), 119.8 (CF_3), 117.2 (ArCH), 57.9 (CH_2), 54.2 (CH), 44.5 (CH_2), 25.0 (CH_3), 23.7 (CH_3), 23.5 (CH_2), 23.4 (CH_3), 19.6 (CH_2), 13.9 (CH_3); IR (film): ν = 2960 (NH stretch), 1697, 1458, 1319, 877; HRMS for the carboxylate urea ($C_{14}H_{16}F_3N_2O_3^-$) (ESI^-): m/z: act: 317.1160 $[M]^-$ cal: 317.1118 $[M]^-$.

6. References

1 J.-M. Lehn, *Supramolecular Chemistry: Concepts and Perspectives*, John Wiley & Sons, Hoboken, 1st edn., 1995.

2 J.-M. Lehn, *Angew. Chem. Int. Ed. Engl.*, 1990, **29**, 1304–1319.

3 B. Dietrich, J.-M. Lehn and J.-P. Sauvage, *Tetrahedron Lett*, 1969, **10**, 2885–2888.

4 J.-M. Lehn, *Angew. Chem. Int. Ed. Engl.*, 1988, **27**, 89–112.

5 J.-M. Lehn, *Chem. Soc. Rev.*, 2007, **36**, 151–160.

6 V. Balzani, A. Credi and M. Venturi, *Molecular Devices and Machines: Concepts and Perspectives for the Nanoworld*, John Wiley & Sons, Hoboken, 2nd edn., 2008.

7 S. Kubik, *Supramolecular Chemistry*, De Gruyter, Berlin, 2020.

8 J. W. Steed, D. R. Turner and K. J. Wallace, *Core Concepts in Supramolecular Chemistry and Nanochemistry*, John Wiley & Sons, Hoboken, 1st edn., 2007.

9 J. D. van der Waals, PhD thesis, University of Leiden, 1873.

10 H. Margenau, *Rev. Mod. Phys.*, 1939, **11**, 1–35.

11 J. S. Rowlinson, *Nature*, 1973, **244**, 414–417.

12 D. E. Koshland, *Angew. Chem., Int. Ed. Engl.*, 1994, **33**, 2375–2378.

13 W. M. Latimer and W. H. Rodebush, *J. Am. Chem. Soc.*, 1920, **42**, 1419–1433.

14 T. S. Moore and T. F. Winmill, *J. Chem. Soc., Trans.*, 1912, **101**, 1635–1676.

15 R. M. Izatt, *Chem. Soc. Rev.*, 2017, **46**, 2380–2384.

16 G. M. Lein and D. J. Cram, *J. Chem. Soc., Chem. Commun.*, 1982, 301.

17 G. W. Gokel and M. F. Fedders, in *Comprehensive Heterocyclic Chemistry II*, ed. A. R. Katritzky, C. W. Rees, E. F. V. Scriven and G. R. Newkome, Elsevier, Amsterdam, 1996, vol. 9, pp. 863–892.

18 V. Richards, *Nat. Chem.*, 2016, **8**, 1090–1090.

19 J.-P. Sauvage, *Angew. Chem., Int. Ed.*, 2017, **56**, 11080–11093.

20 C. J. Bruns and J. F. Stoddart, *Acc. Chem. Res.*, 2014, **47**, 2186–2199.

21 B. L. Feringa, *Angew. Chem., Int. Ed.*, 2017, **56**, 11060–11078.

22 J. S. Murray and P. Politzer, *Wiley Interdiscip. Rev.: Comput. Mol. Sci.*, 2017, **7**, e1326.

23 T. Soderberg, *Organic Chemistry with a Biological Emphasis Volume I*, Chemistry Publications, University of Minnesota Morris, Morris, 2019, vol. 1.

24 S.-J. Park and M.-K. Seo, in *Interface Science and Technology*, Elsevier , Amsterdam, 1st edn., 2011, vol. 18, pp. 1–57.

25 P. C. Hiemenz and R. Rajagopalan, *Principles of Colloid and Surface Chemistry*, CRC Press, Boca Raton, 3rd edn., 2016.

26 F. L. Leite, C. C. Bueno, A. L. Da Róz, E. C. Ziemath and O. N. Oliveira, *Int. J. Mol. Sci.*, 2012, **13**, 12773–12856.

27 M. L. Waters, *Curr. Opin. Chem. Biol.*, 2002, **6**, 736–741.

28 S. A. Sharber, W. J. Mullin and S. W. Thomas, *Chem. Mater.*, 2021, **33**, 6640–6661.

29 B. W. Gung and J. C. Amicangelo, *J. Org. Chem.*, 2006, **71**, 9261–9270.

30 A. P. West, S. Mecozzi and D. A. Dougherty, *J. Phys. Org. Chem*, 1997, **10**, 347–350.

31 D. A. Dougherty, *Acc. Chem. Res.*, 2012, **46**, 885–893.

32 A. J. Stone, *J. Phys. Chem. A*, 2017, **121**, 1531–1534.

33 A. Shahi and E. Arunan, *Phys. Chem. Chem. Phys.*, 2014, **16**, 22935–22952.

34 H. J. Schneider, *J. Phys. Org. Chem.*, 2022, **35**, 1–11.

35 T. Steiner, *Angew. Chem., Int. Ed.*, 2002, **41**, 48–76.

36 D. Herschlag and M. M. Pinney, *Biochemistry*, 2018, **57**, 3338–3352.

37 J. D. Smith, C. D. Cappa, K. R. Wilson, R. C. Cohen, P. L. Geissler and R. J. Saykally, *Proc. Natl. Acad. Sci. U. S. A.*, 2005, **102**, 14171–14174.

38 R. C. Dougherty, *J. Chem. Phys.*, 1998, **109**, 7378.

39 D. Lombardo, M. A. Kiselev, S. Magazù and P. Calandra, *Adv. Condens. Matter Phys.*, 2015, **2015**, 1–22.

40 R. Azarmi and A. Ashjaran, *J. Chem. Pharm. Res.*, 2015, **7**, 632–640.

41 V. S. Kulkarni and C. Shaw, in *Essential Chemistry for Formulators of Semisolid and Liquid Dosages*, Elsevier, Amsterdam, 2016, pp. 5–19.

42 B. E. Rapp, in *Microfluidics: Modelling, Mechanics and Mathematics*, Elsevier, Amsterdam, 2017, pp. 421–444.

43 A. Wu, Y. Gao and L. Zheng, *Green Chem.*, 2019, **21**, 4290–4312.

44 T. J. Moyer, J. A. Finbloom, F. Chen, D. J. Toft, V. L. Cryns and S. I. Stupp, *J. Am. Chem. Soc.*, 2014, **136**, 14746–14752.

45 W. Kim, J. Thévenot, E. Ibarboure, S. Lecommandoux and E. L. Chaikof, *Angew. Chem. Int. Ed.*, 2010, **49**, 4257–4260.

46 J. N. Israelachvili, *Intermolecular and Surface Forces*, Elsevier, Amsterdam, 3rd edn., 2011.

47 Y. Kang, K. Liu and X. Zhang, *Langmuir*, 2014, **30**, 5989–6001.

48 G. Yu, K. Jie and F. Huang, *Chem. Rev.*, 2015, **115**, 7240–7303.

49 X. Zhang and C. Wang, *Chem. Soc. Rev.*, 2011, **40**, 94–101.

50 K. Liu, Y. Yao, Y. Liu, C. Wang, Z. Li and X. Zhang, *Langmuir*, 2012, **28**, 10697–10702.

51 C. Wang, Q. Chen, Z. Wang and X. Zhang, *Angew. Chem. Int. Ed.*, 2010, **49**, 8612–8615.

52 A. V. Kabanov, T. K. Bronich, V. A. Kabanov, K. Yu and A. Eisenberg, *J. Am. Chem. Soc.*, 1998, **120**, 9941–9942.

53 C. Shan, X. Huang, H. Wei, W. Wei, H. Sun and X. Tang, *RSC Adv.*, 2014, **4**, 11216–11218.

54 J.-F. Gohy, B. G. G. Lohmeijer, S. K. Varshney and U. S. Schubert, *Macromolecules*, 2002, **35**, 7427–7435.

55 X. Zhang, Z. Chen and F. Würthner, *J. Am. Chem. Soc.*, 2007, **129**, 4886–4887.

56 A. Wilson, G. Gasparini and S. Matile, *Chem. Soc. Rev.*, 2014, **43**, 1948–1962.

57 C. B. Minkenberg, L. Florusse, R. Eelkema, G. J. M. Koper and J. H. van Esch, *J. Am. Chem. Soc.*, 2009, **131**, 11274–11275.

58 F. Hammami, H. Ghalla and S. Nasr, *Comput. Theor. Chem.*, 2015, **1070**, 40–47.

59 S. Shinde, A. Incel, M. Mansour, G. D. Olsson, I. A. Nicholls, C. Esen, J. Urraca and B. Sellergren, *J. Am. Chem. Soc.*, 2020, **142**, 11404–11416.

60 C. Pérez-Casas and A. K. Yatsimirsky, *J. Org. Chem.*, 2008, **73**, 2275–2284.

61 J. R. Hiscock, G. P. Bustone, B. Wilson, K. E. Belsey and L. R. Blackholly, *Soft Matter*, 2016, **12**, 4221–4228.

62 L. R. Blackholly, H. J. Shepherd and J. R. Hiscock, *CrystEngComm*, 2016, **18**, 7021–7028.

63 L. J. White, J. E. Boles, N. Allen, L. S. Alesbrook, J. M. Sutton, C. K. Hind, K. L. F. Hilton, L. R. Blackholly, R. J. Ellaby, G. T. Williams, D. P. Mulvihill and J. R. Hiscock, *J. Mater. Chem. B.*, 2020, **8**, 4694–4700.

64 L. J. White, S. N. Tyuleva, B. Wilson, H. J. Shepherd, K. K. L. Ng, S. J. Holder, E. R. Clark and J. R. Hiscock, *Chem. - Eur. J.*, 2018, **24**, 7761–7773.

65 L. J. White, N. J. Wells, L. R. Blackholly, H. J. Shepherd, B. Wilson, G. P. Bustone, T. J. Runacres and J. R. Hiscock, *Chem. Sci.*, 2017, **8**, 7620–7630.

66 N. Allen, L. J. White, J. E. Boles, G. T. Williams, D. F. Chu, R. J. Ellaby, H. J. Shepherd, K. K. L. Ng, L. R. Blackholly, B. Wilson, D. P. Mulvihill and J. R. Hiscock, *Chem. Med. Chem.*, 2020, **15**, 2193–2205.

67 S. N. Tyuleva, N. Allen, L. J. White, A. Pépés, H. J. Shepherd, P. J. Saines, R. J. Ellaby, D. P. Mulvihill and J. R. Hiscock, *Chem. Commun.*, 2019, **55**, 95–98.

68 J. E. Boles, R. J. Ellaby, H. J. Shepherd and J. R. Hiscock, *RSC Adv.*, 2021, **11**, 9550–9556.

69 N. O. Dora, E. Blackburn, J. E. Boles, G. T. Williams, L. J. White, S. E. G. Turner, J. D. Hothersall, T. Askwith, J. A. Doolan, D. P. Mulvihill, M. D. Garrett and J. R. Hiscock, *RSC Adv.*, 2021, **11**, 14213–14217.

70 C. J. L. Murray et al., *Lancet*, 2022, **399**, 629–655.

71 H. Sung, J. Ferlay, R. L. Siegel, M. Laversanne, I. Soerjomataram, A. Jemal and F. Bray, *Ca-Cancer J. Clin.*, 2021, **71**, 209–249.

72 M. Eckert, *Ann. Phys.*, 2012, **524**, A83–A85.

73 Nobel Prize in Physics 1914 Presentation, https://www.nobelprize.org/prizes/physics/1914/press-release/, (accessed 8 September 2022).

74 J.-P. Zhang, P.-Q. Liao, H.-L. Zhou, R.-B. Lin and X.-M. Chen, *Chem. Soc. Rev.*, 2014, **43**, 5789.

75 C. S. Ho, C. W. K. Lam, M. H. M. Chan, R. C. K. Cheung, L. K. Law, L. C. W. Lit, K. F. Ng, M. W. M. Suen and H. L. Tai, *Clin. Biochem. Rev.*, 2003, **24**, 3–12.

76 T. Portolés, E. Pitarch, F. J. López, F. Hernández and W. M. A. Niessen, *Rapid Commun. Mass Spectrom.*, 2011, **25**, 1589–1599.

77 Y. Wang, J. Sun, J. Qiao, J. Ouyang and N. Na, *Anal. Chem.*, 2018, **90**, 14095–14099.

78 S. Banerjee and S. Mazumdar, *Int. J. Anal. Chem.*, 2012, **2012**, 1–40.

79 M. Przybylski and M. O. Glocker, *Angew. Chem., Int. Ed. Engl.*, 1996, **35**, 806–826.

80 K. K. L. Ng, M. Dimitrovski, J. E. Boles, R. J. Ellaby, L. J. White and J. R. Hiscock, *Supramol. Chem.*, 2020, **32**, 414–424.

81 T. L. Gumbs, L. J. White, N. J. Wells, H. J. Shepherd and J. R. Hiscock, *Supramol. Chem.*, 2018, **30**, 286–295.

82 V. M. Wallace, N. R. Dhumal, F. M. Zehentbauer, H. J. Kim and J. Kiefer, *J. Phys. Chem. B*, 2015, **119**, 14780–14789.

83 J. Kiefer, K. Noack and B. Kirchner, *Curr. Phys. Chem.*, 2011, **1**, 340–351.

84 S. K. Bharti and R. Roy, *TrAC, Trends Anal. Chem.*, 2012, **35**, 5–26.

85 M. A. Nanny, J. M. Bortiatynski and P. G. Hatcher, *Environ. Sci. Technol.*, 1997, **31**, 530–534.

86 J. E. Del Bene, I. Alkorta and J. Elguero, *J. Phys. Chem. A*, 2008, **112**, 7925–7929.

87 J. E. Del Bene, S. A. Perera and R. J. Bartlett, *J. Phys. Chem. A*, 1999, **103**, 8121–8124.

88 G. A. Kumar and M. A. McAllister, *J. Org. Chem.*, 1998, **63**, 6968–6972.

89 M. H. Abraham, R. J. Abraham, J. Byrne and L. Griffiths, *J. Org. Chem.*, 2006, **71**, 3389–3394.

90 Z. Huang, H. Sun, H. Zhang, Y. Wang and F. Li, *J. Comput. Chem.*, 2011, **32**, 2055–2063.

91 Y. Xu, J. Yao, P. Yao, H. Li and S. Han, *Chin. J. Chem. Eng.*, 2010, **18**, 455–461.

92 P. Thordarson, *Chem. Soc. Rev.*, 2011, **40**, 1305–1323.

93 D. Brynn Hibbert and P. Thordarson, *Chem. Commun.*, 2016, **52**, 12792–12805.

94 R. B. Martin, *Chem. Rev.*, 1996, **96**, 3043–3064.

95 M. P. Evstigneev, A. S. Buchelnikov, V. V. Kostjukov, I. S. Pashkova and V. P. Evstigneev, *Supramol. Chem.*, 2013, **25**, 199–203.

96 L. K. S. von Krbek, C. A. Schalley and P. Thordarson, *Chem. Soc. Rev.*, 2017, **46**, 2622–2637.

97 Y. Shrot and L. Frydman, *J. Magn. Reson.*, 2008, **195**, 226–231.

98 J. T. Edward, *J. Chem. Educ.*, 1970, **47**, 261.

99 L. Maibaum, A. R. Dinner and D. Chandler, *J. Phys. Chem. B.*, 2004, **108**, 6778–6781.

100 A. Fluksman and O. Benny, *Anal. Methods*, 2019, **11**, 3810–3818.

101 Á. Piñeiro, X. Banquy, S. Pérez-Casas, E. Tovar, A. García, A. Villa, A. Amigo, A. E. Mark and M. Costas, *J. Phys. Chem. B.*, 2007, **111**, 4383–4392.

102 R. J. Williams, J. N. Phillips and K. J. Mysels, *Trans. Faraday Soc.*, 1955, **51**, 728–737.

103 Y. Hussein and M. Youssry, *Materials*, 2018, **11**, 688.

104 B. Lorber, F. Fischer, M. Bailly, H. Roy and D. Kern, *Biochem. Mol. Biol. Educ.*, 2012, **40**, 372–382.

105 E. Tomaszewska, K. Soliwoda, K. Kadziola, B. Tkacz-Szczesna, G. Celichowski, M. Cichomski, W. Szmaja and J. Grobelny, *J. Nanomater.*, 2013, **2013**, 1–10.

106 W. I. Goldburg, *Am. J. Phys.*, 1999, **67**, 1152–1160.

107 S. Bhattacharjee, *J. Controlled Release*, 2016, **235**, 337–351.

108 M. Kaszuba, J. Corbett, F. M. Watson and A. Jones, *Philos. Trans. R. Soc., A*, 2010, **368**, 4439–4451.

109 J. D. Clogston and A. K. Patri, in *Characterization of Nanoparticles Intended for Drug Delivery*, ed. S. E. McNeil, Humana Press, Totowa, 2011, vol. 697, pp. 63–70.

110 Y. Agrawal and V. Patel, *J. Adv. Pharm. Technol. Res.*, 2011, **2**, 81.

111 R. Vogel, A. K. Pal, S. Jambhrunkar, P. Patel, S. S. Thakur, E. Reátegui, H. S. Parekh, P. Saá, A. Stassinopoulos and M. F. Broom, *Sci. Rep.*, 2017, **7**, 17479.

112 A. Rodger, in *Encyclopedia of Biophysics*, ed. G. C. K. Roberts, Springer, Berlin, Heidelberg, 1st edn., 2013, pp. 311–316.

113 B. Nordén, A. Rodger and T. Dafforn, *Linear Dichroism and Circular Dichroism*, Royal Society of Chemistry, Cambridge, 2010.

114 S. Subadini, P. R. Hota, D. P. Behera and H. Sahoo, in *Optical Spectroscopic and Microscopic Techniques*, ed. H. Sahoo, Springer Nature Singapore, Singapore, 1st edn., 2022, pp. 19–33.

115 D. B. Goldstein, *Annu. Rev. Pharmacol. Toxicol.*, 1984, **24**, 43–64.

116 F. Fonseca, C. Pénicaud, E. E. Tymczyszyn, A. Gómez-Zavaglia and S. Passot, *Appl. Microbiol. Biotechnol.*, 2019, **103**, 6867–6883.

117 K. Tsuda, *Am. J. Hypertens.*, 2003, **16**, 259–261.

118 G. M. Cooper, *The Cell: A Molecular Approach*, Sinauer Associates, Sunderland, 2nd edn., 2000.

119 T. J. Denich, L. A. Beaudette, H. Lee and J. T. Trevors, *J. Microbiol. Methods*, 2003, **52**, 149–182.

120 J. Gruenberg and M. J. Clague, *Curr. Opin. Cell Biol.*, 1992, **4**, 593–599.

121 D. A. Los and N. Murata, *Biochim. Biophys. Acta, Biomembr.*, 2004, **1666**, 142–157.

122 K. B. Tiwari, S. Sen, C. Gatto and B. J. Wilkinson, in *Staphylococcus aureus*, ed. K. C. Price, Humana Press, Totowa, 2021, pp. 55–68.

123 C. Sohlenkamp and O. Geiger, *FEMS Microbiol. Rev.*, 2016, **40**, 133–159.

124 G. Tiwari, R. Tiwari, S. Bannerjee, L. Bhati, S. Pandey, P. Pandey and B. Sriwastawa, *Int. J. Pharm. Invest.*, 2012, **2**, 2–11.

125 B. Chertok, M. J. Webber, M. D. Succi and R. Langer, *Mol. Pharm.*, 2013, **10**, 3531–3543.

126 T. M. Allen and P. R. Cullis, *Science (1979)*, 2004, **303**, 1818–1822.

127 C. P. J. Vendrik, J. J. Bergers, W. H. De Jong and P. A. Steerenberg, *Cancer Chemother. Pharmacol.*, 1992, **29**, 413–429.

128 A. York, *Nat. Rev. Microbiol.*, 2020, **18**, 63–63.

129 K. Hu, Y. Jiang, Y. Xie, H. Liu, R. Liu, Z. Zhao, R. Lai and L. Yang, *J. Phys. Chem. B*, 2015, **119**, 8553–8560.

130 S. Troeira Henriques, Y.-H. Huang, S. Chaousis, C. K. Wang and D. J. Craik, *ChemBioChem*, 2014, **15**, 1956–1965.

131 G. Townshend, G. S. Thompson, L. J. White, J. R. Hiscock and J. L. Ortega-Roldan, *Chem. Commun.*, 2020, **56**, 4015–4018.

132 W. A. Lea and A. Simeonov, *Expert Opin. Drug Discovery*, 2011, **6**, 17–32.

133 N. J. Moerke, *Curr. Protoc. Chem. Biol.*, 2009, **1**, 1–15.

134 J. E. Boles, C. Bennett, J. Baker, K. L. F. Hilton, H. A. Kotak, E. R. Clark, Y. Long, L. J. White, H. Y. Lai, C. K. Hind, J. M. Sutton, M. D. Garrett, A. Cheasty, J. L. Ortega-Roldan, M. Charles, C. J. E. Haynes and J. R. Hiscock, *Chem. Sci.*, 2022, **13**, 9761–9773.

135 J. van Brakel, in *Handbook of the Philosophy of Science, Philosophy of Chemistry*, ed. A. I. Woody, R. Findlay and P. Needham, Elsevier, Amsterdam, 2012, vol. 6, pp. 191–229.

136 V. A. Davankov, in *Encyclopedia of Separation Science*, ed. I. D. Wilson, Elsevier, Amsterdam, 1997, pp. 4681–4684.

137 S. W. Lewis, in *Encyclopedia of Forensic Sciences*, ed. J. A. Siegel, P. J. Saukko and M. M. Houck, Elsevier, 2nd edn., 2013, pp. 621–626.

138 M. Inaki, J. Liu and K. Matsuno, *Philos. Trans. R. Soc., B*, 2016, **371**, 20150403.

139 A. B. George and K. S. Korolev, *PLoS Comput. Biol.*, 2018, **14**, e1006645.

140 S. M. Travis, N. N. Anderson, W. R. Forsyth, C. Espiritu, B. D. Conway, E. P. Greenberg, P. B. McCray, R. I. Lehrer, M. J. Welsh and B. F. Tack, *Infect. Immun.*, 2000, **68**, 2748–2755.

7. Appendix

7.1. Characterisation NMR

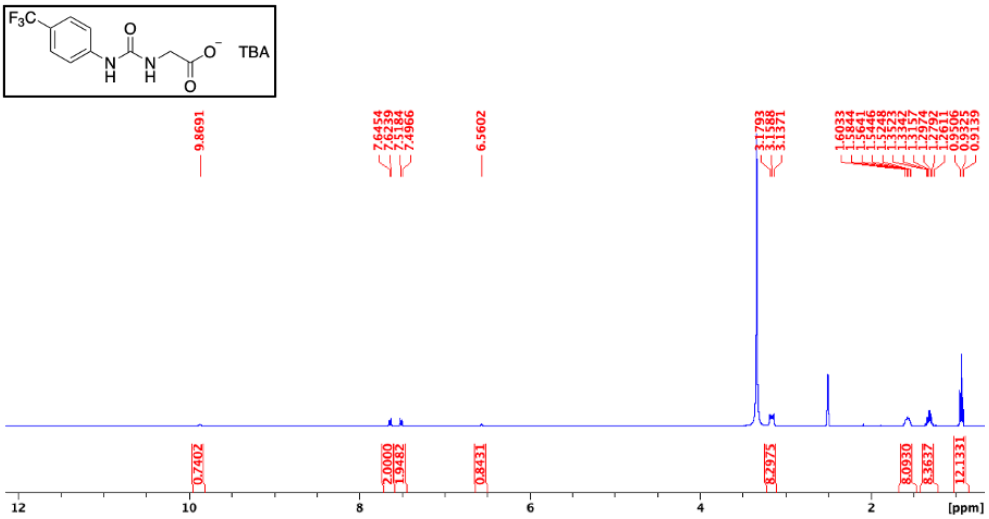

Figure S1 - ^{1}H NMR spectrum of compound **9** in DMSO-d_6 conducted at 298 K.

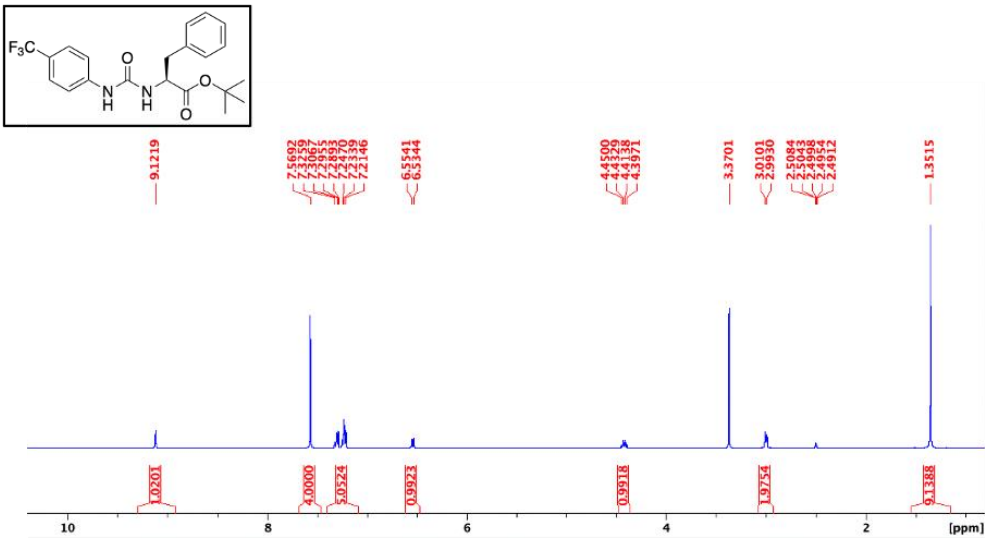

Figure S2 - ^{1}H NMR spectrum of compound **12** in DMSO-d_6 conducted at 298 K.

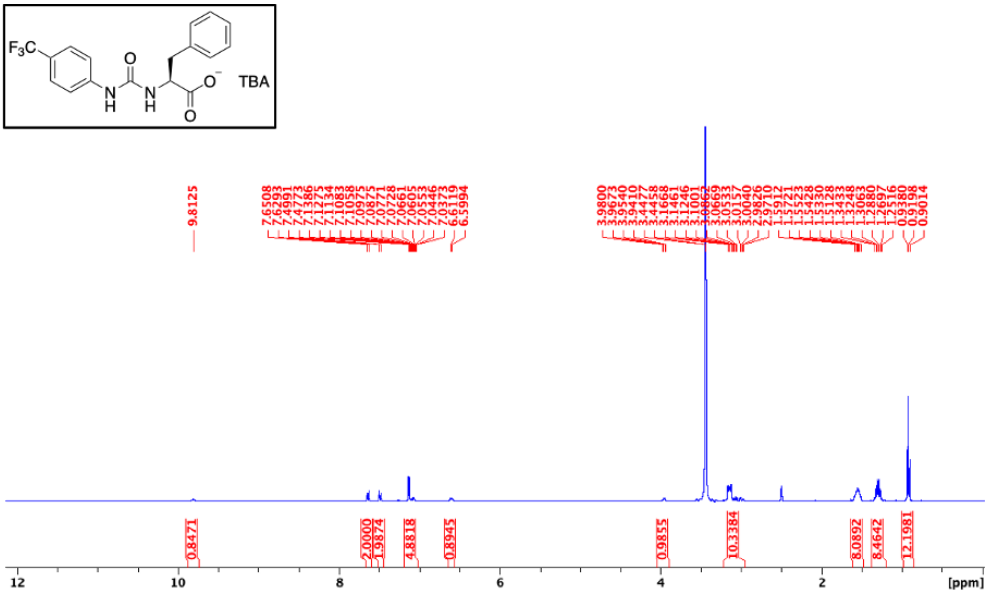

Figure S3 - ^{1}H NMR spectrum of compound **13** in DMSO-d_6 conducted at 298 K.

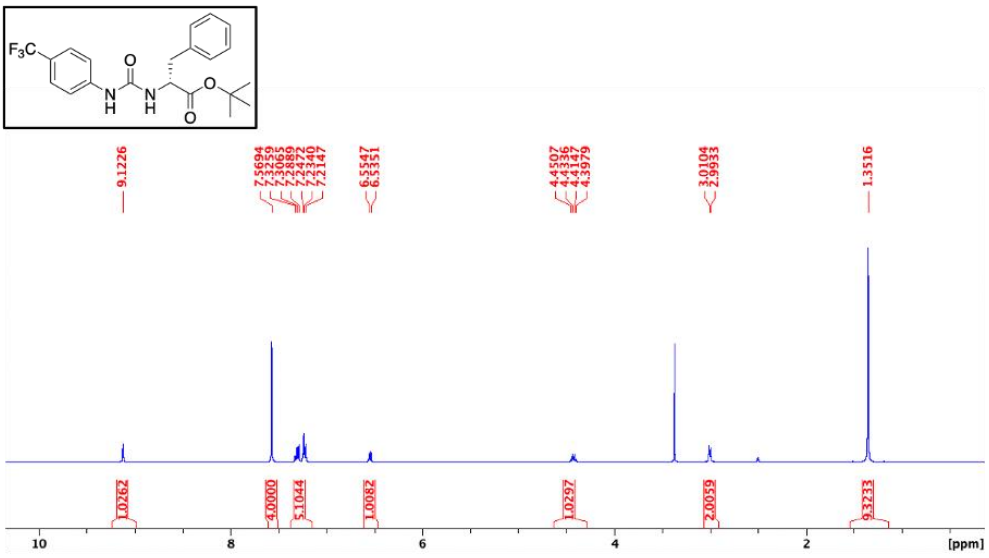

Figure S4 - ^{1}H NMR spectrum of compound **14** in DMSO-d_6 conducted at 298 K.

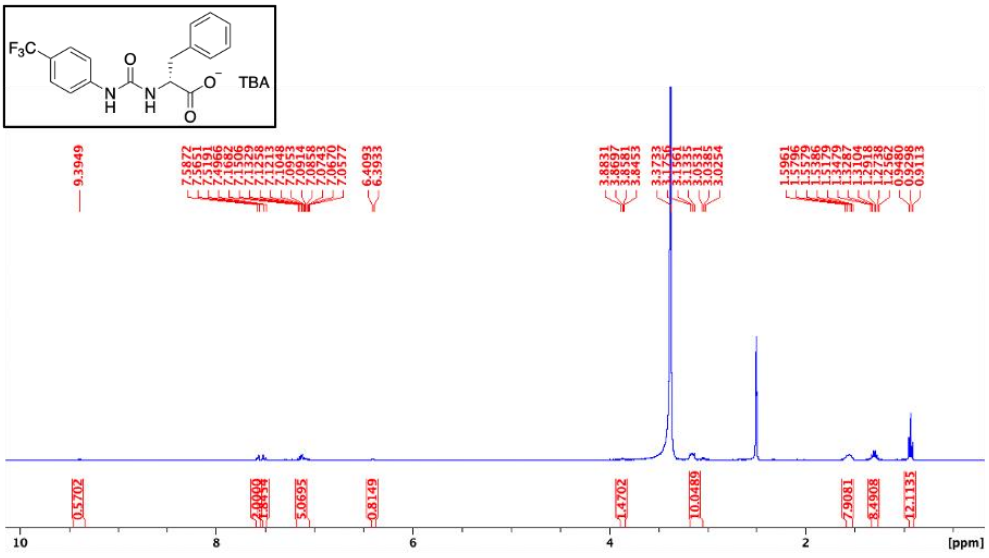

Figure S5 - ^{1}H NMR spectrum of compound **15** in DMSO-d_6 conducted at 298 K.

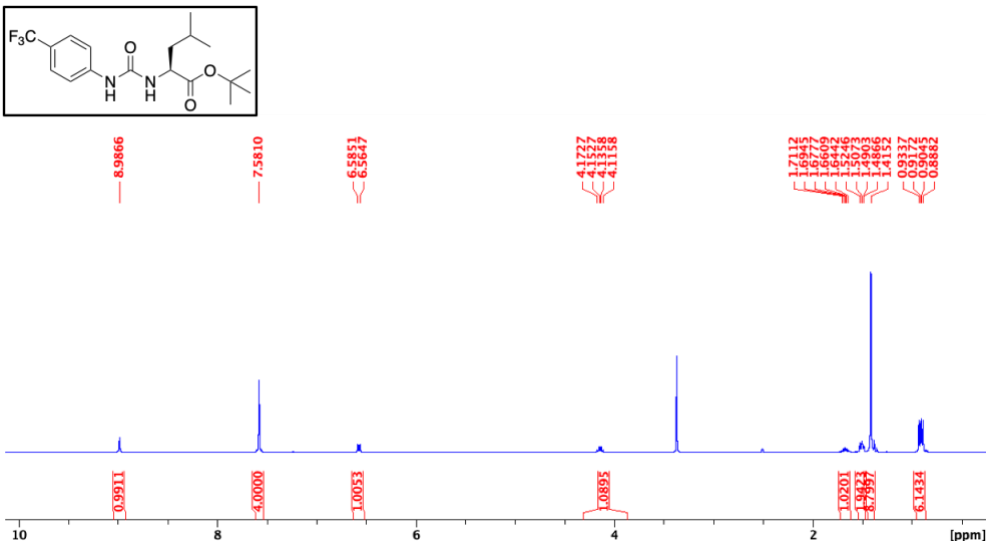

Figure S6 - ^{1}H NMR spectrum of compound **16** in DMSO-d_6 conducted at 298 K.

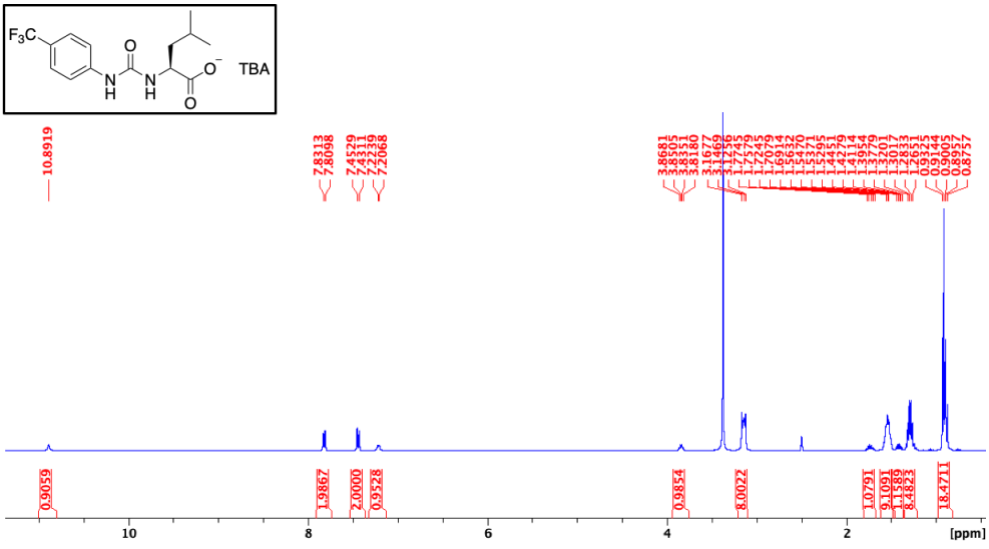

Figure S7 - ^{1}H NMR spectrum of compound **17** in DMSO-d_6 conducted at 298 K.

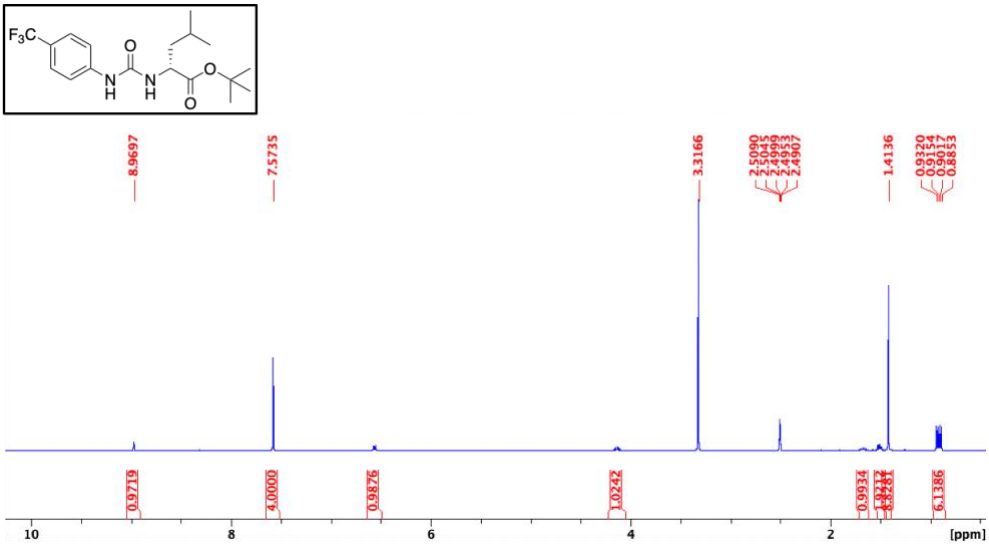

Figure S8 - ^{1}H NMR spectrum of compound **18** in DMSO-d_6 conducted at 298 K.

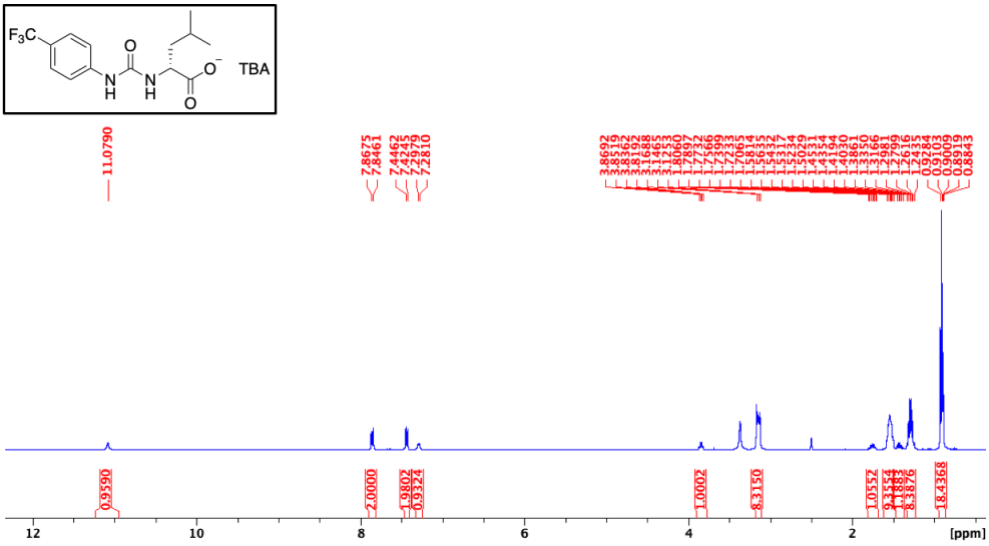

Figure S9 - ^{1}H NMR spectrum of compound **19** in DMSO-d_6 conducted at 298 K.

7.2. Quantitative ^{1}H NMR Studies

7.2.1. DMSO-d_6/ 1.0 % DCM

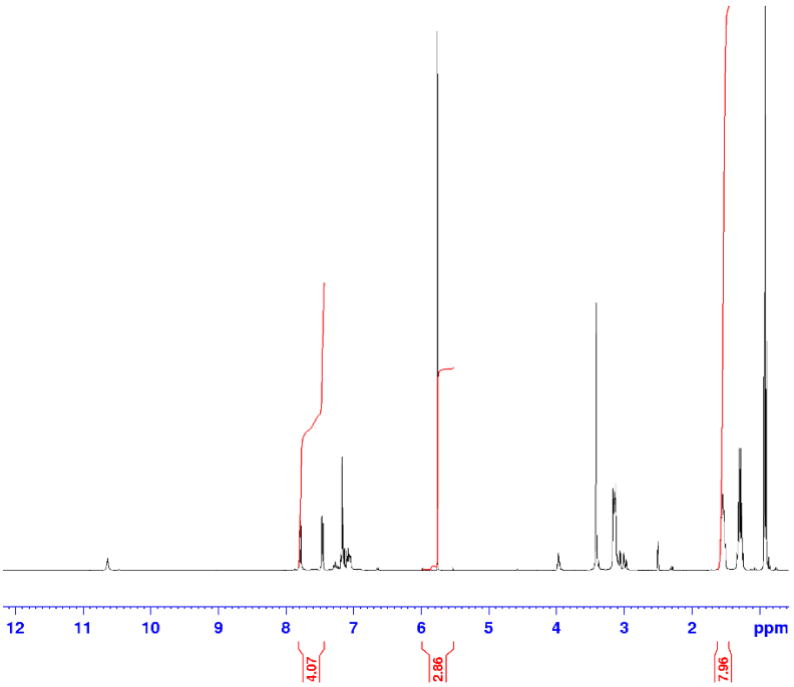

Figure S10 - ^{1}H NMR spectrum (d_1 = 60 s) of compound **13** (112 mM) in DMSO-d_6/1.0 % DCM. Comparative integration indicates no loss of the anionic component and 0.53 % of the cationic component of **13** has become NMR silent.

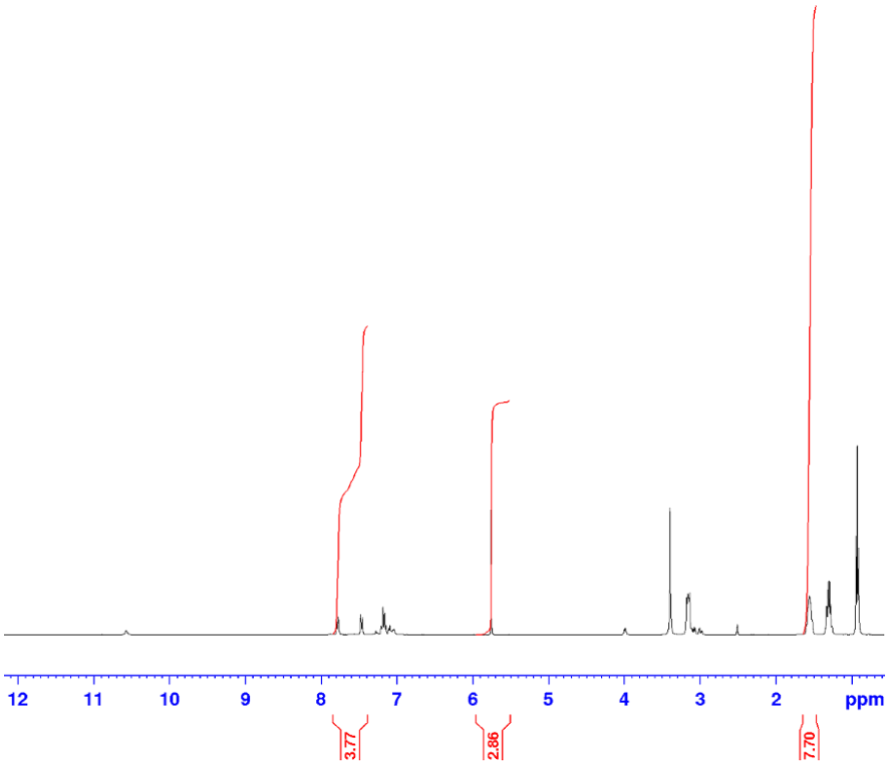

Figure S11- ^{1}H NMR spectrum (d_1 = 60 s) of compound **15** (112 mM) in DMSO-d_6/1.0 % DCM. Comparative integration indicates 6 % of the anionic component and 4 % of the cationic component of **15** has become NMR silent.

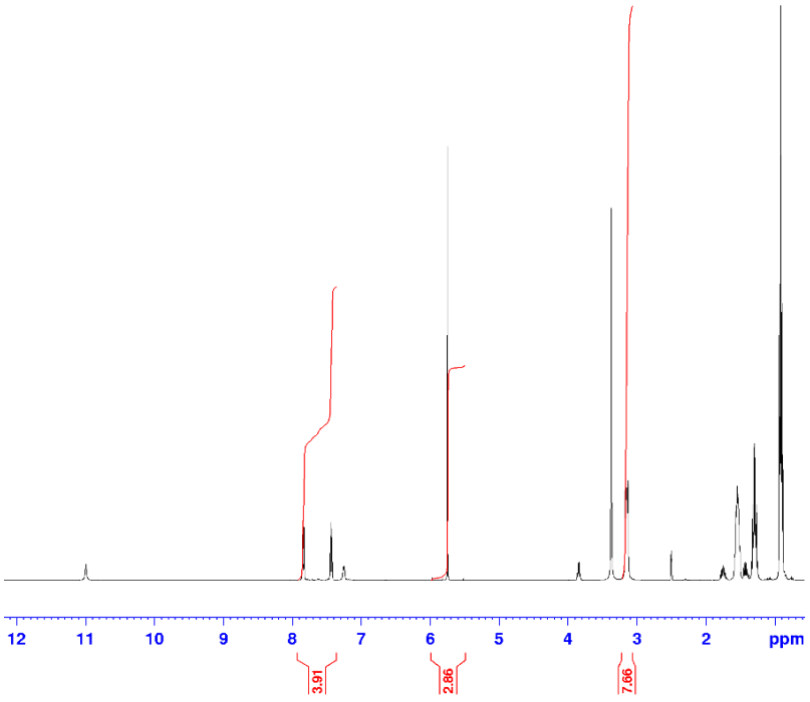

Figure S12- ^{1}H NMR spectrum (d_1 = 60 s) of compound **17** (112 mM) in DMSO-d_6/1.0 % DCM. Comparative integration indicates 2 % of the anionic component and 4 % of the cationic component of **17** has become NMR silent.

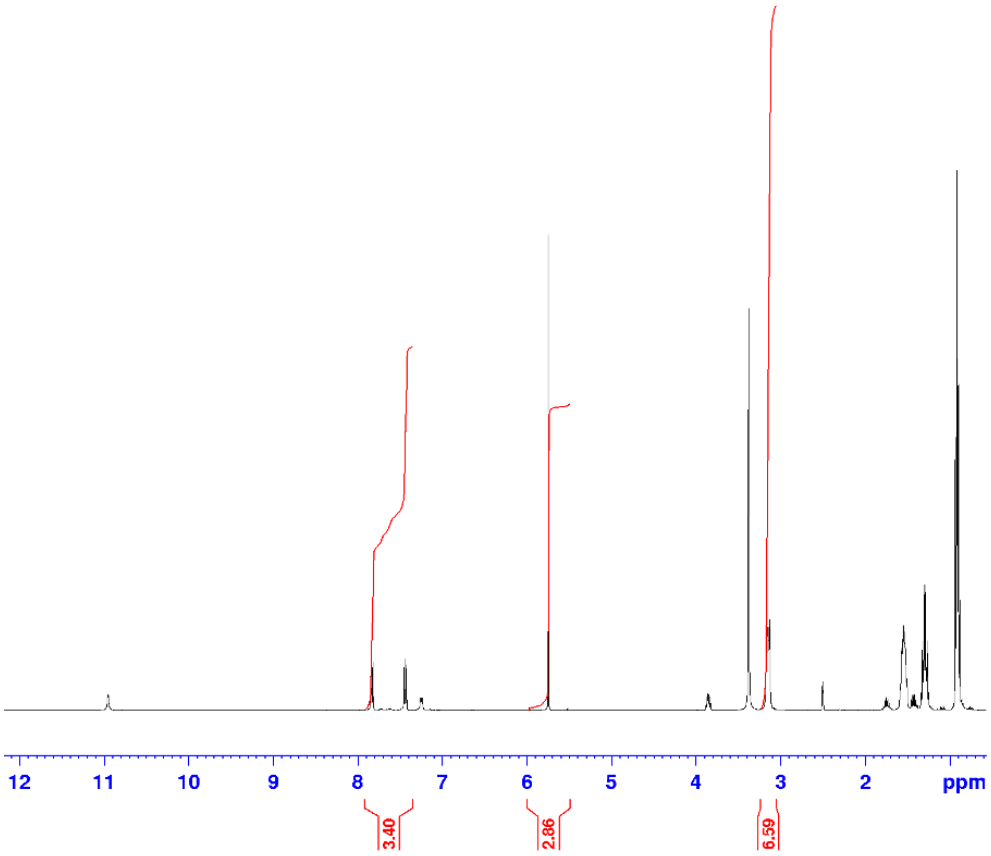

Figure S13 - ^{1}H NMR spectrum (d_1 = 60 s) of compound **19** (112 mM) in DMSO-d_6/1.0 % DCM. Comparative integration indicates 15 % of the anionic component and 18 % of the cationic component of **19** has become NMR silent.

7.2.2. D_2O/ 5.0 % EtOH

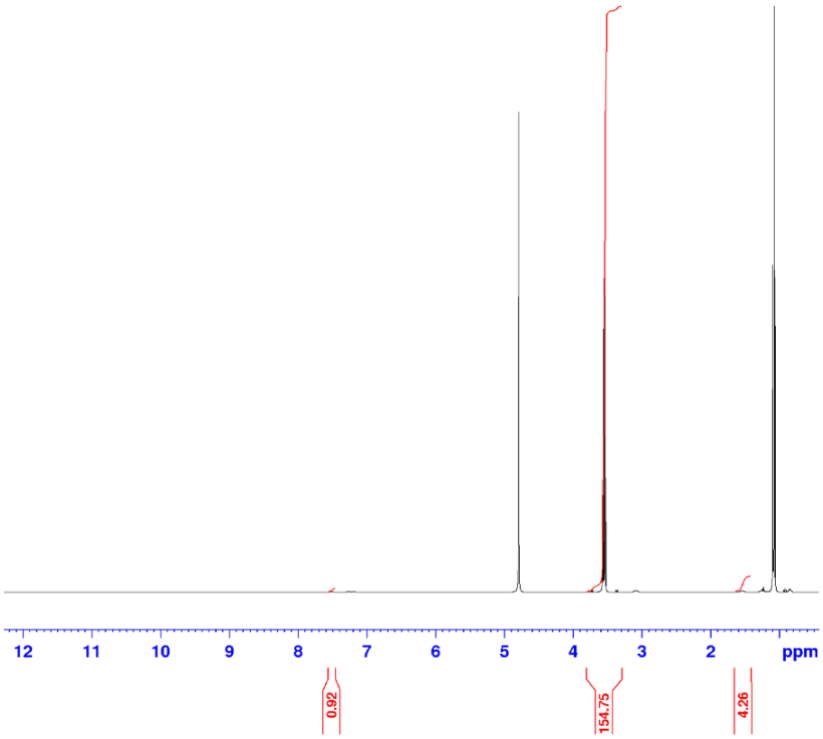

Figure S14 - ^1H NMR spectrum (d_1 = 60 s) of compound **13** (5.56 mM) in D_2O/5.0 % EtOH. Comparative integration indicates 77 % of the anionic component and 47 % of the cationic component of **13** has become NMR silent.

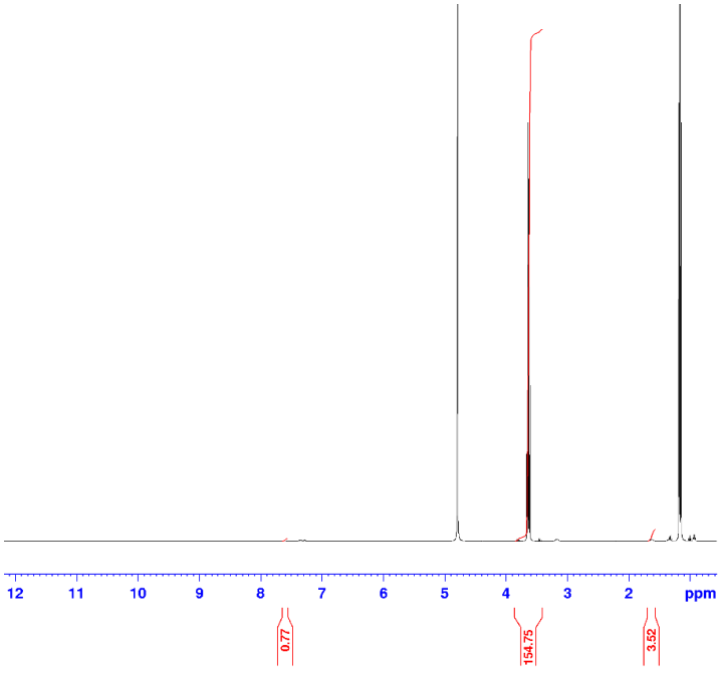

Figure S15 - ^1H NMR spectrum (d_1 = 60 s) of compound **15** (5.56 mM) in D_2O/5.0 % EtOH. Comparative integration indicates 81 % of the anionic component and 56 % of the cationic component of **15** has become NMR silent.

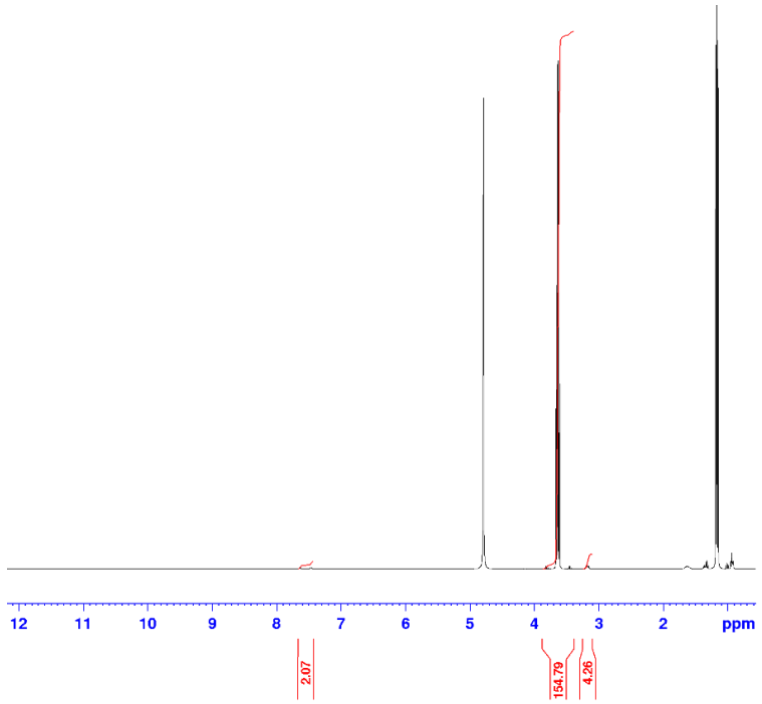

Figure S16 - ^{1}H NMR spectrum (d_1 = 60 s) of compound **17** (5.56 mM) in D_2O/5.0 % EtOH. Comparative integration indicates 48 % of the anionic component and 47 % of the cationic component of **17** has become NMR silent.

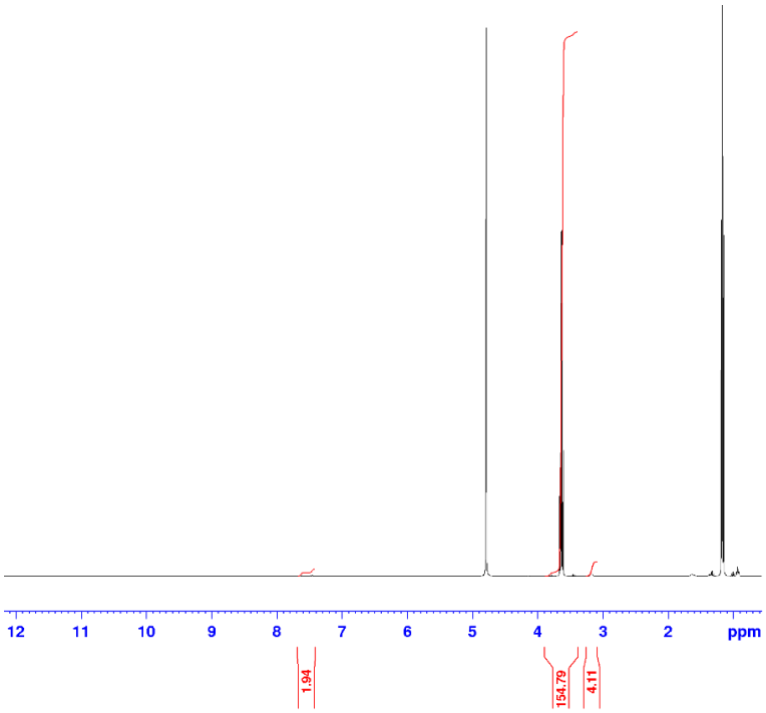

Figure S17 - ^{1}H NMR spectrum (d_1 = 60 s) of compound **19** (5.56 mM) in D_2O/5.0 % EtOH. Comparative integration indicates 51 % of the anionic component and 49 % of the cationic component of **19** has become NMR silent.

7.3. ^{1}H DOSY NMR Studies

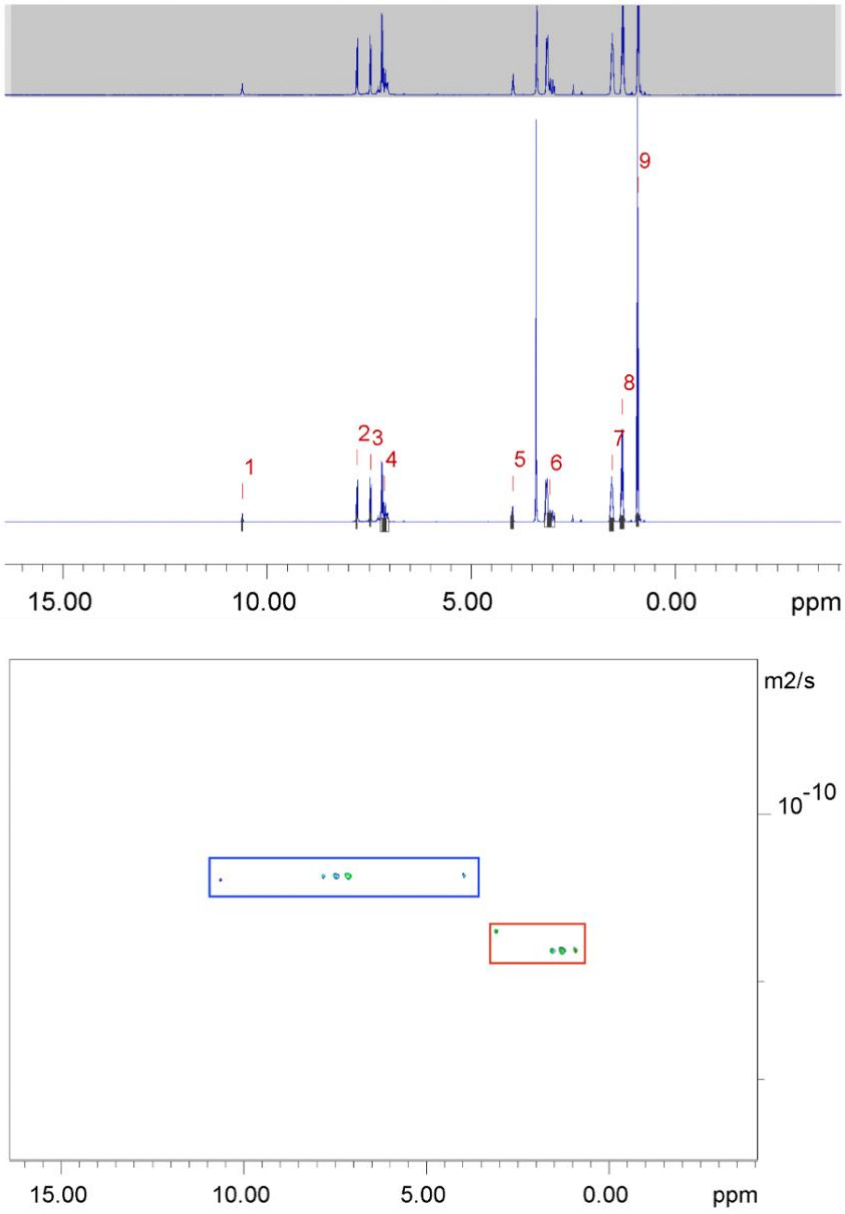

Peak name	F2 [ppm]	Io	error	D [m2/s]	error
1	10.610	7.03e+08	5.841e+04	1.30e-10	2.408e-14
2	7.797	2.75e+09	5.991e+04	1.30e-10	6.279e-15
3	7.468	2.79e+09	5.845e+04	1.29e-10	6.016e-15
4	7.124	8.56e+09	1.197e+05	1.29e-10	4.018e-15
5	3.988	1.34e+09	7.616e+04	1.29e-10	1.627e-14
6	3.078	9.81e+09	1.471e+05	1.62e-10	5.304e-15
7	1.553	8.47e+09	9.874e+04	1.75e-10	4.419e-15
8	1.301	1.14e+10	9.922e+04	1.77e-10	3.329e-15
9	0.923	1.84e+10	8.030e+04	1.75e-10	1.654e-15

Figure S18 – ^{1}H DOSY NMR of compound **13** (55.56 mM) in a DMSO-d_6/ 0.5 % H_2O solution conducted at 298 K and a table reporting the diffusion constants calculated for each peak used to determine the hydrodynamic diameter (d_H) of the anionic component. The anionic component is highlighted in blue and corresponds to peaks 1-5, while the cationic component is highlighted in red and corresponds to peaks 6-9. d_H = 1.70 nm.

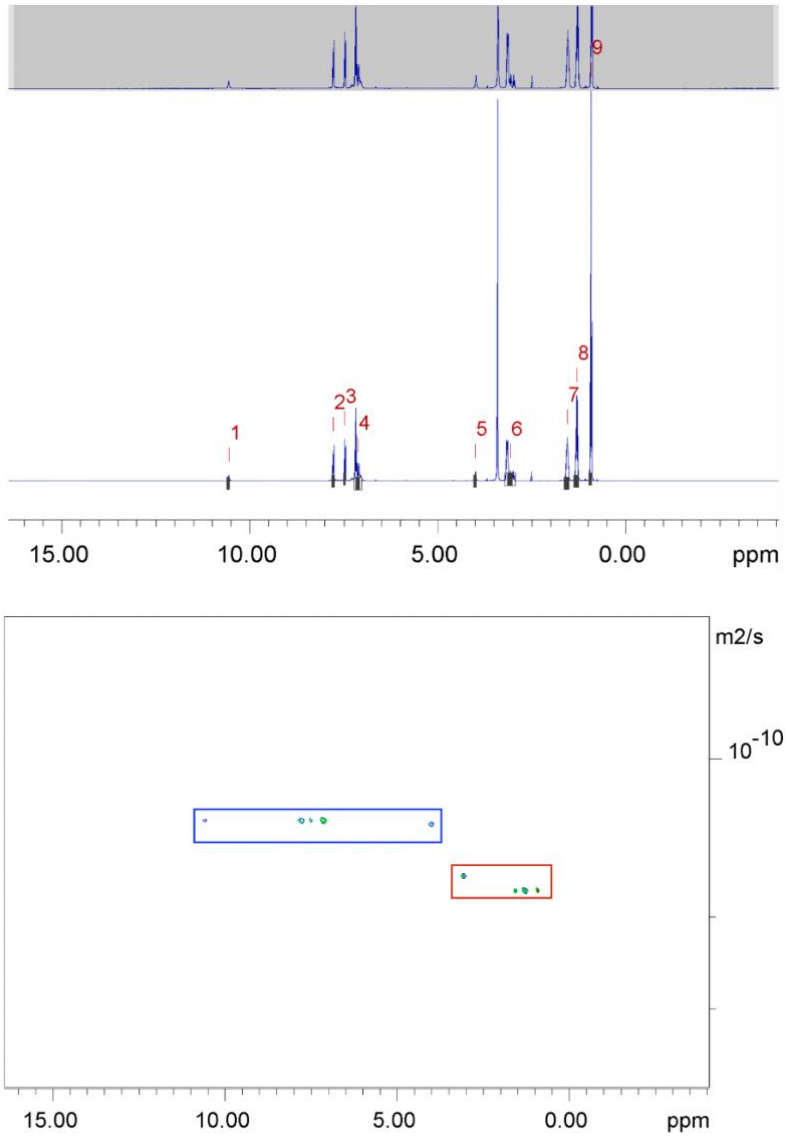

Peak name	F2 [ppm]	Io	error	D [m2/s]	error
1	10.568	6.77e+08	8.274e+04	1.31e-10	3.527e-14
2	7.780	2.67e+09	8.020e+04	1.32e-10	8.744e-15
3	7.479	2.70e+09	7.400e+04	1.31e-10	7.933e-15
4	7.126	7.56e+09	1.245e+05	1.31e-10	4.755e-15
5	4.003	1.17e+09	8.845e+04	1.33e-10	2.222e-14
6	3.077	8.99e+09	1.602e+05	1.68e-10	6.432e-15
7	1.566	7.88e+09	1.167e+05	1.79e-10	5.671e-15
8	1.308	1.03e+10	1.190e+05	1.79e-10	4.421e-15
9	0.935	1.68e+10	9.043e+04	1.79e-10	2.059e-15

Figure S19 – ^{1}H DOSY NMR of compound **15** (55.56 mM) in a DMSO-d_6/ 0.5 % H_2O solution conducted at 298 K and a table reporting the diffusion constants calculated for each peak used to determine the hydrodynamic diameter (d_H) of the anionic component. The anionic component is highlighted in blue and corresponds to peaks 1-5, while the cationic component is highlighted in red and corresponds to peaks 6-9. d_H = 1.67 nm.

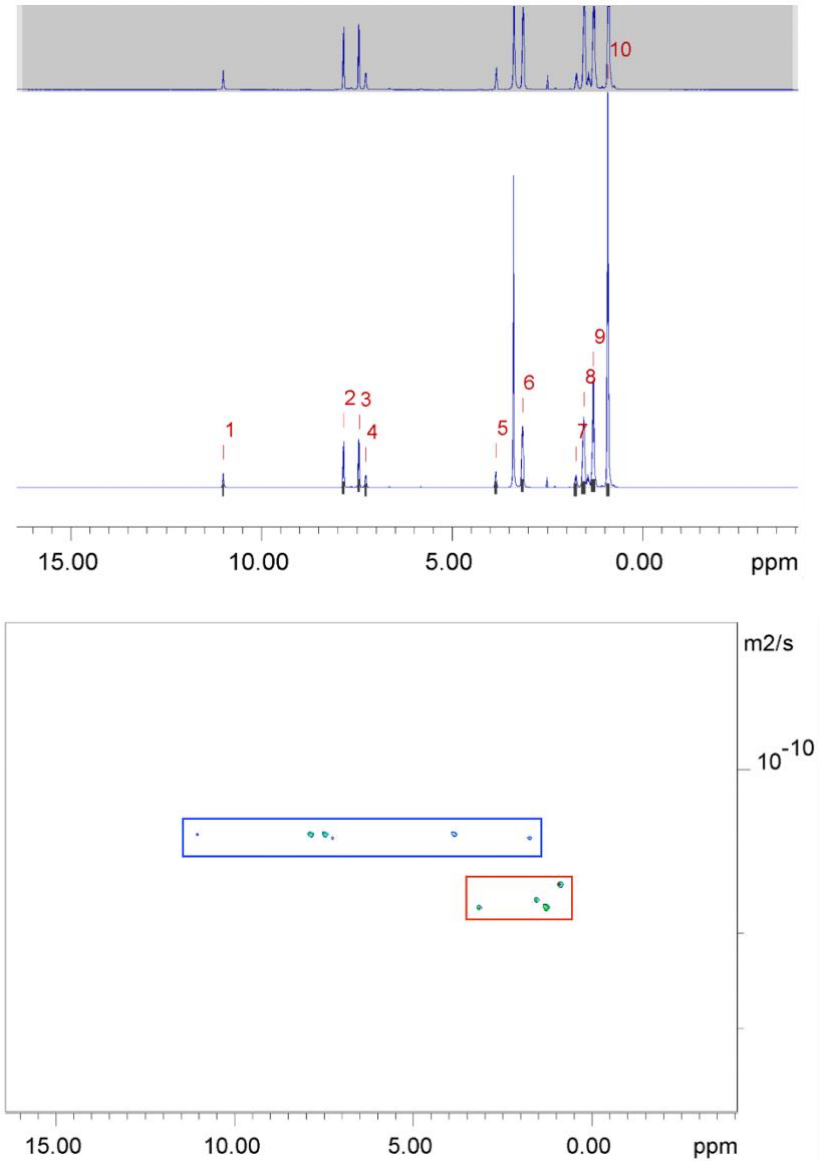

Peak name	F2 [ppm]	Io	error	D [m2/s]	error
1	11.002	1.46e+09	1.277e+05	1.31e-10	2.530e-14
2	7.850	5.20e+09	1.511e+05	1.32e-10	8.446e-15
3	7.449	5.18e+09	1.454e+05	1.31e-10	8.111e-15
4	7.268	1.81e+09	1.405e+05	1.34e-10	2.296e-14
5	3.854	2.37e+09	1.542e+05	1.31e-10	1.873e-14
6	3.154	1.25e+10	1.725e+05	1.81e-10	5.360e-15
7	1.761	2.23e+09	1.648e+05	1.33e-10	2.159e-14
8	1.552	1.70e+10	2.017e+05	1.73e-10	4.413e-15
9	1.300	2.01e+10	2.032e+05	1.80e-10	3.923e-15
10	0.915	4.64e+10	1.733e+05	1.63e-10	1.318e-15

Figure S20- ^{1}H DOSY NMR of compound **17** (55.56 mM) in a DMSO-d_6/ 0.5 % H_2O solution conducted at 298 K and a table reporting the diffusion constants calculated for each peak used to determine the hydrodynamic diameter (d_H) of the anionic component. The anionic component is highlighted in blue and corresponds to peaks 1-5 and 7, while the cationic component is highlighted in red and corresponds to peaks 6 and 8-10. d_H = 1.66 nm.

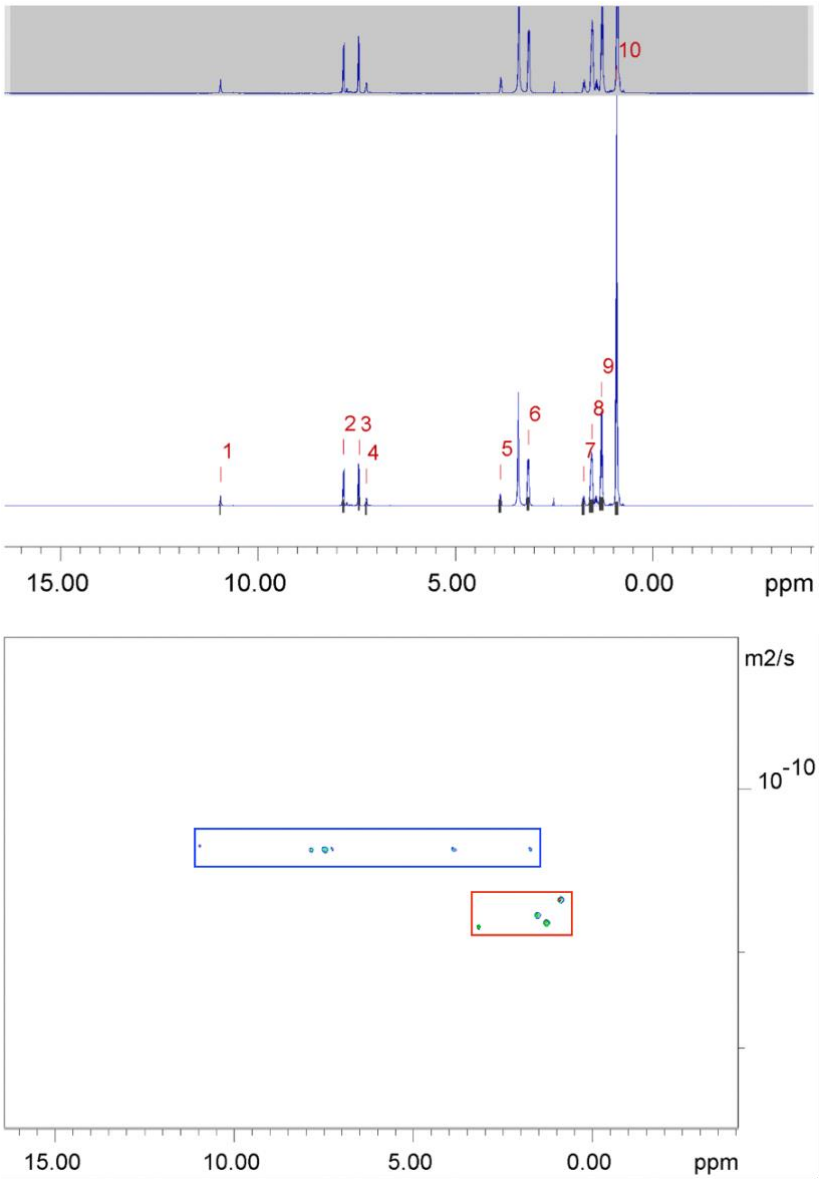

Peak name	F2 [ppm]	Io	error	D [m2/s]	error
1	10.952	6.35e+08	5.186e+04	1.28e-10	2.301e-14
2	7.838	2.45e+09	6.193e+04	1.29e-10	7.145e-15
3	7.448	2.56e+09	5.791e+04	1.28e-10	6.391e-15
4	7.255	7.27e+08	5.629e+04	1.29e-10	2.190e-14
5	3.865	1.24e+09	7.675e+04	1.29e-10	1.754e-14
6	3.159	6.81e+09	8.296e+04	1.78e-10	4.649e-15
7	1.757	1.20e+09	7.804e+04	1.29e-10	1.851e-14
8	1.552	9.23e+09	9.579e+04	1.70e-10	3.786e-15
9	1.301	1.08e+10	9.916e+04	1.77e-10	3.471e-15
10	0.915	2.49e+10	8.302e+04	1.61e-10	1.158e-15

Figure S21 - ^{1}H DOSY NMR of compound **19** (55.56 mM) in a DMSO-d_6/ 0.5 % H_2O solution conducted at 298 K and a table reporting the diffusion constants calculated for each peak used to determine the hydrodynamic diameter (d_H) of the anionic component. The anionic component is highlighted in blue and corresponds to peaks 1-5 and 7, while the cationic component is highlighted in red and corresponds to peaks 6 and 8-10. d_H = 1.70 nm.

7.4. ^{1}H NMR Self-association Studies

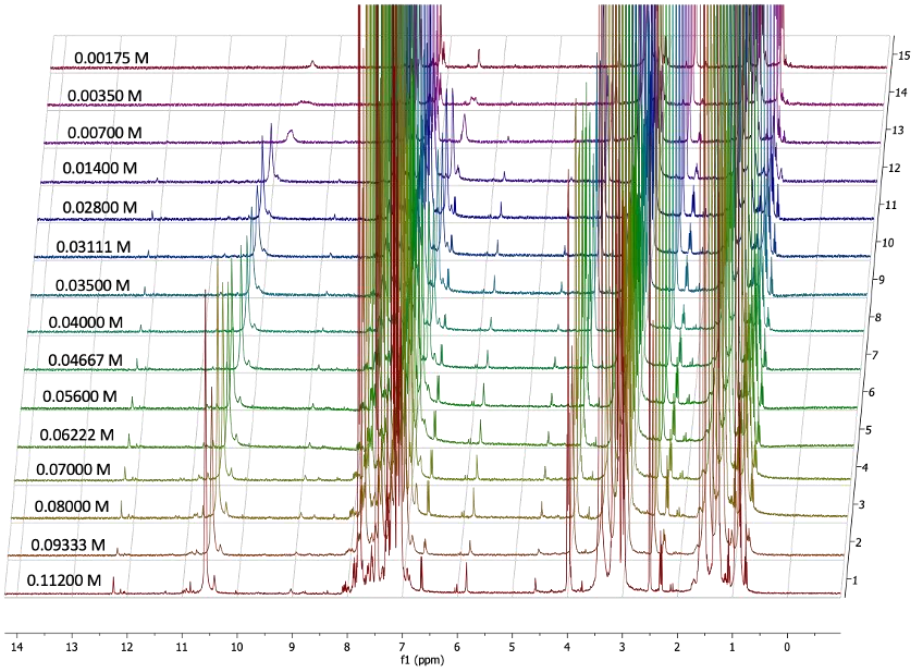

Figure S22 – ^{1}H NMR stack plot of compound **13** in a DMSO-d_6 / 0.5 % H_2O solution. Samples were prepared in series with an aliquot of the most concentrated solution undergoing serial dilution.

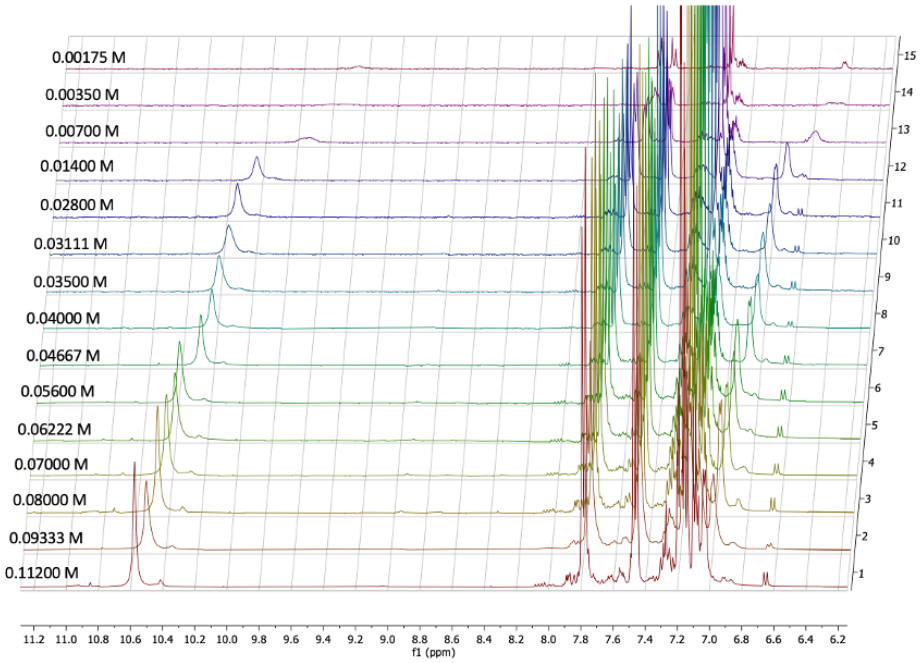

Figure S23 - Enlarged ^{1}H NMR stack plot of compound **13** in a DMSO-d_6 / 0.5 % H_2O solution. Samples were prepared in series with an aliquot of the most concentrated solution undergoing serial dilution.

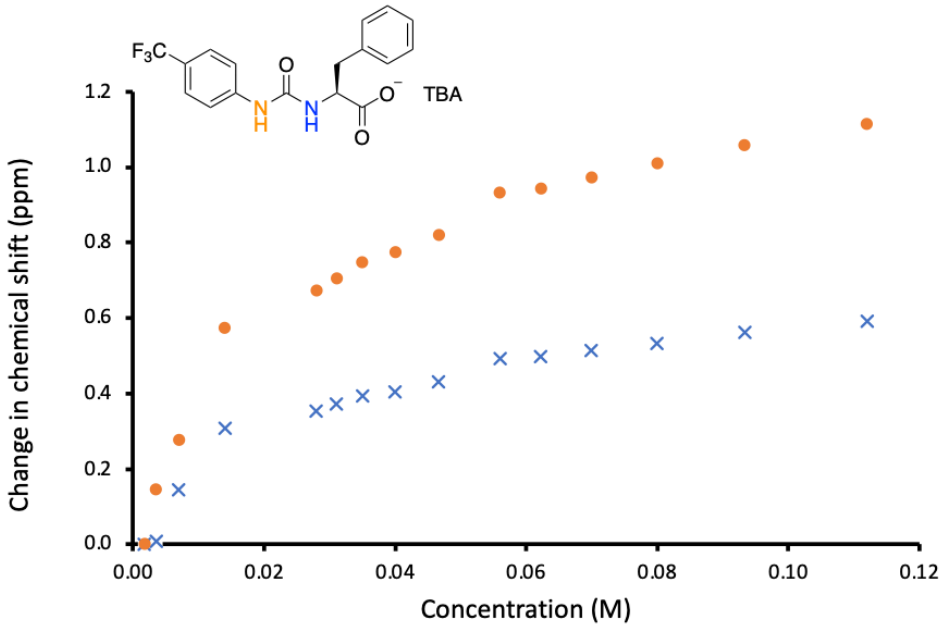

Figure S24 – Graph illustrating the ^{1}H NMR down-field change in chemical shift of urea NH resonances with increasing concentration of compound **13** in DMSO-d_6 0.5% H_2O (298 K).

Equal K/Dimerization model:

K_e = 55.52 M^{-1} ± 4.2402 % K_{dim} = 27.76 M^{-1} ± 2.1201 %

http://app.supramolecular.org/bindfit/view/3bb6b512-7ffd-4fb2-b22c-3423a512b003

CoEK model:

K_e = 21.17 M^{-1} ± 6.1138% K_{dim} = 10.58 M^{-1} ± 3.0569 %

p = 2.86 ± 14.5893 %

http://app.supramolecular.org/bindfit/view/0d92b6d7-4c95-488c-bc2d-3fe43e1e4cb7

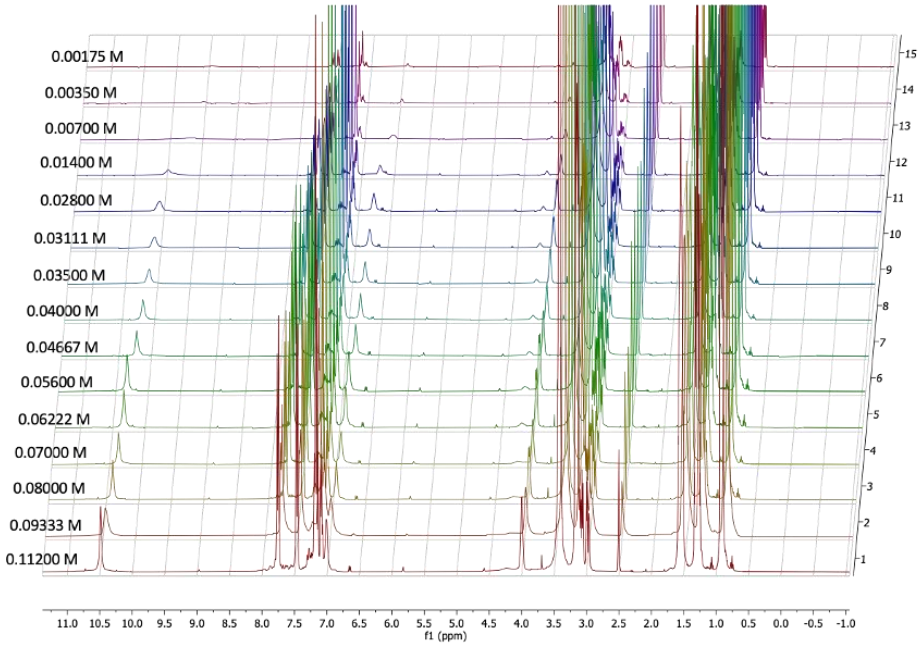

Figure S25 – ^{1}H NMR stack plot of compound **15** in a DMSO-d_6 / 0.5 % H_2O solution. Samples were prepared in series with an aliquot of the most concentrated solution undergoing serial dilution.

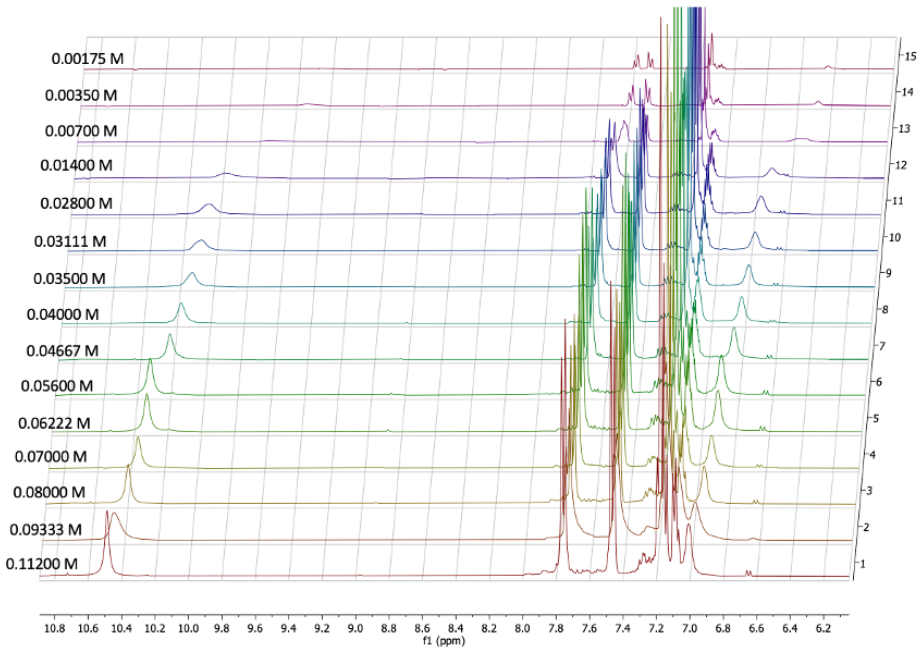

Figure S26 - Enlarged ^{1}H NMR stack plot of compound **15** in a DMSO-d_6 / 0.5 % H_2O solution. Samples were prepared in series with an aliquot of the most concentrated solution undergoing serial dilution.

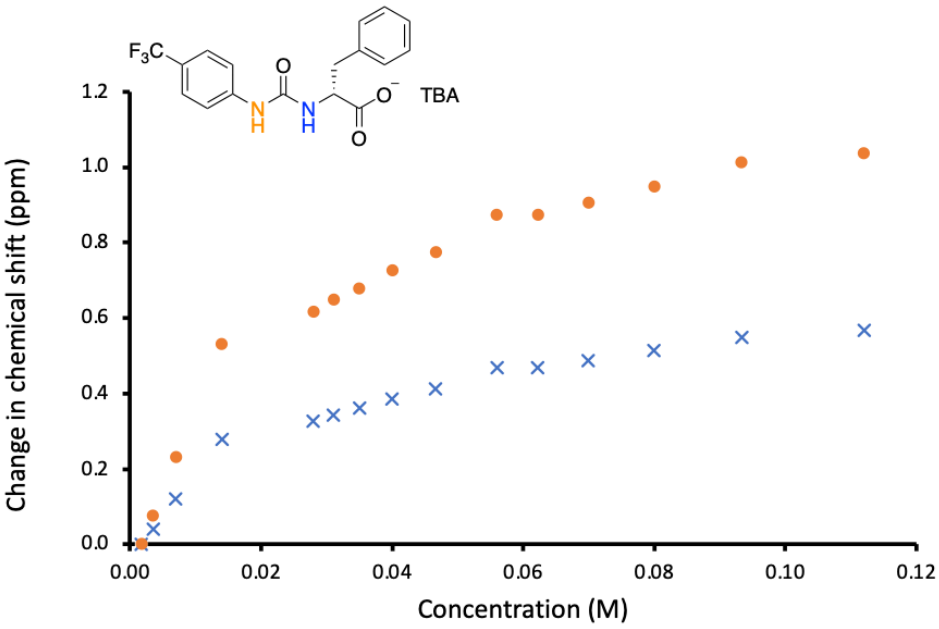

Figure S27 – Graph illustrating the ^{1}H NMR down-field change in chemical shift of urea NH resonances with increasing concentration of compound **15** in DMSO-d_6 0.5% H_2O (298 K).

Equal K/Dimerization model:

K_e = 45.90 M^{-1} ± 5.0312 % K_{dim} = 22.95 M^{-1} ± 2.5156 %

http://app.supramolecular.org/bindfit/view/3abcecc0-ffc9-4e4e-917f-14958fbcf026

CoEK model:

K_e = 17.84 M^{-1} ± 8.5196 % K_{dim} = 8.92 M^{-1} ± 4.2598 %

p = 2.62 ± 19.6152 %

http://app.supramolecular.org/bindfit/view/91f0f17f-4882-4fec-bd09-cfce15a99d6b

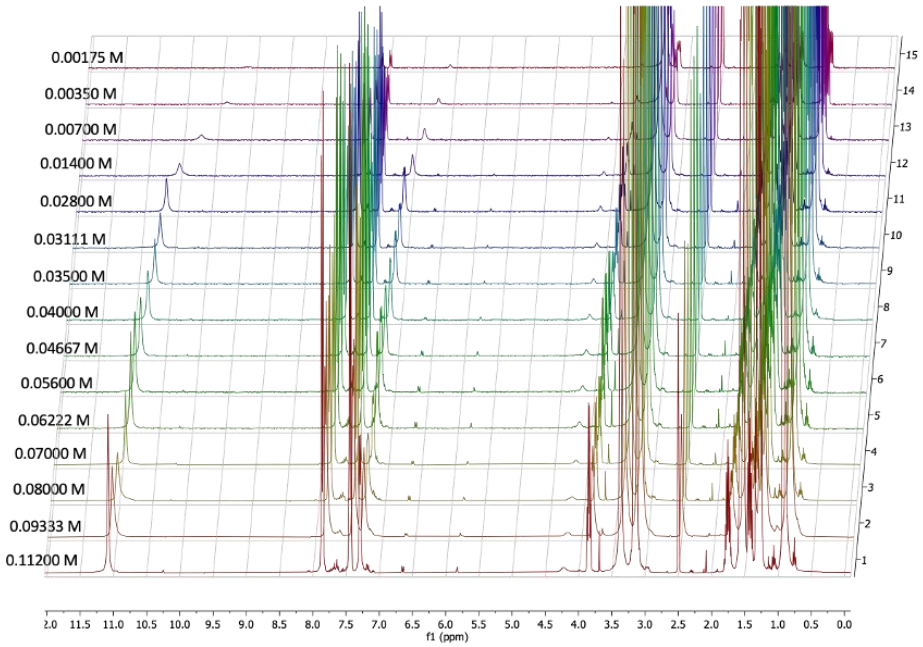

Figure S28 - ^{1}H NMR stack plot of compound **17** in a DMSO-d_6 / 0.5 % H_2O solution. Samples were prepared in series with an aliquot of the most concentrated solution undergoing serial dilution.

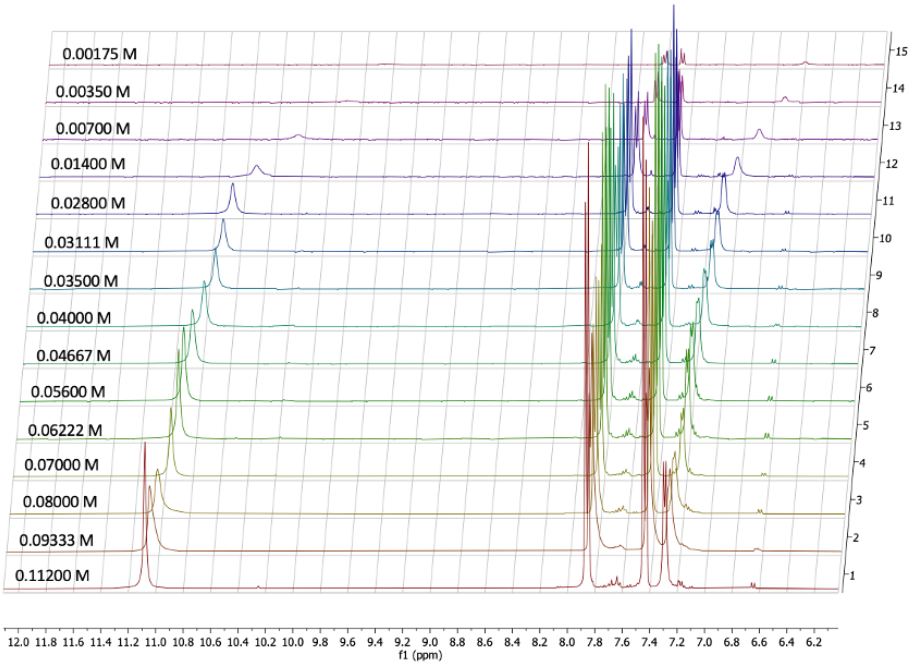

Figure S29 - Enlarged ^{1}H NMR stack plot of compound **17** in a DMSO-d_6 / 0.5 % H_2O solution. Samples were prepared in series with an aliquot of the most concentrated solution undergoing serial dilution.

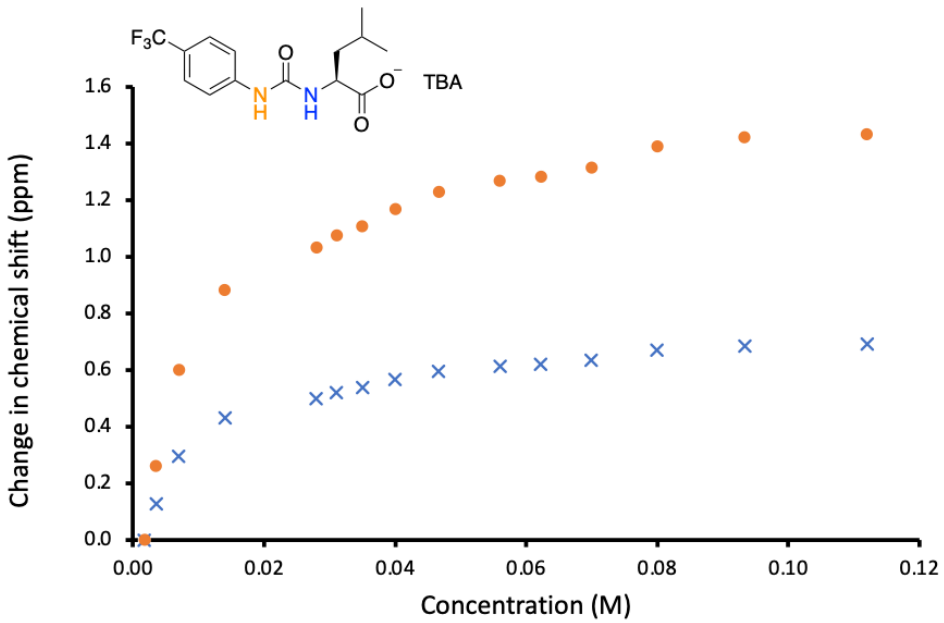

Figure S30 – Graph illustrating the ^{1}H NMR down-field change in chemical shift of urea NH resonances with increasing concentration of compound **17** in DMSO-d_6 0.5% H_2O (298 K).

Equal K/Dimerization model:

K_e = 242.72 M^{-1} ± 3.8023 % K_{dim} = 121.36 M^{-1} ± 1.9011 %

http://app.supramolecular.org/bindfit/view/51ce652b-7b2b-4974-8812-79d1ae73fc4f

CoEK model:

K_e = 560.90 M^{-1} ± 5.2131 % K_{dim} = 280.45 M^{-1} ± 2.6065 %

p = 2.29 ± 9.2496

http://app.supramolecular.org/bindfit/view/c48548c8-ee64-4855-8686-7c76c927c103

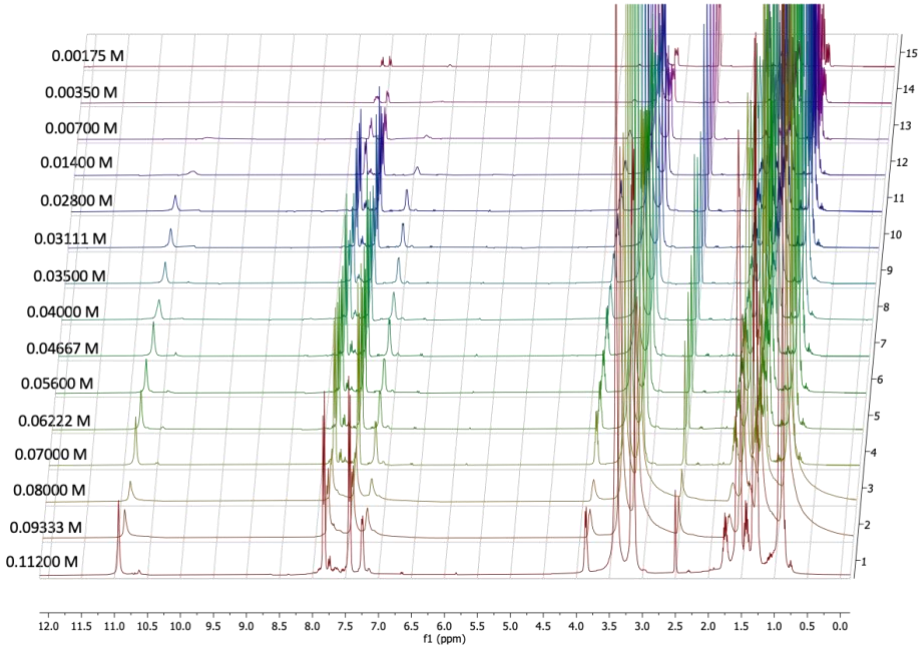

Figure S31 – ^{1}H NMR stack plot of compound **19** in a DMSO-d_6 / 0.5 % H_2O solution. Samples were prepared in series with an aliquot of the most concentrated solution undergoing serial dilution.

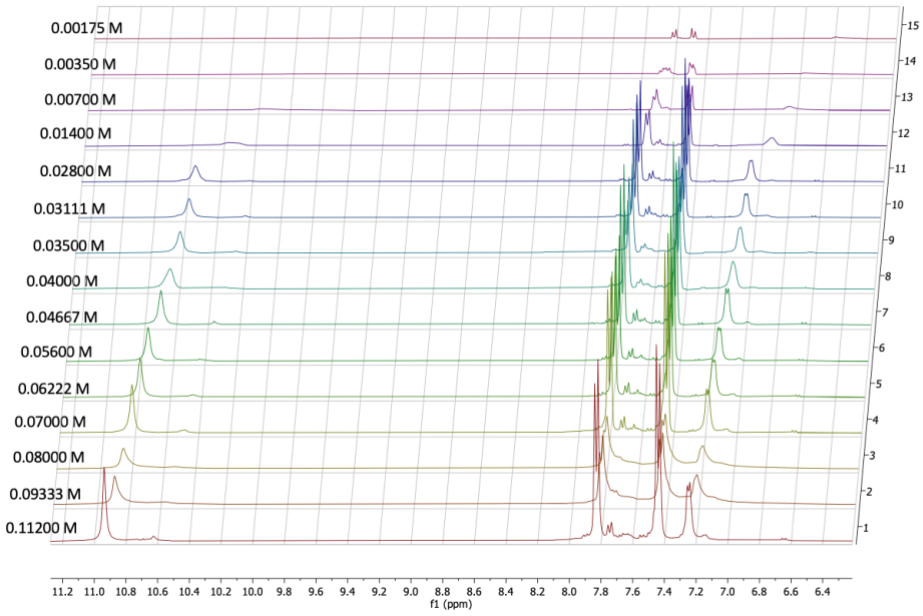

Figure S32 - Enlarged ^{1}H NMR stack plot of compound **19** in a DMSO-d_6 / 0.5 % H_2O solution. Samples were prepared in series with an aliquot of the most concentrated solution undergoing serial dilution.

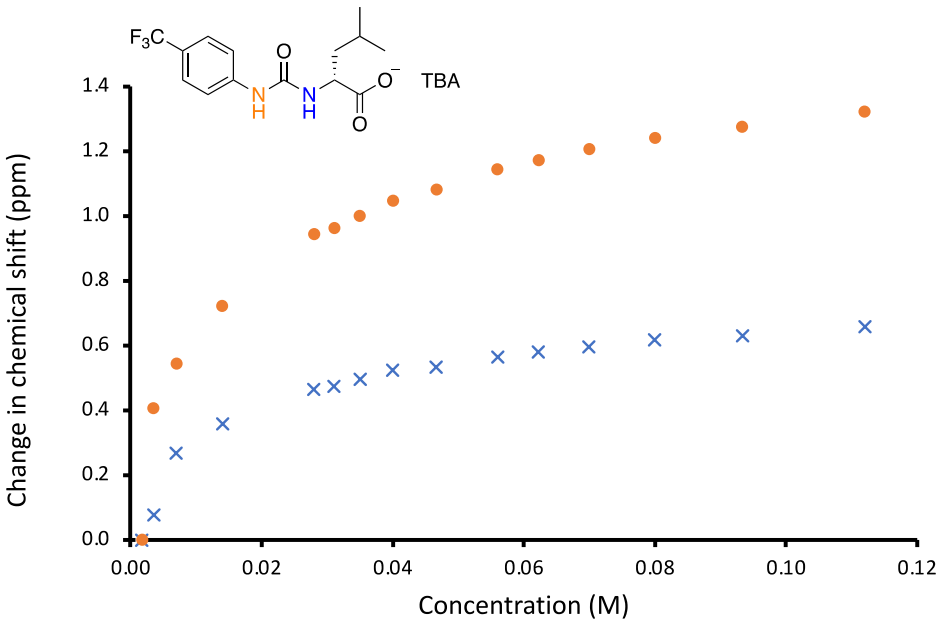

Figure S33 – Graph illustrating the ^{1}H NMR down-field change in chemical shift of urea NH resonances with increasing concentration of compound **19** in DMSO-d_6 0.5% H_2O (298 K).

Equal K/Dimerization model:

K_e = 180.55 M^{-1} ± 6.4767 % K_{dim} = 90.27 M^{-1} ± 3.2384 %

http://app.supramolecular.org/bindfit/view/b8b3ad35-c95a-4b43-ab01-9424006b8cf2

CoEK model:

K_e = 351.80 M^{-1} ± 7.1786 K_{dim} = 175.90 M^{-1} ± 3.5893

p = 3.41 ± 12.6925

http://app.supramolecular.org/bindfit/view/3c8e5c40-cd1e-4e18-9c93-530cc3f7c71c

7.5. DLS Studies

7.5.1. Size Distribution Data in EtOH:H_2O (1:19)

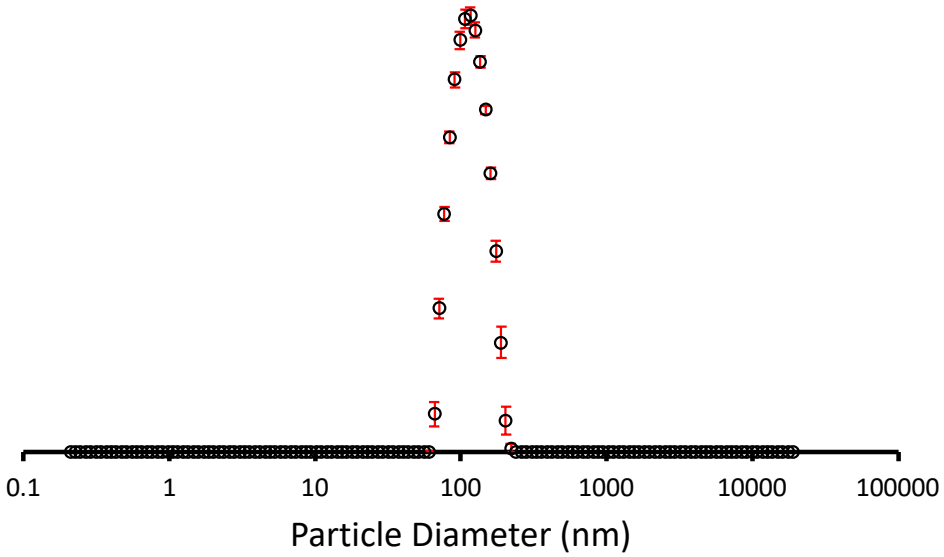

Figure S34 – The average intensity particle size distribution of aggregates formed by compound **13** (5.56 mM) in 1:19 EtOH:H_2O calculated using 10 DLS runs at 298 K.

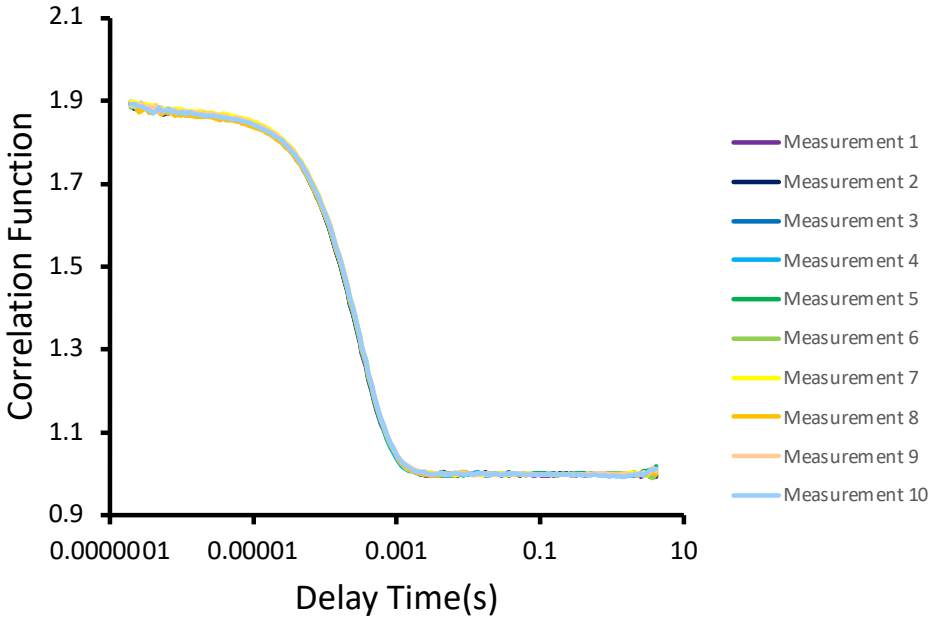

Figure S35 – The correlation function data for 10 DLS runs of compound **13** (5.56 mM) in 1:19 EtOH:H_2O at 298 K.

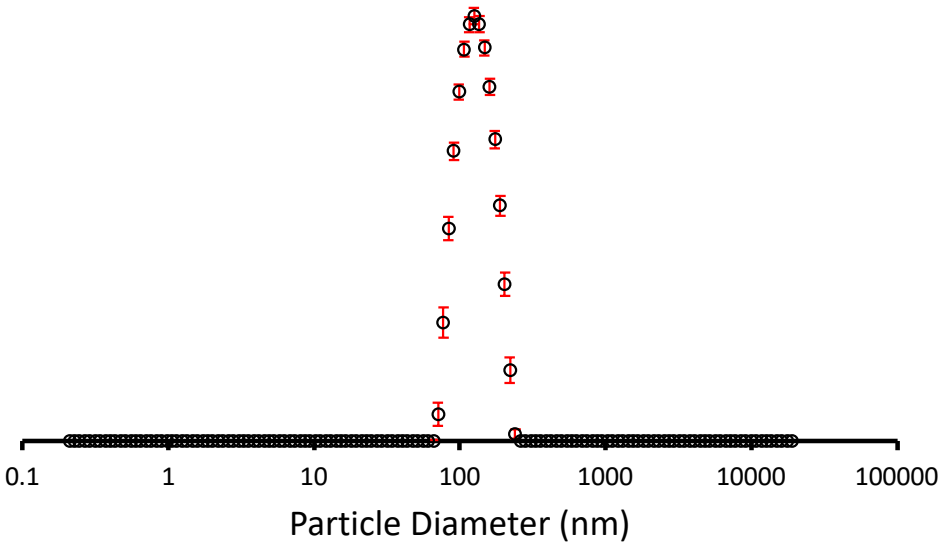

Figure S36 – The average intensity particle size distribution of aggregates formed by compound **15** (5.56 mM) in 1:19 EtOH: H_2O calculated using 10 DLS runs at 298 K.

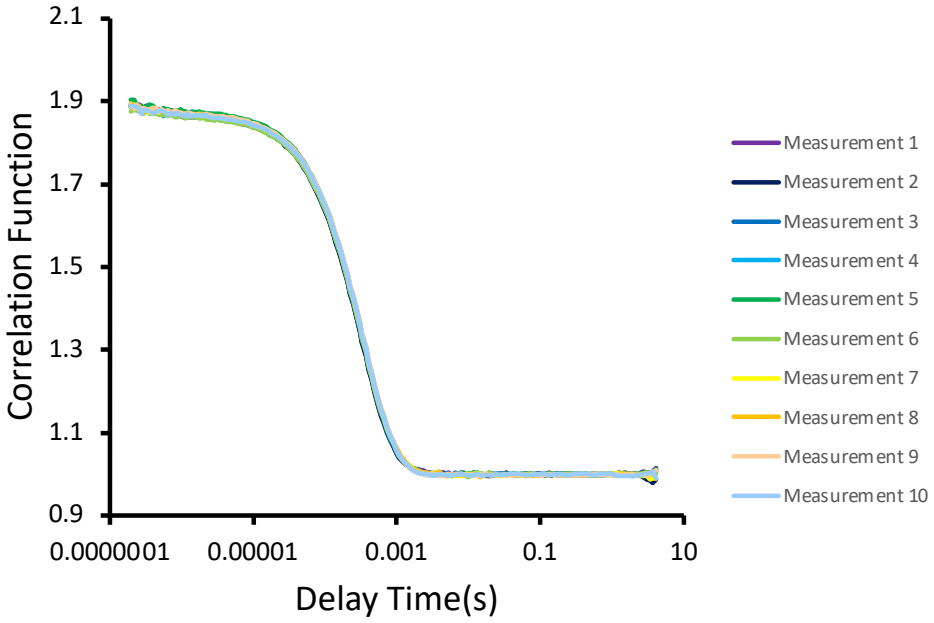

Figure S37 – The correlation function data for 10 DLS runs of compound **15** (5.56 mM) in 1:19 EtOH: H_2O at 298 K.

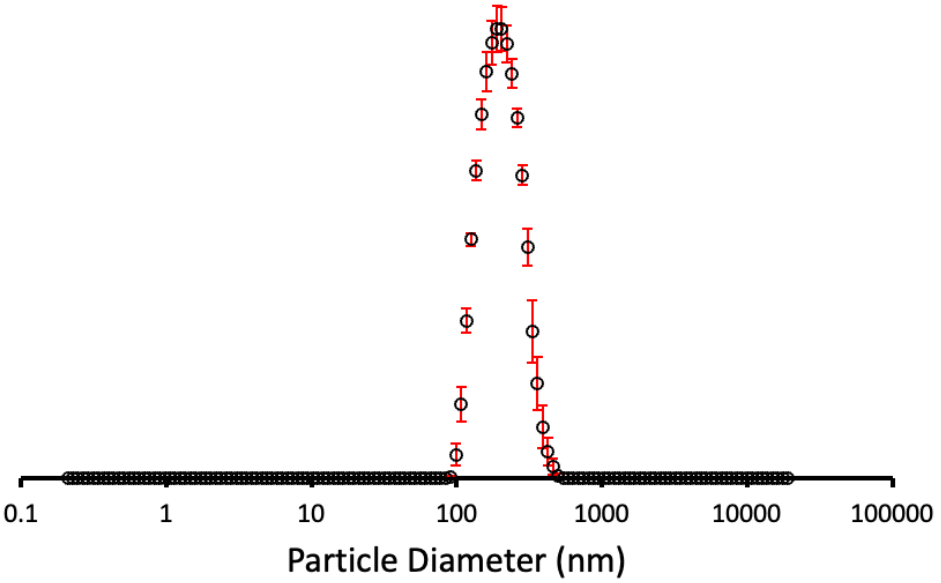

Figure S38 - The average intensity particle size distribution of aggregates formed by a 1:1 mixture of compounds **13** and **15** (5.56 mM) in 1:19 EtOH:H_2O calculated using 10 DLS runs at 298 K.

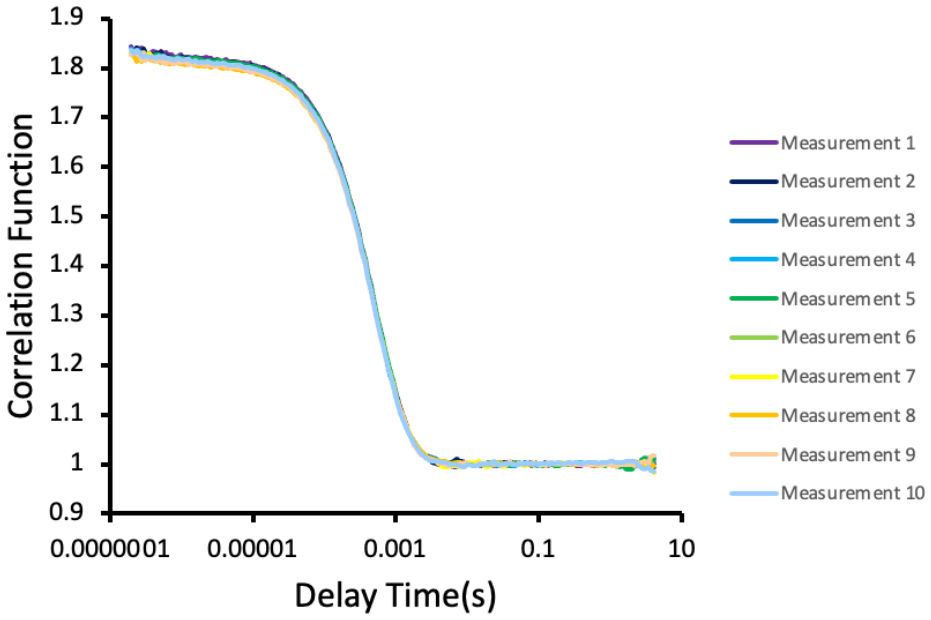

Figure S39 - The correlation function data for 10 DLS runs of a 1:1 mixture of compounds **13** and **15** (5.56 mM) in 1:19 EtOH:H_2O at 298 K.

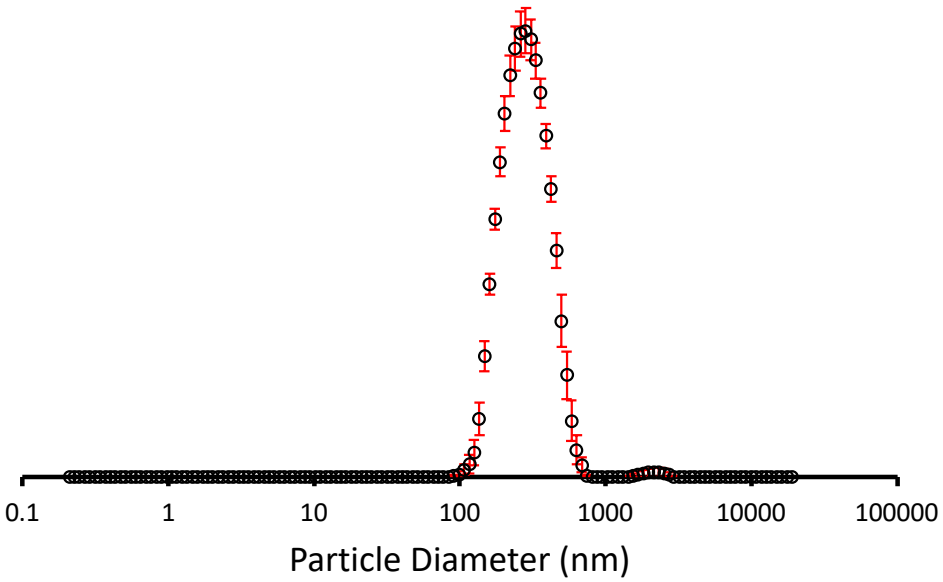

Figure S40 – The average intensity particle size distribution of aggregates formed by compound **17** (5.56 mM) in 1:19 EtOH:H_2O calculated using 10 DLS runs at 298 K.

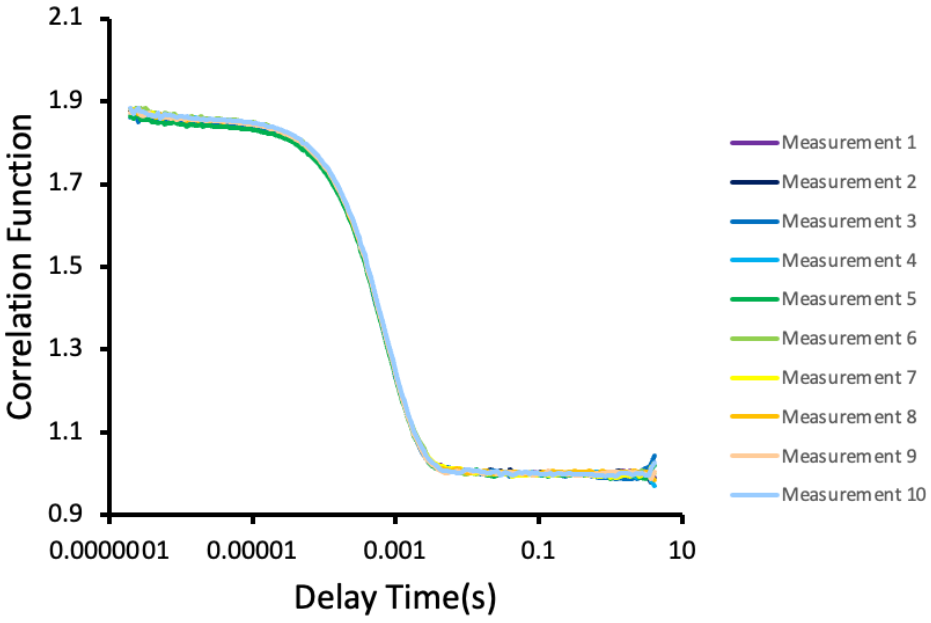

Figure S41 – The correlation function data for 10 DLS runs of compound **17** (5.56 mM) in 1:19 EtOH:H_2O at 298 K.

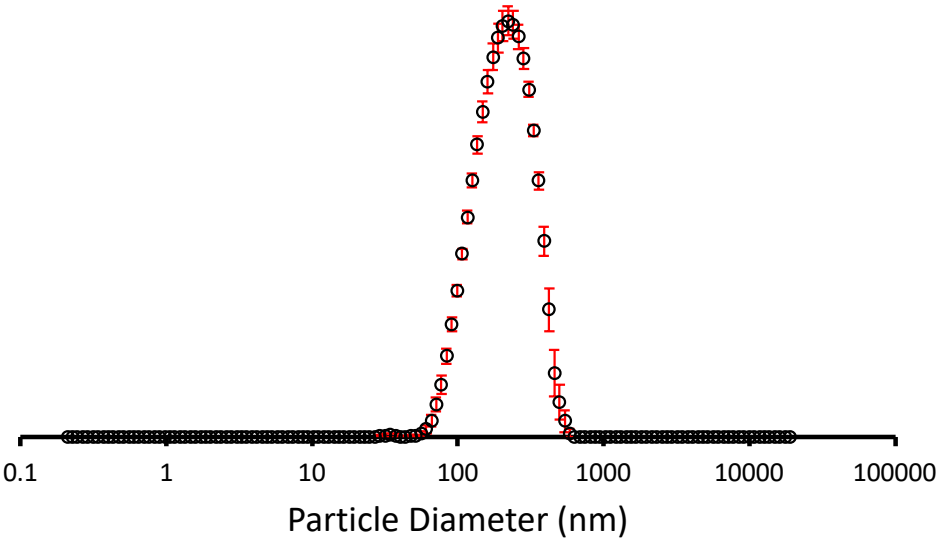

Figure S42 – The average intensity particle size distribution of aggregates formed by compound **19** (5.56 mM) in 1:19 EtOH:H_2O calculated using 10 DLS runs at 298 K.

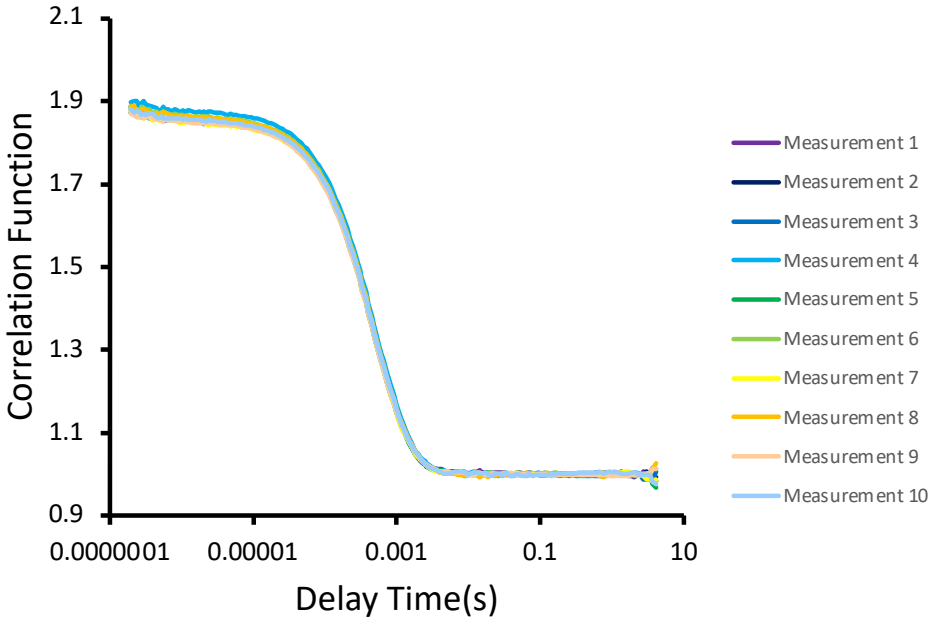

Figure S43 – The correlation function data for 10 DLS runs of compound **19** (5.56 mM) in 1:19 EtOH:H_2O at 298 K.

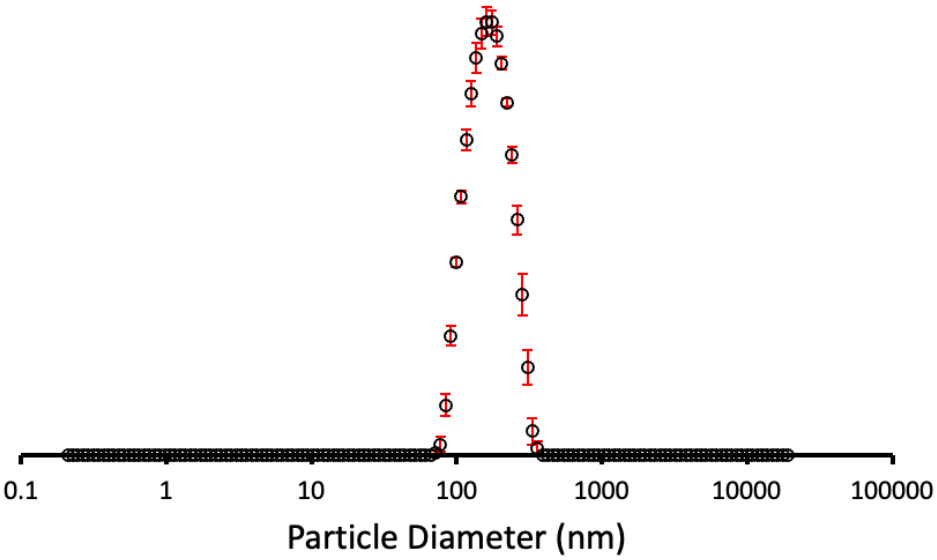

Figure S 44 - The average intensity particle size distribution of aggregates formed by a 1:1 mixture of compounds **17** and **19** (5.56 mM) in 1:19 EtOH:H_2O calculated using 10 DLS runs at 298 K.

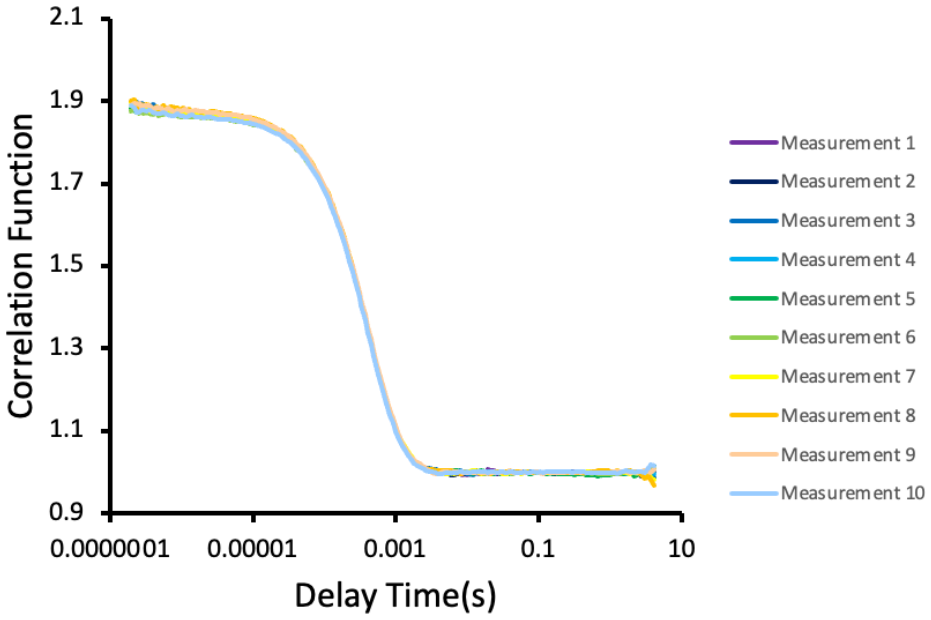

Figure S45 - The correlation function data for 10 DLS runs of a 1:1 mixture of compounds **17** and **19** (5.56 mM) in 1:19 EtOH:H_2O at 298 K.

7.5.2. Summary

Table S1 – The average intensity particle size distribution calculated from 10 DLS runs for **13**, **15**, **17** and **19**, and 1:1 mixtures of isomers **13**+**15** and isomers **17**+**19** obtained at 5.56 mM in EtOH:H_2O (1:19). An annealing process was applied in which the samples were heated to approximately 313 K before being cooled down to a measurement temperature of 298 K. [a] 1:1 mixture. Error = standard error of the mean and given to 1 decimal place.

Compound	Peak maxima (nm)	PDI (%)
13	118.54 (± 1.0)	13.09 (± 0.9)
15	132.50 (± 1.2)	14.15 (± 0.7)
13 + **15**[a]	208.71 (± 3.4)	19.08 (± 0.8)
17	296.71 (± 4.4)	18.51 (± 1.6)
19	221.30 (± 3.3)	22.76 (± 0.3)
17 + **19** [a]	172.99 (± 1.8)	18.31 (± 0.7)

7.5.3. Size Distribution Data in TSB

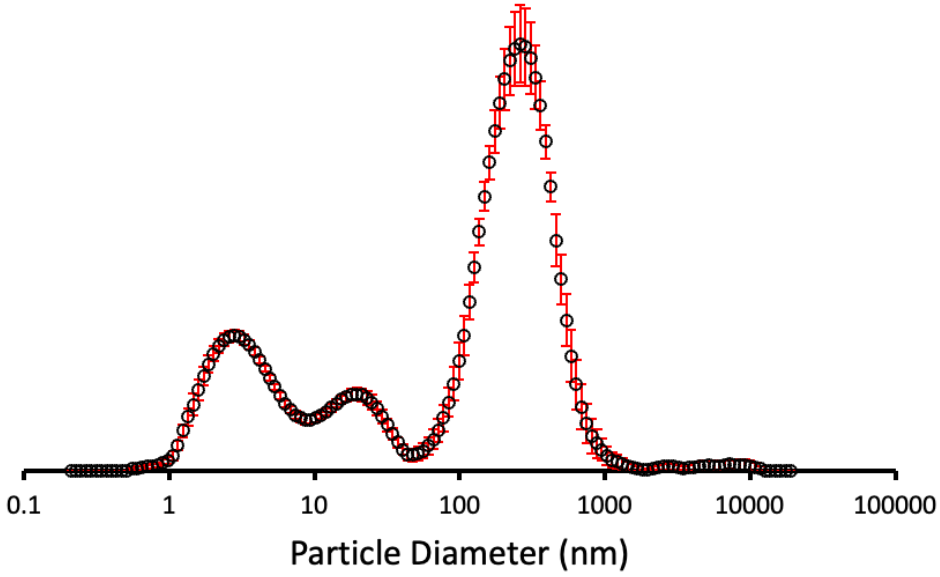

Figure S46 - The average intensity particle size distribution of aggregates formed by compound **9** (1.39 mM) in a 1:3 solution of 5 % EtOH in H_2O:TSB calculated using 10 DLS runs at 298 K. d_H = 285.38 nm.

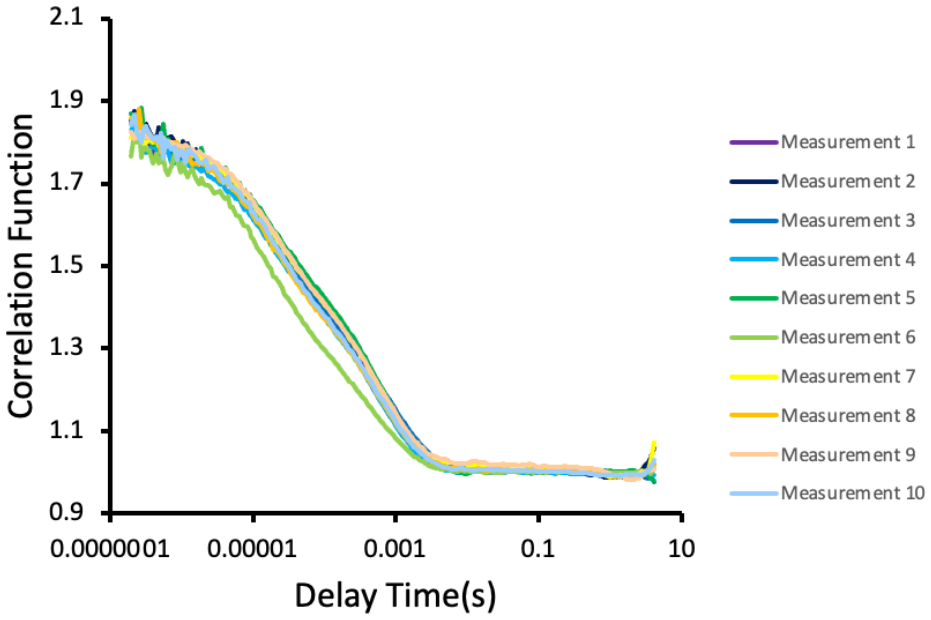

Figure S47 - The correlation function data for 10 DLS runs of compound **9** (1.39 mM) in a 1:3 solution of 5 % EtOH in H_2O:TSB at 298 K.

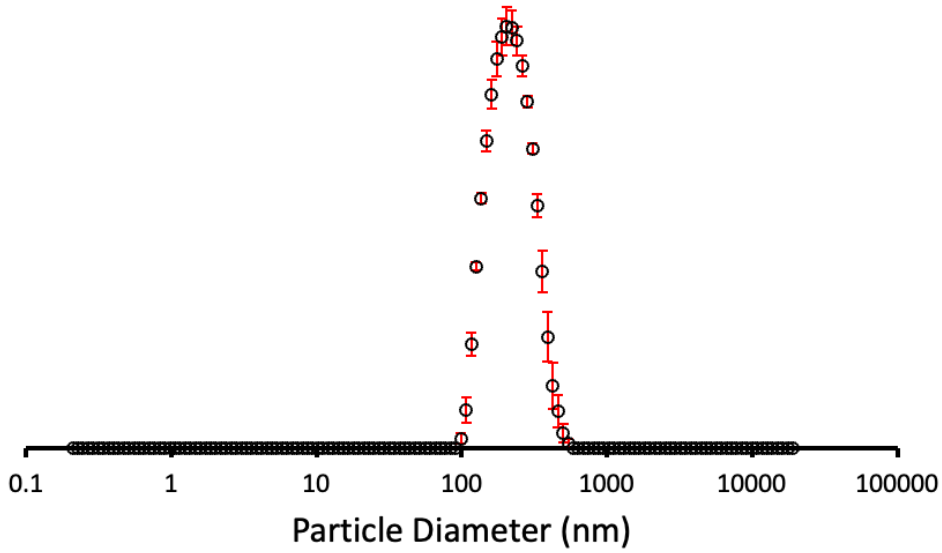

Figure S 48 - The average intensity particle size distribution of aggregates formed by compound **13** (1.39 mM) in a 1:3 solution of 5 % EtOH in H_2O:TSB calculated using 10 DLS runs at 298 K. d_H = 227.49 nm.

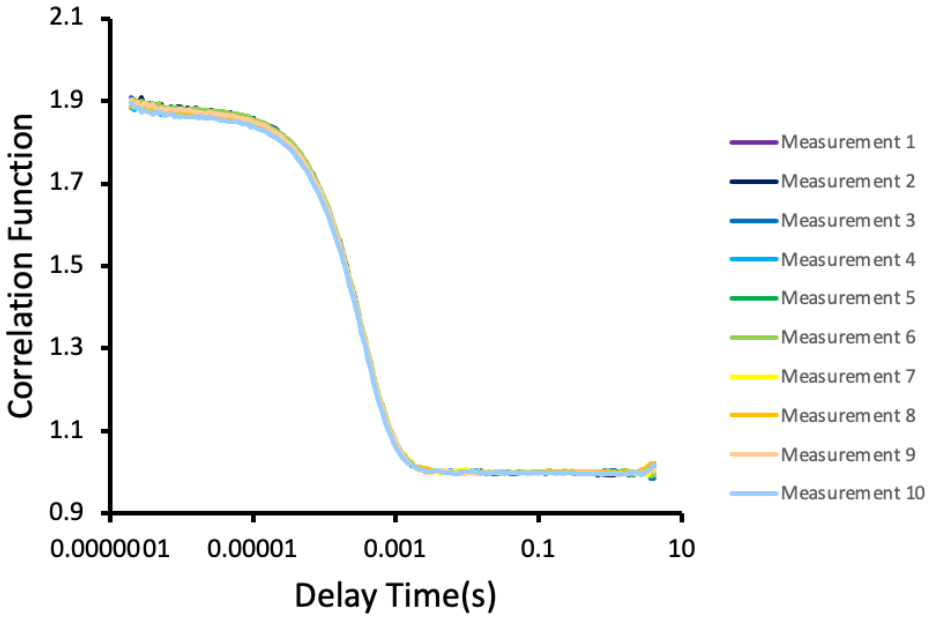

Figure S49 - The correlation function data for 10 DLS runs of compound **13** (1.39 mM) in a 1:3 solution of 5 % EtOH in H_2O:TSB at 298 K.

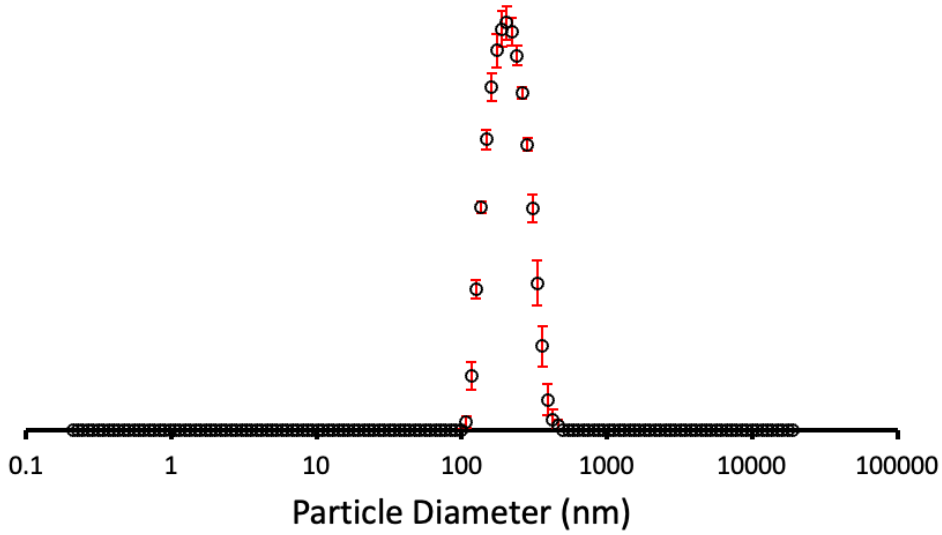

Figure S50 - The average intensity particle size distribution of aggregates formed by compound **15** (1.39 mM) in a 1:3 solution of 5 % EtOH in H_2O:TSB calculated using 10 DLS runs at 298 K. d_H = 215.37 nm.

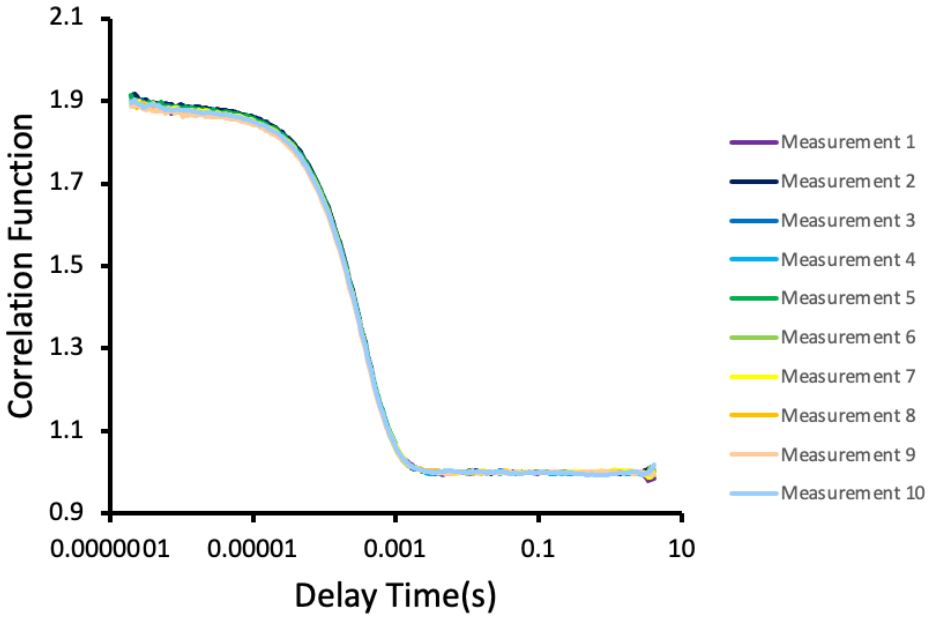

Figure S51 - The correlation function data for 10 DLS runs of compound **15** (1.39 mM) in a 1:3 solution of 5 % EtOH in H_2O:TSB at 298 K.

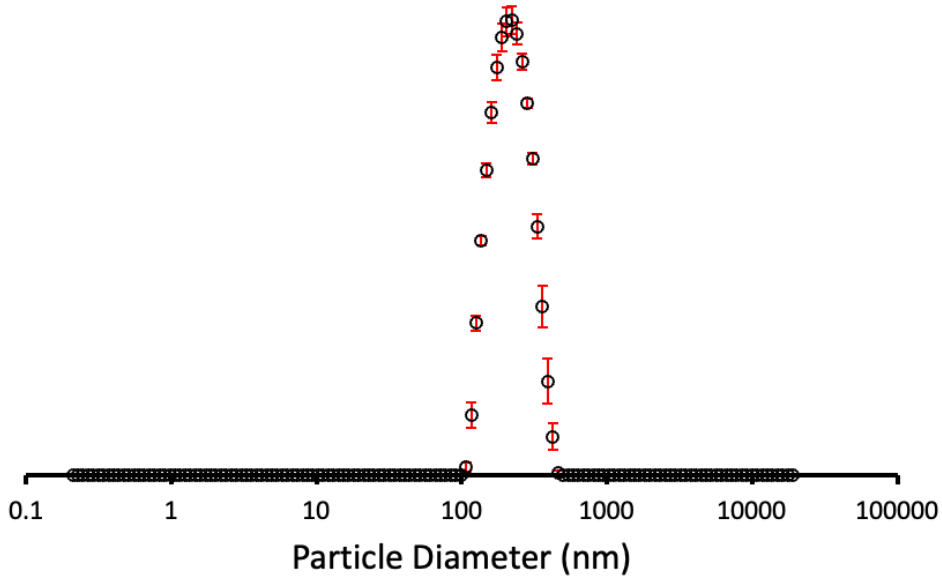

Figure S52 - The average intensity particle size distribution of aggregates formed by a 1:1 mixture of compounds **13** and **15** (1.39 mM) in a 1:3 solution of 5 % EtOH in H_2O:TSB calculated using 10 DLS runs at 298 K. d_H = 226.14 nm.

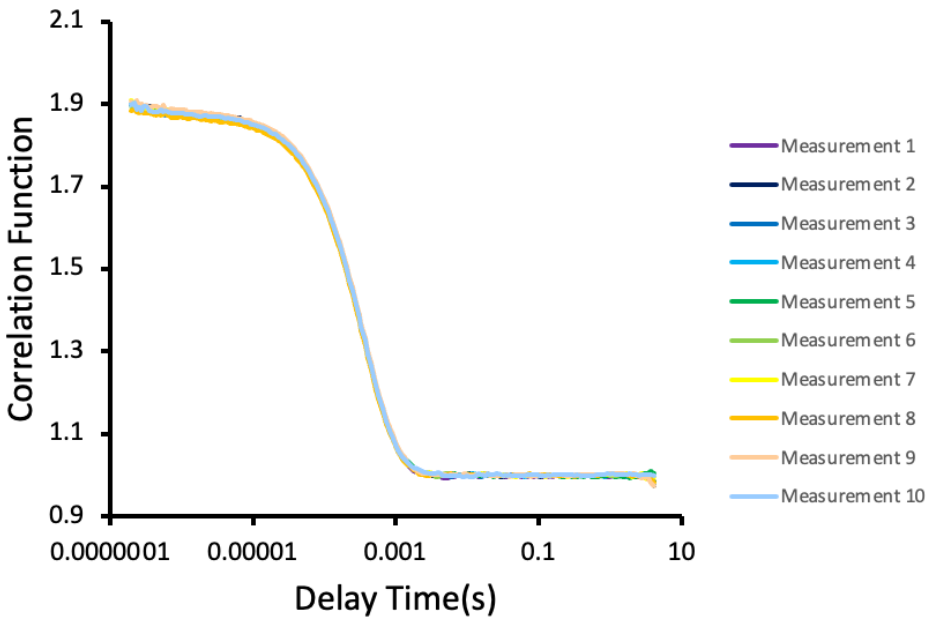

Figure S53 - The correlation function data for 10 DLS runs of a 1:1 mixture of compounds **13** and **15** (1.39 mM) in a 1:3 solution of 5 % EtOH in H_2O:TSB at 298 K.

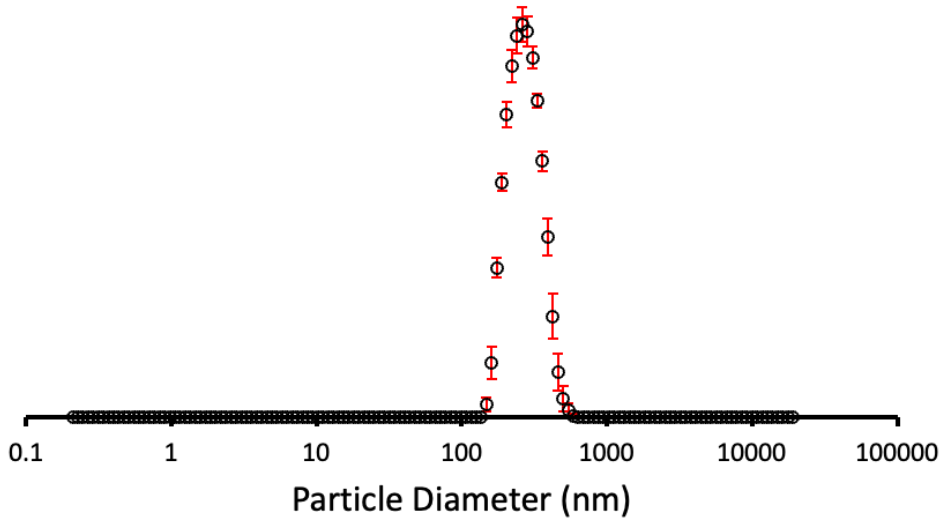

Figure S54 - The average intensity particle size distribution of aggregates formed by compound **17** (1.39 mM) in a 1:3 solution of 5 % EtOH in H_2O:TSB calculated using 10 DLS runs at 298 K. d_H = 276.19 nm.

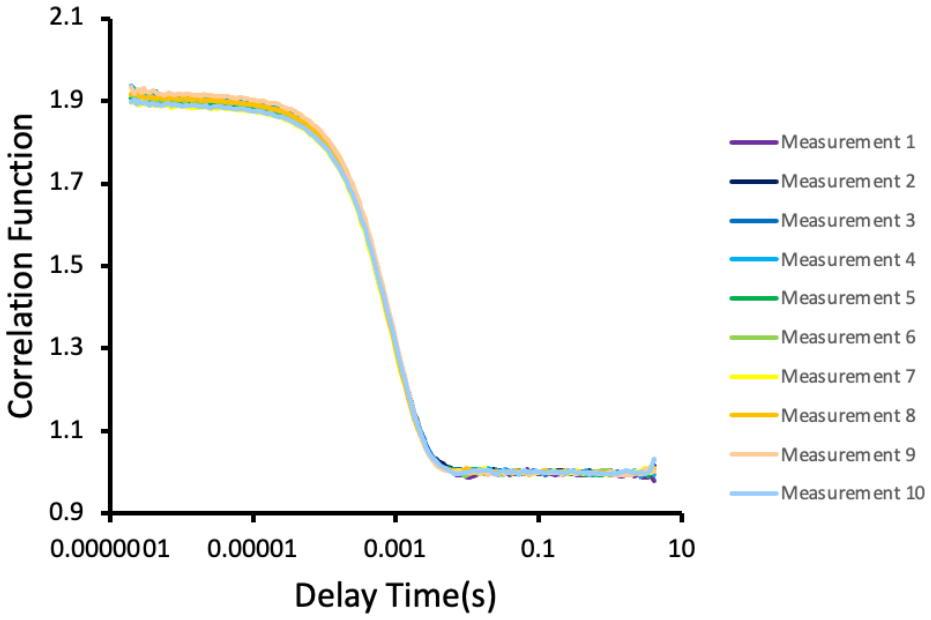

Figure S55 - The correlation function data for 10 DLS runs of compound **17** (1.39 mM) in a 1:3 solution of 5 % EtOH in H_2O:TSB at 298 K.

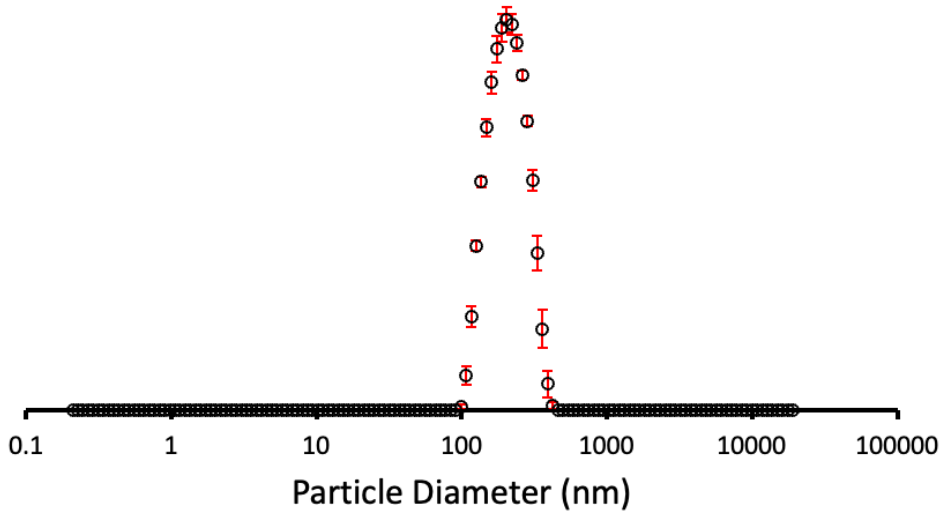

Figure S56 - The average intensity particle size distribution of aggregates formed by compound **19** (1.39 mM) in a 1:3 solution of 5 % EtOH in H_2O:TSB calculated using 10 DLS runs at 298 K. d_H = 213.25 nm.

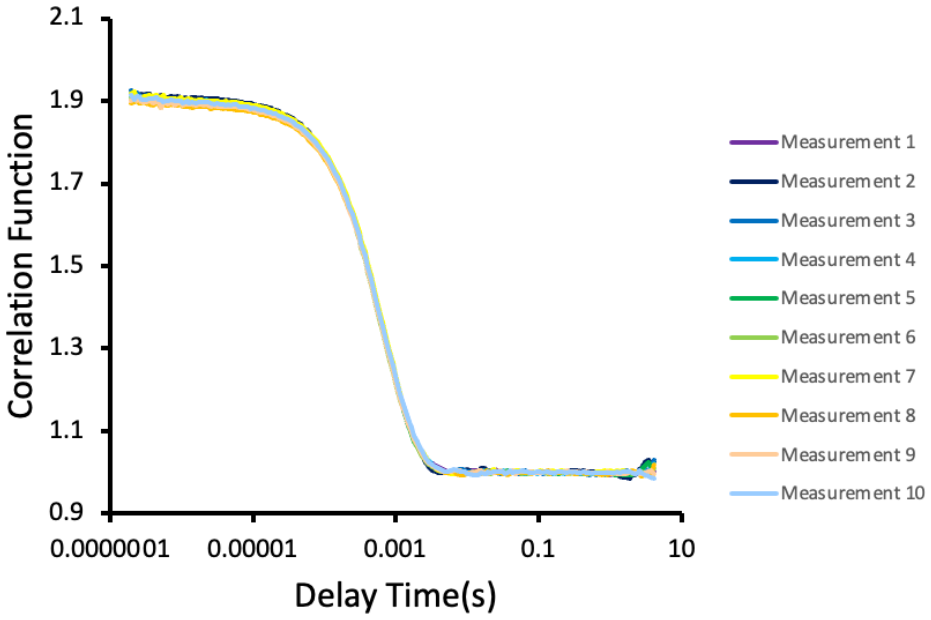

Figure S57 - The correlation function data for 10 DLS runs of compound **19** (1.39 mM) in a 1:3 solution of 5 % EtOH in H_2O:TSB at 298 K.

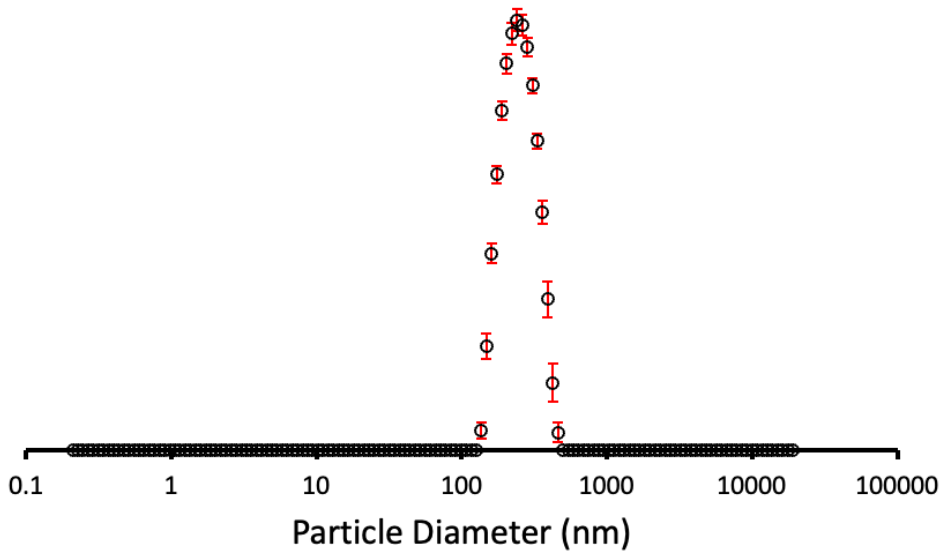

Figure S 58 - The average intensity particle size distribution of aggregates formed by a 1:1 mixture of compounds **17** and **19** (1.39 mM) in a 1:3 solution of 5 % EtOH in H_2O:TSB calculated using 10 DLS runs at 298 K. d_H = 226.14 nm.

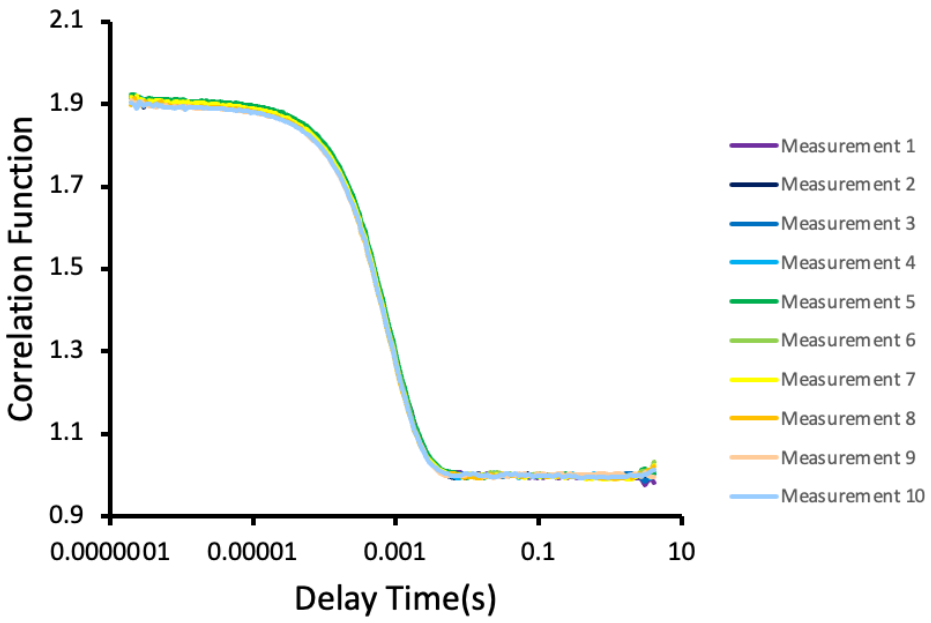

Figure S 59 - The correlation function data for 10 DLS runs of a 1:1 mixture of compounds **17** and **19** (1.39 mM) in a 1:3 solution of 5 % EtOH in H_2O:TSB at 298 K.

7.5.4. Summary

Table S2 - The average intensity particle size distribution calculated from 10 DLS runs for **13**, **15**, **17** and **19**, and racemic mixtures of isomers **13**+**15** and isomers **17**+**19** obtained at 1.39 mM in a 1:3 solution of 5% EtOH in H_2O:TSB. An annealing process was applied in which the samples were heated to approximately 313 K before being cooled down to a measurement temperature of 298 K. [a] 1:1 mixture. Error = standard error of the mean and given to 1 decimal place.

Compound	Peak maxima (nm)	PDI (%)
9	285.38 (± 11.3)	27.89 (± 0.8)
13	227.49 (± 3.7)	17.25 (± 0.4)
15	215.37 (± 3.0)	14.21 (± 0.9)
13 + 15 [a]	226.14 (± 2.2)	18.34 (± 0.6)
17	276.19 (± 4.1)	14.28 (± 1.3)
19	213.25 (± 2.1)	17.16 (± 0.7)
17 + 19 [a]	255.38 (± 2.7)	14.94 (± 1.0)

7.5.5. Size Distribution Data in IMDM with 10 % FBS

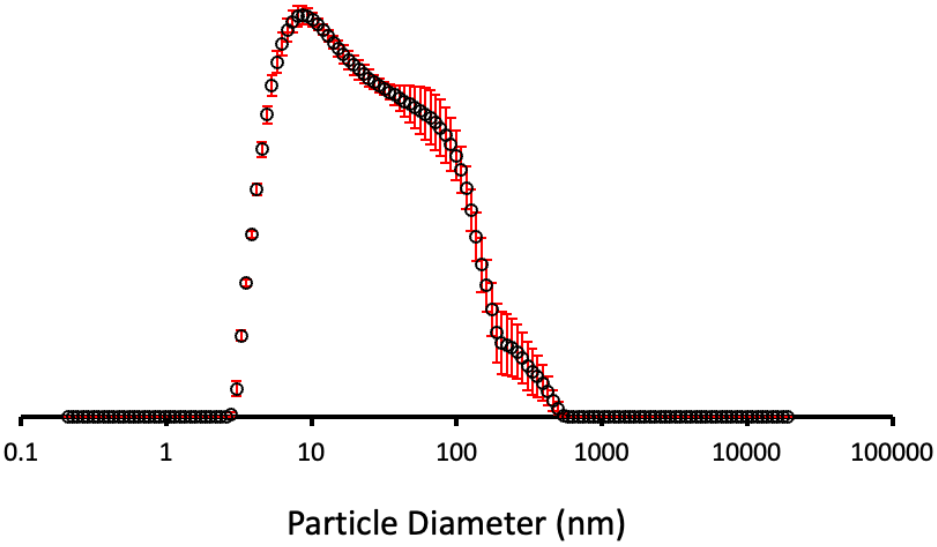

Figure S60 - The average intensity particle size distribution of aggregates formed by compound **9** (1.67 mM) in a 1:5 solution of 5 % EtOH in H_2O: IMDM with 10 % FBS calculated using 10 DLS runs at 298 K. d_H = 16.98 nm.

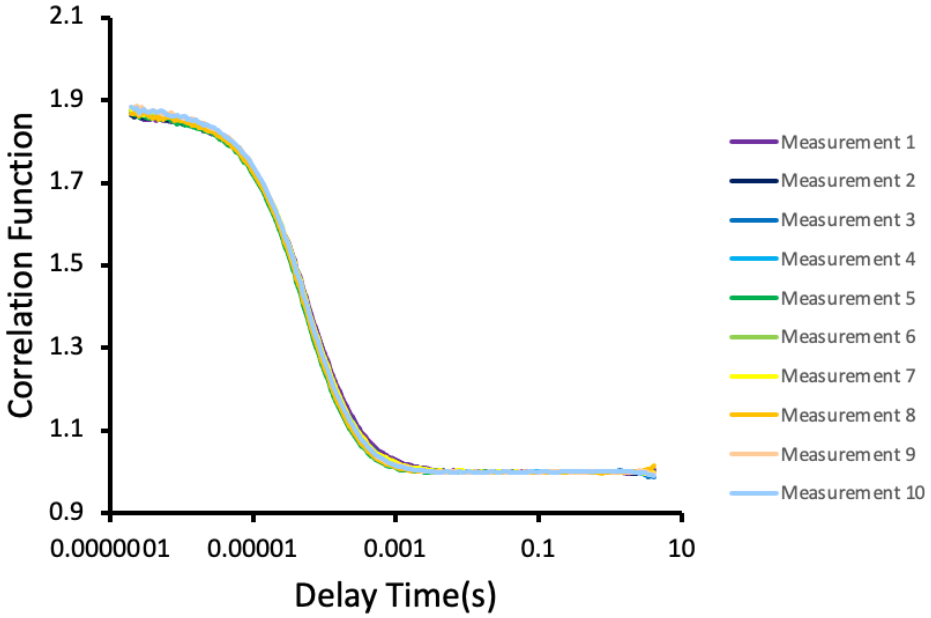

Figure S61 - The correlation function data for 10 DLS runs of compound **9** (1.67 mM) in a 1:5 solution of 5 % EtOH in H_2O: IMDM with 10 % FBS at 298 K.

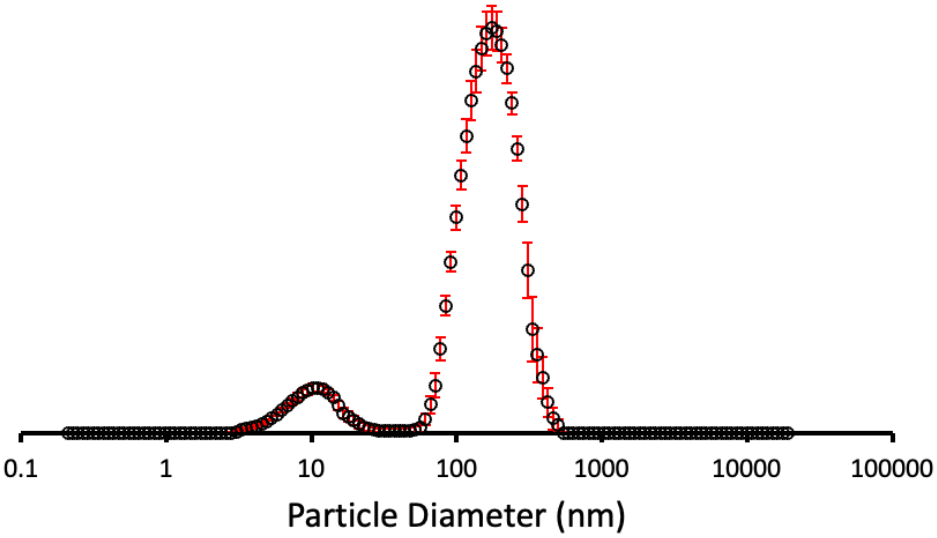

Figure S62 - The average intensity particle size distribution of aggregates formed by compound **13** (1.67 mM) in a 1:5 solution of 5 % EtOH in H_2O: IMDM with 10 % FBS calculated using 10 DLS runs at 298 K. d_H = 181.42 nm.

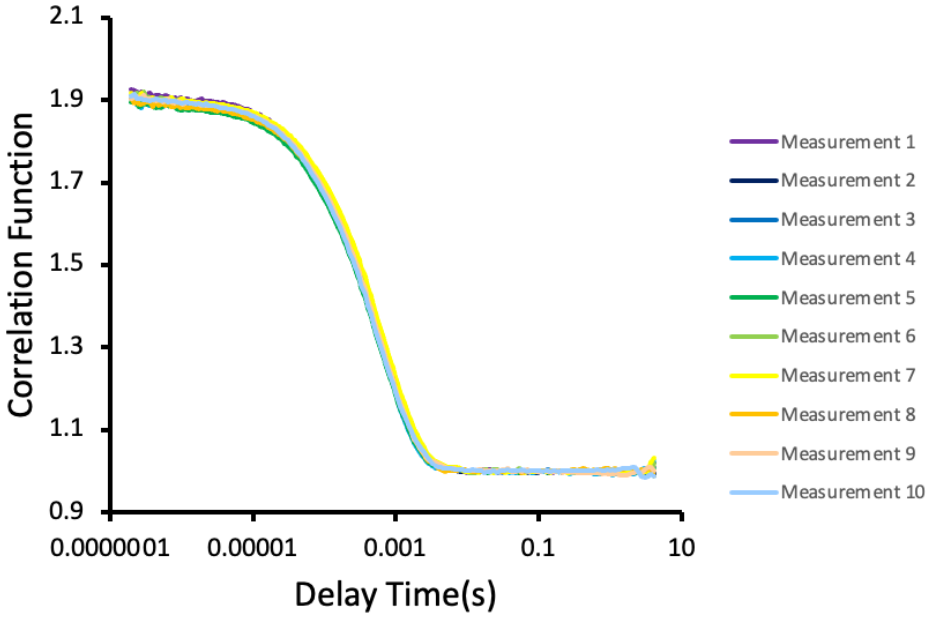

Figure S63 - The correlation function data for 10 DLS runs of compound **13** (1.67 mM) in a 1:5 solution of 5 % EtOH in H_2O: IMDM with 10 % FBS at 298 K.

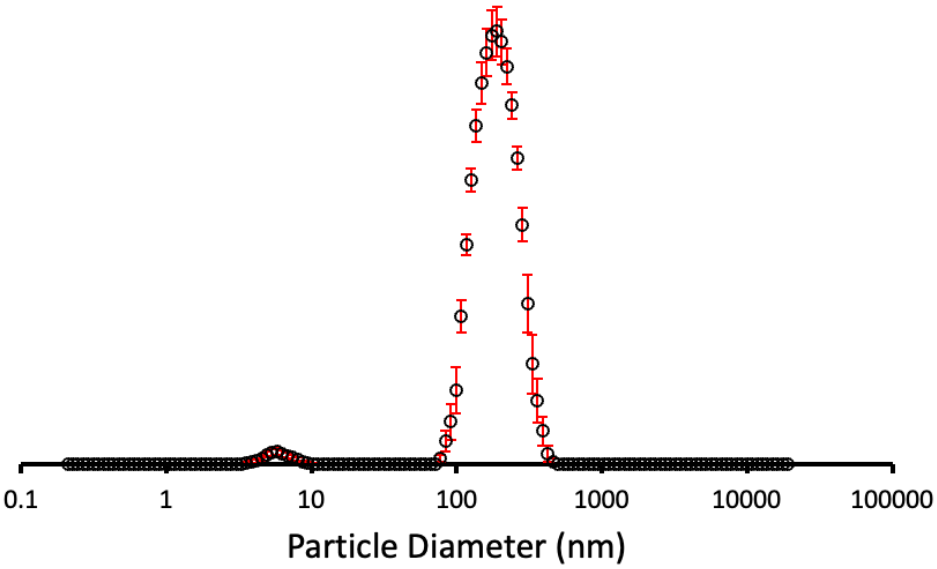

Figure S64 - The average intensity particle size distribution of aggregates formed by compound **15** (1.67 mM) in a 1:5 solution of 5 % EtOH in H_2O: IMDM with 10 % FBS calculated using 10 DLS runs at 298 K. d_H = 194.28 nm.

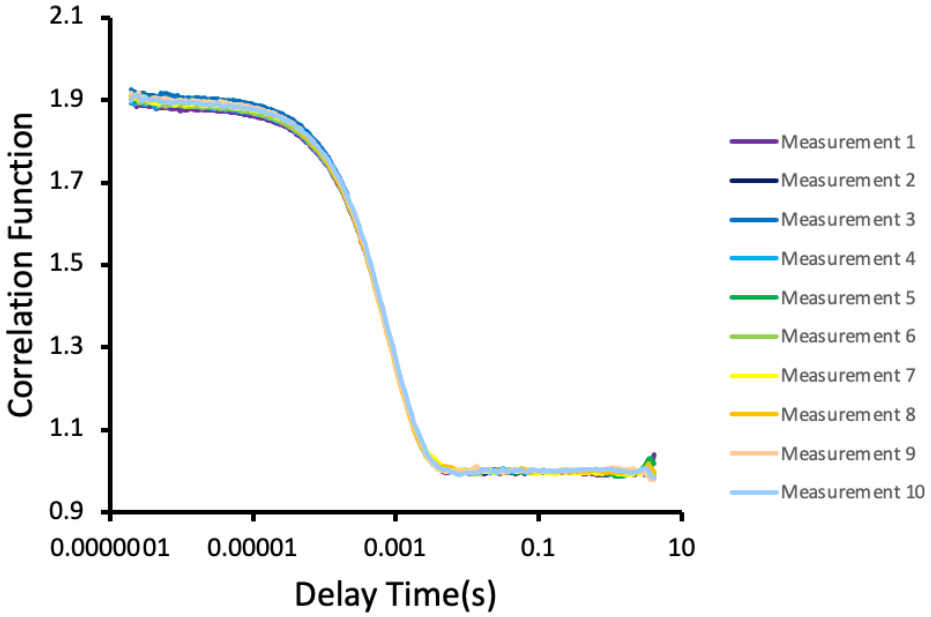

Figure S65 - The correlation function data for 10 DLS runs of compound **15** (1.67 mM) in a 1:5 solution of 5 % EtOH in H_2O: IMDM with 10 % FBS at 298 K.

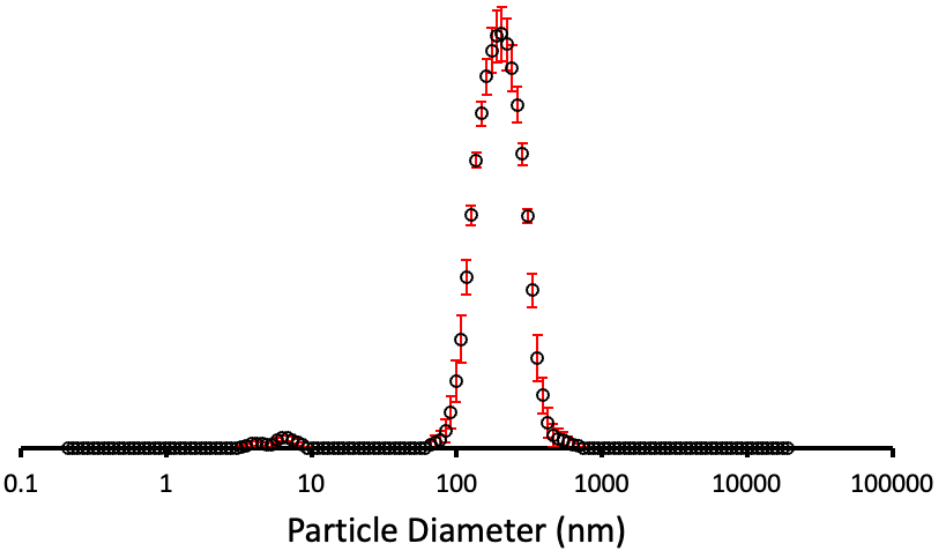

Figure S66 – The average intensity particle size distribution of aggregates formed by a 1:1 mixture of compounds **13** and **15** (1.67 mM) in a 1:5 solution of 5 % EtOH in H_2O: IMDM with 10 % FBS calculated using 10 DLS runs at 298 K. d_H = 208.27 nm.

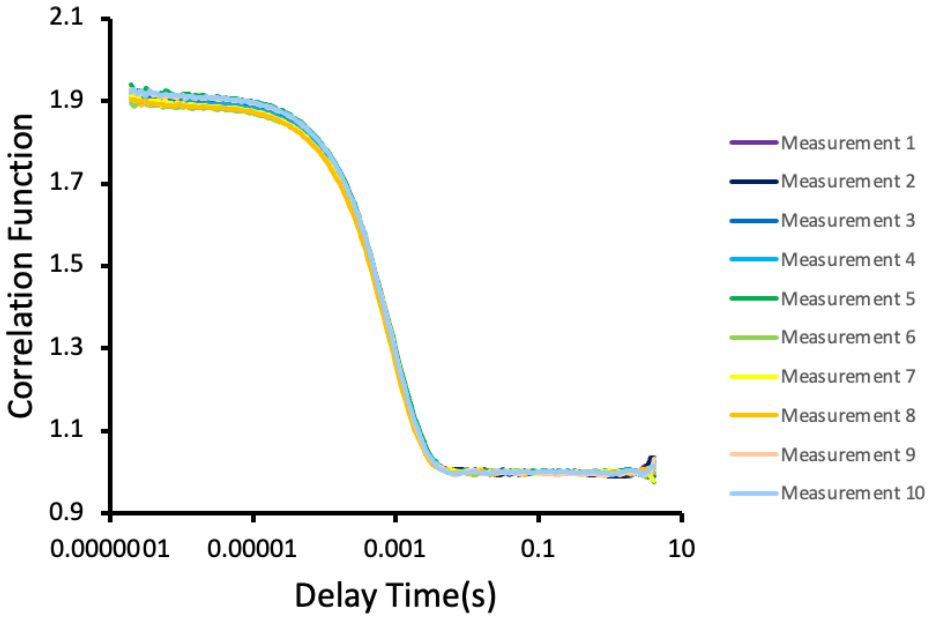

Figure S67 - The correlation function data for 10 DLS runs of a 1:1 mixture of compounds **13** and **15** (1.67 mM) in a 1:5 solution of 5 % EtOH in H_2O: IMDM with 10 % FBS at 298 K.

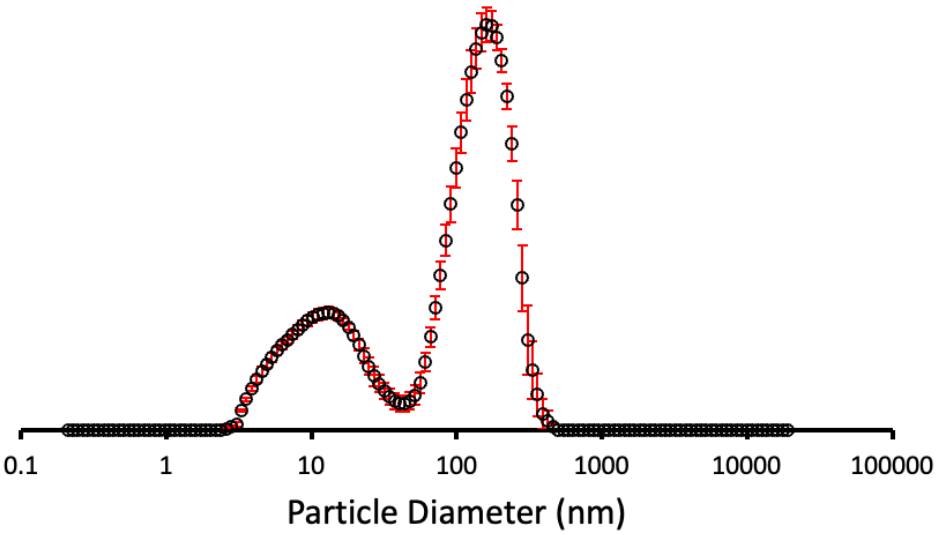

Figure S68 - The average intensity particle size distribution of aggregates formed by compound **17** (1.67 mM) in a 1:5 solution of 5 % EtOH in H_2O: IMDM with 10 % FBS calculated using 10 DLS runs at 298 K. d_H = 159.59 nm.

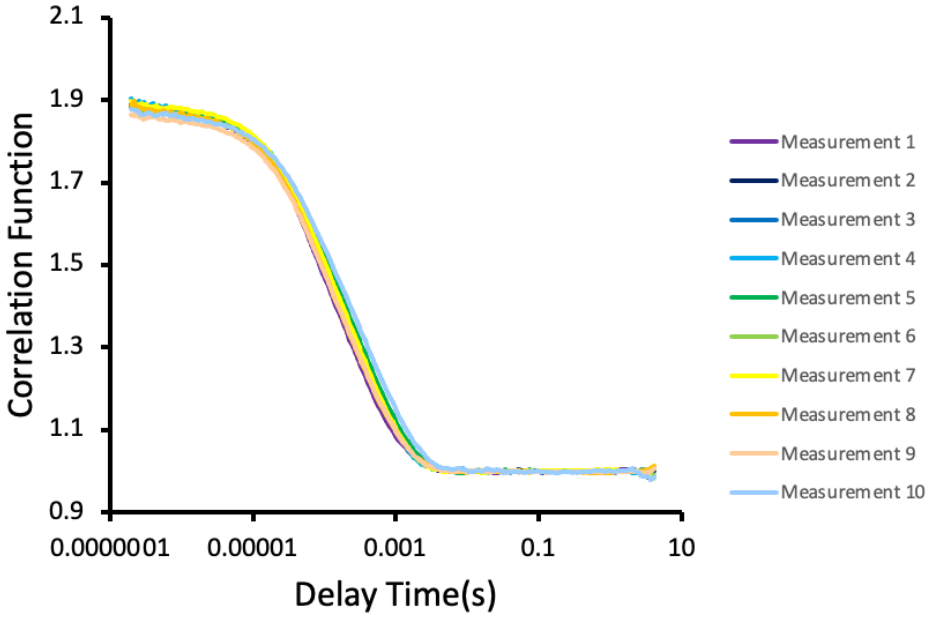

Figure S69 - The correlation function data for 10 DLS runs of compound **17** (1.67 mM) in a 1:5 solution of 5 % EtOH in H_2O: IMDM with 10 % FBS at 298 K.

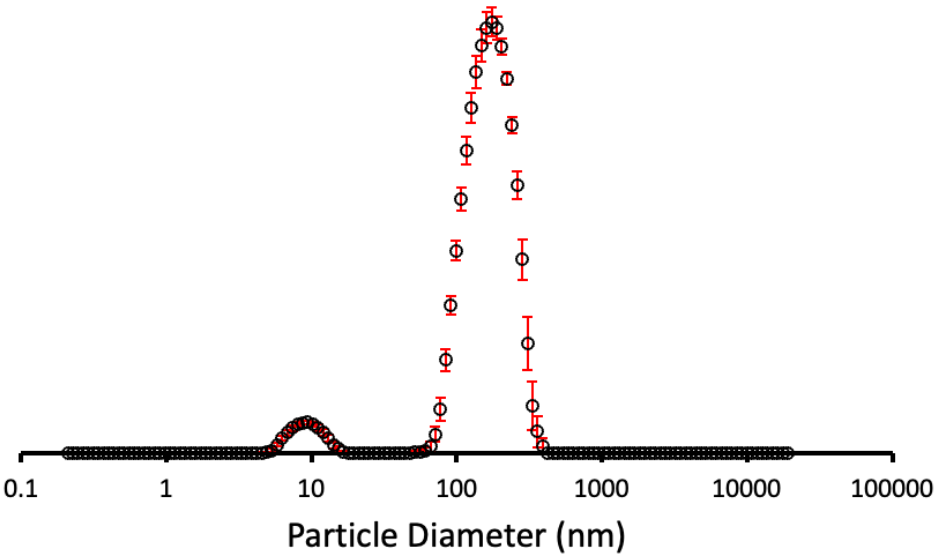

Figure S70 - The average intensity particle size distribution of aggregates formed by compound **19** (1.67 mM) in a 1:5 solution of 5 % EtOH in H_2O: IMDM with 10 % FBS calculated using 10 DLS runs at 298 K. d_H = 175.01 nm.

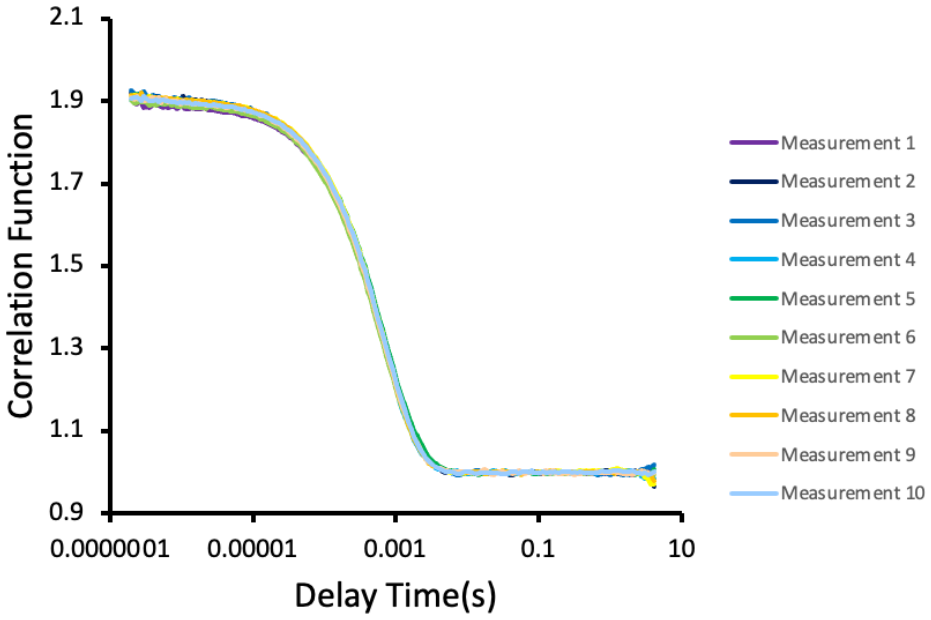

Figure S71 - The correlation function data for 10 DLS runs of compound **19** (1.67 mM) in a 1:5 solution of 5 % EtOH in H_2O: IMDM with 10 % FBS at 298 K.

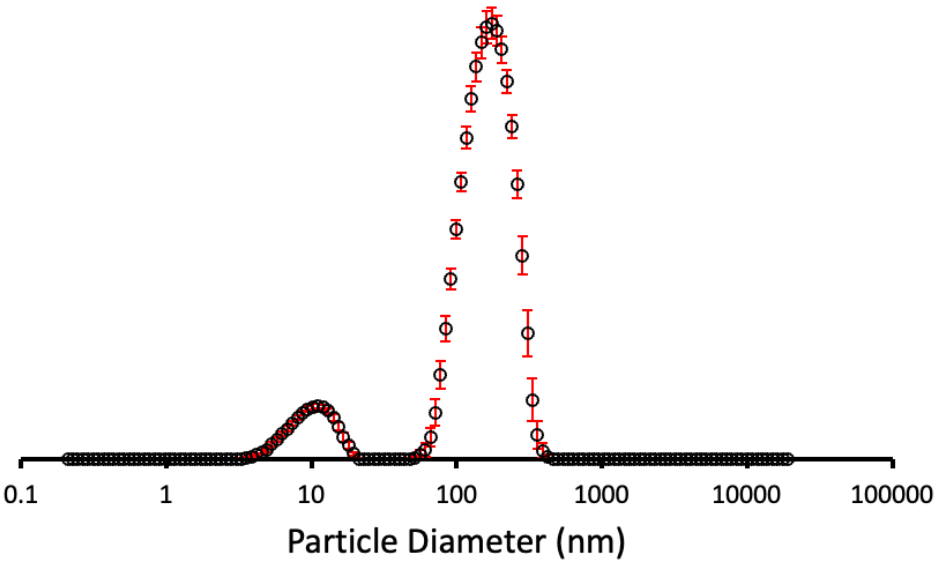

Figure S72 - The average intensity particle size distribution of aggregates formed by a 1:1 mixture of compounds **17** and **19** (1.67 mM) in a 1:5 solution of 5 % EtOH in H_2O: IMDM with 10 % FBS calculated using 10 DLS runs at 298 K. d_H = 172.44 nm.

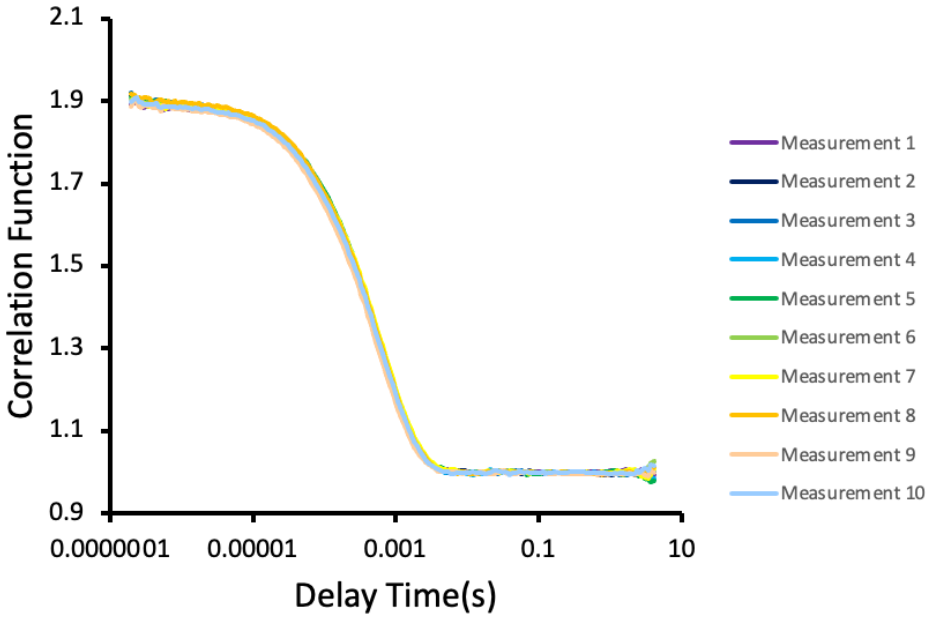

Figure S73 - The correlation function data for 10 DLS runs of a 1:1 mixture of compounds **17** and **19** (1.67 mM) in a 1:5 solution of 5 % EtOH in H_2O: IMDM with 10 % FBS at 298 K.

7.5.6. Summary

Table S3 – The average intensity particle size distribution calculated from 10 DLS runs for **13**, **15**, **17** and **19**, and racemic mixtures of isomers **13**+**15** and isomers **17**+**19** obtained at 1.67 mM in a 1:5 solution of 5 % EtOH in H_2O: IMDM with 10 % FBS. An annealing process was applied in which the samples were heated to approximately 313 K before being cooled down to a measurement temperature of at 298 K. [a] 1:1 mixture. Error = standard error of the mean and given to 1 decimal place.

Compound	Peak maxima (nm)	PDI (%)
9	16.98 (± 2.3)	24.44 (± 0.6)
13	181.42 (± 6.4)	28.11 (± 0.6)
15	194.28 (± 3.1)	19.51 (± 0.6)
13 + 15 [a]	208.27 (± 3.1)	17.52 (± 0.7)
17	159.59 (± 6.1)	30.57 (± 0.4)
19	175.01 (± 3.3)	24.40 (± 0.4)
17 + 19 [a]	172.44 (± 2.5)	28.61 (± 0.6)

7.5.7. Size Distribution Data in PBS

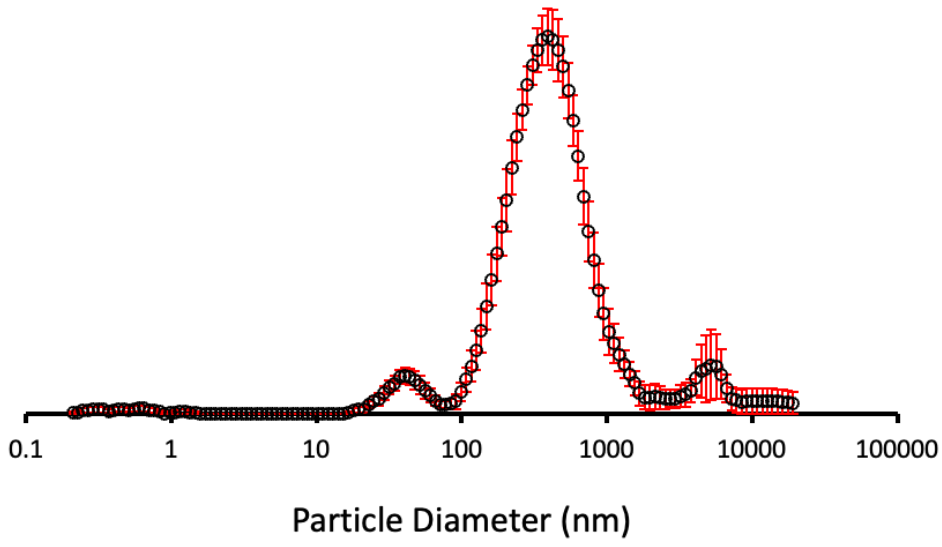

Figure S74 - The average intensity particle size distribution of aggregates formed by compound **9** (1.39 mM) in a 1:3 solution of 5 % EtOH in H_2O:PBS calculated using 10 DLS runs at 298 K. d_H = 439.80 nm.

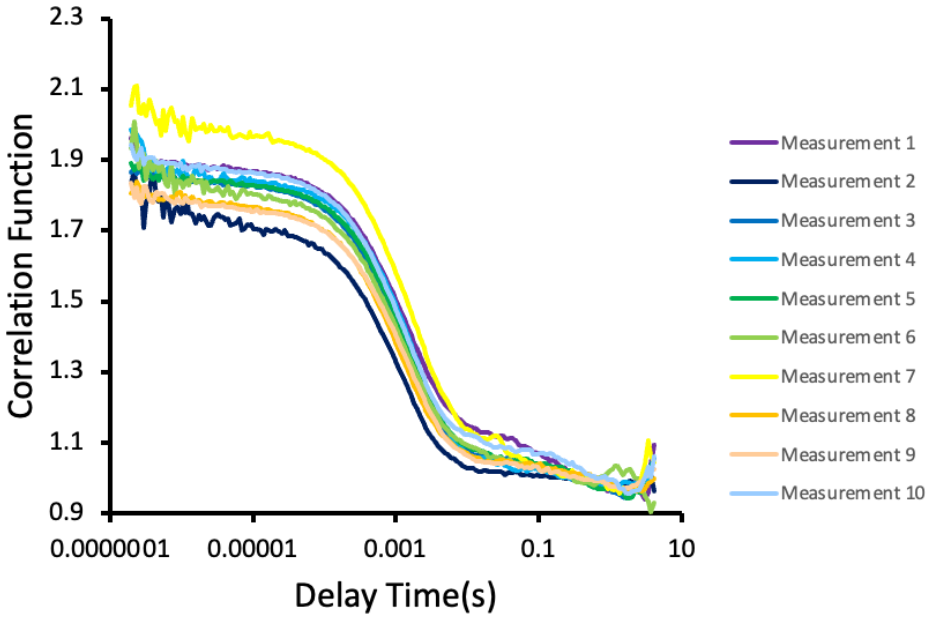

Figure S75 - The correlation function data for 10 DLS runs of compound **9** (1.39 mM) in a 1:3 solution of 5 % EtOH in H_2O:PBS at 298 K.

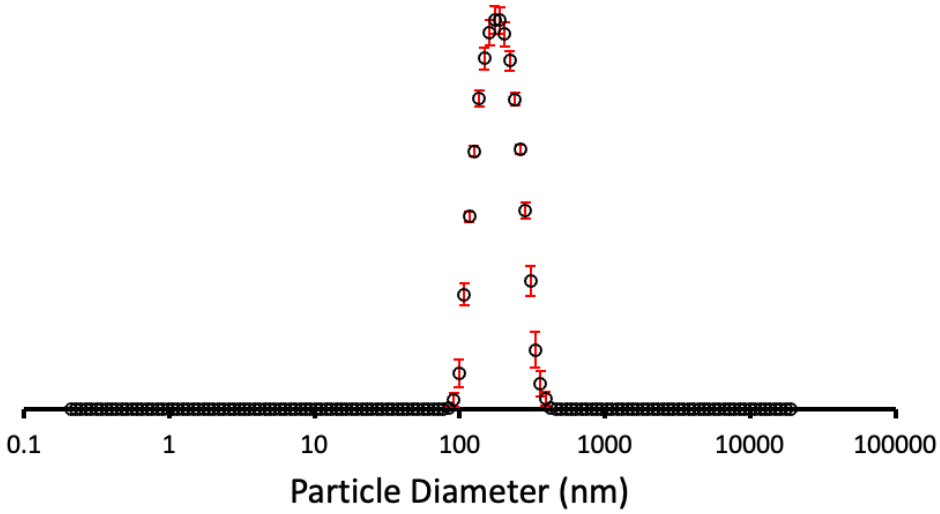

Figure S76 - The average intensity particle size distribution of aggregates formed by compound **13** (1.39 mM) in a 1:3 solution of 5 % EtOH in H_2O:PBS calculated using 10 DLS runs at 298 K. d_H = 191.38 nm.

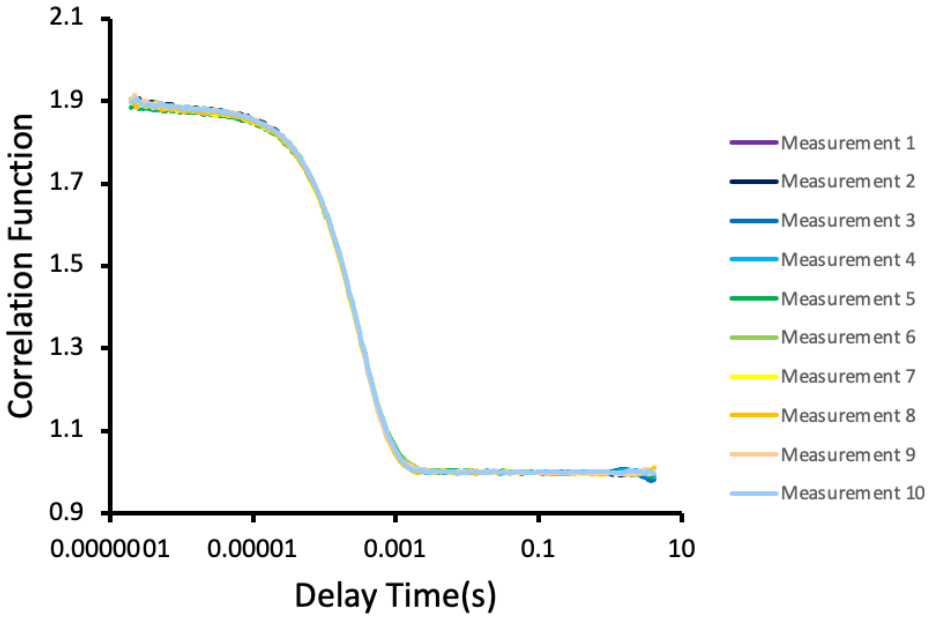

Figure S77 - The correlation function data for 10 DLS runs of compound **13** (1.39 mM) in a 1:3 solution of 5 % EtOH in H_2O:PBS at 298 K.

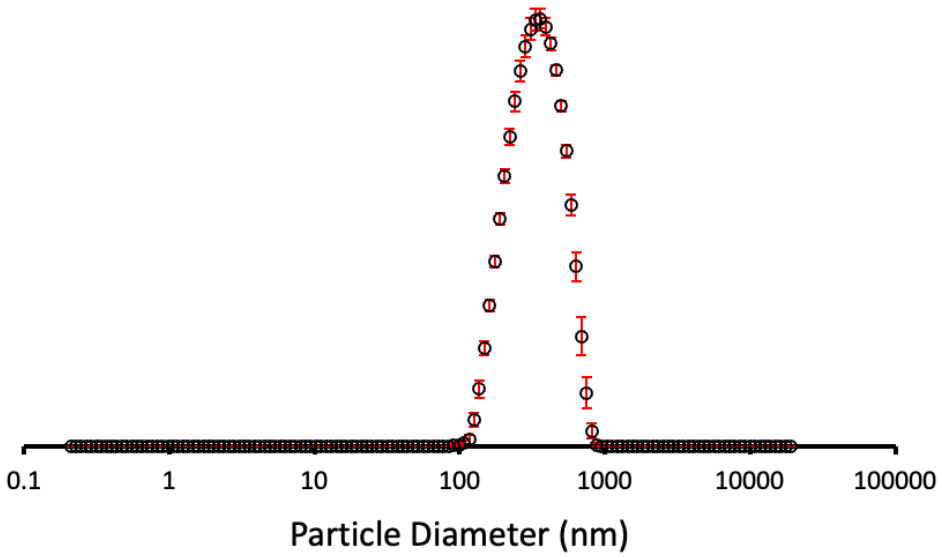

Figure S78 - The average intensity particle size distribution of aggregates formed by compound **15** (1.39 mM) in a 1:3 solution of 5 % EtOH in H_2O:PBS calculated using 10 DLS runs at 298 K. d_H = 355.86 nm.

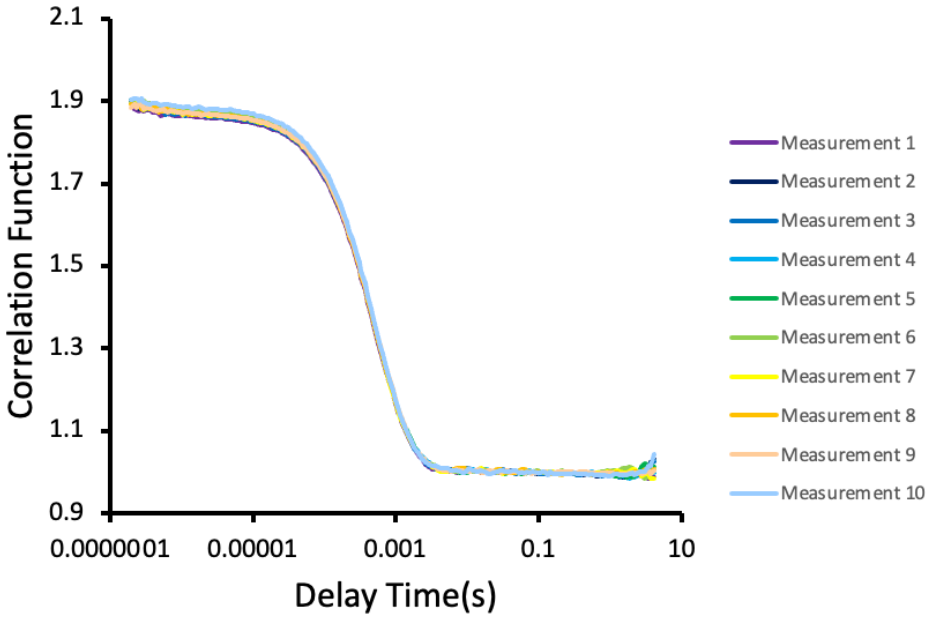

Figure S79 - The correlation function data for 10 DLS runs of compound **15** (1.39 mM) in a 1:3 solution of 5 % EtOH in H_2O:PBS at 298 K.

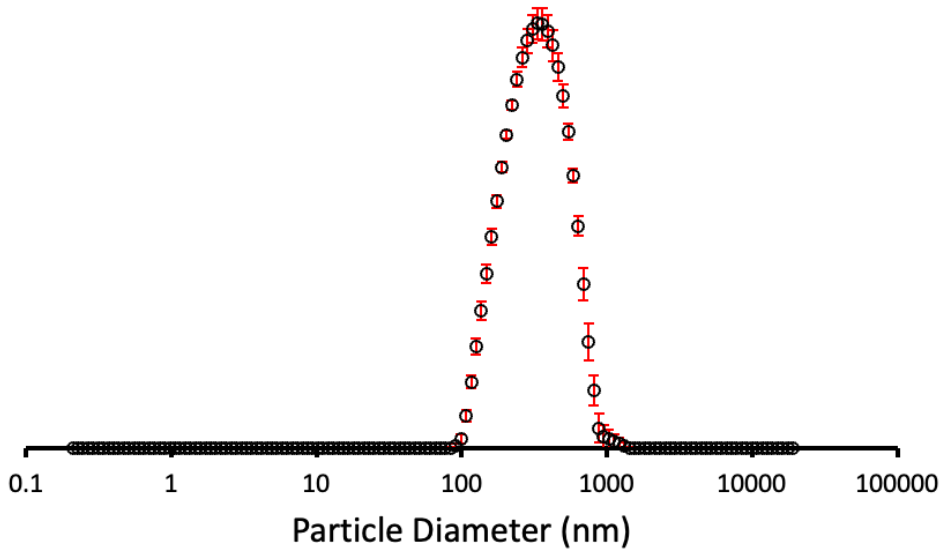

Figure S80 - The average intensity particle size distribution of aggregates formed by a 1:1 mixture of compounds **13** and **15** (1.39 mM) in a 1:3 solution of 5 % EtOH in H_2O:PBS calculated using 10 DLS runs at 298 K. d_H = 355.32 nm.

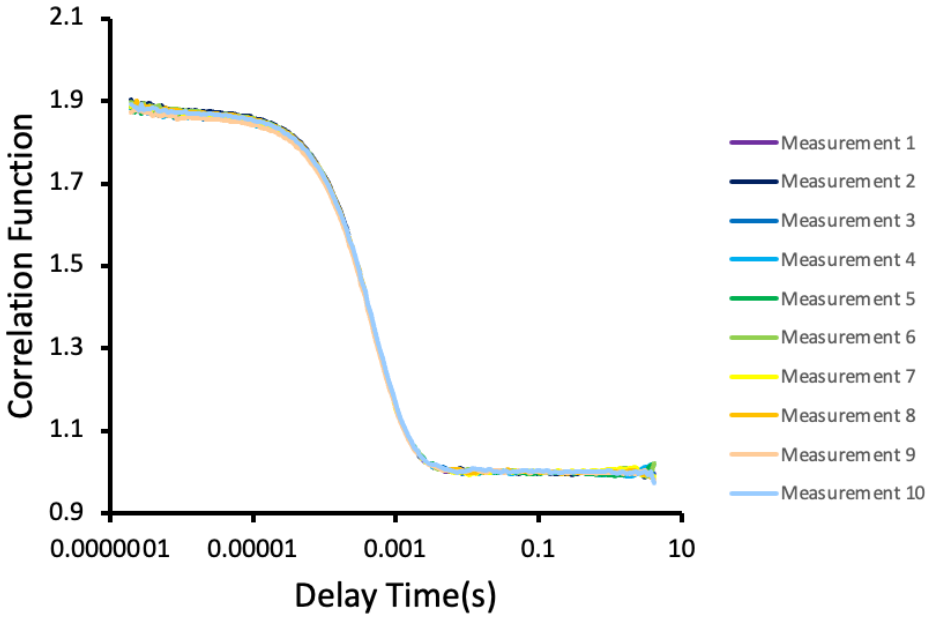

Figure S81 – The correlation function data for 10 DLS runs of a 1:1 mixture of compounds **13** and **15** (1.39 mM) in a 1:3 solution of 5% EtOH in H_2O:PBS at 298 K.

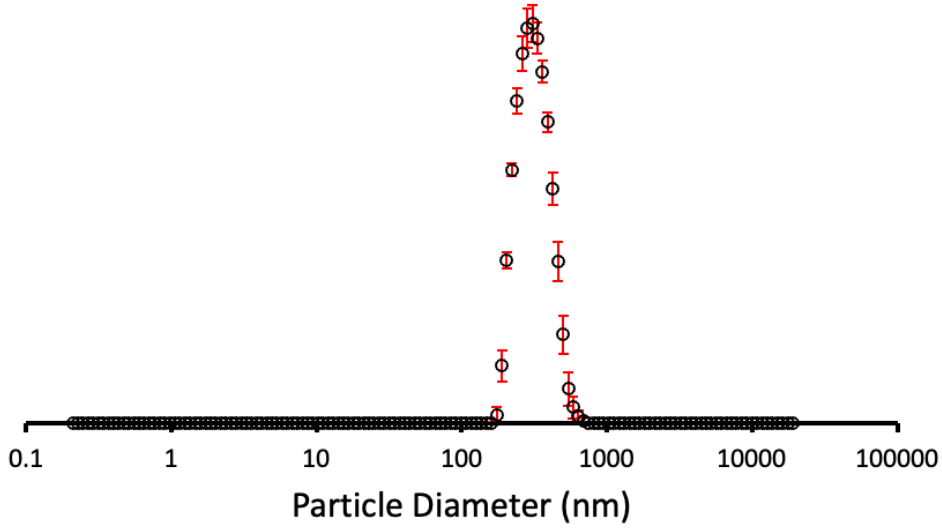

Figure S82 - The average intensity particle size distribution of aggregates formed by compound **17** (1.39 mM) in a 1:3 solution of 5 % EtOH in H_2O:PBS calculated using 10 DLS runs at 298 K. d_H = 319.84 nm.

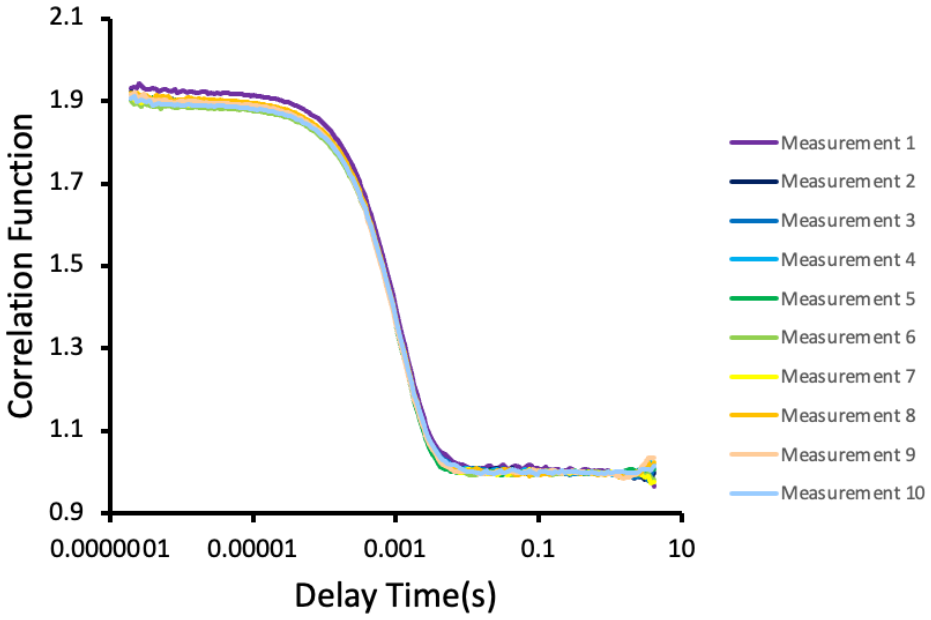

Figure S83 - The correlation function data for 10 DLS runs of compound **17** (1.39 mM) in a 1:3 solution of 5 % EtOH in H_2O:PBS at 298 K.

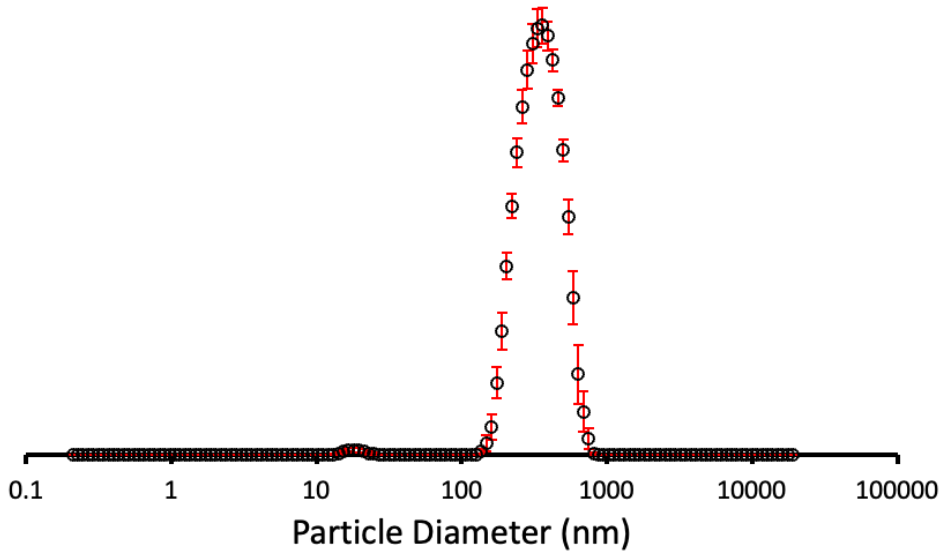

Figure S84 - The average intensity particle size distribution of aggregates formed by compound **19** (1.39 mM) in a 1:3 solution of 5 % EtOH in H_2O:PBS calculated using 10 DLS runs at 298 K. d_H = 359.73 nm.

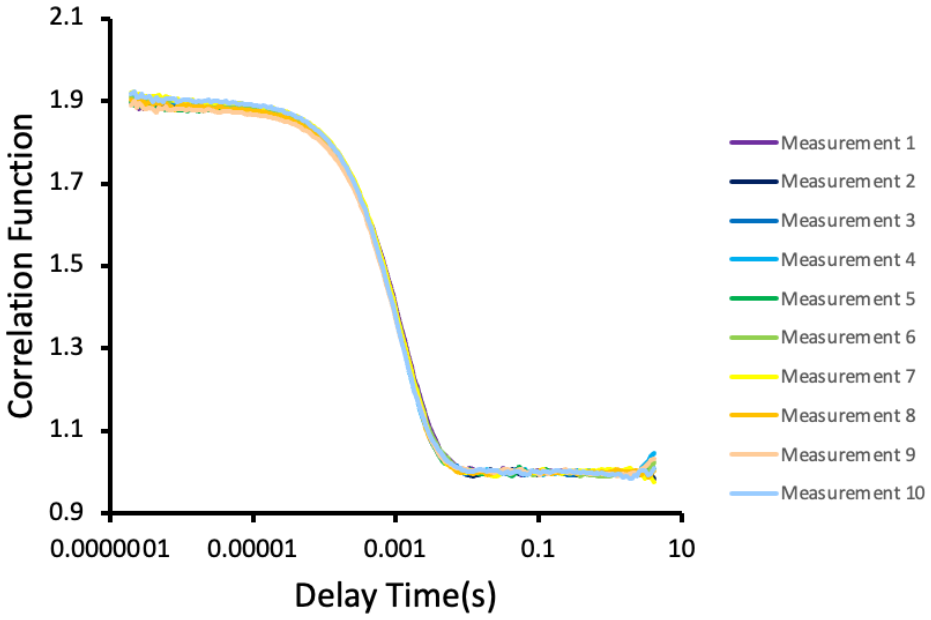

Figure S85 - The correlation function data for 10 DLS runs of compound **19** (1.39 mM) in a 1:3 solution of 5 % EtOH in H_2O:PBS at 298 K.

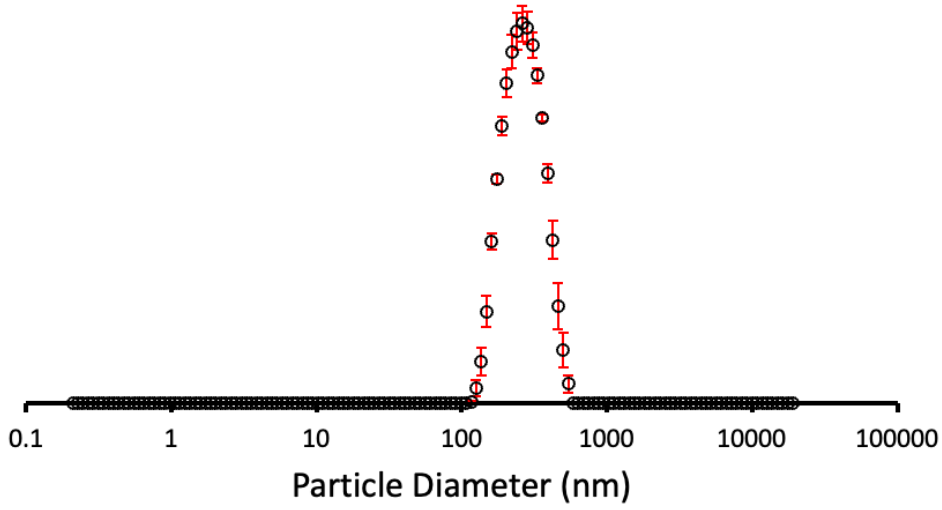

Figure S86 - The average intensity particle size distribution of aggregates formed by a 1:1 mixture of compounds **17** and **19** (1.39 mM) in a 1:3 solution of 5 % EtOH in H_2O:PBS calculated using 10 DLS runs at 298 K. d_H = 275.00 nm.

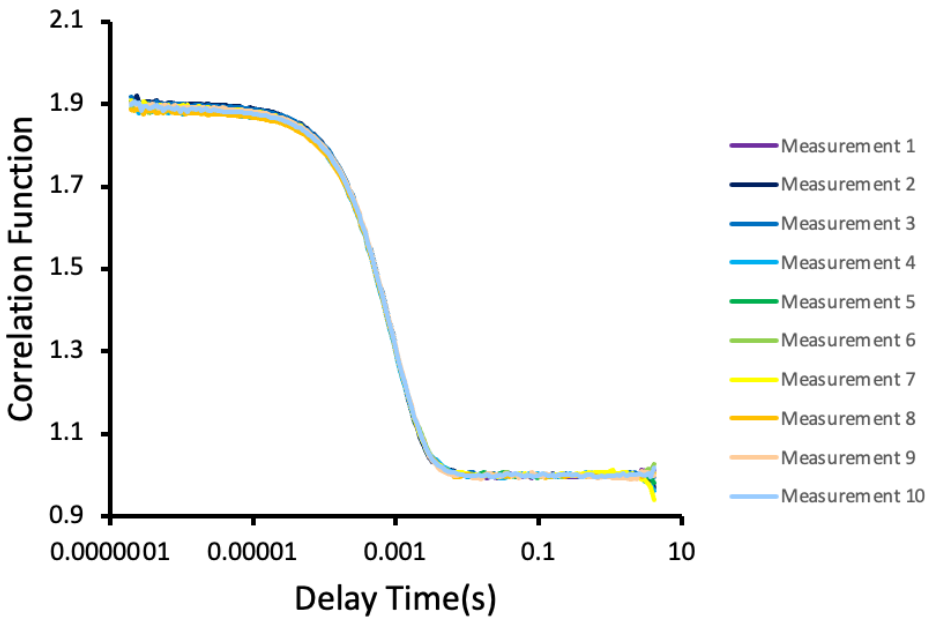

Figure S87 - The correlation function data for 10 DLS runs of a 1:1 mixture of compounds **17** and **19** (1.39 mM) in a 1:3 solution of 5 % EtOH in H_2O:PBS at 298 K.

7.5.8. Summary

Table S4 - The average intensity particle size distribution calculated from 10 DLS runs for **13**, **15**, **17** and **19**, and racemic mixtures of isomers **13**+**15** and isomers **17**+**19** obtained at 1.39 mM in a 1:3 solution of 5 % EtOH in H_2O:PBS. An annealing process was applied in which the samples were heated to approximately 313 K before being cooled down to a measurement temperature of 298 K. [a] 1:1 mixture. Error = standard error of the mean and given to 1 decimal place.

Compound	Peak maxima (nm)	PDI (%)
9	439.80 (± 18.1)	27.62 (± 0.9)
13	191.38 (± 1.7)	15.50 (± 1.2)
15	355.86 (± 3.9)	23.48 (± 0.3)
13 + 15 [a]	355.32 (± 4.9)	23.34 (± 0.2)
17	319.84 (± 2.4)	15.29 (± 1.2)
19	359.73 (± 7.1)	21.75 (± 1.0)
17 + 19 [a]	275.00 (± 3.0)	19.06 (± 1.0)

7.6. Zeta Potential Studies

7.6.1. Zeta Potential in EtOH:H_2O (1:19)

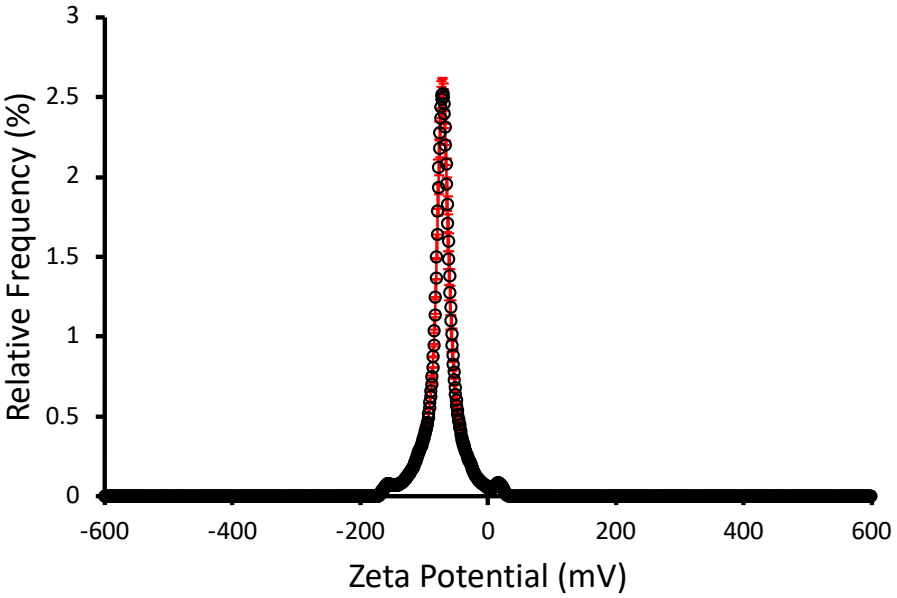

Figure S88 – The average zeta potential distribution for compound **13** (5.56 mM) in 1:19 EtOH:H_2O calculated using 10 runs at 298 K. Average measurement value: - 63.95 mV.

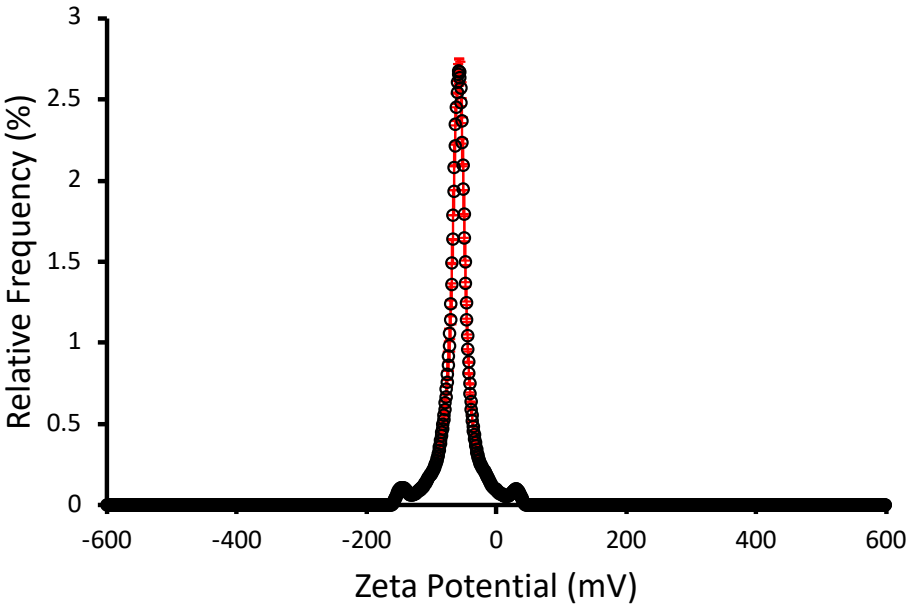

Figure S89 – The average zeta potential distribution for compound **15** (5.56 mM) in 1:19 EtOH:H_2O calculated using 10 runs at 298 K. Average measurement value: - 62.55 mV.

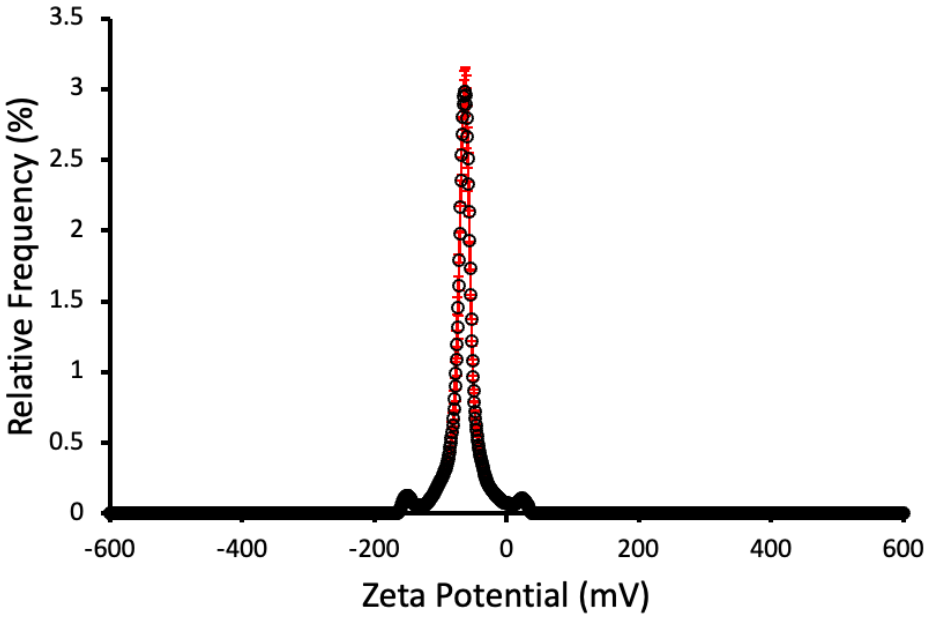

Figure S90 - The average zeta potential distribution for a 1:1 mixture of compounds **13** and **15** (5.56 mM) in 1:19 EtOH:H_2O calculated using 10 runs at 298 K. Average measurement value: - 65.75 mV.

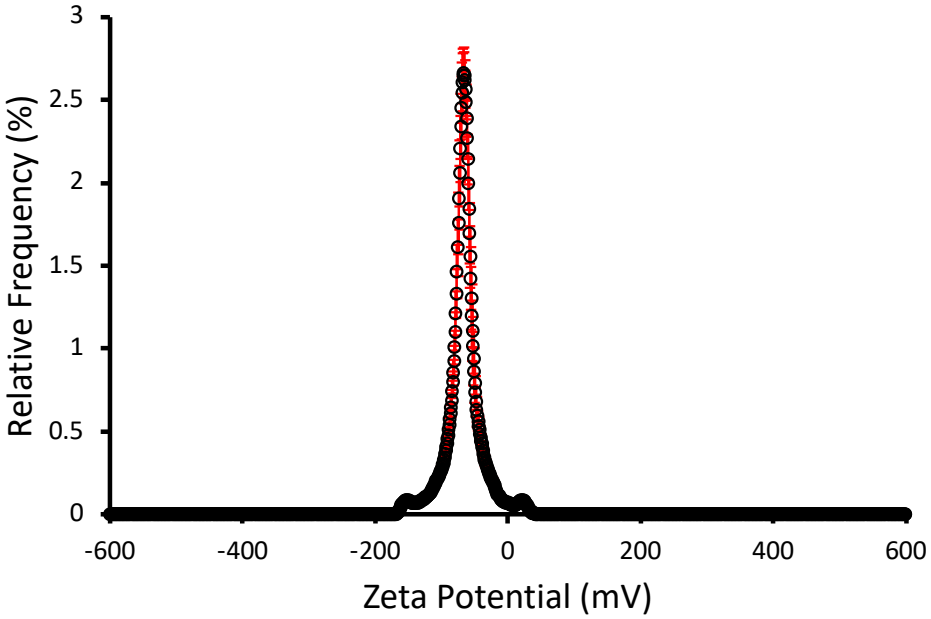

Figure S91 – The average zeta potential distribution for compound **17** (5.56 mM) in 1:19 EtOH:H_2O calculated using 10 runs at 298 K. Average measurement value: - 68.81 mV.

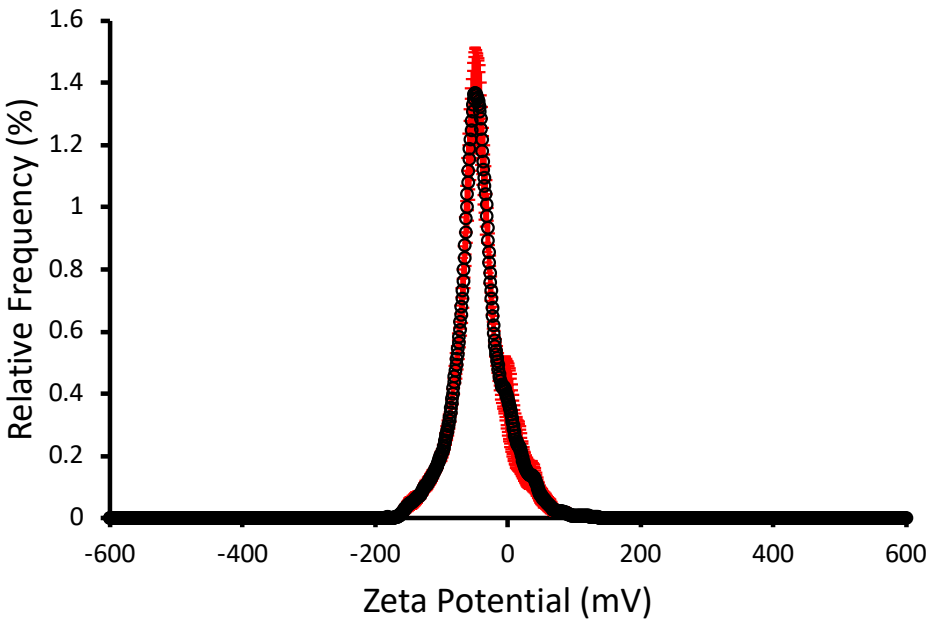

Figure S92 – The average zeta potential distribution initially obtained for compound **19** (5.56 mM) in 1:19 EtOH:H_2O calculated using 10 runs at 298 K. Average measurement value: - 56.64 mV.

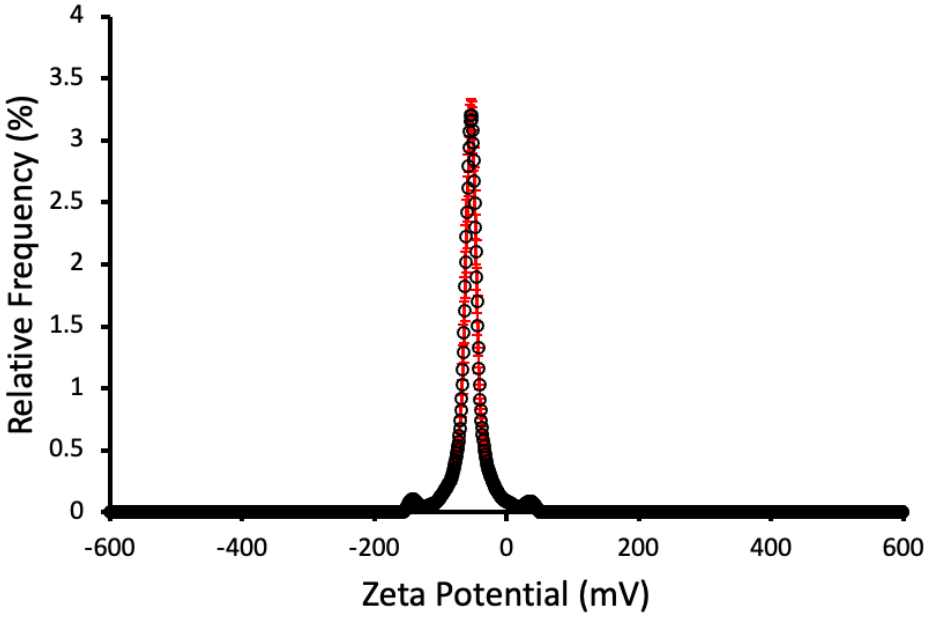

Figure S93 – The repeated average zeta potential distribution for compound **19** (5.56 mM) in 1:19 EtOH:H_2O calculated using 10 runs at 298 K. Average measurement value: - 58.09 mV.

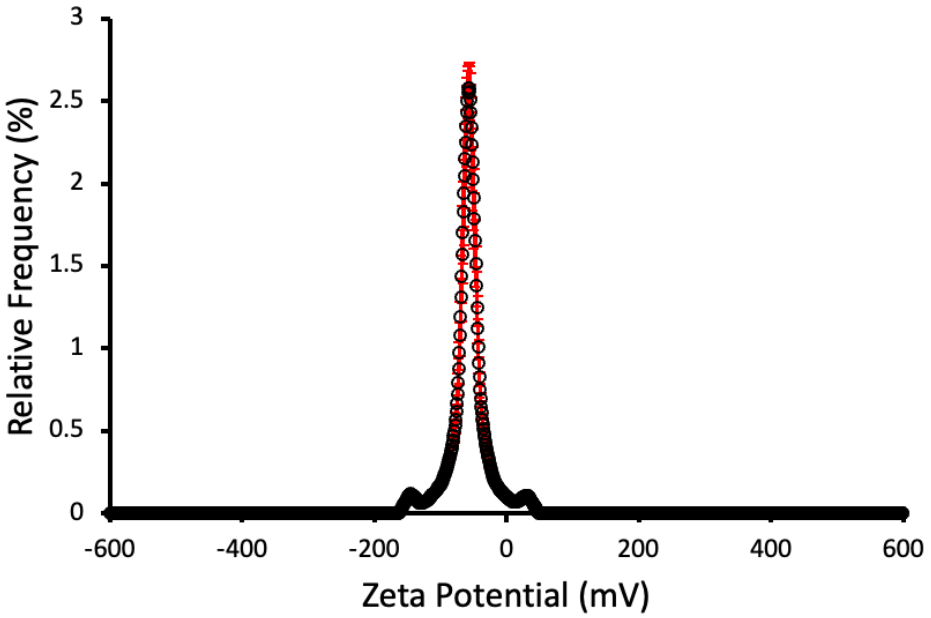

Figure S94 - The average zeta potential distribution for a 1:1 mixture of compounds **17** and **19** (5.56 mM) in 1:19 EtOH:H_2O calculated using 10 runs at 298 K. Average measurement value: - 60.29 mV.

7.6.2. Summary

Table S5 - Summary of the zeta potential (ZP) for compounds **13**, **15**, **17** and **19**, and racemic mixtures of isomers **13**+**15** and isomers **17**+**19** at 5.56 mM in EtOH:H_2O (1:19). [a] 1:1 mixture.

Compound	Zeta Potential (mV)
13	- 63.95
15	- 62.55
13 + **15**[a]	- 65.75
17	- 68.81
19	- 56.64
17 + **19**[a]	- 60.29

7.6.3. Zeta Potential in TSB

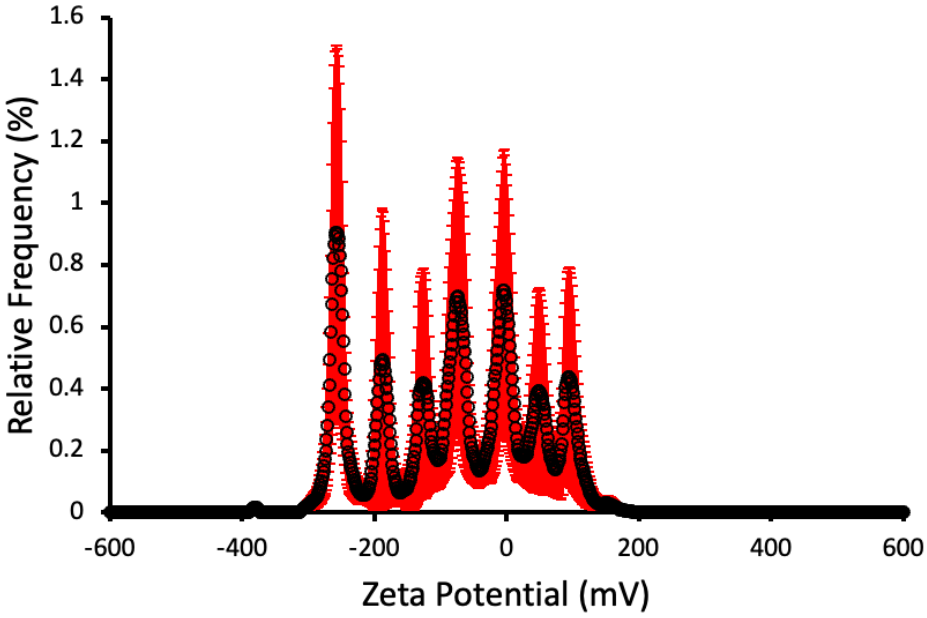

Figure S95 - The average zeta potential distribution for compound **9** (1.39 mM) in a 1:3 solution of 5 % EtOH in H_2O:TSB calculated using 10 runs at 298 K. Average measurement value: - 6.76 mV.

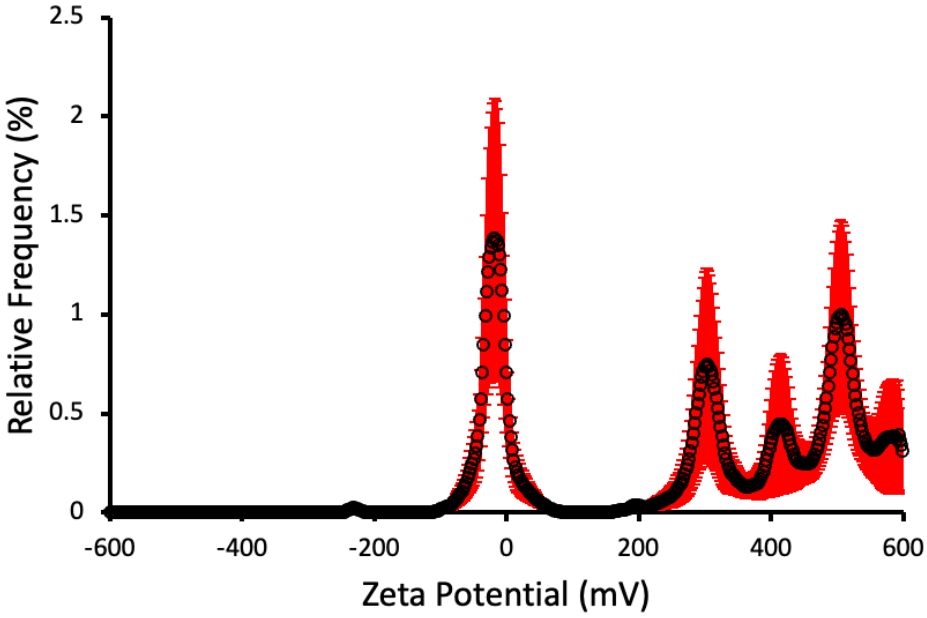

Figure S96 - The average zeta potential distribution for compound **13** (1.39 mM) in a 1:3 solution of 5 % EtOH in H_2O:TSB calculated using 10 runs at 298 K. Average measurement value: - 23.11 mV.

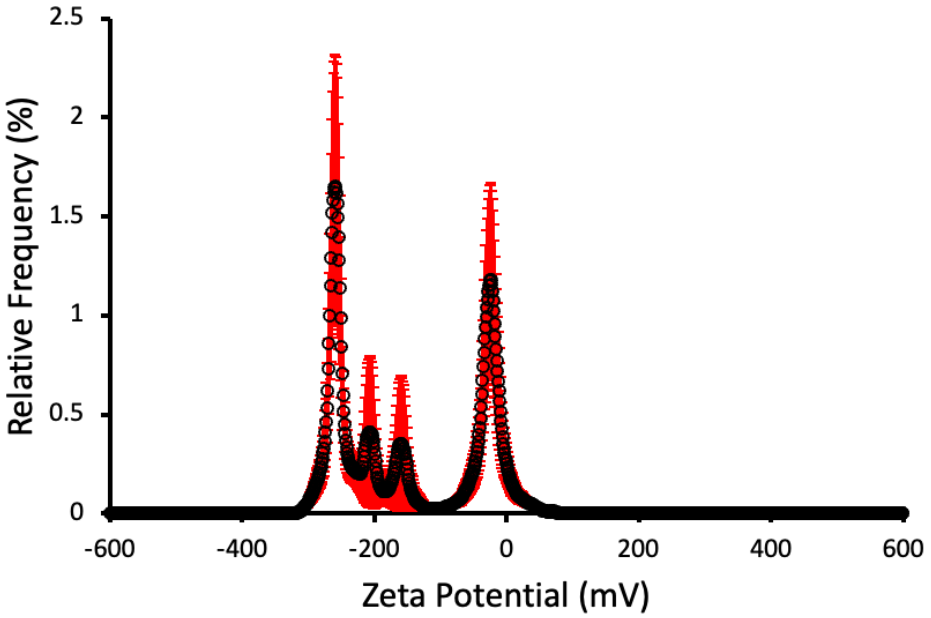

Figure S97 - The average zeta potential distribution for compound **15** (1.39 mM) in a 1:3 solution of 5 % EtOH in H_2O:TSB calculated using 10 runs at 298 K. Average measurement value: - 24.00 mV.

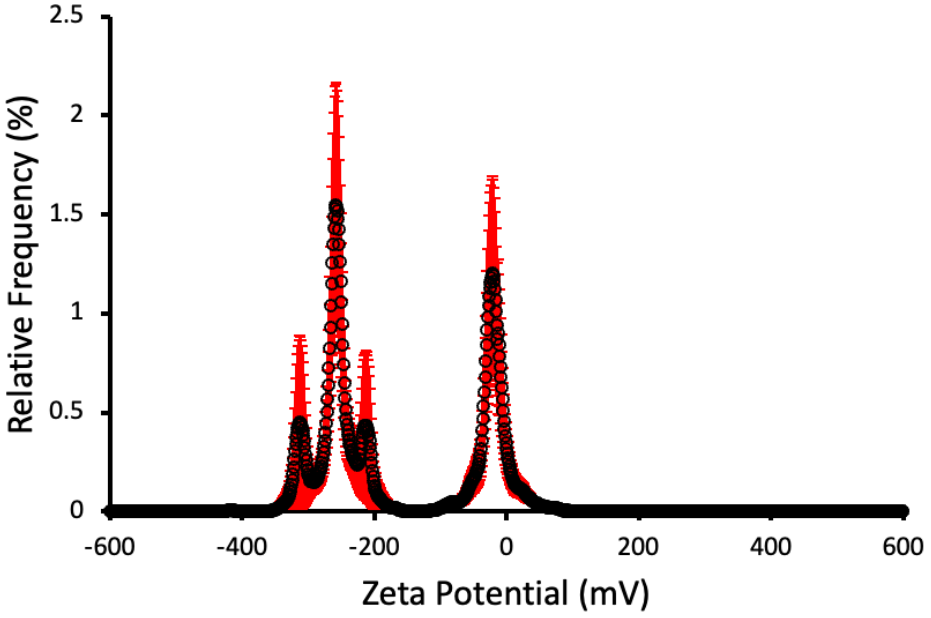

Figure S98 - The average zeta potential distribution for a 1:1 mixture of compounds **13** and **15** (1.39 mM) in a 1:3 solution of 5 % EtOH in H_2O:TSB calculated using 10 runs at 298 K. Average measurement value: - 22.72 mV.

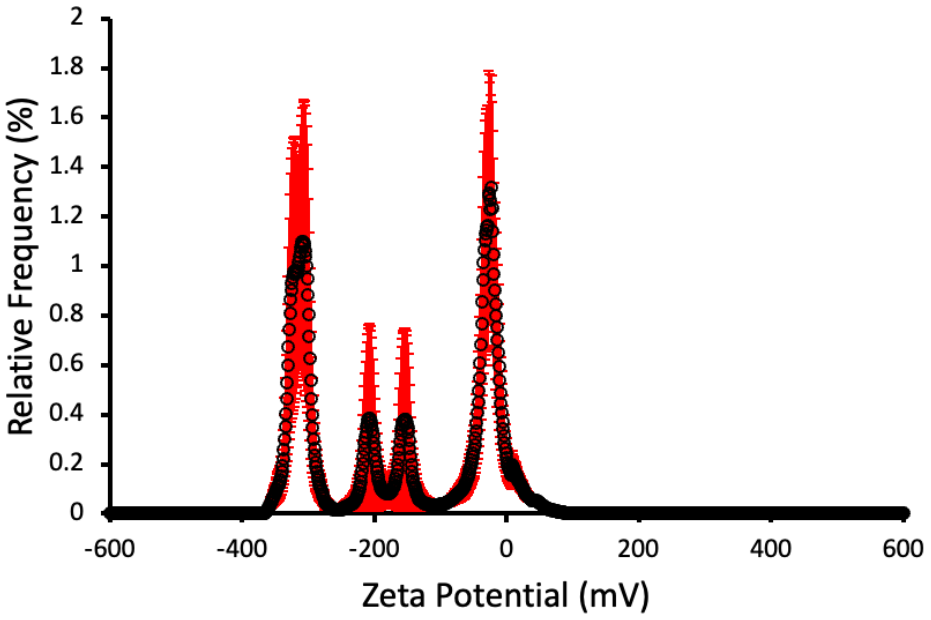

Figure S99 - The average zeta potential distribution for compound **17** (1.39 mM) in a 1:3 solution of 5 % EtOH in H_2O:TSB calculated using 10 runs at 298 K. Average measurement value: - 21.71 mV.

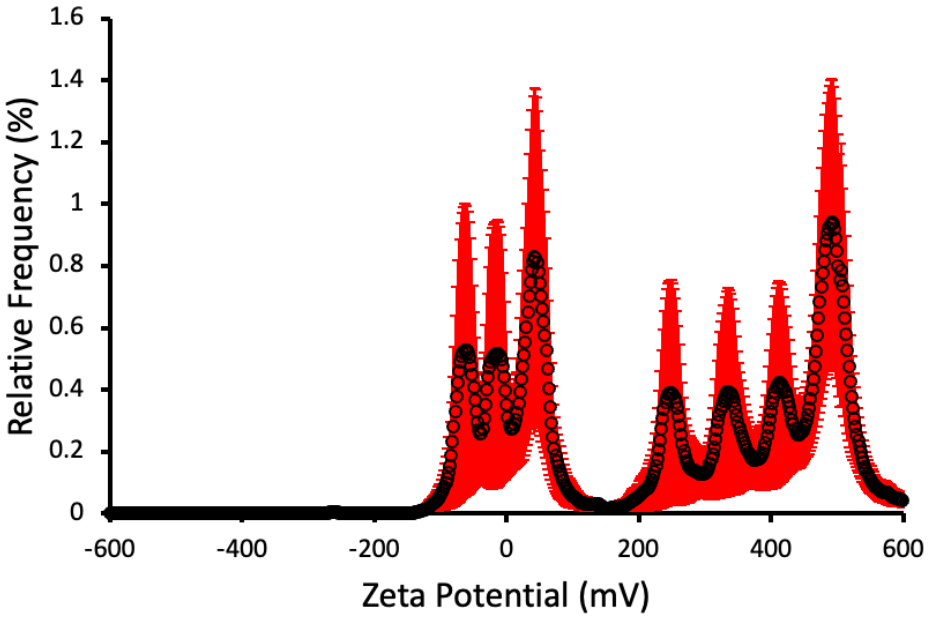

Figure S100 - The average zeta potential distribution for compound **19** (1.39 mM) in a 1:3 solution of 5 % EtOH in H_2O:TSB calculated using 10 runs at 298 K. Average measurement value: - 21.13 mV.

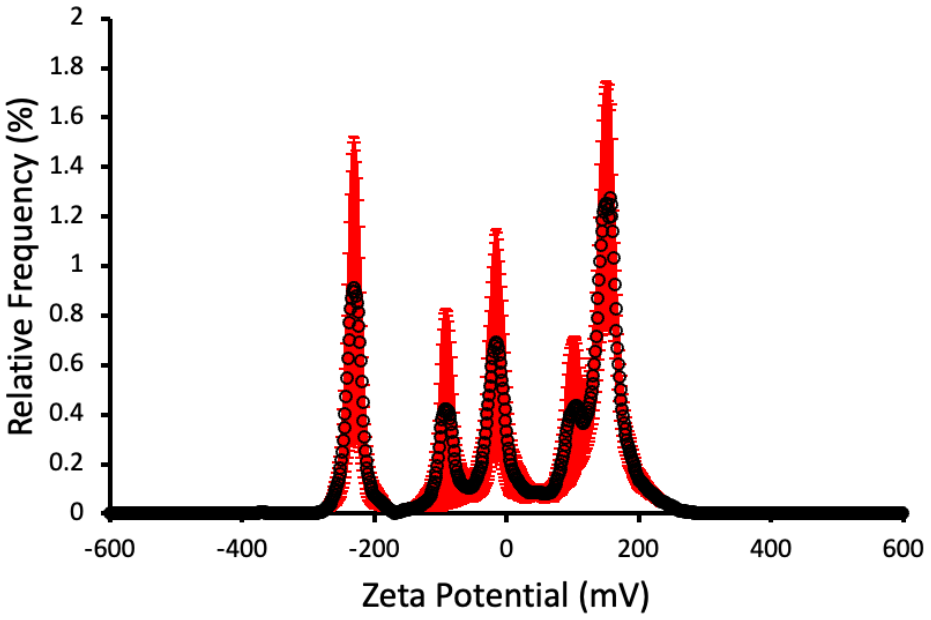

Figure S101 - The average zeta potential distribution for a 1:1 mixture of compounds **17** and **19** (1.39 mM) in a 1:3 solution of 5 % EtOH in H_2O:TSB calculated using 10 runs at 298 K. Average measurement value: - 20.15 mV.

7.6.4. Summary

Table S6 - Summary of the zeta potential (ZP) for compounds **13**, **15**, **17** and **19**, and racemic mixtures of isomers **13**+**15** and isomers **17**+**19** at 1.39 mM in a 1:3 solution of 5 % EtOH in H_2O:TSB at 298 K. [a] 1:1 mixture.

Compound	Zeta potential (mV)
9	- 6.76
13	- 23.11
15	- 24.00
13 + 15 [a]	- 22.72
17	- 21.71
19	- 21.13
17 + 19 [a]	- 20.15

7.6.5. Zeta Potential in IMDM with 10 % FBS

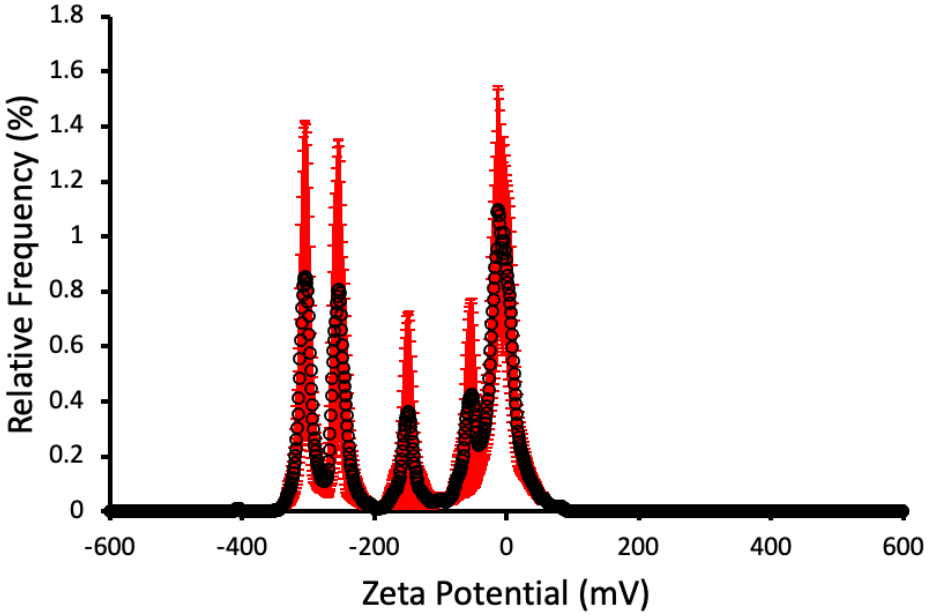

Figure S102 - The average zeta potential distribution for compound **9** (1.67 mM) in a 1:5 solution of 5 % EtOH in H_2O: IMDM with 10 % FBS calculated using 10 runs at 298 K. Average measurement value: - 6.20 mV.

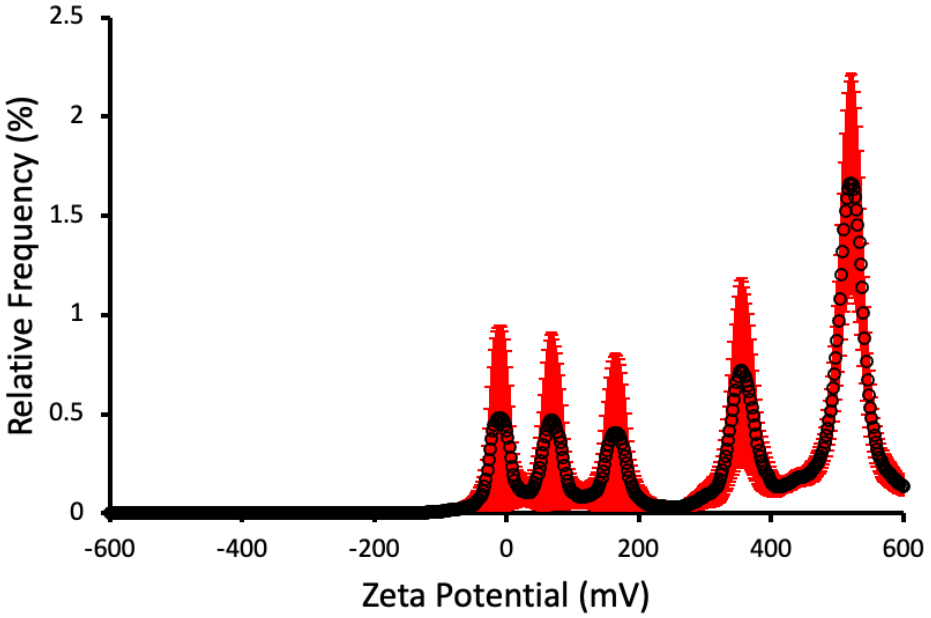

Figure S103 - The average zeta potential distribution for compound **13** (1.67 mM) in a 1:5 solution of 5% EtOH in H_2O: IMDM with 10 % FBS calculated using 10 runs at 298 K. Average measurement value: - 14.13 mV.

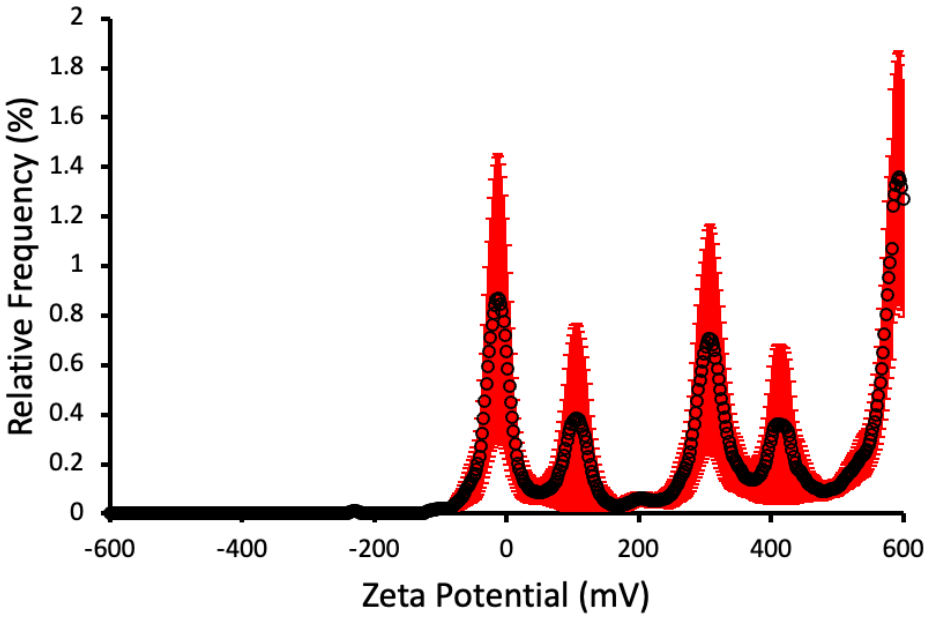

Figure S104 - The average zeta potential distribution for compound **15** (1.67 mM) in a 1:5 solution of 5 % EtOH in H_2O: IMDM with 10 % FBS calculated using 10 runs at 298 K. Average measurement value: - 14.70 mV.

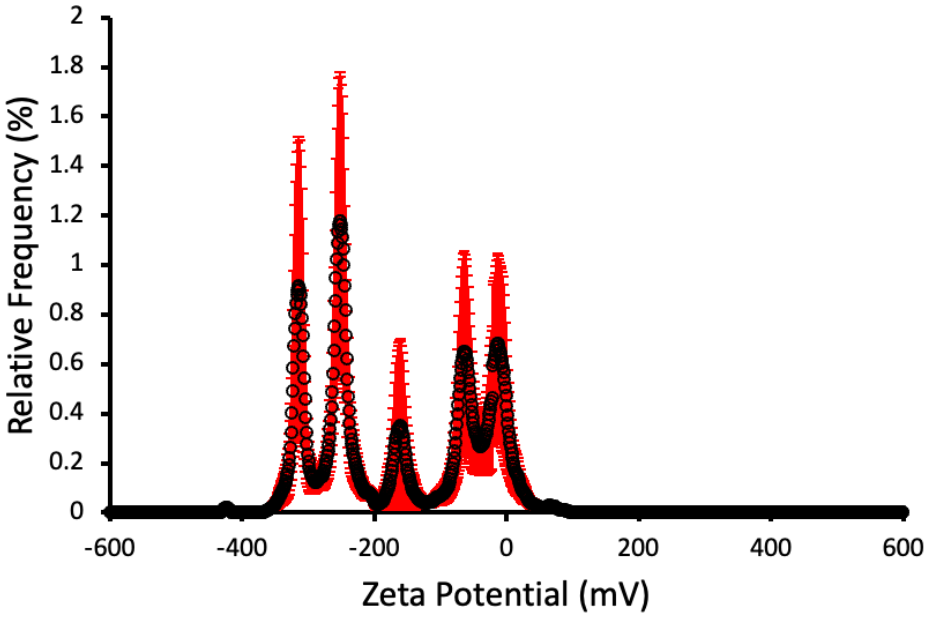

Figure S105 - The average zeta potential distribution for a 1:1 mixture of compounds **13** and **15** (1.67 mM) in a 1:5 solution of 5 % EtOH in H_2O: IMDM with 10 % FBS calculated using 10 runs at 298 K. Average measurement value: - 15.80 mV.

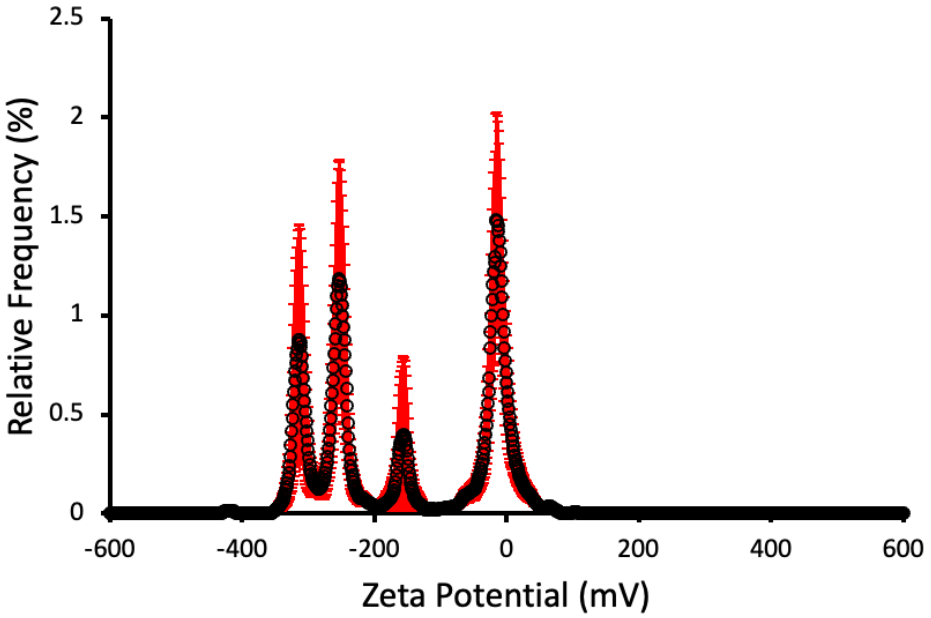

Figure S106 - The average zeta potential distribution for compound **17** (1.67 mM) in a 1:5 solution of 5 % EtOH in H_2O: IMDM with 10 % FBS calculated using 10 runs at 298 K. Average measurement value: - 12.91 mV.

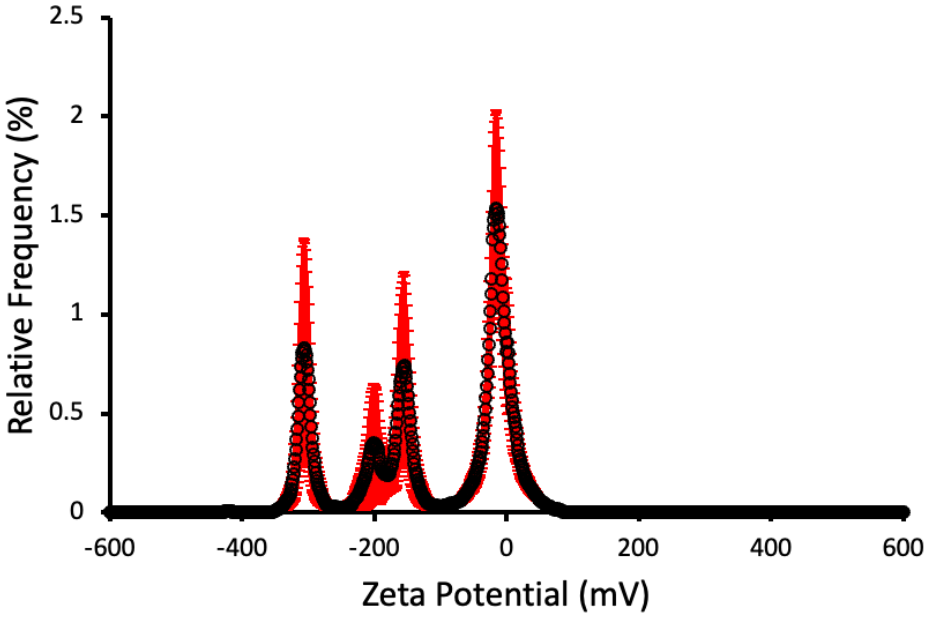

Figure S107 - The average zeta potential distribution for compound **19** (1.67 mM) in a 1:5 solution of 5 % EtOH in H_2O: IMDM with 10 % FBS calculated using 10 runs at 298 K. Average measurement value: - 12.38 mV.

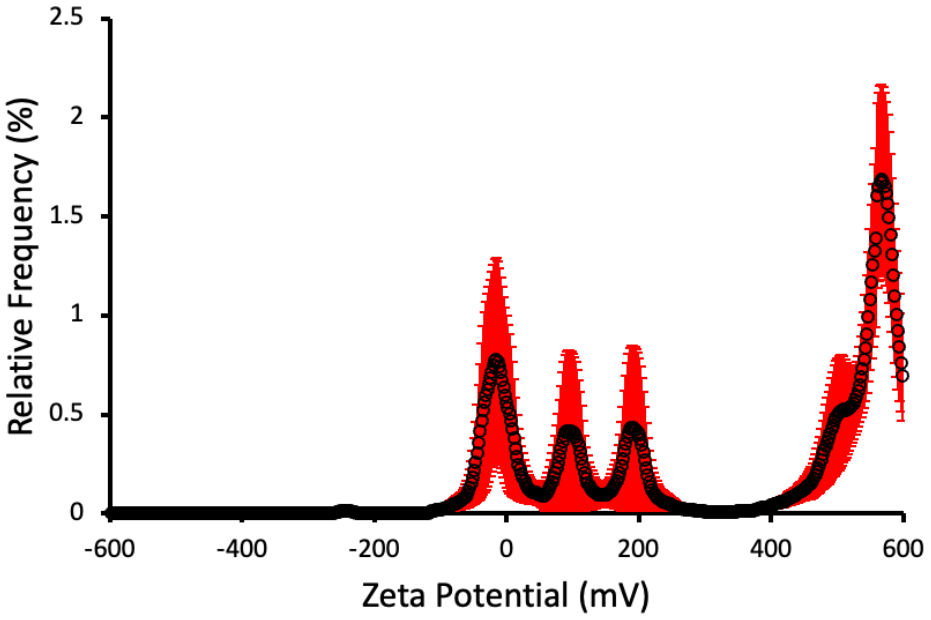

Figure S108 - The average zeta potential distribution for a 1:1 mixture of compounds **17** and **19** (1.67 mM) in a 1:5 solution of 5 % EtOH in H_2O: IMDM with 10 % FBS calculated using 10 runs at 298 K. Average measurement value: - 13.91 mV.

7.6.6. Summary

Table S7 - Summary of the zeta potential (ZP) for compounds **13**, **15**, **17** and **19**, and racemic mixtures of isomers **13**+**15** and isomers **17**+**19** at 1.67 mM in a 1:5 solution of 5 % EtOH in H_2O: IMDM with 10 % FBS at 298 K. [a] 1:1 mixture.

Compound	Zeta potential (mV)
9	- 6.20
13	- 14.13
15	- 14.70
13 + 15 [a]	- 15.80
17	- 12.91
19	- 12.38
17 + 19 [a]	- 13.91

7.6.7. Zeta Potential in PBS

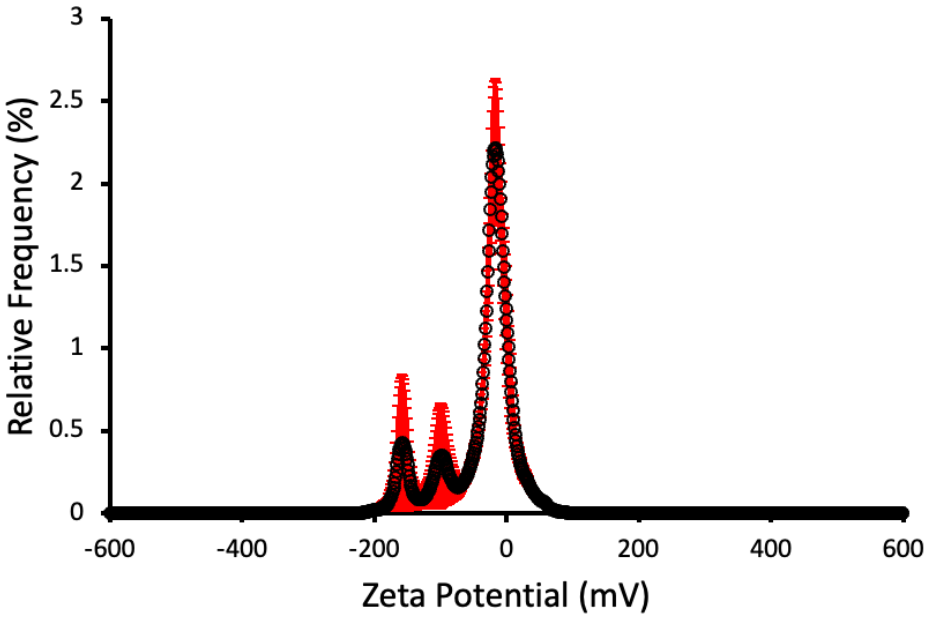

Figure S109 - The average zeta potential distribution for compound **9** (1.39 mM) in a 1:3 solution of 5 % EtOH in H_2O:PBS calculated using 10 runs at 298 K. Average measurement value: - 9.05 mV.

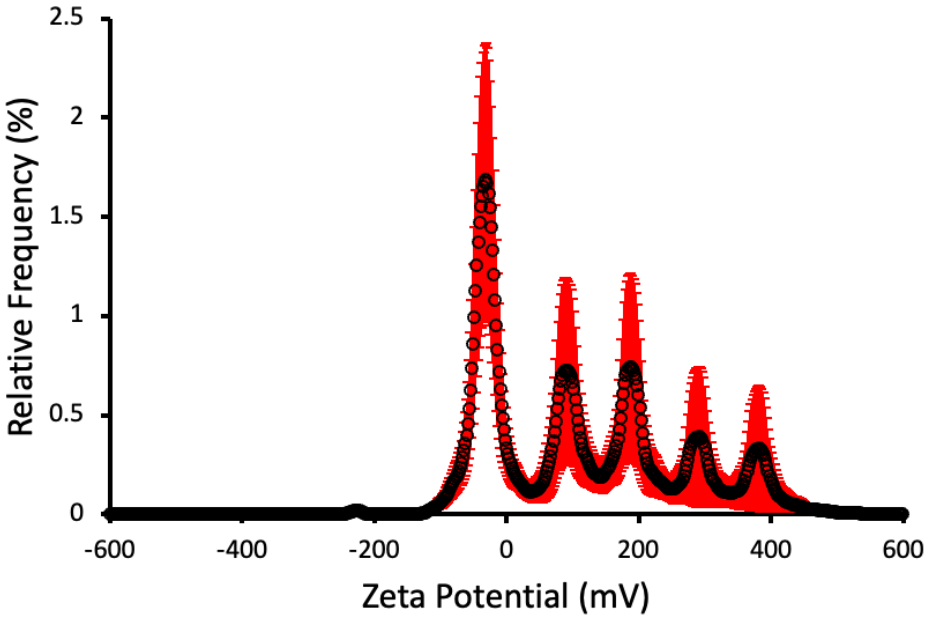

Figure S110 - The average zeta potential distribution for compound **13** (1.39 mM) in a 1:3 solution of 5 % EtOH in H_2O:PBS calculated using 10 runs at 298 K. Average measurement value: -31.47 mV.

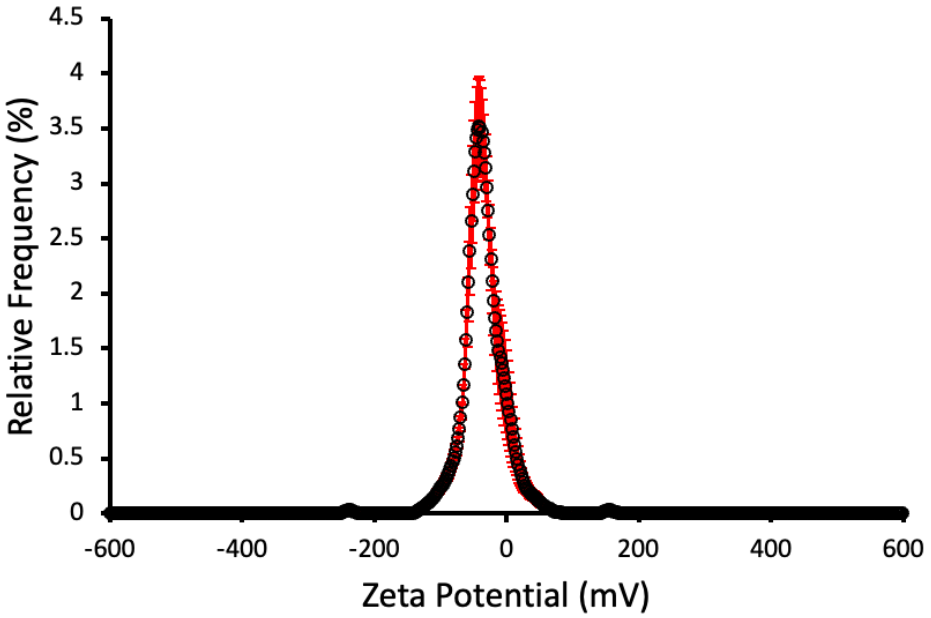

Figure S111 - The average zeta potential distribution for compound **15** (1.39 mM) in a 1:3 solution of 5 % EtOH in H_2O:PBS calculated using 10 runs at 298 K. Average measurement value: -41.64 mV.

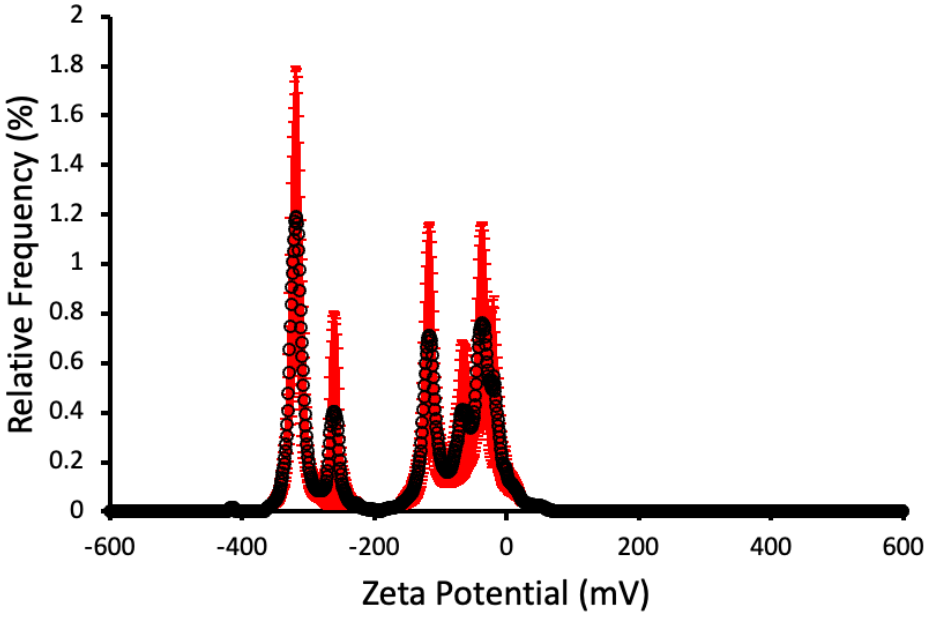

Figure S112 - The average zeta potential distribution for a 1:1 mixture of compounds **13** and **15** (1.39 mM) in a 1:3 solution of 5 % EtOH in H_2O:PBS calculated using 10 runs at 298 K .Average measurement value: - 28.84 mV.

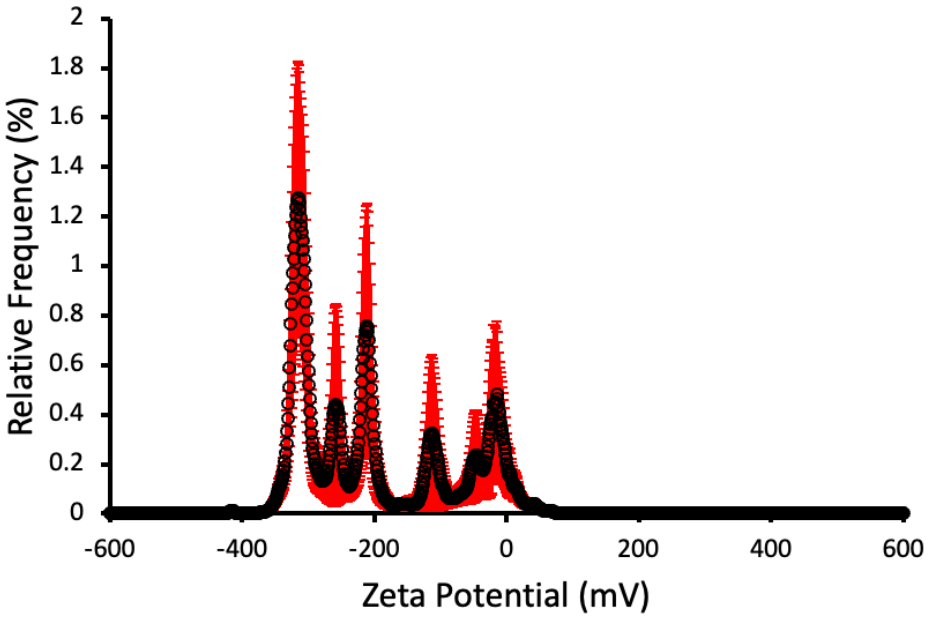

Figure S113 – The average zeta potential distribution for compound **17** (1.39 mM) in a 1:3 solution of 5 % EtOH in H_2O:PBS calculated using 10 runs at 298 K. Average measurement value: -27.11 mV.

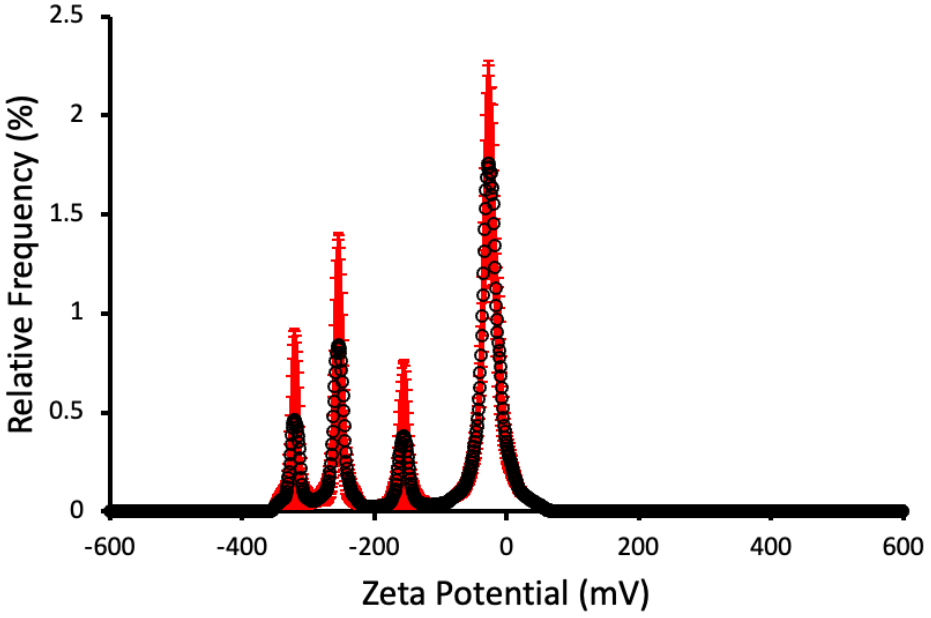

Figure S114 - The average zeta potential distribution for compound **19** (1.39 mM) in a 1:3 solution of 5 % EtOH in H_2O:PBS calculated using 10 runs at 298 K. Average measurement value: -20.90 mV.

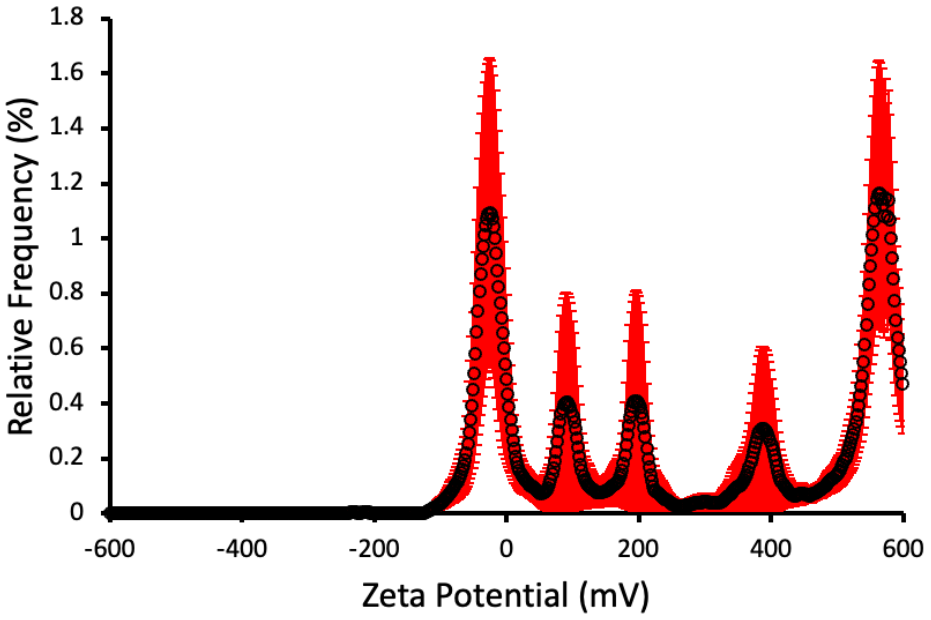

Figure S115 – The average zeta potential distribution for a 1:1 mixture of compounds **17** and **19** (1.39 mM) in a 1:3 solution of 5 % EtOH in H_2O:PBS calculated using 10 runs at 298 K. Average measurement value: - 23.16 mV.

7.6.8. Summary

Table S8 – Summary of the zeta potential (ZP) for compounds **13**, **15**, **17** and **19**, and racemic mixtures of isomers **13**+**15** and isomers **17**+**19** at 1.39 mM in a 1:3 solution of 5 % EtOH in H_2O:PBS at 298 K. [a] 1:1 mixture.

Compound	**Zeta potential (mV)**
9	- 9.05
13	- 31.47
15	- 41.64
13 + 15 [a]	- 28.34
17	- 27.11
19	- 20.90
17 + 19 [a]	- 23.16

7.7. Single Crystal X-ray Structures

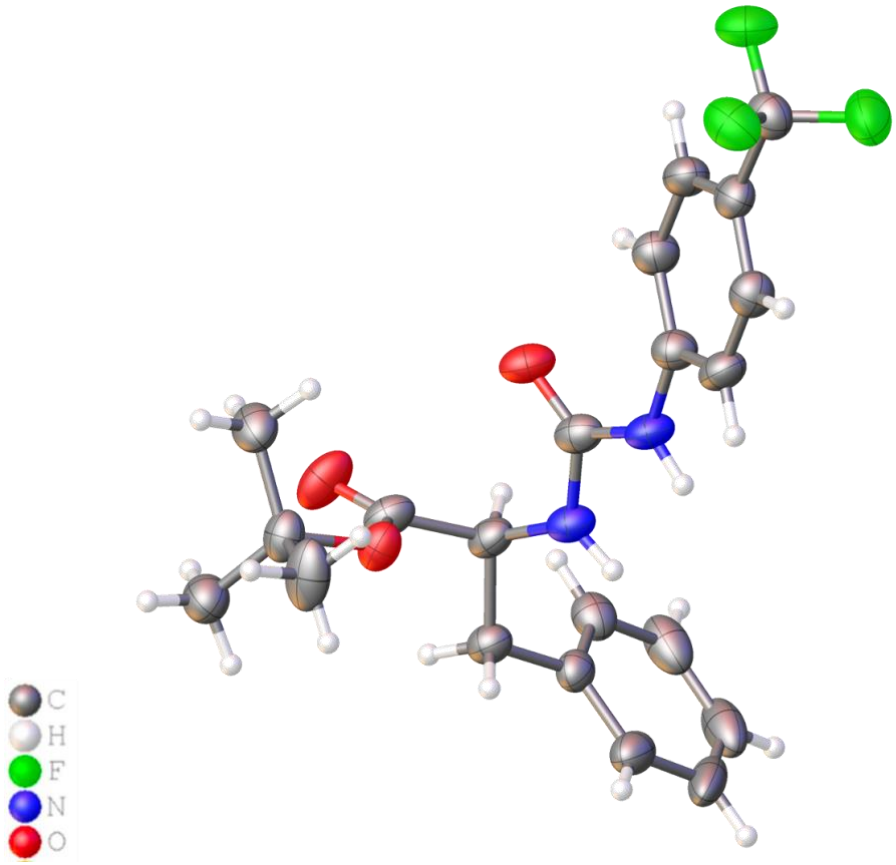

Figure S116 - Single crystal X-ray structure of **12**: red = oxygen; green = fluorine; blue = nitrogen; white = hydrogen; grey = carbon. CCDC 2205765, $C_{21}H_{23}F_3N_2O_3$ (M = 408.41): orthorhombic, space group P 21 21 21, a = 5.7353(4) Å, b = 18.3597(18) Å, c = 19.4042(15) Å, α = 90°, β = 90°, γ = 90°, V = 2043.2(3) Å^3, Z = 4, T = 100(1) K, CuK\α = 1.5418 Å, Dcalc = 1.328 g/cm^3, 13037 reflections measured (9.114 ≤ 2Θ ≤ 144.834), 3930 unique (R_{int} = 0.0790, R_{sigma} = 0.0731) which were used in all calculations. The final R_1 was 0.0717 (I > 2σ(I)) and wR_2 was 0.1927 (all data).

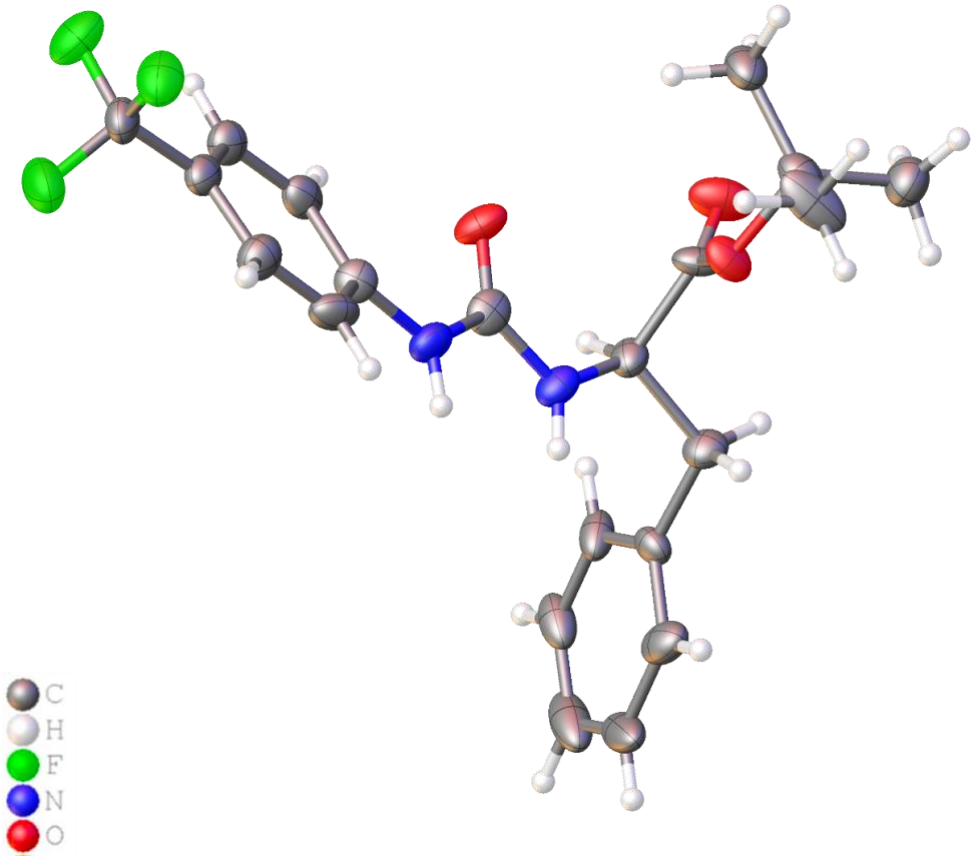

Figure S117 – Single crystal X-ray structure of **14**: red = oxygen; green = fluorine; blue = nitrogen; white = hydrogen; grey = carbon. CCDC 2205765, $C_{21}H_{23}F_3N_2O_3$ (M = 408.41): orthorhombic, space group P 21 21 21, a = 5.7453(6) Å, b = 18.227(3) Å, c = 19.3974(16) Å, α = 90°, β = 90°, γ = 90°, V = 2036.8(4) Å^3, Z = 4, T = 100(1) K, CuK\α = 1.5418 Å, Dcalc = 1.332 g/cm^3, 4808 reflections measured (9.118 ≤ 2Θ ≤ 144.298), 3301 unique (R_{int} = 0.1545, R_{sigma} = 0.1629) which were used in all calculations. The final R_1 was 0.1056 (I > 2σ(I)) and wR_2 was 0.3038 (all data).

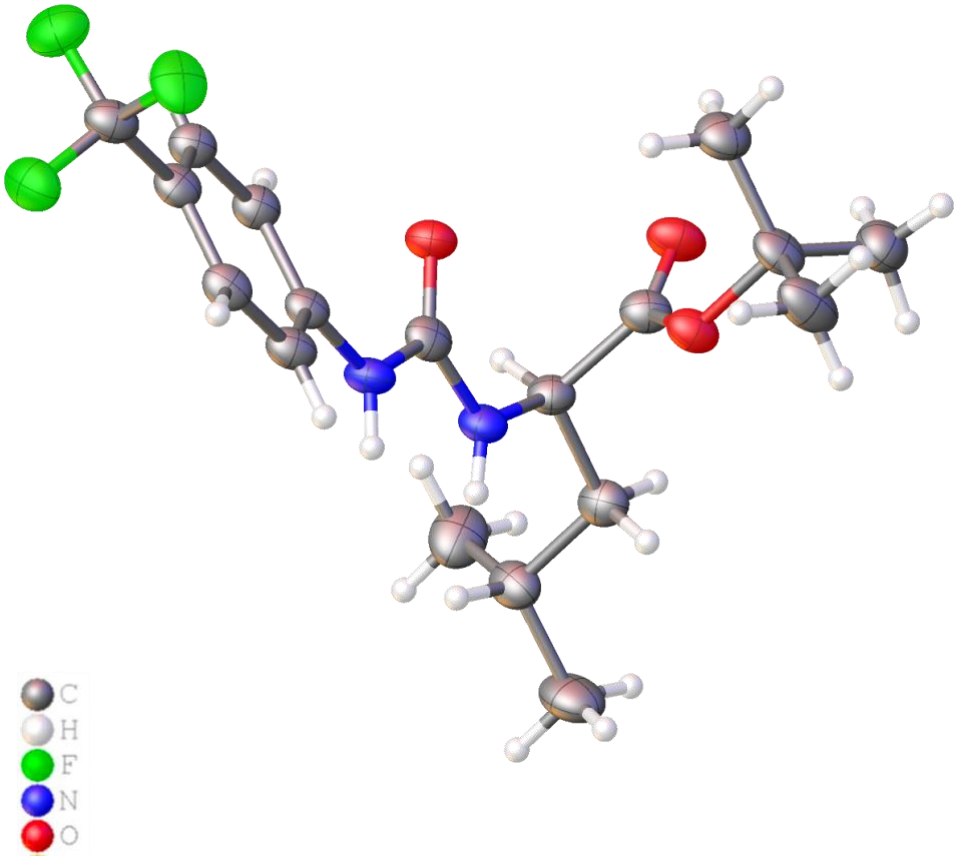

Figure S118 – Single crystal X-ray structure of **16**: red = oxygen; green = fluorine; blue = nitrogen; white = hydrogen; grey = carbon. CCDC 2205765, $C_{18}H_{25}F_3N_2O_3$ (M = 374.40): orthorhombic, space group P 21 21 21, a = 5.5098(7) Å, b = 18.427(4) Å, c = 18.838(3) Å, α = 90°, β = 90°, γ = 90°, V = 1912.6(6) Å^3, Z = 4, T = 100(1) K, CuK\α = 1.5418 Å, Dcalc = 1.300 g/cm^3, 12906 reflections measured (9.390 ≤ 2Θ ≤ 148.174), 3720 unique (R_{int} = 0.1367, R_{sigma} = 0.1210) which were used in all calculations. The final R_1 was 0.0591 (I > 2σ(I)) and wR_2 was 0.1361 (all data).

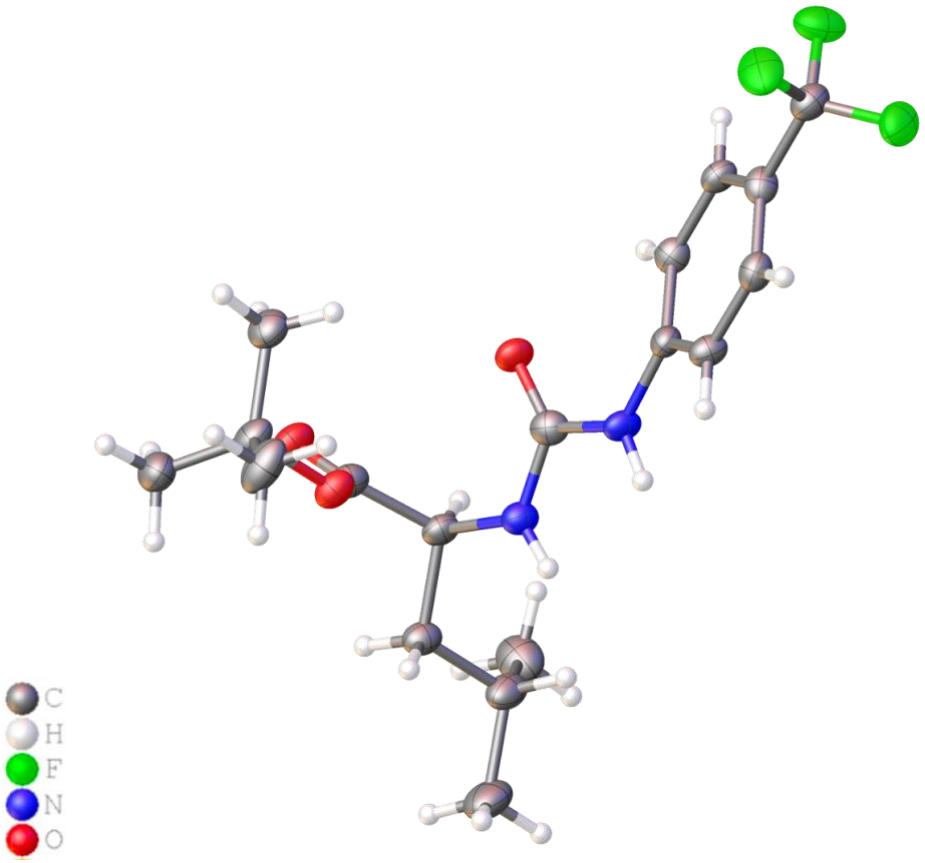

Figure S119 – Single crystal X-ray structure of **18**: red = oxygen; green = fluorine; blue = nitrogen; white = hydrogen; grey = carbon. CCDC 2205765, $C_{18}H_{25}F_3N_2O_3$ (M = 374.40): orthorhombic, space group P 21 21 21, a = 5.5068(4) Å, b = 18.3998(17) Å, c = 18.8406(14) Å, α = 90°, β = 90°, γ = 90°, V = 1909(3) Å^3, Z = 4, T = 100(1) K, CuK\α = 1.5418 Å, Dcalc = 1.303 g/cm^3, 12686 reflections measured (9.388 ≤ 2Θ ≤ 143.696), 3691 unique (R_{int} = 0.0935, R_{sigma} = 0.0908) which were used in all calculations. The final R_1 was 0.0663 (I > 2σ(I)) and wR_2 was 0.1531 (all data).

7.7.1. Hydrogen Bonding Tables

Table S9 - Hydrogen bond distances and angles observed for **12**, **14**, **16** and **18**, calculated from the single crystal X-ray structure shown in Figures S50 - S53.

Compound	Hydrogen bond donor	Hydrogen atom	Hydrogen bond acceptor	Hydrogen bond length (D•••A) (Å)	Hydrogen bond angle (D-H•••A) (°)
12	N1	H1	O1	3.482(7)	144.4(3)
	N1	H1	O2	3.372(7)	136.0(4)
	N2	H2	O2	2.824(7)	141.9(3)
14	N1	H1	O1	3.471(10)	171.84(11)
	N1	H1	O2	3.35(1)	135.3(5)
	N2	H2	O2	2.813(10)	143.7(5)
16	N1	H1	O1	3.271(6)	155.4(3)
	N2	H2	O2	2.858(5)	140.4(3)
18	N1	H1	O1	2.861(6)	155.8(3)
	N2	H2	O2	3.270(6)	141.1(3)

7.8. Mass Spectroscopy

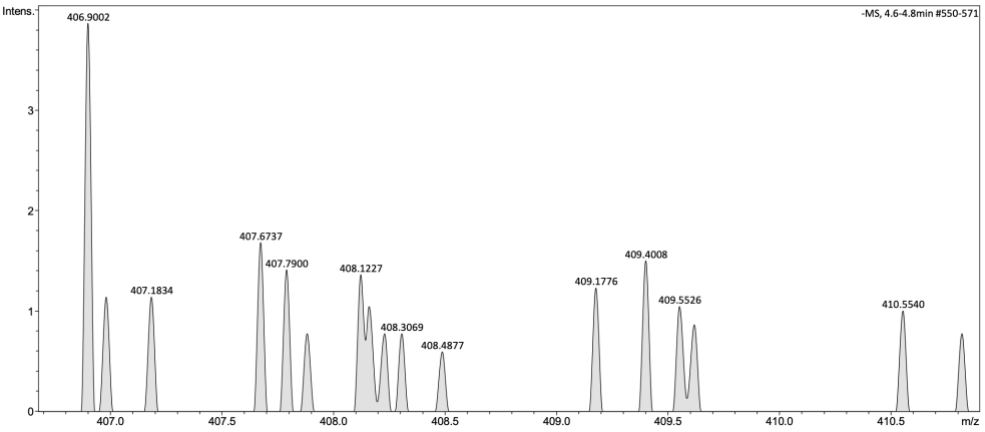

Figure S120 – A high-resolution mass spectrum (ESI^-) obtained for compound **12** in methanol, *m/z* $[M]^-$.

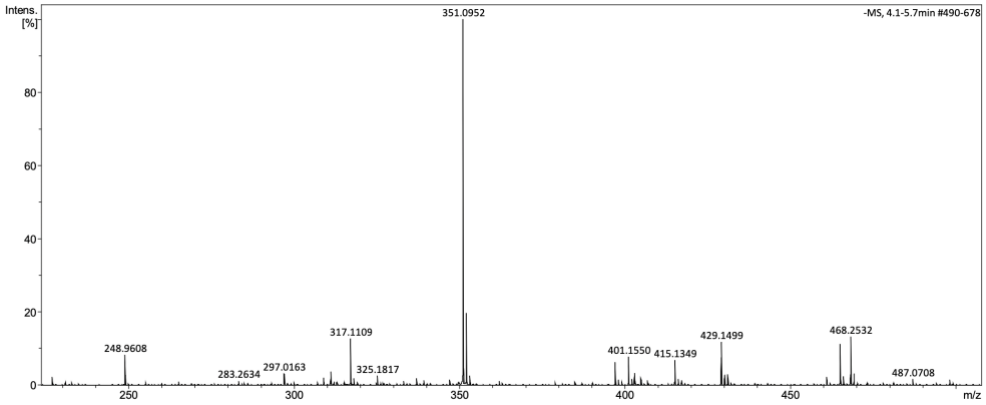

Figure S121 - A high-resolution mass spectrum (ESI^-) obtained for compound **13** in methanol, *m/z* $[M]^-$.

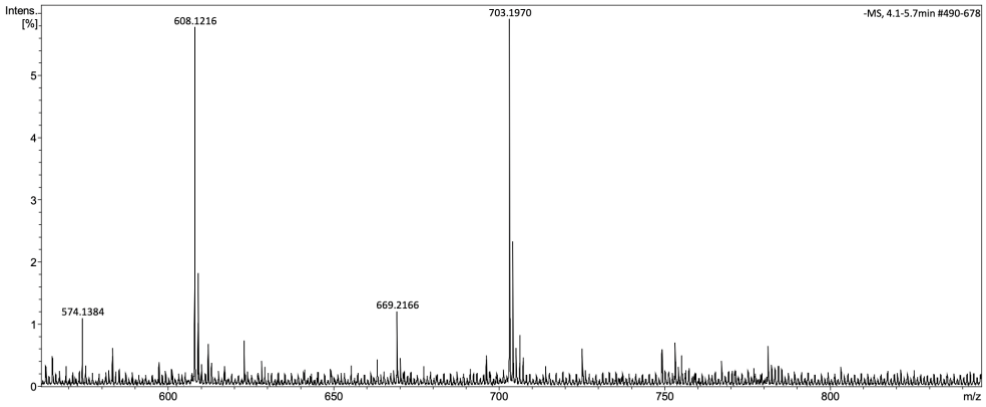

Figure S122 - A high-resolution mass spectrum (ESI^-) obtained for dimeric species of compound **13** in methanol, *m/z* $[M + M + H]^-$.

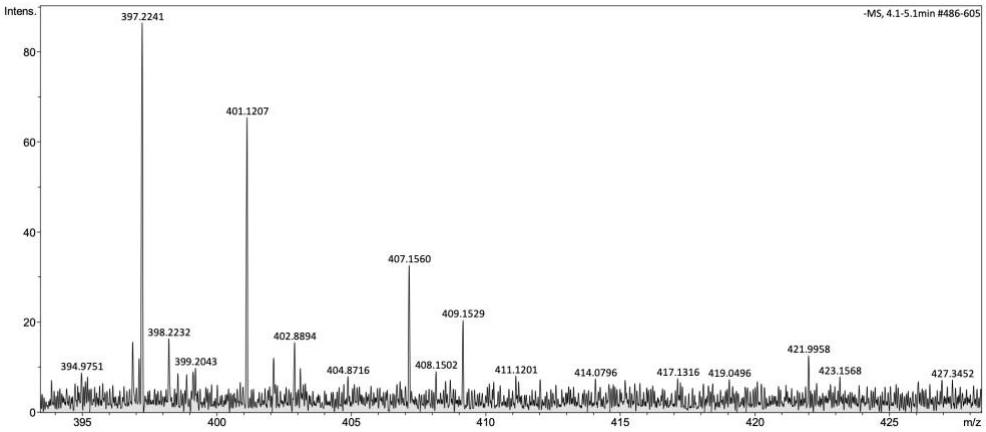

Figure S123 - A high-resolution mass spectrum (ESI^-) obtained for compound **14** in methanol, *m/z* $[M]^-$.

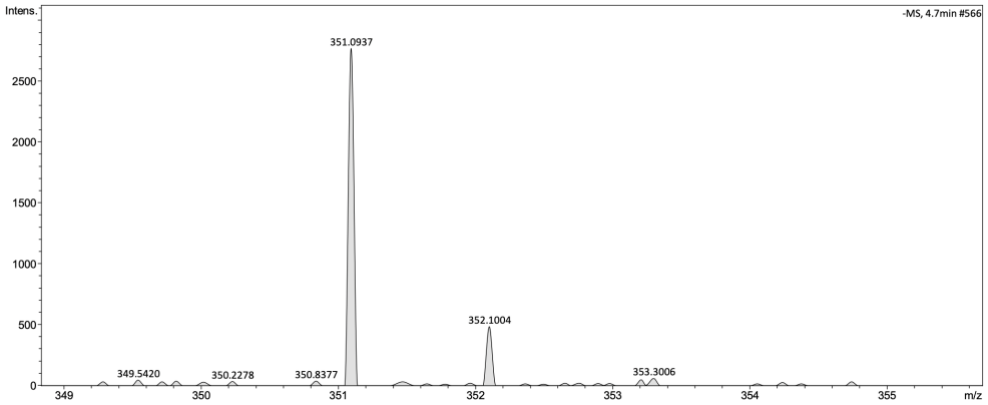

Figure S124 - A high-resolution mass spectrum (ESI^-) obtained for compound **15** in methanol, *m/z* $[M]^-$.

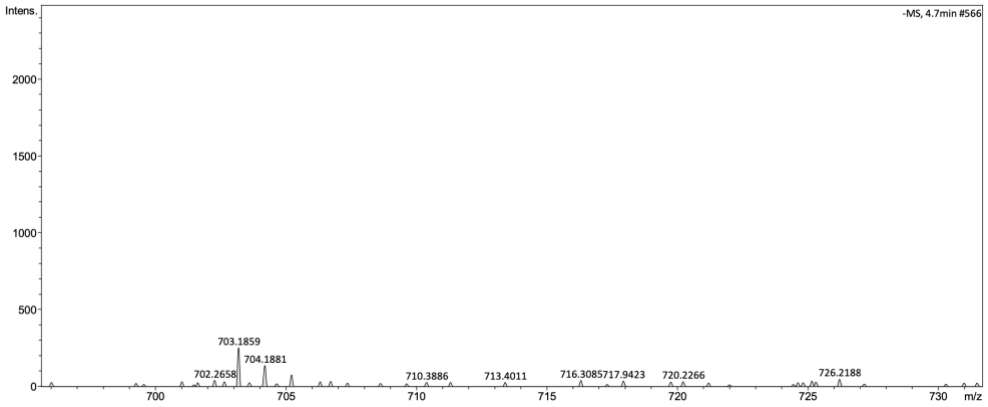

Figure S125 - A high-resolution mass spectrum (ESI^-) obtained for dimeric species of compound **15** in methanol, *m/z* $[M + M + H]^-$.

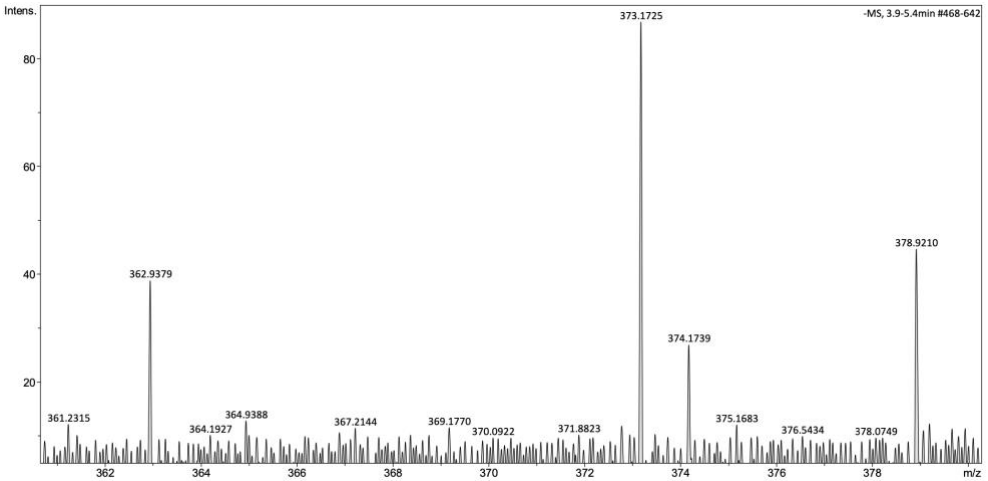

Figure S126 - A high-resolution mass spectrum (ESI^-) obtained for compound **16** in methanol, *m/z* $[M]^-$.

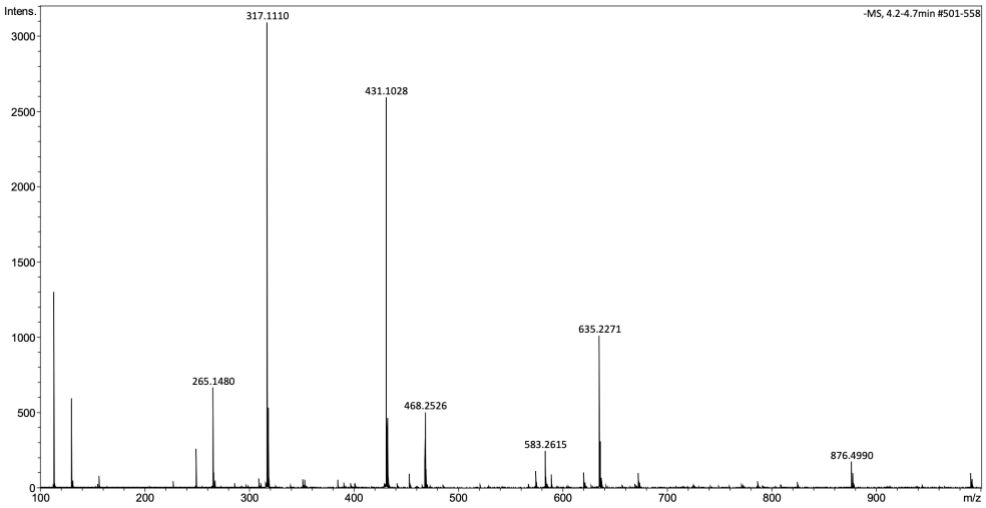

Figure S127 - A high-resolution mass spectrum (ESI^-) obtained for compound **17** in methanol, *m/z* $[M]^-$.

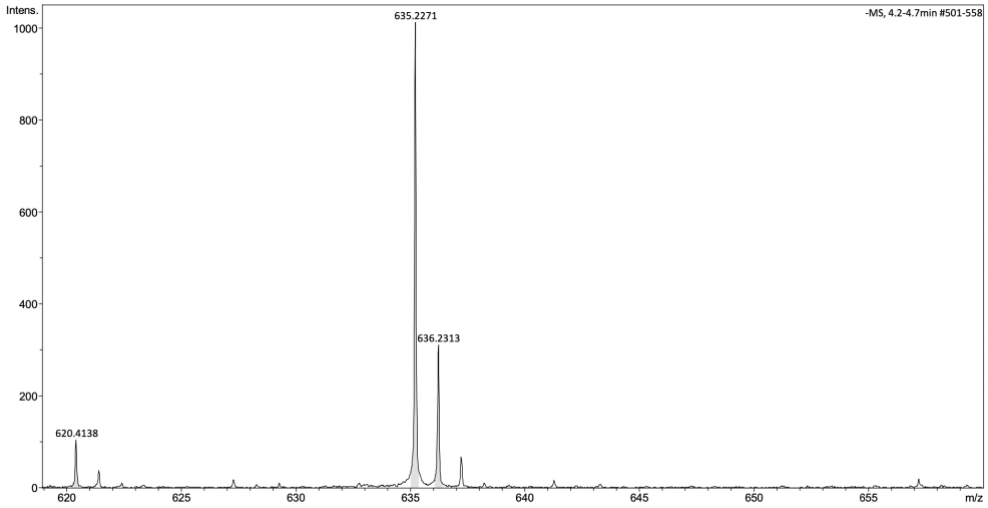

Figure S128 - A high-resolution mass spectrum (ESI^-) obtained for dimeric species of compound **17** in methanol, *m/z* $[M + M + H]^-$.

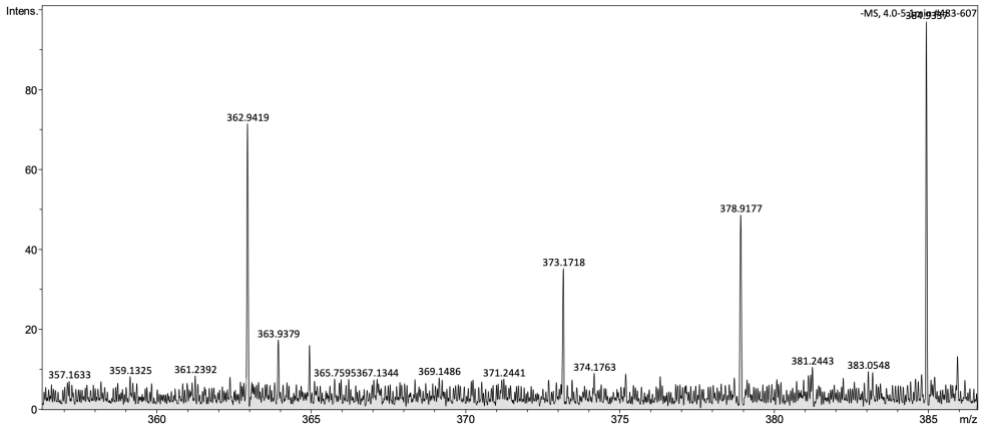

Figure S129 - A high-resolution mass spectrum (ESI^-) obtained for compound **18** in methanol, *m/z* $[M]^-$.

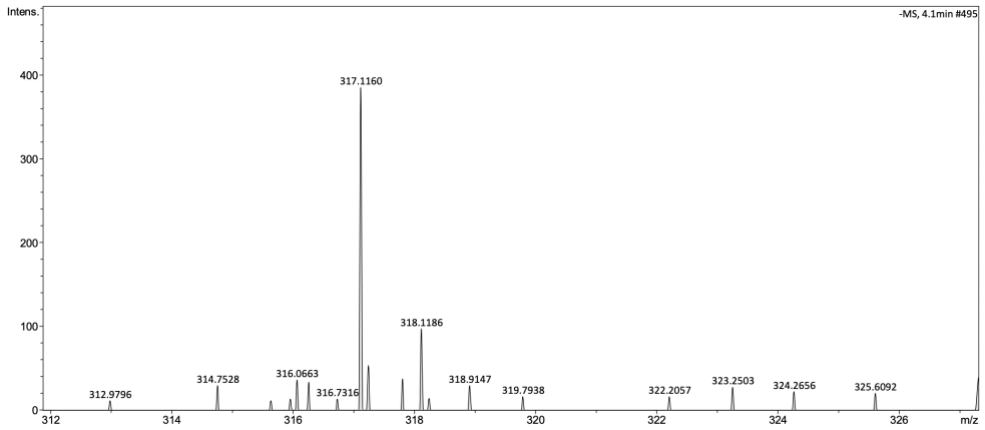

Figure S130 - A high-resolution mass spectrum (ESI^-) obtained for compound **19** in methanol, *m/z* $[M]^-$.

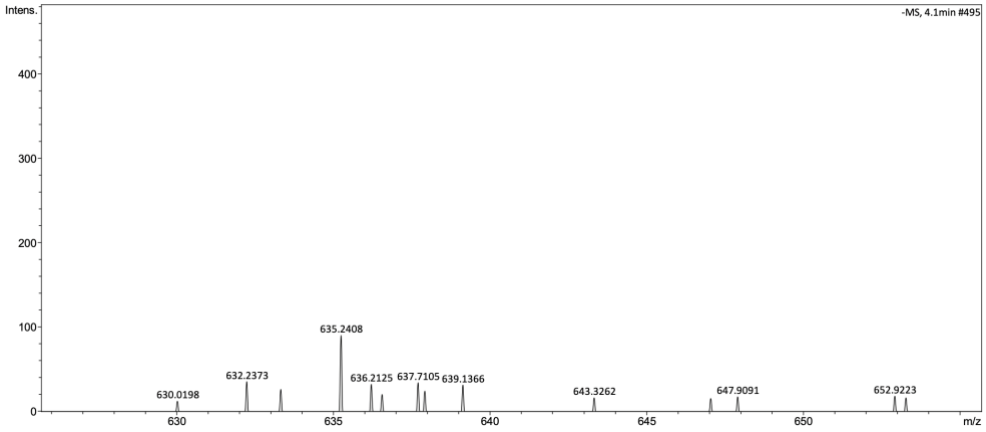

Figure S131 - A high-resolution mass spectrum (ESI^-) obtained for dimeric species of compound **13** in methanol, *m/z* $[M + M + H]^-$.

7.8.1. Summary

Table S10 – Summary of high-resolution electrospray ionisation mass spectrometry (ESI-MS) theoretical and experimentally derived values.

	m/z $[M]^-$		m/z $[M + M + H]^-$	
SSA	**Theoretical**	**Actual**	**Theoretical**	**Actual**
12	408.1661	408.1227	N/A	N/A
13	351.0962	351.0952	703.1996	703.1970
14	408.1661	408.1502	Not observed	
15	351.0962	351.0937	703.1996	703.1859
16	374.1817	374.1739	N/A	N/A
17	317.1118	317.1110	635.2308	635.2271
18	374.1817	374.1763	Not observed	
19	317.1118	317.1160	635.2308	635.2408

7.9. Circular Dichroism Studies

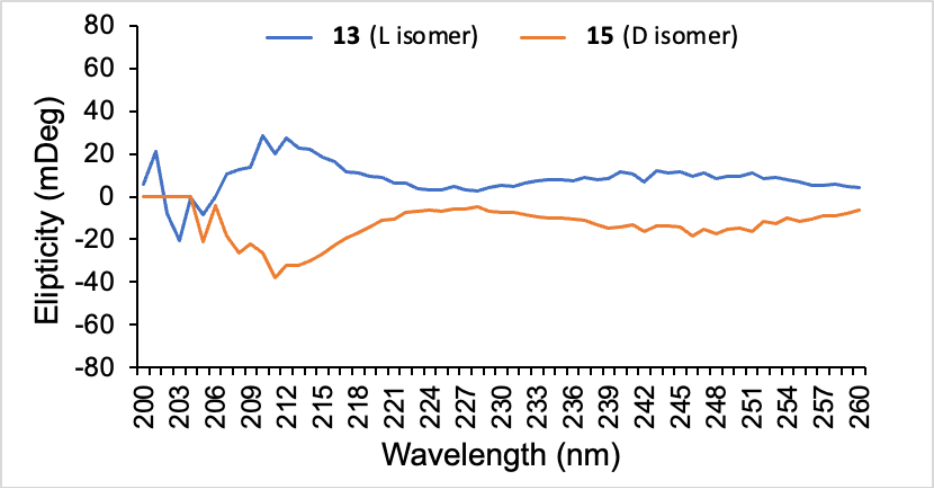

Figure S132 - The circular dichroism spectrum for **13** and **15** at 1 mM in EtOH:H_2O (1:19).

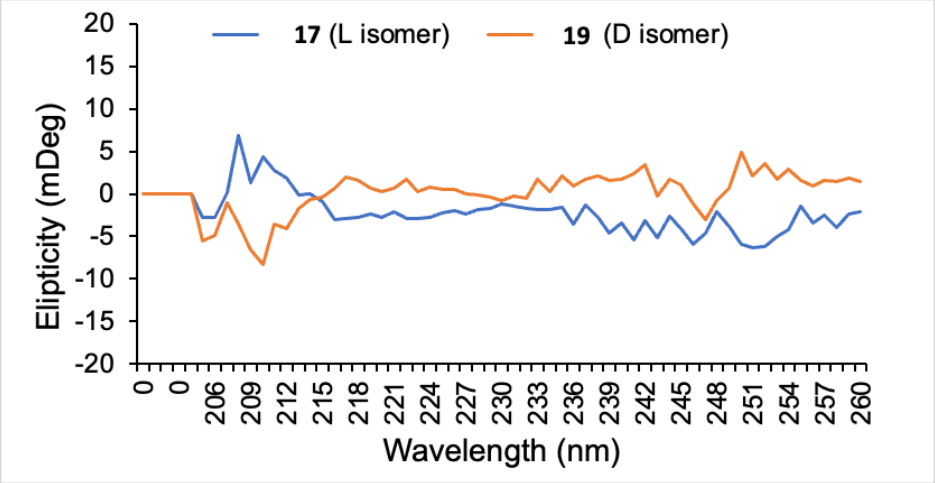

Figure S133 - The circular dichroism spectrum for **17** and **19** at 1 mM in EtOH:H_2O (1:19).

7.10. Biological Assays

7.10.1. Antimicrobial (MIC) Data

Table S11 – The minimum inhibitory concentration (MIC) values determined for **9**, **13**, **15**, **17**, **19** and racemic mixtures of the isomers (**13**+**15** and **17**+**19**) against 7 different Gram-positive *Staphylococcus aureus* (*S. aureus*), *Enterococcus faecalis* (*E. faecalis*) and *Enterococcus faecium* (*E. faecium*) bacteria strains. [a] racemic (1:1) mixture.

MIC (mM)							
Compound	***S. aureus* 9144**	***S. aureus* 13616**	***S. aureus* USA 300**	***S. aureus* 1199B**	***E. Faecalis* NCTC 775**	***E. Faecalis* NCTC 12201**	***E. Faecium* NCTC 12204**
9	1.390	> 2.780	> 2.780	> 2.780	> 2.780	> 2.780	> 2.780
13	0.087	0.087	0.087	0.174	> 2.780	> 2.780	> 2.780
15	0.174	0.087	0.087	0.174	2.780	> 2.780	> 2.780
13 + 15 [a]	0.087	0.087	0.087	0.087 – 0.349	> 2.780	> 2.780	> 2.780
17	0.087	0.087	> 2.780	0.087	> 2.780	> 2.780	> 2.780
19	0.174	0.087	> 2.780	2.780	2.780	> 2.780	> 2.780
17 + 19 [a]	0.174	0.087	0.174	0.174	> 2.780	> 2.780	> 2.780

7.10.2. Anticancer (GI_{50}) Data

Table S12 - The concentration of compound required to reduce/ inhibit cellular growth by 50% (GI_{50}) determined for **9**, **13**, **15**, **17**, **19** , racemic mixtures of the isomers (**13**+**15** and **17**+**19**), cisplatin and TBA chloride against non-cancerous RPE-1 cells, ovarian cancer cells (A2780 SRB) and cisplatin resistant ovarian cancer cells (A2780 CisR SRB). [a] racemic (1:1) mixture. – not yet determined.

	RPE-1 SRB Assays			**A2780 SRB Assays**			**A2780 CisR SRB Assays**		
Compound	**Mean GI_{50} (μM)**	**SD +/-**	**R^2 > 0.9 n=**	**Mean GI_{50} (μM)**	**SD +/-**	**R^2 > 0.9 n=**	**Mean GI_{50} (μM)**	**SD +/-**	**R^2 > 0.9 n=**
Cisplatin	3.593	1.01	2	0.532	0.3	4	12.7175	6	4
TBA Cl	162.65	30.61	2	113.78	3.36	4	222.46	5.64	3
9	194	96.87	2	120.75	9.9	4	325.06	35.3	3
13	-	-	-	176.08	13.86	4	390.28	23.06	3
15	-	-	-	99.97	10.10	5	196.9	9.04	4
13 + 15 [a]	-	-	-	86.81	1	3	160.35	5.37	3
17	-	-	-	-	-	-	-	-	-
19	-	-	-	-	-	-	-	-	-
17 + 19 [a]	-	-	-	-	-	-	-	-	-

7.10.3. Toxicity and Haemolysis Data

Table S13 – The toxicity of **9**, **13**, **15**, **17**, **19** and racemic mixtures of the isomers (**13**+**15** and **17**+**19**) determined by observing the number of Galleria moth larvae that survived out of 10 after injection of compound. PBS and EtOH:H_2O (1:19) solution were used as controls. [a] racemic (1:1) mixture.

	Galleria moth larvae survived				
Compound	**Day 1**	**Day 2**	**Day 3**	**Day 4**	**Day 5**
9	10	9	8	6	6
13	10	4	4	4	4
15	9	9	9	7	5
13 + 15 [a]	9	8	4	4	4
17	9	9	9	6	5
19	10	9	8	8	8
17 + 19 [a]	7	7	7	4	3
PBS	10	10	10	10	10
EtOH:H_2O (1:19)	10	10	10	10	10

Table S14 – The haemolysis of red blood cells determined for **9**, **13**, **15**, **17**, **19** and racemic mixtures of the isomers (**13**+**15** and **17**+**19**) obtained at 1.39 mM. EtOH:H_2O (1:19) solution was used as a control. [a] racemic (1:1) mixture.

Compound	**Haemolysis at 1.39 mM (%)**	**Standard deviation**
9	0.30	0.56
13	0.50	0.48
15	- 0.34	0.54
13 + 15 [a]	0.30	0.52
17	- 0.44	1.78
19	- 0.23	1.22
17 + 19 [a]	0.80	0.54
1:19 EtOH/H_2O	0.50	0.05